Epitaxial engineering of ferrimagnetic double perovskites

TECHNISCHE UNIVERSITÄT DARMSTADT

vom Fachbereich Material- und Geowissenschaften

zur Erlangung des akademischen Grades eines
Doktors der Ingenieurwissenschaften (Dr.-Ing.)

genehmigte Dissertation von

B. Tech. Vikas Shabadi
geb. in Bangalore, Indien

Darmstadt 2017 – D17

Referent:	Prof. Dr. Lambert Alff
Zweitreferent:	Prof. Dr. Wolfgang Donner
Tag der Einreichung:	01.03.2017
Tag der mündlichen Prüfung:	21.04.2017

तमसो मा ज्योतिर् गमय ||
tamaso mā jyotir gamaya ||

From darkness (of ignorance) to light (of knowledge).

– Brihadaranyaka Upanishad, ~700 BC

To my four pillars of strength –
my parents Siddaram & Vasanthi,
brother Guruprerana and
my beautiful wife Nandita,
for their unconditional love and support.

Eidesstattliche Erklärung

Hiermit versichere ich an Eides statt, dass ich die vorliegende Dissertation selbständig und nür mit den angegebenen Hilfsmitteln angefertigt habe.

Darmstadt, im März 2017

Vikas Shabadi

Abstract

Double perovskite (DP) oxides of the type $A_2BB'O_6$ (*A*: 12-coordinated large di/tri-valent cation; *B/B'*: octahedrally coordinated transition metals) offer a unique material framework to engineer a wide range of physical functionalities. In its simplest form, the DP structure involves a cubic array of *A*-cations which is interspersed by corner-sharing BO_6 and $B'O_6$ octahedra, often arranged in a rock-salt type order. The choice of the *B/B'* cations and their coupling within the ordered DP structure are known to largely determine the electronic structure and the resulting functionality of the compounds. Compounds such as the $3d^5$-$4d^1$ coupled Sr_2FeMoO_6 (which exhibits fully spin polarized charge carriers and large magnetoresistance at room-temperature[1]) and the $3d^3$-$5d^3$ coupled Sr_2CrOsO_6 (which shows a high ferrimagnetic ordering temperature and a positive temperature coefficient of coercivity[2]) stand as prominent examples for the diversity of physical functionalities achievable in these compounds. Yet, it is interesting to note that a vast majority of all possible DP compounds remain experimentally unexplored,[3] mainly due to the meta-stable nature of some compounds and/or due to challenging synthesis procedures. With recent advances in thin film technology, particularly with techniques such as pulsed laser deposition (PLD), the ability to stabilize complex multi-cation oxides by epitaxial strain under non-equilibrium growth conditions has been well established. Furthermore, the PLD process has also been noted to support spontaneous cation ordering driven by a contrast in size/charge of cations. These developments provide an effective alternative route to overcome the synthesis challenges associated with meta-stable DP compounds.

In this work, we use the PLD based thin film approach to explore ferrimagnetic insulating phases among DPs. Such phases when stabilized as thin films can have wide range of possible device applications in the areas of spin-electronics and modern computing. In addition, such compounds can also be viable templates for achieving single phase type I multiferroism, if the *A*-sites are subsequently substituted with a ferroelectric active cation such as Bi^{3+}. The study was carried out across two families of double perovskites, namely 3*d*-3*d* and 3*d*-5*d* (the nomenclature refers to the elemental periods from which the *B* and *B'* cations are chosen). Within the 3*d*-3*d* family, we chose to explore Bi_2FeCrO_6 (BFCO), a compound theoretically predicted to be a robust ferrimagnetic-ferroelectric. Epitaxial thin films of BFCO grown via PLD on single crystal $SrTiO_3$ (STO) substrates were phase pure and fully strained. Distinct and intense superstructure peaks (SPs) were observed in XRD scans along the pseudo-cubic [111] direction. Considering the low scattering contrast between Fe and Cr, intensity of the SPs appeared suspiciously high. Using the photon energy dependence of contrast between atomic

scattering factors of Fe and Cr, a spontaneous chemical ordering at the *B*-site was ruled out. Detailed structural calculations showed that the experimentally observed superstructure occurs due to crystal distortions involving unequal shifts of cations along the pseudo-cubic [111] direction. This result helped to clarify the discrepancies in magnetic and structural order reported for BFCO. It was also established that the observation of the XRD SPs alone may not be sufficient proof of chemical ordering in DPs. Consequently a very weak magnetization of 0.06 $\mu_B/f.u.$ was achieved for BFCO.

The key findings from BFCO paved way for further work on 3*d*-5*d* family of DPs which, owing to larger possible *B/B'* cation size/charge contrasts, offer better prospect of achieving structural and magnetic order. However 3*d*-5*d* compounds for insulating magnetism or multiferroic purposes have so far been neglected due to rarity of insulating phases among them as well as complicated synthesis involved. Using density functional calculations, new ferrimagnetic insulating phases were identified in two promising DPs La_2MnReO_6 (LMRO) and La_2NiReO_6 (LNRO). Motivated by the findings, stoichiometric ceramic pellets for PLD growth of LMRO and LNRO were fabricated via an evacuated sealed quartz tube sintering process. Subsequently, established PLD procedures were used to epitaxially stabilize phase pure films of LMRO and LNRO on single crystalline STO substrates. In contrast to BFCO, both 3*d*-5*d* compounds showed a theoretically consistent and significant magnetization of 2.20 (LMRO) and 0.38 (LNRO) $\mu_B/f.u.$ suggesting presence of a stable magnetic and chemical order. A cross-sectional atomic resolution transmission electron microscopy and energy dispersive X-ray analysis confirmed the *B/B'* chemical order in LMRO. X-ray magnetic circular dichroism measurements showed consistent observation in accordance with the ferrimagnetic order and also provided evidence of an unquenched orbital moment. Furthermore, a metal to insulator transition observed in LMRO added to the functional qualities of the compound. This transition was noted to result from an orbital symmetry selective hybridization of 3*d* and 5*d* orbitals and the same was confirmed by dynamic mean field theory calculations. The results illustrate the untapped potential of double perovskites as functional oxides and the effectiveness of the PLD based thin film approach to realize them.

Curriculum vitae

Vikas Shabadi, born on 14th of February 1988 in Bangalore, India. Married since 05/2013.

School education:

06/1991 – 03/2004	**Primary & secondary schooling – Sindhi High School, Bangalore India** – Affiliated to Central Board of Secondary Education, New Delhi - India
06/2004 – 03/2006	**Senior secondary schooling – National Academy for Learning, Bangalore** – Affiliated to Central Board of Secondary Education, New Delhi - India

University education:

06/2006 – 05/2010	**Bachelor of Technology (B.Tech)** **National Institute of Technology Karnataka (NITK), Surathkal – India** – Metallurgical & Materials Engineering
10/2010 – 03/2017	**Graduate & Doctoral Studies** **Advanced Thin Film Technology Div., Institute of Materials Science** **Darmstadt University of Technology, Germany** – Supervisor: Prof. Dr. Lambert Alff – Thesis: *"Epitaxial engineering of ferrimagnetic double perovskites"*

Work experiences

05/2007 – 08/2010	**Internship – Materials Research Center (MRC),** Indian Institute of Science, Bangalore, India.
05/2008 – 08/2008	**Internship - Laboratoire de Métallurgie Physique et Génie des Matériaux,** Université Lille 1 – EGIDE – Campus France Fellowship
05/2009 – 08/2009	**Internship - Advanced Thin Film Technology Div.** TU Darmstadt – DAAD WISE Fellowship
10/2010 – 03/2017	**Doctoral Candidate - Advanced Thin Film Technology Div.** TU Darmstadt – DAAD Ph.D. Fellowship

List of scientific contributions

Journals:

"Origin of superstructures in (double) perovskite thin films"
V. Shabadi, M. Major, P. Komissinskiy, M. Vafaee, A. Radetinac, M. Baghaie Yazdi, W. Donner and L. Alff
J. Appl. Phys. **116** (2014) 114901

"Orbital symmetry selective metal-insulator transition in cation ordered 3*d*-5*d* double perovskite"
V. Shabadi, A. Kulkarni, P. Komissinskiy, I. Slipukhina, R. PariaSena, A. Jakobsson, F. Gulloiu, F. Wilhelm, A. Rogalev, R. Gupta, H. Zhang, J. Hadermann, M. Ležaić and L. Alff
(Manuscript in preparation)

Conferences & workshops:

"PLD grown thin-films of multiferroic double perovskite Bi_2FeCrO_6"
V. Shabadi, P. Komissinskiy and L. Alff
International School of Oxide Electronics (ISOE2011) – Corsica, France, 3. – 15. October 2011.

"Fe-Cr cation ordering in PLD grown thin-films of multiferroic double perovskite Bi_2FeCrO_6"
V. Shabadi, P. Komissinskiy, M. Vafaee, A. Radetinac and L. Alff
DPG-Spring Meet 2012, Berlin, Germany, 25. – 30. March 2012.

"Epitaxial thin films of the multiferroic double perovskite Bi_2FeCrO_6"
V. Shabadi, M. Vafaee, M. Baghaie Yazdi, A. Radetinac, P. Komissinskiy and L. Alff
DPG-Spring Meet 2013, Regensburg, Germany, 10. – 15. March 2013.

"Investigation of 3*d*-3*d* and 3*d*-5*d* oxides with double perovskite structure as potential room-temperature multiferroics"
V. Shabadi, M. Vafaee, M. Baghaie Yazdi, A. Radetinac, P. Komissinskiy and L. Alff
20th Workshop on Oxide Electronics (WOE20) – NUS Singapore, 22. – 25. September 2013

"Investigation of 3*d*-3*d* and 3*d*-5*d* oxides with double perovskite structure as potential room-temperature multiferroics"
V. Shabadi, M. Vafaee, M. Baghaie Yazdi, A. Radetinac, P. Komissinskiy and L. Alff
58th Conference on Magnetism and Magnetic Materials, Denver – CO, USA, 4. – 8. November 2013.

"Investigation of *A*-site bismuth based double perovskites as potential room-temperature multiferroics"
V. Shabadi, M. Vafaee, M. Baghaie Yazdi, A. Radetinac, P. Komissinskiy and L. Alff
DPG-Spring Meet 2014, Dresden, Germany, 30. March – 4. April 2014.

"Investigation of 3*d*-3*d* and 3*d*-5*d* oxides with double perovskite structure as potential room-temperature multiferroics"
V. Shabadi, P. Komissinskiy and L. Alff
IEEE International Magnetics Conference 2014, Dresden, Germany, 4. – 8. May 2014.

"Investigation of superstructure in multiferroic Bi_2FeCrO_6 thin films"
V. Shabadi, M. Major, P. Komissinskiy, M. Vafaee, A. Radetinac, M. Baghaie Yazdi, W. Donner and L. Alff
21st International Workshop on Oxide Electronics (IWOE21), Lake George, NY, USA, 28. – September – 1. October 2014

"Origin of superstructures in (double) perovskite thin films"
V. Shabadi, M. Major, P. Komissinskiy, M. Vafaee, A. Radetinac, M. Baghaie Yazdi, W. Donner and L. Alff

DPG-Spring Meet 2015, Berlin, Germany, 15. – 20. March 2015.
"Ferrimagnetism and spontaneous cation ordering in 3*d*-5*d* double perovskites"
V. Shabadi, A. Kulkarni, P. Komissinskiy, I. Slipukhina, R. Paria Sena, J. Hadermann, R. Gupta, H. Zhang, M. Ležaić and L. Alff
Workshop: Challenges in Multiferroics & Magnetoelectrics, Jülich, Germany, 12. – 14. October 2015.

"Epitaxial engineering of ferrimagnetic 3*d*-5*d* double perovskites as templates for single phase multiferroics"
V. Shabadi, A. Kulkarni, P. Komissinskiy, I. Slipukhina, R. ParíaSena, J. Hadermann, R. Gupta, H. Zhang, M. Ležaić and L. Alff
DPG-Spring Meet 2016, Regensburg, Germany, 6. – 11. March 2016.

Science slams:

"Spintronics & thin film technology"
V. Shabadi
Indo-German Grand Science Slam 2012, Deutsche Wissenschafts- und Innovationshaus (DWIH) Indien, New Delhi, India, 27. October 2012
Winner: **1st Place** – Cash Prize: € 6.000

Teaching & supervision assignments:

Bachelor – Grundpraktikum II: Solid state synthesis and energy-dispersive X-ray analysis of superconducting $YBa_2Cu_3O_{7-\delta}$.
Summer semester module: 11-01-1026. During years: 2011 – 2014

Master – Research Lab I: Thin film growth by Pulsed Laser Deposition (PLD) and *in-situ* RHEED monitoring.
Winter semester module: 11-01-4101. During years: 2012 – 2014

Master thesis supervision: "Epitaxial thin films of antiferromagnetic $LaMnO_3$"
Student: Nawnit Kumar, DAAD Sandwich Fellow
WiSe 2013-14

Master thesis supervision: "Structure-Property correlations in thin films of La_2MnReO_6 grown by pulsed laser deposition"
Student: Ashish Kulkarni, DAAD Sandwich Fellow
WiSe 2014-15

Master thesis supervision: "Synthesis of thin films of $BiLaMnReO_6$ using pulsed laser deposition and its characterization"
Student: Shivani Gour, DAAD Sandwich Fellow
WiSe 2015-16

Acknowledgements

My first association with ATFT was when I arrived in Darmstadt as a 19 year old bachelor student wanting to do an internship in the winter break. The memory of being picked up by Prof. Alff at DA Hauptbahnhof and driving together in his car to Lichtwiese for the first time remains fresh in my mind. Since then, the time I spent here helped me gain invaluable experiences both professionally and personally. So for all of this, and for being a great source of motivation and support, I would like to thank my mentor-supervisor – Prof. Dr. Lambert Alff. I also thank him for introducing me to the world of oxide thin film technology and for giving me an opportunity to pursue this doctoral research. I thank DAAD and DFG for funding me through their fellowship programs. Furthermore, I thank the following people for various ways in which they have supported me in undertaking this work:

Prof. Dr. Wolfgang Donner for being a second referee – supervisor for my research and for teaching me valuable concepts in crystallography and structural studies.

Prof. Dr. Marjana Ležaić for her support in helping me understand theoretical aspects of this work and also for accepting my request to be an examiner on the defense panel.

Prof. Dr. Oliver Gutfleisch for allowing me to use his laboratory facilities for quartz-glass melting and also for accepting my request to be an examiner on the defense panel.

Dr. Philipp Komissinskiy for being an invaluable mentor, and a go-to person for any challenges I faced, for introducing me to the PLD techniques and for his constant selfless efforts and contribution towards ensuring successful outcome of work.

Prof. Dr. Hongbin Zhang for his support and help in addressing theoretical aspects of this work. Prof. Dr. Joke Hadermann for her support in performing advanced electron microscopy. Dr. Marton Major for sharing his experience in crystallography and structural studies. Dr. Ivetta Slipukhina, Dr. Adam Jakobsson, Dr. Robert Paria Sena, Dr. Francois Guillou, Dr. Fabrice Wilhelm, Dr. Andrei Rogalev for various ways in which they have helped in this work.

Dr. Mehran Vafaee and Ashish Kulkarni for all the exciting times I spent with them while working together on double perovskites. Dr. Erwin Hildebrandt, Dr. Aldin Radetinac, Mehrdad Baghaie, Marion Bracke, Jürgen Schreek, Gabi Haindl, Arzhang Mani, Patrick Salg, Sharath Ulhas, Supratik Dasgupta, Martin Hottes and all other past and present colleagues at the FB11 for their support in different ways and wonderful years of co-working.

An unfortunate accident I had in July 2016, which led to two surgeries and a long recovery period was an excruciating personal setback. The sole credit to me being back on my feet today goes to my wife Nandita. In those distressing months on the bed, when I could not even use the washroom by my own, she took over complete responsibility of our lives and of getting me through the arduous medical treatment while still managing her own full time job. There is nothing I can do to thank her enough, but I acknowledge that without her support I could not have completed this work. A special mention in this context to my dear friend Aldin, who helped in various ways during this trying period.

My dearest family members Siddaram, Vasanthi, Guruprerana, Ashok, Alka and Kartikeya for their constant support, unconditional love and motivation; for imbibing in me great human values; for their selfless and relentless efforts to provide my wife and I with the best opportunities to pursue our dreams. Finally, I thank all other persons who have directly or indirectly supported me/contributed to this work. If someone hasn't been individually named above, please be assured that it is unintentional; I request your forgiveness for the same and I remain thankful for your support.

Preface

This dissertation reports the work I carried out as a part of my doctoral research under the supervision of Prof. L. Alff. The funding for a large portion of my research stay at TU Darmstadt was derived from a DAAD Ph.D. Fellowship. The decision to pursue research in the field of double perovskite compounds was inspired from the early stage discussions with my supervisor. My research consisted of two individual work-lines: first focusing on 3*d*-3*d* double perovskites and the second on 3*d*-5*d* double perovskites. As a lead investigator in this project, I was responsible for conceptualizing and designing the experimental study under advisory supervision of P. Komissinsskiy and Prof. L. Alff. During the project I also collaborated and co-worked with other laboratories and individuals; these collaborative inputs have been acknowledged where appropriate.

The study on 3*d*-3*d* double perovskites is presented in chapter 3. Planning of experiments, optimizing target synthesis procedure, fabrication of thin film samples, structural, chemical and magnetic characterization were performed by myself. Advanced structural investigation of superstructure was performed in collaboration with Prof. W. Donner and M. Major. Results were analyzed and interpreted by M. Major and myself. A version of this chapter was published in the Journal of Applied Physics [V. Shabadi *et al.*, J. Appl. Phys. **116**, 114901 (2014)]. The manuscript was written together by M. Major and myself under the supervision of P. Komissinsikiy, Prof. W. Donner and Prof. L. Alff.

The study on 3*d*-5*d* double perovskites La_2MnReO_6 and La_2NiReO_6 is presented in chapter 4. The idea to work on these compounds was jointly conceived by Prof. L. Alff, M. Vafaee and myself; it was partly based on experiences/challenges in our prior works on other double perovskites and also partly inspired from a paper by Ležaić *et al.* in 2011.[4] Some preliminary efforts towards experimental realization of these compounds were undertaken by M. Vafaee and myself, after which M. Vafaee left the project. Thereafter, further efforts to establishing reproducible routines for solid state synthesis of stable PLD targets for such sensitive materials were undertaken with support from the Glass workshop. Fabrication of thin film samples, basic structural, chemical and functional characterization and analysis of the results were performed by myself and A. Kulkarni (a Masters student supervised within this project). Theoretical inputs via DFT calculations were provided by Prof. M. Ležaić (FZ Jülich) and her colleagues. Electron microscopy imaging was performed by Prof. Joke Hadermann (Uni Antwerpen). XMCD experiments were undertaken at the ESRF ID12 – Circular Polarization Beamline under the supervision of the beamline scientists F. Guillou, F. Wilhelm and A. Rogalev. Prof. H. Zhang performed DMFT calculations based on our initial findings and contributed to valuable discussions. Collective interpretation of all data was done by me under supervision of Prof. L. Alff and P. Komissinskiy taking into account the discussions with all collaborators. A. Kulkarni also contributed in data analysis for some experiments. A manuscript for publication on outcomes of this chapter was prepared by A. Kulkarni and myself with P. Komissinskiy and Prof. L. Alff as supervisory authors. I thank all the above co-workers for their contributions and Prof. L. Alff for the opportunity to undertake this study.

Vikas Shabadi
TU Darmstadt
February 2017

Index

1. Introduction

Most elements making up the earth's crust are often found as oxides – either as simple binary oxides or also more complex oxides. Due to their natural abundance, oxides have always been a natural target of human scientific endeavors. In terms of works reported in the literatures, it was noted that some of the earliest recorded studies from the beginning of the 20th century, were on calcites and spinels – which are prevalent naturally found oxides.[5,6] During the mid-century times, the focus shifted to oxide perovskites – particularly with the works of Michael Glazer *et al.* who made remarkable contributions towards understanding perovskite crystallography.[7,8] This laid out a fundamental foundation for a huge number of works that studied structure-property correlations in perovskites in the years to follow. The next major landmark came with the realization of the world's first high temperature superconductor in Y-Ba-Cu oxides stabilized as thin films.[9,10] This opened up an enormous amount of opportunity for path-breaking device innovations and well as for unraveling exotic physics. The advancement in thin film technology that followed in the subsequent years have been aimed at realizing several material functionalities for device applications such as magnetism, ferroelectricity and electrical transport among others. In the present day, thin film based research on functional perovskites is driven by a constant need for device miniaturization, faster performances and energy efficiency.

1.1. Perovskites

Named after the Russian mineralogist Lev Perovski, 'Perovskites' refers to the class of compounds with a general formula ABX_3 where A and B are two differently sized cations and X is an anion that bonds with both A and B. In the scope of this work, we restrict ourselves to systems with Oxygen as the anion and therefore generally refer to the oxide perovskites of the form ABO_3. Due to the versatile capability of incorporating a large portion of elements of the periodic table into its structure, perovskites are arguably one of the largest studied classes of materials across the branches of chemistry, physics and materials science.[11,12]

1.1.1. Crystal structure

In its simplest form, the perovskite structure (Fig. 1.1 (a)) involves a cubic unit cell with the usually larger of the two cations - A occupying the corners and B occupying the body center while the face centers are occupied the anion O^{2-}. Alternatively the simple cubic perovskite

structure can also be viewed as a three dimensional array of corner-sharing BO_6 octahedra interspersed with the large *A*-cation at the center of the cube which coordinates with 12 surrounding oxygen anions located at the cube edges. Such an ideal cubic from of the perovskite requires a specific cationic size ratio of the *A* and *B* sites. By simple geometry, it can be determined that bond lengths *A*-O / *B*-O must be equal to $\sqrt{2}$. Such cubic perovskites belong to the *Pm*3*m*, where the atoms occupy equivalent positions as listed in Table 1.1.[13]

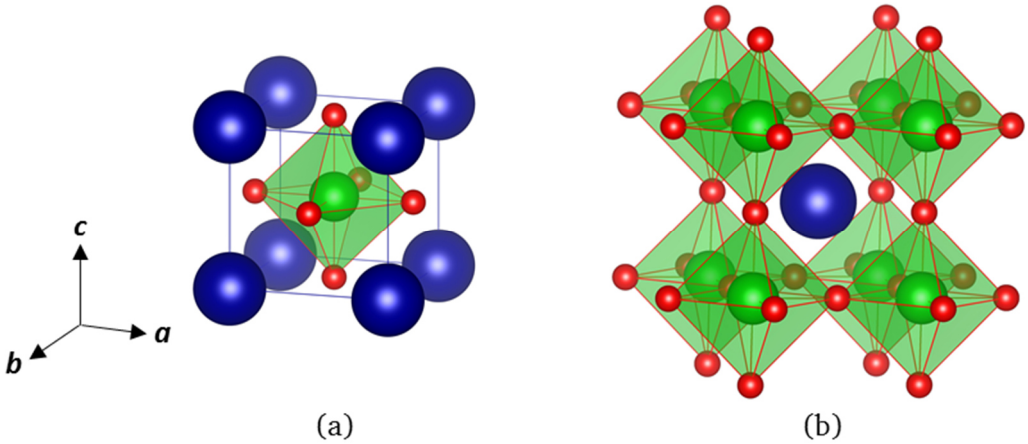

Fig. 1.1 (a) & (b) Crystal structures of a cubic perovskite created using VESTA visualization program[14]. Blue, green and red spheres represent A-site cations, B-site cations and Oxygen anions, respectively.

Table 1.1: Atomic positions of elements in a cubic perovskite.

Ion	Wycoff site	Crystal co-ordinates
A cation	(2a)	(0, 0, 0)
B cation	(2a)	$\left(\frac{1}{2},\frac{1}{2},\frac{1}{2}\right)$
O anion	(6b)	$\left(\frac{1}{2},\frac{1}{2},0\right)\left(\frac{1}{2},0,\frac{1}{2}\right)\left(0,\frac{1}{2},\frac{1}{2}\right)$

However in reality, only some ABO_3 perovskites exist in the ideal cubic state as described above. Strontium titanate ($SrTiO_3$) is one well known example of a perovskite that has an almost undistorted cubic structure.[15] Variations in the ionic radii of the cations involved often leads to a deviation from the ideal cubic perovskite regime. Early work by Goldschmidt suggested an empirical calculation to predict the tendencies of perovskite distortions.[16] A

tolerance factor τ was defined in order to measure the deviation of the perovskite structure from its ideal cubic from due to different ionic radii of the cations involved:

$$\text{Goldschmidt tolerance factor, } \tau = \frac{r_A + r_O}{\sqrt{2}(r_B + r_O)}$$

Where r_A, r_B and r_O are radii of the *A*-site cation, *B*-site cation and the O^{2-} anion, respectively. In general the stability regime of cubic perovskites is considered to lie in the range $0.89 < \tau < 1.02$.[17] Smaller values of r_A than the ideal value leads to a smaller τ, and correspondingly larger deviations lead to crystal structures with lower symmetry. In general lower values of τ (~0.80) has been known to yield orthorhombic structures and larger values (>1.02) lead to hexagonal variants. Such symmetry lowering deviations in perovskites are in reality accommodated by different kinds of distortions of the structure itself. These distortions can be classified in to three major types:

i. Shifts/displacements of cations

ii. Tilts of the oxygen octahedral

iii. Distortions of the oxygen octahedral

Extensive crystallographic investigations to classify and categorize the prevalent octahedral tilt distortions were performed by A. M. Glazer *et al.* in 1974 [8,18]. 23 different tilt distortion systems were derived which lead to 15 different space groups. Details on this classification and certain corresponding examples are available in Ref. [8].

1.1.2. Electronic structure of perovskites

This section has been formulated based on the excerpts from Ref. [19]. Extensive theoretical and experimental studies have been undertaken in order to develop an understanding of the electronic structure of perovskites. Due to the complexity the phenomena and a myriad of physical observations, several different models and theories need to be simultaneously considered in order to describe the electronic structure of perovskites. At the fundamental level, the oversimplified Ionic Model can be used for a basic understanding, where perovskites are considered purely ionic compounds. Here it is assumed that the *A* and *B* species completely loose electrons to create the O^{2-} anions within in the ABO_3 perovskites. In common practice, standard cationic oxidation states of common *A* site elements such as Na, Sr/Ca/Ba and La which are known to be 1+, 2+ and 3+ respectively are noted. The oxidation state of the *B* site element is then deduced simply based on principle of charge neutrality, as $os_B = 6$ -

os_A (where os_A and os_B are oxidation states of *A* and *B* cations respectively). The number 6 corresponds to the total negative charge of the three oxygen anions (|3*(-2)|). For instance, let's consider the case of $SrTiO_3$ (STO). *A*-site species strontium is known to have an os_A of 2+. From the above charge neutrality equation, one arrives at an os_B of 4 and thereby titanium is deduced to be in the 4+ state. From this we can establish that the elemental titanium in the [Ar]$3d^2 4s^2$ goes into a closed shell [Ar] configuration in $SrTiO_3$. (STO) Similarly Sr^{2+} and O^{2-} are also in a closed shell [Kr] and [Ne] configurations respectively. As a thumb rule, it can be considered that a perovskite such as STO which contains all species in a closed shell configuration will be an insulator and is indeed the case for this material. On the other hand perovskites containing non-closed shell species, take for example $SrVO_3$ where a V^{4+} cation has [Ar]$3d^1$ configuration is known to show metallic conductivity. However, such a thumb rule and the pure ionic model may not apply exhaustively to perovskites since several other factors do play a role and often taken into consideration in theoretical evaluations of the electronic structure and the resulting behavior.[19]

As noted by Wolfram *et al.*[19], the reason that the simple ionic model is insufficient to explain electronic structure and physical behavior in perovskites is simply because the various charged species of the ABO_3 system (Eg.: A^{2+}, B^{4+} and O^{2-}) are not isolated charges but indeed interact electrostatically with each other and also with the electrons surrounding them. For instance electrons of the *A* and *B* cations experience a repulsive potential of the negatively charged O^{2-} anions that surround them and conversely the electrons of the oxygen anions experience an attractive potential of the surrounding positively charged cations. Such an electrostatic potential existing at a given site of a crystal lattice due all other surrounding ions is termed as the "site Madelung potential" and is named after Erwin Madelung, a German physicist. Typically these potentials are in the range of 20 to 50 eV in perovskites. Firstly the Madelung potentials are responsible and key factor in the stability of the perovskite structure. It is this potential that energetically drives the transfer of electrons within the perovskite and is therefore responsible for the ionic configurations of the constituent elements. The Madelung potential is also responsible for shifting of the localized electron energies. Furthermore, the combined electrostatic crystal field leads to the lifting of the degeneracy of orbitals. These shifts in energy of electron states is illustrated in Figure 1.2 (a). 2*p* states of oxygen are split into a double degenerate $p_\perp$ state and a non-degenerate $p_\parallel$ state which are perpendicular and parallel to the *B*-O bond axis respectively. The lowest unoccupied s state of the A-cation is shifted by the Madelung potential but no effect of the crystal field is seen because of its non-degeneracy and its spherical symmetry centered at a site of cubic symmetry. On the contrary, the *d* states of the *B* site cation which sits surrounded by oxygen ions, are split by an

electrostatic crystal field due to the octahedral environment into a 3 fold degenerate t_{2g} (d_{xy}, d_{yz}, d_{zx}) orbitals and the 2 fold degenerate e_g (d_{x2-y2}, d_{z2-r2}) orbitals. Since the d_{xz}, d_{zy} and d_{xz} orbitals lie in between the x, y and z axes, they have lesser overlap with the axial 2p orbitals of the surrounding oxygen atoms and are therefore lowered in energy (lower Coulomb repulsion) in comparison to their e_g counterparts. This is further graphically elaborated in Figure 1.2 (b).

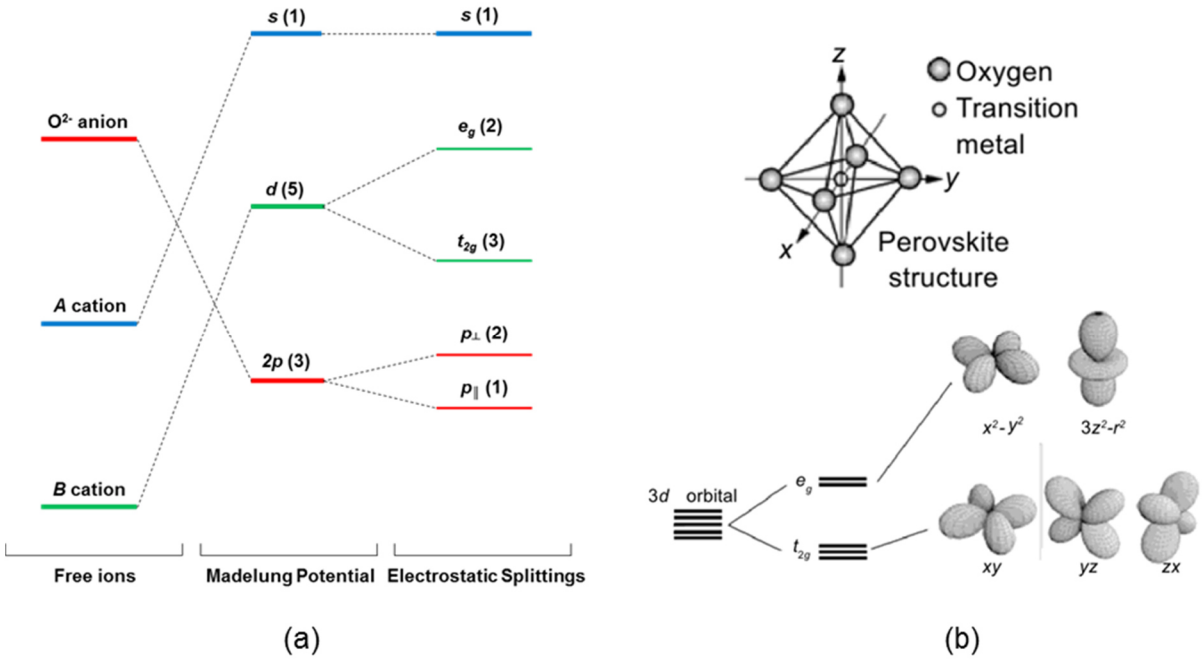

Fig. 1.2 (a) Changes in the ionic energy states due to the electrostatic potentials (Adapted from Ref. [19]); (b) d – orbital splitting in an octahedral environment (Taken from Ref. [20]).

In addition to the abovementioned electrostatic and crystal field effects, several other physical effects have been noted to affect the electronic structure in perovskites. Covalent mixing is one such effect which arises due to overlapping of electron wave functions within a crystal. This can lead to hybridization of the p and d orbitals to form states of mixed nature. Such an effect is almost always existing in perovskites which once again renders the simple ionic model insufficient to fully explain the electronic structure. While the covalent mixing is able to explain transfer of electrons within a crystal, in reality such an overlap of wave-functions and thereby transfer of charge may also take place from ions in one unit cell to the neighboring cells and similarly across the entire crystal. This leads to the formation of energy bands and requires consideration of electronic behavior in terms of band structures. As an example, a typical theoretically calculated band structures for the insulating perovskite $SrTiO_3$ in Fig 1.3. The figure demonstrates presence of the distinct bandgap of ~ 2 eV at the Fermi

level which separates the conduction bands (above), which are mainly composed of Ti 3*d* t_{2g} and e_g bands from the upper valence band (below) constituted predominantly by O 2*p* states hybridized with Sr and Ti states. Thus electronic structure of perovskites is a complex but important attribute that requires a simultaneous consideration of several theoretical models to characterize.

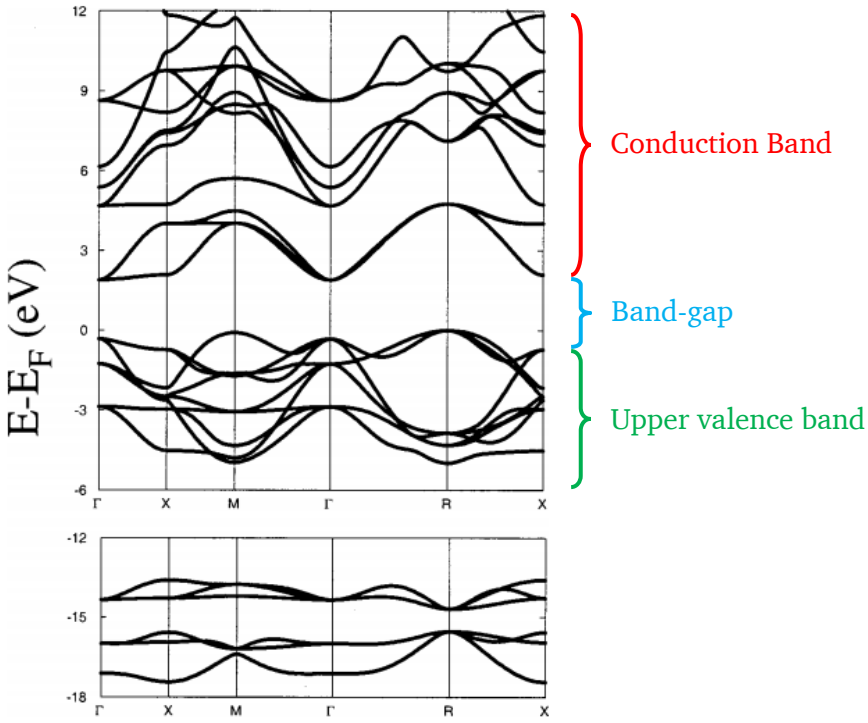

Fig. 1.3 Calculated band structure for cubic perovskite $SrTiO_3$ (Adapted from Ref. [21]).

1.2. Double perovskites

From the preceding section, it can be inferred that the unique quality of perovskites lies in the ability to tune their electronic structure to a large extent by choosing various combinations of *A* and *B*-site cations. It is due to this versatility that a wide range of functionalities can be deterministically engineered in perovskites. For instance, depending upon the distribution of the electronic bands, one can have either insulating, semiconducting or metallic perovskites; based on electron-electron correlations, some perovskites may be ferromagnetic, antiferromagnetic or diamagnetic; based on optical absorption characteristics, perovskites may also be rendered optically transparent or opaque; atomic displacements can also yield ferroelectricity; and sometimes, perovskites can be multifunctional by the co-existence of two

or more of the above qualities. Thus a wide range of properties could be engineered into perovskites depending upon the desired functionality.

In addition to compositional variations of *A* and *B* cations in the simple ABO_3 perovskites, another effective approach to functional engineering that has been widely explored is the partial substitution of *A* or *B* cations. Particularly interesting are compounds, where exactly half of the *A* or *B* sites are substituted by a second cation giving rise to compounds of the form $A_{0.5}A'_{0.5}BO_3$ and $AB_{0.5}B'_{0.5}O_3$. In some compounds, the substituted cations have been found occupy the cationic sites in an ordered manner within the crystal structure. For such compounds, it has been common practice to denote with a doubled chemical formula as $AA'B_2O_6$ and $A_2BB'O_6$. These ordered half-substituted multi-cation perovskites are commonly referred to as double perovskites and constitute a significantly large field of research by themselves. This study is focused on the *B*-site ordered double perovskite and hence we restrict this introductory section also to the $A_2BB'O_6$ type of compounds. For a more detailed introduction, the reader is directed to Ref. [3,22] which provide extensive reviews on the structure and properties of $A_2BB'O_6$ double perovskites. Some aspects from these review articles have been adapted into this introduction due to their relevance to this study. However, it should be noted both these reviews cover mainly the bulk studies on double perovskites. Thin film approach to double perovskites is comparatively younger and smaller field of study at the moment, but has been gaining growing amount of relevance in recent years.

Some of the earliest reports on this class of compounds date back to the 1960's where possibilities of room temperature magnetism in Rhenium based double perovskites were explored by Longo and Ward.[23] A more recent revival of the field was marked by the publication of Kobayashi et al in 1998 who reported on half-metallicity or the fully spin-polarized electronic conduction in Sr_2FeMoO_6 double perovskites.[1] The possible application of such a material in spin-electronic devices garnered huge amount of interest in this compound and paved way for several exploratory efforts on the double perovskite compound in the following years. The versatility of the double perovskite compounds lie in their ability to accommodate a vast number of elemental combinations which can be a boon to materials engineers aiming to tailor functionalities by design. In their review article, Vasala *et al.* estimate that - within structural limitations, there are nearly 2×10^4 possible double perovskite compositions, among which only about 1000 compounds have been so far experimentally reported in the literature.[3] This stands as evidence for the large untapped potential of double perovskites as functional oxides.

1.2.1. Crystal structure

The crystal structure of double perovskites is an extension of the simple perovskite structure discussed in section 1.1.1. A three dimensional cubic array of *A*-sites are here again coordinated with 12 surrounding oxygen atoms and are usually filled by a divalent or trivalent cation (usually an alkaline earth metal or lanthanide). The octahedrally coordinated *B*-sites are equally populated by a combination of two transition metals in contrast to just one transition metal in case of a simple perovskite. Additionally, there exists an ordering of the *B*-site cations as discussed in the following section. Once again, the simplest case would be a high symmetry cubic structure which can be categorized within the *Fm*3*m* space group. Similar to the case of the simple perovskites, the structure can undergo symmetry lowering via cooperative tilts and distortions of the oxygen octahedral when there is a mismatch in sizes of the *B* and *B'* cations.[24,25]

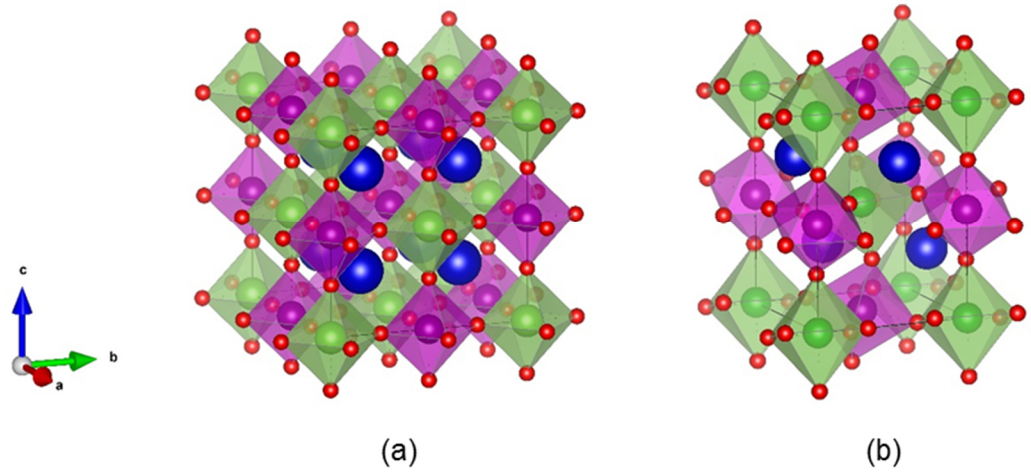

Fig. 1.4 (a) Crystal structure of a cubic double perovskite belonging to an *Fm*3*m* space group; (b) Crystal structure of a double perovskite with reduced symmetry to monoclinic $P2_1/n$ space group for a double perovskite with t = 0.93. Both structure were constructed using the Vesta crystal visualization program.[14]

Similar to the Goldschmidt tolerance factor defined for simple perovskites, a modified tolerance factor, t is applied to double perovskites which takes into account the effect of the ionic radii of both transition metal cations at the B-sites.[26] This is expresses as:

$$t = \frac{r_A + r_O}{\sqrt{2}\left(\frac{r_B}{2} + \frac{r_{B'}}{2} + r_O\right)}$$

Where r_A, r_B, $r_{B'}$, and r_O are the radii of the respective ions taken from tabulated values by Shannon.[27] When t has values close to 1, a stable cubic structure is realized as described

within the *Fm*3*m* space group. Figure 1 (a) shows a three dimensional illustration of such a cubic double perovskite unit cell with $t \approx 1$. Several detailed crystallographic works have studied the effects on the double perovskite structure with deviating values of t and also established a list of all possible tilt systems and space groups for the ordered double perovskites.[24] However only a few tilt systems and space groups have been found to be commonly occurring for most $A_2BB'O_6$ type compounds.[3] Tetragonal space group $I\ 4/m$ is found to be common for cases with $0.97 < t < 1.00$. For $t < 0.97$, orthorhombic and monoclinic structures are known to occur with the monoclinic $P2_1/n$ being the most commonly found space group for $A_2BB'O_6$ double perovskites.[3,26] A crystallographic illustration of such a monoclinic unit cell for a compound with $t \sim 0.93$ is shown in Fig. 1.4 (b).

1.2.2. Cation ordering

As derived from preceding discussions, the process of tailoring functionalities in double perovskites involves modification of their electronic structures by cationic substitutions. In this context, it has been observed that structural ordering of cations is a crucial requirement for achieving the desired functional response. Vasala *et al.* reviewed three possible ways of *B* and *B'* cation ordering in $A_2BB'O_6$ double perovskites – namely columnar, layered and rock-salt type.[3] Columnar and layered ordering involves alternating of the *B* and *B'* cations along one and two crystal directions respectively and are relatively uncommon. The most predominantly found is the rock-salt type order which involves alternation of the *B* and *B'* cations along all three crystallographic directions (Fig. 1(a)).[3] On a two dimensional plane containing the *B*-site cations, rock-salt ordering creates a checker-board type pattern as illustrated schematically in Fig. 1.5 (a). In reality, deviations from the ideal ordered state have been found to occur in experimentally synthesized samples. This can occur when *B* and *B'* cations are misplaced at their sites forming what is commonly referred to as the anti-site defect (Fig. 1.5 (b)). Thus experimentally synthesized samples of double perovskite compounds can be highly ordered or highly disordered or partially ordered depending upon the extent of anti-site disorder. In reality, small amount of anti-site defects are always existent due to entropy forces and as noted by Vasala *et al.*, there can be several ways in which this disorder can manifest in samples. In some cases, anti-sites can be distributed randomly; or sometimes they may accumulate together forming a boundary referred to as anti-phase boundary, separating two ordered domains. Some samples may only have anti-site defects or anti-phase boundaries and some may have a mixture of both. Furthermore, some compounds may show separate ordered and disordered domains.[3] Thus cation order/disorder in double perovskites is a complex microstructural phenomena and often requires non-trivial evaluation.

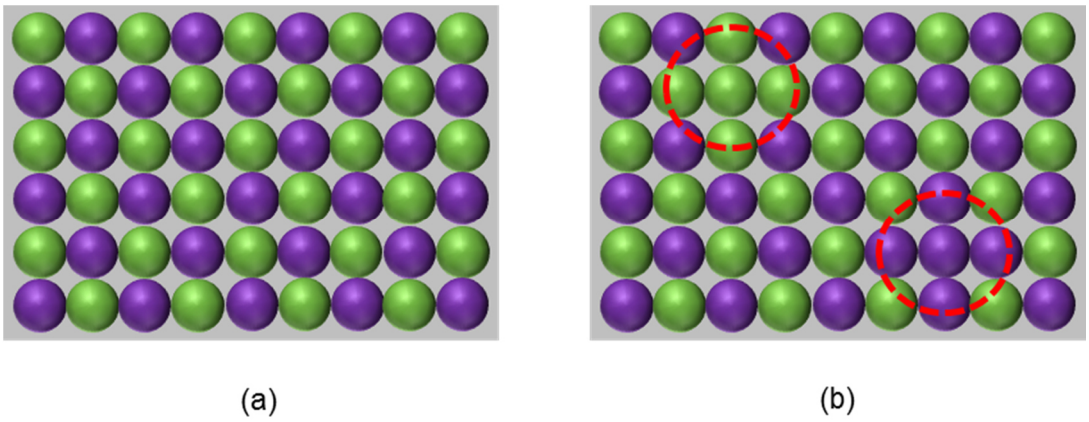

Fig. 1.5. Schematic illustration of the cationic arrangement pattern on a 2-dimensional plane as a consequence of (a) perfect rock-salt ordering; (b) rock-salt ordered structure containing anti-site defects.

B-site ordering in double perovskite samples can be evaluated by X-ray diffraction (XRD). Ordering of cations leads to a doubling of the unit-cell which can be detected by observation of superstructure peaks. However, doubling of unit-cell can also be caused by other known structural distortions in perovskites which may hinder a precise evaluation of order.[28] In addition to XRD, atomic resolution imaging techniques such as transmission electron microscopy can be effective in detecting ordering. Furthermore, functional responses such as magnetization have also been used as a method to evaluate cation ordering in the corresponding functional double perovskites.[29]

In spite of the entropic forces tending to disorder the *B*-site cations, there exist several hundreds of double perovskite which have a stable cation ordered structure. This indicates that there is a certain driving force and energy advantage associated with ordering. Through several studies in the past, it has been established and accepted that this driving force is derived from a difference in charges ($\Delta C = |C_{B'} - C_B|$) and a difference in ionic sizes ($\Delta r = |r_{B'} - r_B|$) of the *B* / *B*' cations (Fig. 1.6 (a)).[25,30] Two like charges always repel each other and the strength of the repulsion is proportional to the magnitude of their charge. Thus in case of double perovskites with a larger ΔC, placing a higher charged *B*' cations directly next to each other will experience a higher electrostatic repulsion as opposed to case when each of the *B*' cations are surrounded by the lower charged *B* cation, as would be the situation in case of a rock-salt order. Thus overcoming this electrostatic repulsion provides an energy gain that underplays the entropy term thereby leading to the *B*-site ordering. On the other hand if ΔC were 0, there is no electrostatic energy difference between the ordered and the disordered state which results in a lack of a driving force towards ordering. Similarly, for double

perovskites having B-cations with a larger Δr, the entropic factor is counteracted by the lattice strain energy which drives the system to an ordered state.[3]

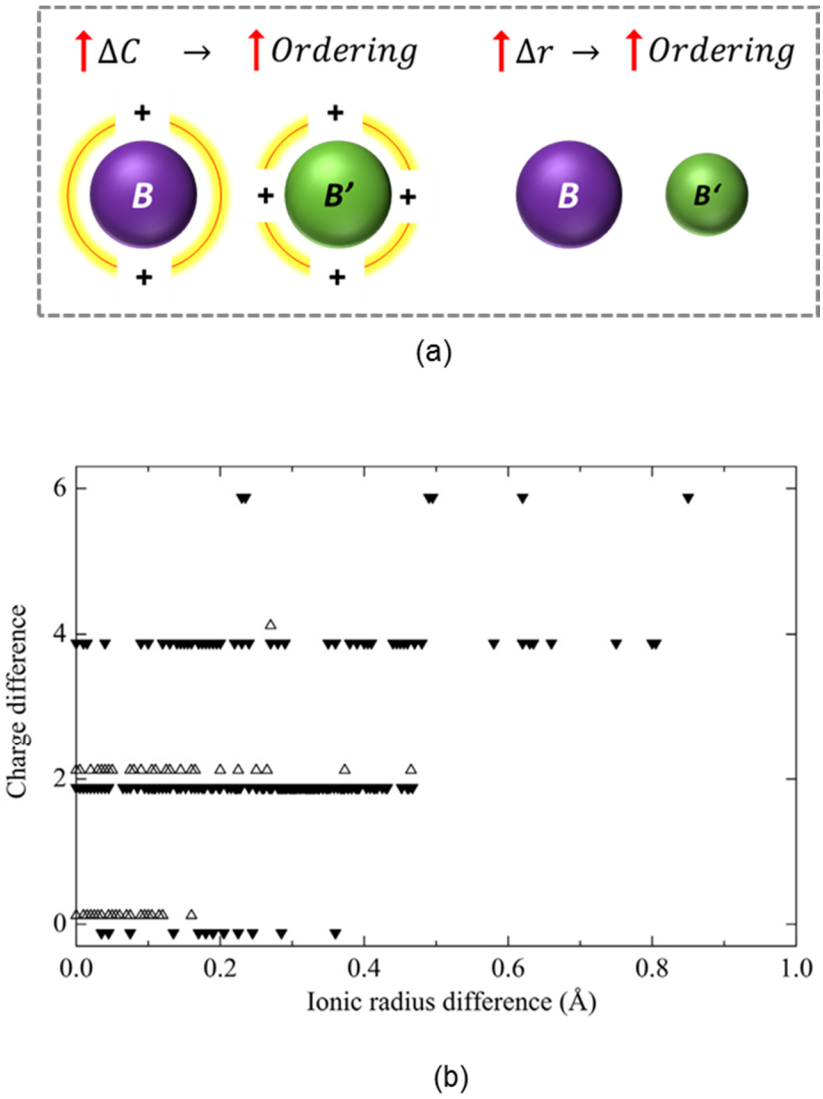

Fig. 1.6 (a) Schematic illustration of the two parameters driving cation ordering in double perovskites: difference in charge (ΔC) and difference in ionic radii (Δr). (b) A statistical plot showing ordered (indicated by solid triangles) and disordered (indicated by hollow triangles) double perovskites for different values of ΔC and Δr (Taken from Ref. [3])

Fig. 1.6 (b) shows a statistically generated plot created by Vasala *et al.* who reviewed state of the achieved ordering in nearly a 1000 literature reported bulk double perovskite compounds.[3] The hollow triangles represent disordered compounds and the filled dark triangles represent ordered compounds – either partly or highly ordered. As expected from the preceding discussions, it can be seen that for cases of large charge differences ($\Delta C = 4$ & 6),

most reported compounds showed ordering which is driven by the electrostatic energy gain. At lower charge difference conditions ($\Delta C = 0$ or 2), compounds were found to be both ordered and disordered, however the disordered compounds are concentrated more at the lower end of Δr. For cases with ($\Delta r > 0.17 - 0.20$), the compounds are mostly ordered. Thus, setting aside few exceptions, these statistics (with a significant large sample space) confirm that larger differences in charge / size of the *B*-site cations energetically favour the cation ordered state in double perovskites.

1.2.3. Magnetic ordering

Double perovskites offer the possibility to engineer a wide variety of magnetic properties. In most compounds, the transition metals at *B*-sites are the active sources of their observed magnetic responses. Since the structure consists of chains of *B*-cations separated by non-magnetic oxygen anion, the operating mode of magnetic interaction is the indirect exchange or also known as superexchange. Fundamentally, superexchange is a the most prevalent type of magnetic interaction in perovskite compounds and involves the exchange between the spins of the *B*-cations mediated by the overlapping oxygen *p*-orbital along the $B - O - B$ chains. The schematic drawing shown in Fig. 1.7 (a) illustrates the basic mechanism of superexchange. Consider the two metal cations '*B*' in an ideal ionic perovskite structure where the *d*-orbitals directly overlap with the p-orbital of intermediate oxygen anion. The arrows signify the electrons and their spin state - either spin-up or spin-down. It is considered in this simplistic case that the magnetic moment of the metals cations *B* is coming from one unpaired electron each in their *d*-shells. In addition, the oxygen has two electrons in its *p*-orbital. In the case that the two spins of the metal cations are aligned anti-parallel as in the cases (i,ii,iii), the ground state spin-order in (i) can mix with the excited states of (ii) and (iii). By virtue of this, the magnetic electrons are capable of delocalizing across the whole $B - O - B$ unit, thereby lowering the kinetic energy. On the other hand, if the two metal spin moments are aligned in a parallel fashion as case in (iv,v,vi), mixing of the ground state (iv) with states (v) and (vi) is not possible; as these states are forbidden by the exclusion principle. Thus there is no kinetic energy lowering in this case. Due to the above apparent energy advantage, indirect interactions of the metal *d*-shell electrons across the intermediate oxygen creates a stable anti-parallel ordering of the metal spins. This is the antiferromagnetic superexchange.[31]

In another circumstance indirect exchange can also yield a parallel or a ferromagnetic coupling. Consider a case of exchange interaction between an occupied e_g orbital and an unoccupied e_g orbital on the neighboring magnetic ion through an oxygen ion. Now consider a case of electron delocalization due to hopping of the e_g electron from the occupied to the ion

with unoccupied e_g. Now considering that the spin of the electron is conserved during the hopping, there is an energy advantage if the hopping electron arrives at the e_g orbital such that its spin has same alignment with respect to the t_{2g} electrons in that ion due to Hund's rule coupling. This thus drives a ferromagnetic arrangement.[31] Thus different ground state ordering patterns have been found in various systems depending upon several factors including the electronic configurations of the cationic *d*-orbitals involved. In their published works during 1960's, Goodenough, Kanamori and Anderson categorized these interactions and laid out few semi-empirical rules to identify nature of the superexchange ordering in different situations. Details of these can be found in Ref. [32–34]. In addition to the *d*-orbital configuration, the bond angle of the interacting $B - O - B$ system is also found to be a crucial parameter affecting superexchange. In an ideal cubic perovskite, this bond angle is 180˚. Deviations from the cubic system to lower symmetry structures can lead to lowering of the bond angle (that can change the extent of orbital overlap), which can alter strength of the interactions.

In spite of the differences found in certain cases, anti-parallel spin arrangement across the $B - O - B$ chain is still the predominantly found order resulting from Superexchange interactions. This is the reason why most simple perovskites (Eg. $CaMnO_3$, $LaMnO_3$, $BiFeO_3$, $BiCrO_3$ etc) are all rendered to be antiferromagnetic with zero or negligible magnetizations (in canted antiferromagnets).[35,36] This is indeed a problem, when perovskites are intended for magnetic applications. Nevertheless, it is worth noting that this drawback can be effectively overcome in materials such as double perovskites which provide a unique situation to exploit superexchange. Using a combination of two transition metals with different individual spin-moments, a net magnetization (of magnitude equal to a difference in their individual moments) can be created via their anti-parallel coupling as illustrated in Fig. 1.7 (b). Such a magnetic ordering is commonly known as ferrimagnetism and is indeed a functional quality of double perovskites which can be exploited for applications. Several promising multifunctional ferrimagnetic double perovskites have been discovered so far which make them a promising class of materials. Ferrimagnetic Sr_2FeMoO_6 with a fully spin polarized electron transport or half-metallicity[1]; high-magnetic ordering temperatures in $Sr_2CrB'O_6$ compounds (B' = W, Re, Os) are some of the prominent examples.[37,38] In fact, high temperature insulating ferrimagnetism found in compounds such as Sr_2CrOsO_6 ($T_C \sim 725$ K) provides an interesting prospect of double perovskites to be exploited for engineering room temperature type I multiferroics as discussed in the section below.[2]

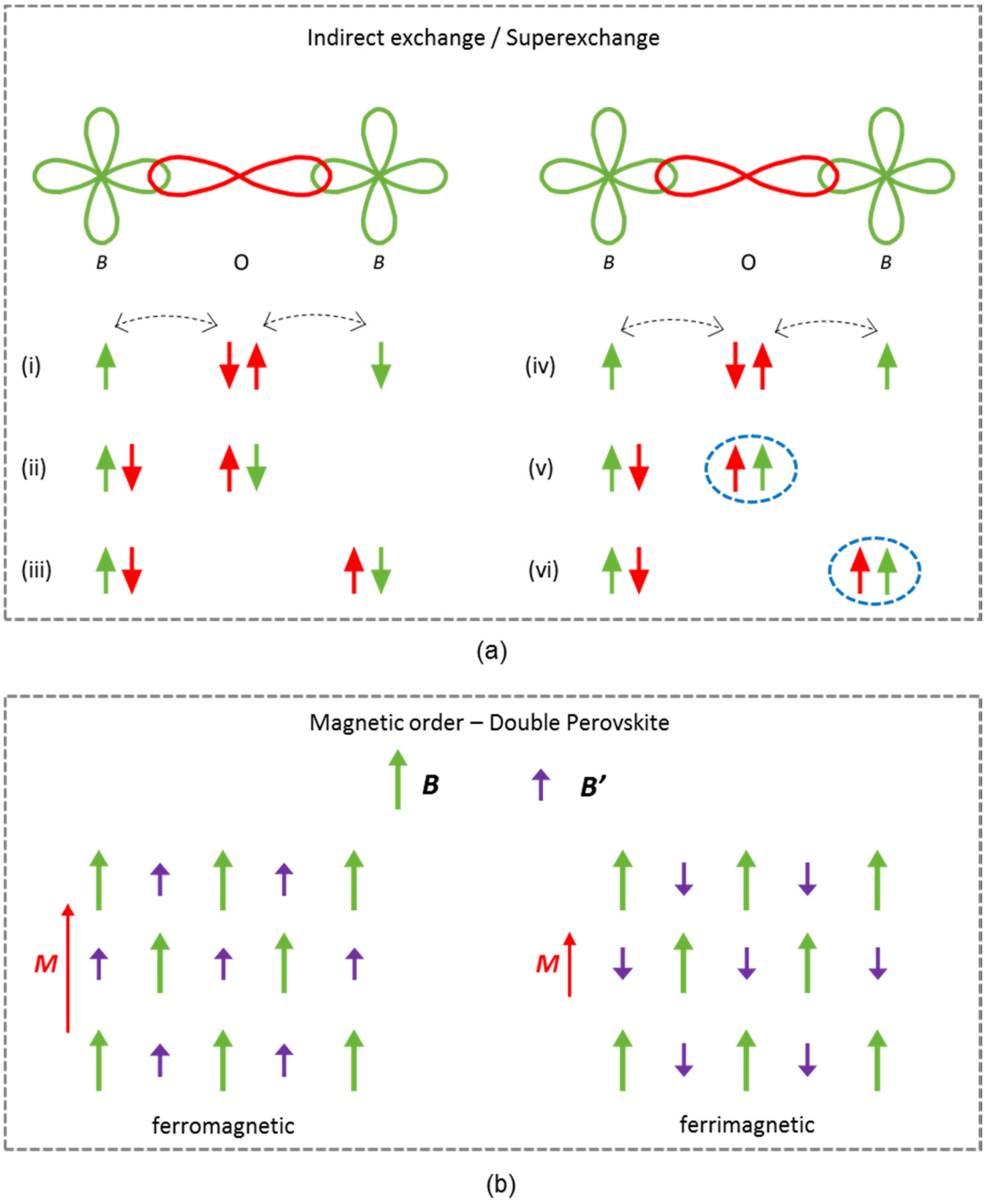

Fig. 1.7 (a) Schematic illustration showing mechanism of indirect / superexchange across the *B* – O – *B* bond (Adapted from Ref. [31]); (b) Schematic illustration of ferromagnetic and ferrimagnetic spin alignments of the B and B' spin sub-lattices in a double perovskite.

1.2.4. Multiferroism in double perovskites

A single phase multiferroic material is defined as one that simultaneously portrays two or more of the ferroic order parameters such as ferroelectricity, ferromagnetism and ferroelasticity.[39] In the context of materials research for devices, the term 'multiferroics' predominantly refers to a material system where magnetism and ferroelectricity are coexistent

even in the absence of any external magnetic or electric fields. Furthermore, a material system where these two types of ordering not only exist but are also coupled to one another are referred to as magnetoelectric multiferroics.[40,41] The reason behind the heightened interest within the materials community to pursue such materials stems from their potential applications in creating high density universal non-volatile memory devices, magnetoelectric sensors, multiferroic tunnel junctions and several other device elements.[42–44] However, in spite of these promising applications, the field of multiferroic materials has been held back due to several reasons. A primary challenge being the scarcity or rarity of such materials, the reasons for which were first theoretically addressed by N. A. Hill (now Spaldin) in 2000.[45] Hill noted that the scarcity of multiferroics stems from a contradiction between the conventional mechanisms that lead to ferromagnetic and ferroelectric ordering. In conventional ferroelectrics, the material needs to be strongly insulating and the polarization is caused by a non-centrosymmetric shift of a cation in the crystal structure. Such a shift is facilitated by an energy lowering covalency which formally requires a d^0 state (Eg.: Ti^{4+} in conventional ferroelectric $BaTiO_3$). On the other hand magnetism results from uncompensated spins in the partially filled *d*-orbitals and most magnetic materials are electrically conducting. Thus magnetism and conventional ferroelectricity are considered to be chemically contra-indicated.[45,46] Consequently the strategy to find multiferroic materials was to either search for alternative mechanisms to magnetism or an alternative mechanism to ferroelectricity; however only the latter has been much explored so far.

Based on the microscopic origin of the alternatively induced ferroelectricity, multiferroics are broadly classified into two groups, namely type I and type II.[47] Type I multiferroics refer to those materials where ferroelectricity and magnetism have different atomic sources within a material. Primary example for such type is $BiFeO_3$, where ferroelectricity is driven by the stereochemical activity of the $6s^2$ lone pair of electrons on the Bi^{3+} cation while the magnetic order is obtained from the *B*-site transition metal Fe^{3+}. In this type of multiferroics, ferroelectricity and magnetism appear largely independently of each other and the coupling between them is usually weak. Thus the goal within this type is to keep all the features intact while improving the magnetoelectric coupling. The second group is referred to as type II multiferroics; here the magnetic order by itself causes the ferroelectricity indicating possibility of a strong coupling between the two. Well known example is $TbMnO_3$ which is a low temperature multiferroic. In this class, complex magnetic structures such as spiral magnetism create the electrically polarized states in the material structure. However, the polarization in such materials is much smaller.[47]

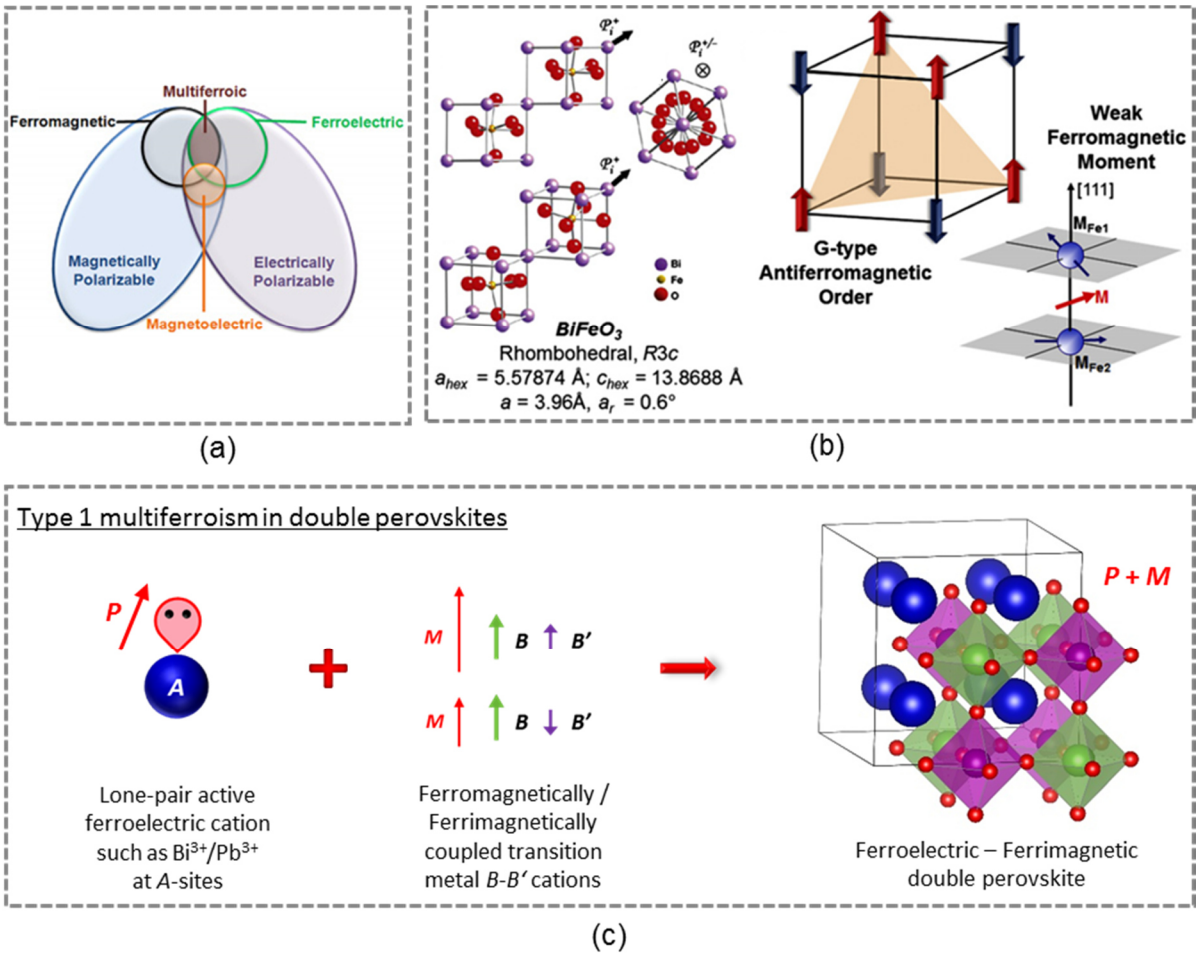

Fig. 1.8 (a) Venn diagram indicating the relationship between multiferroic and magnetoelectric materials (Taken from Ref. [48]); (b) Schematic illustration of the structural and functional properties of multiferroic BiFeO3 (Taken from Ref. [48]); (c) Schematic illustration showing the possibility of combining lone-pair active ferroelectricity with ferro/ferrimagnetism in double perovskite compounds.

Based on the available theoretical treatment and existing classifications, Eerenstein *et al.*[40] proposed a Venn diagram in their review on multiferroics which is shown in Fig. 1.8 (a) as adapted from Ref. [48]. This illustration notes that only small sub-group of all magnetically and electrically polarized materials are either ferromagnetic or ferroelectric and still fewer have both other parameters. In these materials there is a possibility that a material is magnetoelectric allowing electric field control of magnetism or magnetic field control of electric order. However, magnetoelectricity is again an independent functionality that can arise in any magnetically or electrically polarizable material, irrespective of whether the material is multiferroic or not.[48] This further emphasizes the peculiarity and the rarity of the magnetoelectric multiferroic. Thus, for ultimate multiferroic device functionality, Martin *et al.* noted that an ideal material system should be strongly ferroelectric and ferromagnetic in a

single phase at room temperature, with a robust coupling between the two enabling the control of the magnetic order with an electric field.[49]

The simple perovskite compound $BiFeO_3$ (BFO) has been by far the most studied multiferroic compound in the literature. The heightened interest in this compound was first sparked by the work of Wang *et al.* who in 2003 established the possibility to grow high quality thin films of BFO via pulsed laser deposition.[50] Since then there have been several hundreds of independent works that studied and established various structural and functional aspects of the compound (a summary of which is shown in Fig. 1.8 (b)). Bulk BFO is known to crystallize in a rhombohedral polar space group *R*3*c* with a spontaneous ferroelectric polarization along the pseudo-cubic [111]-direction. As seen in Fig. 1.8 (b), the structure consists of two distorted perovskite blocks connected along the pseudo-cubic [111] direction to form a rhombohedral unit cell. The ferroelectric state arises from a large displacement of the Bi-ions with respect to the distorted FeO_6 octahedra. Thin films of BFO were shown to have a significant ferroelectric polarizations up to ~90 μC cm^{-2} which was stable upto temperatures as high as ~1100 K. In spite of the promising ferroelectric properties, the drawback of BFO lies in its magnetic qualities. Due to an existent G-type antiferromagnetic ordering of the Fe^{3+} cations with an ordering temperature TN ~ 643 K, the material does not have a robust spontaneous magnetization. Some theoretical and experiments have established that the BFCO crystal allows small canting of the antiferromagnetic moments in the structure resulting in a weak canted ferromagnetic moment of 0.05 $\mu_B/f.u.$[49] The magnetic properties in thin films of BFO remain heavily debated as the original work of Wang *et al.* showed an anomalously large magnetic moment of 70 emu cm^{-3} which is an order of magnitude larger than that expected for canted antiferromagnetic moment.[50] In the later years, studies by Eerenstein *et al*. and Bea *et al.* suggested formation of magnetic nano-impurities in thin films which resulted in enhanced magnetic moment.[51,52]

The low observed moment in BFO is a consequence of the superexchange interactions which renders the *B*-site cationic spins antiferromagnetically coupled. This is a common drawback with most single perovskite type I multiferroics that have been explored (Eg.: $BiMnO_3$, $BiCrO_3$, $BiCoO_3$, etc.). As discussed in the preceding sections, this problem can be effectively overcome in *B*-site ordered double perovskite compounds where a lone pair driven ferroelectricity of Bi^{3+} *A*-site cations can be successfully combined with a strong *B/B'* site magnetic moment derived either from a ferro / ferrimagnetic order (Fig. 1.8 (c)). However, exploration of multiferroism in double perovskites is a young field of study which has not received a comparable level of attention as BFO due to bigger challenges associated with synthesizing

bismuth based double perovskites. Based on the choice of the *B/B'* transition metal cations and their respective positions in the periodic table, double perovskite compounds may be broadly classified into 3*d*-3*d*, 3*d*-4*d* and 3*d*-5*d* compounds. A few bismuth based 3*d*-3*d* double perovskites (Eg.: Bi_2FeCrO_6, Bi_2MnNiO_6, etc.) have been studied so far, but have each faced some structural or functional drawbacks hindering ideal multiferroic functionality (discussed further in chapter 3).[53] On the other hand bismuth based 3*d*-4*d* or 3*d*-5*d* double perovskites have been seldom studied and undoubtedly deserve being explored (discussed further in chapter 4). With recent developments, advanced thin film technology (as discussed in following sections) has emerged as an effective route to stabilize complex oxides like double perovskites. If this could be successfully extended to engineer reproducible methods to realize some of the unexplored multiferroic double perovskites, a renewed interest could be generated in the field.

1.3. Thin film technology

A thin film can be defined as a material from that extends indefinitely along two dimensions but has a limited dimension along the third perpendicular direction (referred to as thickness) which may range from a few angstroms to a micrometer (10^{-6} m). In the past, traditional thin film technologies were developed mainly for synthesis of metallic and alloy thin films. Coming down from this era, significant advancements have been made over last three decades across various thin film growth techniques which has enabled the application of thin film methods to a wide range of materials beyond just metals or alloys – such as inter-metallics, oxides, nitrides, polymers, composites, etc. In addition to the growth techniques, developments in the available in-situ and ex-situ characterization techniques have also had critical impacts on the development of this approach. In particular to the case of oxide materials, the thin film approach has been a great enabler in terms of exploring new compounds, their functionalities and to understand the microscopic and atomic level origins of their behavior.

1.3.1. Techniques for oxide thin film growth

Among all, three particular thin film techniques have been most used to study oxide thin films. Each have their own advantages, disadvantages and niche capabilities. These have been briefly described below

Molecular beam epitaxy (MBE): MBE technique involves evaporation of the desired elements in an ultra-high vacuum (UHV) chamber with low base pressures ($<10^{-9}$ Torr) where the evaporated atoms travel from the source to the substrate as a molecular beam with

minimal scattering. The flux of the atoms in the beam can be varied, thereby giving a user a precise control of the resulting film stoichiometry. In contrast to the two other techniques discussed below, MBE is a low-energetics deposition system. This allows for growth of very high quality of low defect density thin films. After its remarkable success in growth of III-V semiconductors, MBE has been widely explored as a viable technique for oxides. Growth of simple binary oxides and also the ABO_3 perovskites, has been well achieved for several materials. However, its applicability to more complex multi-cation systems like double perovskites has been restricted due to difficulties in flux rate / stoichiometry control when several cation are involved. Also low energy of the flux species do not have sufficient thermal energy to achieve required adatom mobilities, thereby calling upon the need for using high substrate temperatures.[54]

Sputtering deposition: Sputter deposition or sputtering is a technique that involves ejection of material species from a given target by high energy gas molecules which are subsequently transferred to a substrate for the thin film growth. The energetic gas molecules are derived from a gas plasma which is created by applying a high voltage across the target in the presence of a background gas. Low background gas pressures are used to ensure a sufficient mean-free-path for the material species to reach the substrate. In magnetron sputtering, a magnetic field is imposed in such a way that the gas plasma is confined to a region close to the target. This allows for enhanced target bombardment and consequently better film growth rates and uniformity. In cases involving insulating oxides, charge build up at the target cathode is a problem, hence RF sputtering is used where the sign of the anode-cathode is switched or cycled at a very fast rate (in MHz). Advantages of sputter deposition include possibility of growing films at low temperatures (when required), and control of film growth via external parameters such as the background pressure and sputtering power. A common drawback associated with sputter deposition is the possibility of reactions at the surface of the targets which causes target poisoning, or in other words formation of unwanted phases which may have different sputter characteristics.[55,56]

Pulsed laser deposition (PLD): In pulsed laser deposition, a high energy laser pulse (usually in the UV range) with very short pulse durations (~few 10s of nano-seconds) is directed onto a small area on the surface of an absorbing ceramic target. This large amount of energy absorbed by the target leads to an ablation of a small portion of the target material into a plasma plume. During the ablation process, the overall stoichiometry of the target is transferred to the plasma plume unchanged, and subsequently the charged ions from the plasma arrive at a substrate often held at elevated temperatures. Thermal energy at the

substrate drives the nucleation and growth process that follows. In contrast to sputter deposition, PLD can be carried out both in vacuum as well as in the presence of a background gas. Detailed accounts on the PLD process and its construction are discussed in section 2.1.3. Since the PLD process allows for a stoichiometric transfer from the target, it can be (in contrast to MBE) an ideal technique to grow films of multi-cation complex oxides such as double perovskites. Yet there are some drawbacks of the PLD process, namely defects caused by high particle energies and possibility of larger chunks or droplets of the target material reaching the substrate. It is not a very industrially viable process as it cannot be used for depositing over large areas and also because it is generally a cost intensive process. In spite of these drawbacks, PLD is still a method of choice in research when it comes to exploring new complex materials systems. Over the recent years, the capabilities of PLD has been exploited to achieve remarkable possibilities such as functional interfaces, superlattices, cation-ordered materials, multi-stack material devices, etc.[57,58]

1.3.2. Fundamentals of thin film growth

Following section has been summarized based on inputs from Ref. [57]. Thin film growth often starts with creation of the elemental species and then involves transfer of these species to the substrate surface. Once the material species arrive at the surface of substrate a series of complex multiple processes take place which has been illustrated in Fig. 1.9. An approaching atom can either be absorbed at the surface or reflected back depending upon its kinetic energy. Sticking coefficients of elements also influence the absorption processes. Initial sticking of the atoms is categorized as physisorbtion where the atoms are held mainly by Van-der-Waals forces. The thermal energy of the heated substrates surface can provide a driving force for surface diffusion, where a physisorbed atom moves over the surface of the substrate. Subsequently the adatoms may also be chemisorbed where a bonding with the substrate atoms take place. Once chemisorbed the particles are rather stationary due to a strong bonding. Atoms which arrive at the substrate surface can also damage the surface and penetrate it when coming with extremely high kinetic energies. This destroys the substrate surface and consequently creates defects at the interface. Such a situation is often avoided in PLD processes by using background gases which help in reducing the kinetic energy of the ablated particles. Subsequent process of film formation involves nucleation and growth process. During nucleation adatom embryos are formed which are said to nucleate or achieve a stable size when addition of more atoms to the embryo effectively reduces Gibb's free energy.

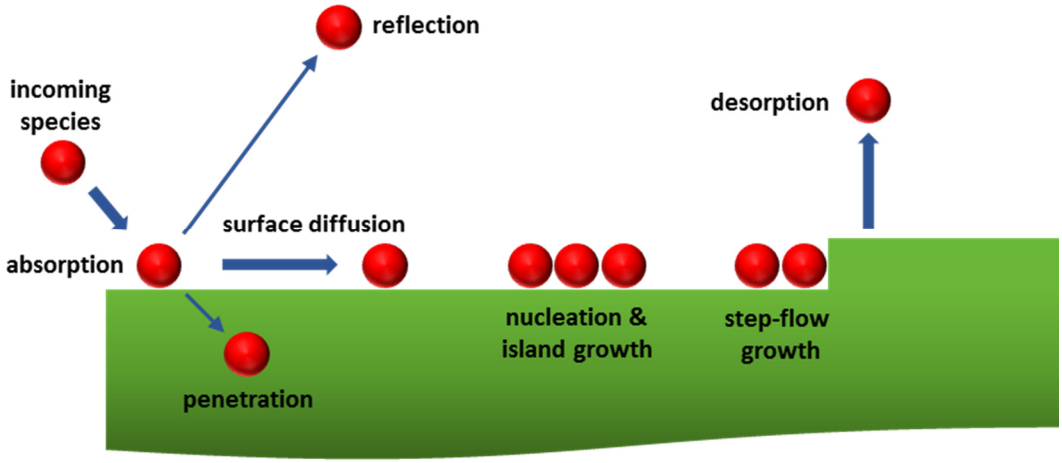

Fig. 1.9 Schematic illustration of the elementary processes occurring at substrate surface at early stages of film growth.

Further growth of the nuclei is characterized by the interplay of several parameters such as the surface energies of the substrate (γ_S), film (γ_F) and the interface (γ_I) and also to some extent parameters such substrate temperature, deposition rate etc. This has been noted to manifest mainly as three different growth modes which have been illustrated in Fig. 1.10.

Frank-van der Merwe (layer-by-layer) growth: This growth mode refers to the illustration shown in Fig. 1.10 (a). It is observed when the total surface energy of a film-layer wetted substrate is lower than the surface energy of the bare substrate ($\gamma_F + \gamma_I < \gamma_S$). Such a situation leads to growth of a complete surface covering monolayer and subsequent additions of monolayers (hence also known as the layer-by-layer or 2D growth mode).

Volmer-Weber (islands) growth: As illustrated in Fig. 1.10 (c), this type of growth mode involves formation of islands of the film material as the system tends to maximize the unwetted substrate area which is the lower energy surface. Thus this corresponds to a thermodynamical situation where ($\gamma_F + \gamma_I > \gamma_S$)

Stranski-Krastanov (mixed) growth: This is the third type of growth mode which has been illustrated in Fig. 1.10 (b). In this mode, which is one of the more often observed mode, the growth starts of as a layer-by-layer process. However, as the film thickness increases, the misfit energy (E_{misfit}) between the substrate and the film increases. At a critical thickness, the E_{misfit} becomes large enough to break the thermodynamic condition favouring the layer-by-layer growth which then causes an island growth mode for addition of further layers.

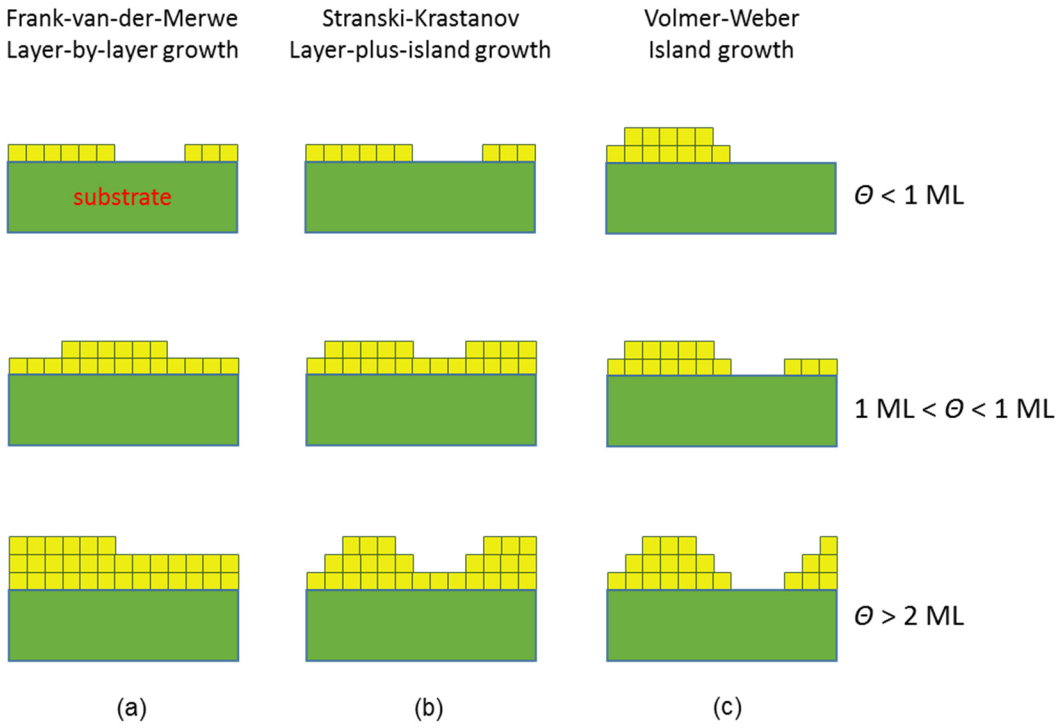

Fig. 1.10 Schematic illustration of the main thin film growth modes. '*Θ*' refers to the coverage of the film material in units of monolayers.

Thus for each system depending upon the corresponding surface energies of the film and substrate material, one can end up having different ways in which the film can grow. However, the 2D or the layer-by-layer mode is the most desired growth mode as it produces the least amount of structural defects in the sample. The film growth process might lead to the formation of films with different crystal morphologies and atomic order. Based on this, the films can be classified as follows:

- Amorphous, when the film does not have any long range order.
- Polycrystalline, when film consists of randomly oriented grains, but a definite crystalline order within the grains.
- Textured, when structurally ordered grains in-turn align themselves along certain preferential orientations.
- Epitaxial, when there is long range structural order in the grains, and there is a definite orientation relationship between the film grains and the substrate.

Perfect epitaxy relates to an ideal single crystalline film layer with no defects fixed in perfect lattice registry on a single crystal substrate. In reality, most films may have slight deviations

from this ideal picture of epitaxy either in the form of defect dislocations or mosiacity (small angle tilts between crystal grains of same orientation)

1.3.3. Thin film approach to meta-stable double perovskites

As discussed in the preceding sections, advancements in technology and fundamental understanding of thin film growth has enabled the realization of a wide range of complex materials. However, use of thin film approaches for study of double perovskites (usually with three cations) is still in a developing stage since only a fraction of all synthesized bulk double perovskites have been adapted in the thin film form and many more remain unexplored by experiment. Particular challenges have been noted to hinder the possibility of high quality growth and reproducibility double perovskite materials. One of the important challenges is to balance the stability of the three cations involved. During synthesis procedures, it may be the case that the constituent cations have different thermodynamic regions of stability, or it may happen with some combinations that a particular cationic species has a high volatility in its precursor form and also in some cases, it may just be thermodynamically impossible to achieve particular desired oxidation state of a cation. These problems may often result into formation of unwanted secondary phases or in worse cases, inability to achieve the required phase at all.

Using the PLD based thin film approach can be an effective alternative to overcome these particular challenges. The fact that the PLD process is kinetically driven, allows us to a certain extent to shift the stability windows of certain cations beyond the thermodynamic limiting boundaries. This way small suitable deposition windows can be created where the required states of the species may co-exist, so that the double perovskite can be stabilized as a pure phase. In addition to the kinetic advantage, the known feature of the PLD process to be able to ensure a stoichiometric transfer of species to the surface of the substrate is a further valuable aspect for double perovskites (where often at least three cations are involved). Another crucial aspect with regard to double perovskites is the chemical ordering, as was discussed in section 1.2.2. Over the past years, several different approaches have been used to achieve *B*-site chemical ordering double perovskite thin films. Three most important of them are discussed below:

1. **Thermal treatment / post annealing:** This approach involves post synthesis thermal treatments of double perovskite compounds under controlled atmospheres. Synthesized samples of double perovskite compounds are subjected to annealing at elevated

temperatures. Series of experiments are made to determine the required temperature and duration which is needed to reach a thermodynamic equilibrium of the ordered phase. Alternatively, as was shown for the *A*-site ordered double perovskite $La_{0.5}Sr_{0.5}CoO_{3-\delta}$ with high ionic mobilities, one could also use an in-situ furnace and structural characterization methods to observe thermal effect on ordering in real time[59]. This is a thermodynamically driven process and can be applied to compounds that consist of non-volatile and thermally stable phases.

2. **Superlattice approach / two target growth:** The superlattice approach involves breaking up a double perovskite into two individual constituent perovskites (La_2FeCrO_6 into $LaFeO_3$ and $LaCrO_3$)[60]. The double perovskite films are then realized by growing precise alternating monolayers of each constituent perovskite say via PLD under a two target approach. Such a process is often undertaken upon a (111) oriented substrates which can yield the required rock-salt ordering of the *B*-site cations. For this process to be viable, it is important that each of the constitutent perovskite can form a stable layer by itself and can be grown under a high-quality layer-by-layer mode. There can always be problems associated with intermixing in this method and also possibilities for large amount of defects due to differences in growth dynamics of the two single layers.

3. **Spontaneous ordering via PLD:** Spontaneous ordering via PLD is an approach that gained a recent popularity for growth of *B*-site ordered double perovskites following the reports in Ref. [61–64]. The ordering process here can be thought to be kinetically driven as it is believed to take place in real-time during the non-equilibrium PLD film growth. Although the mechanism of spontaneous ordering at the atomic level remains to be investigated, the driving force for the ordered occupation is noted to be derived from the difference in ionic radii and the oxidation states of the two *B*-site cations. As discussed in section 1.2.2, under these differences, the lowest energy configuration is that of a rock-salt like occupation which could be the reason behind spontaneity in ordering. On completion of deposition, the films are quenched to room temperature at a higher cooling rates to freeze the atomic positions in the sample thereby preserving the achieved cation ordering. This process involves PLD growth out of a single stoichiometric target for the desired $A_2BB'O_6$ double perovskite. A thermodynamic *P-T* phase diagram is usually plotted to roughly identify the stability regions for the required oxidation states of the cations. To a certain extent, this method of simultaneous growth also allows to balance the oxidation/reduction tendencies between the two *B*-site cations by deterministically varying the PLD growth parameters, thereby enabling to stabilize the phase in its required

state. As a consequence, for any given double perovskite, there often turns out to be only a small window in terms of deposition conditions where the required ordered phase can be stabilized. The challenge of this approach therefore lies in finding this suitable window, which as noted by Ohtomo *et al.*[64], calls for large amounts of trial and error protocols exploring the kinetic and thermodynamic landscape.

From the literatures on each of the above approaches, it can be seen that the thin film approach has had a fair amount of success in realizing several double perovskite phases, some of which have been previously unexplored. General success of the PLD process for multi-cation systems is evident in the literatures and hence is chosen as the suitable method of thin film growth for this study. As for the ordering, since the selected compounds under this work include volatile and thermally unstable species such as Bismuth and Rhenium, the approach involving post deposition thermal treatments would not be suitable. Secondly, the superlattice approach can be difficult, as some of the constituent single perovskites either cannot be grown in a layer by layer mode and some others do not exist as a stable phase. Therefore, the remaining option of realizing double perovskites via spontaneous ordering was taken as the method of choice for this study. The viability of spontaneous ordering process was tested across two families of double perovskite compounds namely 3*d*-3*d* and 3*d*-5*d*, referring to the combination of the two transition elements taken as the *B* and *B'* cations.

2. Experimental methods

This study involved a thin film approach to material synthesis followed by a combination of advanced characterization and measurement techniques. Experimental work was complimented by theoretical calculations and modelling wherever required. Preliminary material synthesis steps involved fabrication of stoichiometric ceramic pellets for each of the double perovskites. The pellets were meant to be used as laser ablation targets. Pulsed Laser Deposition (PLD) under controlled environments was used to grow thin films of the desired compounds on suitable surface treated single crystalline substrates. Post the fabrication, structural, microstructural, chemical and functional properties of the thin films were studied. Following sections provide an overview of fundamentals, experimental set-up and methodology of the various steps undertaken in this work.

2.1. Materials synthesis and sample preparations

2.1.1. Substrates: selection and pre-treatment

Choosing a right substrate and preparing its surface prior to deposition is of prime importance in thin film technology. Substrates act as a foundation and template to the overlaying film. There are several substrate parameters that greatly influence thin film growth: most important among them are: crystal structure & lattice constants, crystal orientation, surface energies, surface roughness and chemical compatibility. Section 1.4 provided an overview on the fundamentals of epitaxy and epitaxial films. Since it is our primary goal to grow epitaxial films with low defect densities in this work, the crystal-structure/orientation and the consequent lattice parameters of the surface mesh is the primary parameter influencing choice of a substrate. The differences in the bulk lattice parameters of the substrate and the film materials is quantified by lattice mismatch *f*, where:

$$f = \frac{a_s - a_f}{a_f},$$

Where a_s and a_f are the lattice constants of the substrate and the film respectively. As shown in figure 2.1 (a) & (b) small amounts of mismatch may be accommodated as strain into the structure of the film. The resulting film may either be tensile or compressive strained depending on the sign of the mismatch. In some materials, it may indeed be a desirable quality to have a strained film to achieve a certain functionality (e.g. strain driven ferroelectricity)[65]. However larger mismatch can lead to misfit dislocations and relaxed films with dislocations and defects that may be undesirable. In extreme cases, one may fail to grow

crystalline films at all when the misfit is so large that it makes it impossible for the incoming film material to nucleate on the substrate surface. Such a situation may lead to the formation of an amorphous film.

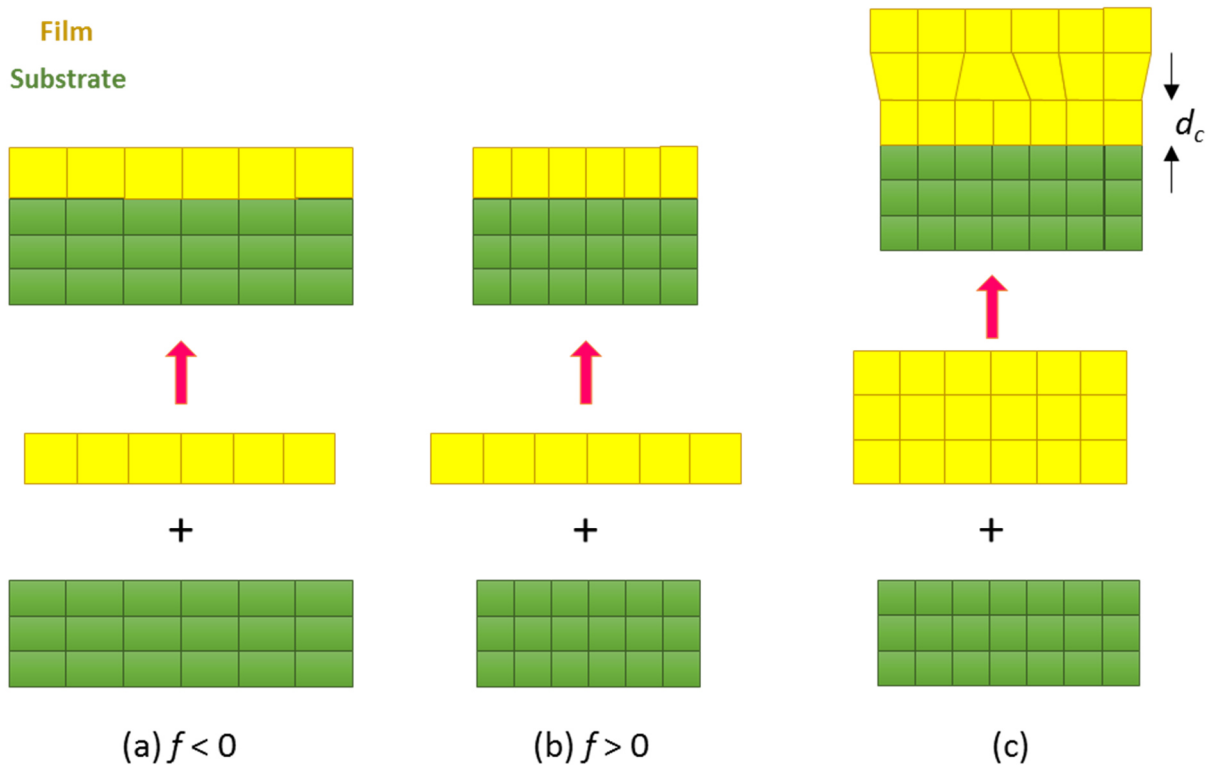

Fig. 2.1 Illustration of the effect of lattice mismatch on heteroepitaxy of a thin film on a substrate (a) film under tensile strain; (b) film under compressive strain; (c) film in a relaxed state above a certain thickness (for $t > d_c$). (Adapted from Ref. [6])

Thus choosing a substrate with the right lattice constants has a large impact on the consequent film growth and phase stabilization. Fig 2.2 shows a list of commercially available perovskite type substrates positioned on a horizontal linear scale of their lattice constants. It may indeed often happen that a large number of double perovskites or any other compounds in general may be just inaccessible via thin film approach due to lack of a suitable substrate. Particularly in this study and other similar studies, where magnetism is a focus of study, one also needs to take into consideration to use a diamagnetic substrate like $SrTiO_3$ (STO) or similar. This is particularly important when use of lab based non-element specific magnetic characterization technique such as SQUID (Superconducting Quantum Interference Device) magnetometry is intended. Paramagnetic substrates such as $GdScO_3$ or $DyScO_3$ may be unfit for SQUID experiments as the paramagnetic contribution of the substrate is much larger than

the magnetic signal of the film and thus the film response would be undetectable. In addition to these restrictions, other substrate parameters discussed above such as surface wettability/surface energies and chemical instability may drastically hinder film growth for some compounds. Thus lack of availability of a suitable substrate may also often be a reason why several double perovskites or other complex oxides may be unreachable at present.[6,66,67]

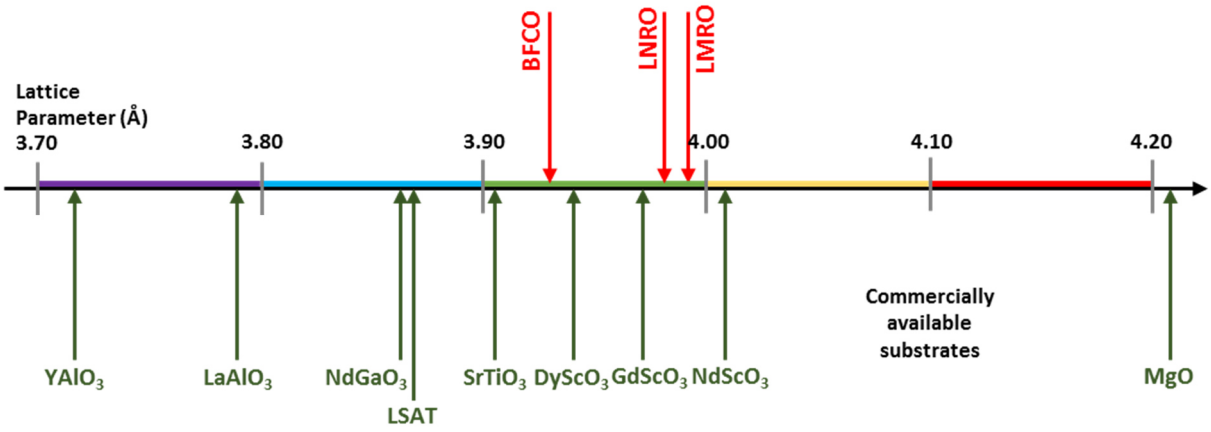

Fig. 2.2 List of commonly used/commercially available oxide single crystal substrates on a schematic scale of their in-plane pseudocubic lattice constants; also bulk pseudocubic in-plane lattice constants of BFCO, LMRO and LNRO have been indicated. (Adapted from Ref. [66])

This work comprises a study of three different double perovskites, first a 3*d*-3*d* compound Bi_2FeCrO_6 (BFCO) and two 3*d*-5*d* compounds La_2MnReO_6 (LMRO) and La_2NiReO_6 (LNRO). As indicated on the horizontal scale in Fig 2.2 the three compounds have a theoretical average bulk in-plane lattice constants of 3.93 Å, 3.99 Å and 3.98 Å respectively. Knowing these theoretically estimated lattice constants and also keeping in mind the necessity to use a diamagnetic substrate that allows for SQUID based magnetometry, the widely studied cubic substrate $SrTiO_3$ (STO) was taken as a substrate of choice for all experiments covered in this work. At ambient conditions, STO has lattice parameter $a=b=c=$ 3.905 Å. These substrates are commercially available and were purchased from the company CrysTec Krystaltechnologie GmbH Berlin. Substrates used were of dimensions 5 X 5 X 0.5 – 1 mm.

Over the recent years, there has been a growing discussion in the oxide thin film community about the need for a STO substrate surface pre-treatment prior to use for thin film growth.[68–70] The goal of the pre-treatment is to create surfaces that are atomically smooth, clean and homogenous that ensures a reproducible and defect free interface and film growth.

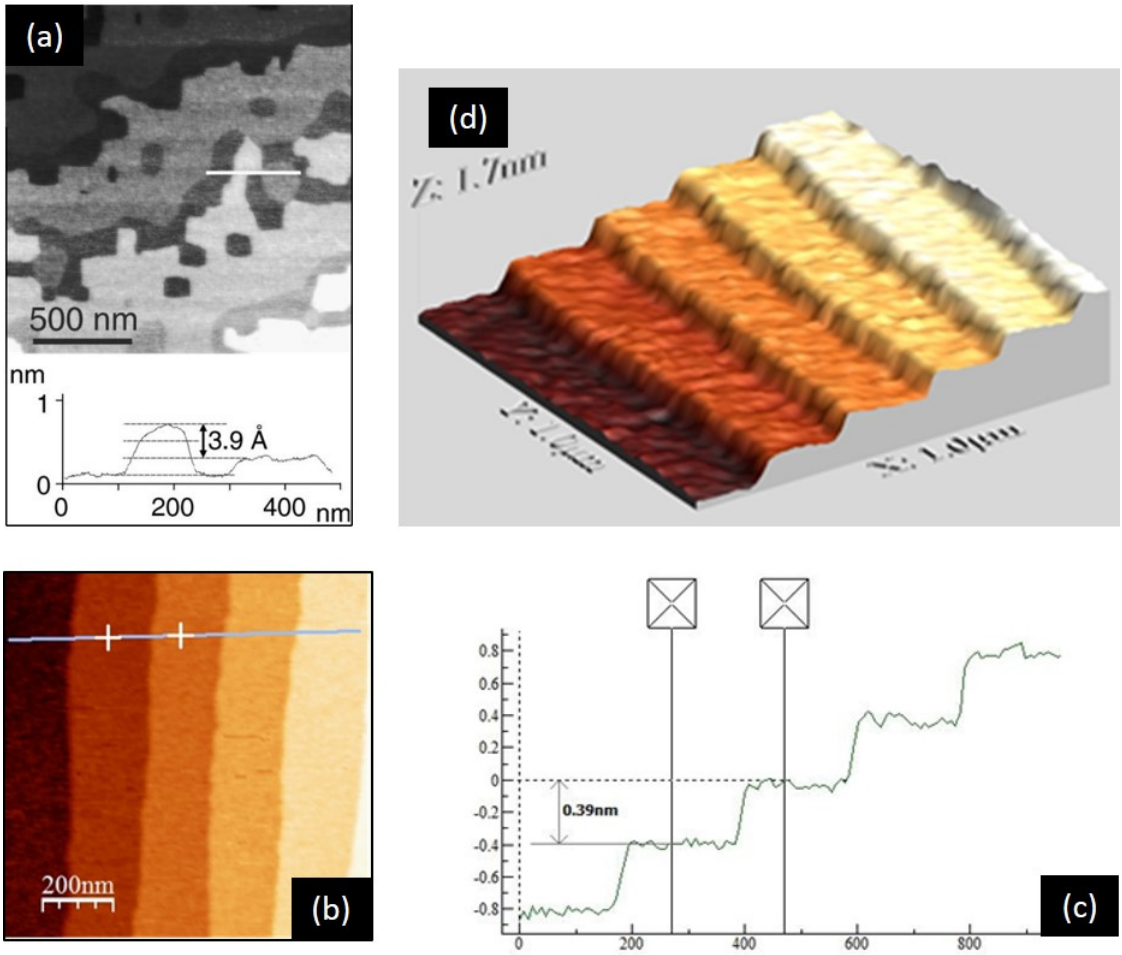

Fig. 2.3 (a) AFM image of a substrate prior to chemical etching showing presence of half unit cell steps (Taken from Ref. [68]); (b) AFM micrograph of a STO substrate post our buffered-HF etch process; (c) z - profile along a line marker indicating full unit cell steps of ~0.39 nm (both axes are plotted on a nanometer scale); (d) 3-dimensional projection of the observed surface in (b).

Early studies on the surface treatment of STO substrate were undertaken by M. Kawasaki *et al.*[70] and G. Koster *et al.*[68] They noted that the commercially available STO substrates whose specifically oriented surfaces are obtained by various crystal cleaving and cutting techniques consist of equal amounts of Sr-O and Ti-O_2 terminated domains that are separated by half unit-cell steps (Fig 2.3(a)). Furthermore mechano-chemical polishing techniques are commonly used to polish the cut surfaces that may render impurities in the surface. The goal of a surface treatment process is thus to remove these impurities and create an atomically smooth single terminated surface. In this study we adopted a method similar to the one suggested by G. Koster *et al.* in to chemically process STO surface prior to deposition.[68] The various steps involved is described in the following section.

Buffered Oxide Etch (BOE)

Buffered Oxide Etch, also known as buffered HF or BHF, is a popular wet etchant used in micro-fabrication. A common buffered oxide etch solution comprises a 6:1 volume ratio of 40% NH_4F in water to 49% HF in water. This solution will etch thermally grown oxide at approximately 2 nanometres per second at 25 degrees Celsius[71].

In-house preparation of the BHF solution

First a 40% NH_4F Solution was prepared by dissolving 40 g of NH_4F salt in 60 ml of water. Then 6 parts by volume of this 40% NH_4F solution was taken in a HF resistant plastic container. To this, one volume part of 49% HF was added to obtain the buffered HF solution. If the available HF acid is not of 49% in strength, a correspondingly different volume of the required HF has to be calculated and accordingly mixed to obtain the commercially recommended BHF composition.

STO substrate treatment procedure

First the as-received substrate surfaces were cleaned dry by blowing Nitrogen gas to remove any dust or particles. Substrates were then subjected to successive ultrasonic cleaning in high purity acetone and isopropanol. The cleaned substrates are then rinsed with deionized water (DI water) and then transferred to another container with fresh DI water. The substrates were fully immersed (polished surface facing up) in DI water and the surface was left to soak undisturbed for 20 to 25 minutes. As per G. Koster *et al.* this step is meant to allow formation of Sr-hydroxide complex from the reaction of the Sr-O blocks on the surface with H_2O.[68] This hydroxide is known to selectively dissolve in acids thereby reducing the etch time required. The soaked substrates were then etched individually for 30 seconds in the above prepared BHF solution. Post the etching the substrates were rinsed in a stream of distilled water and once again rinsed with ethanol (99.99%). Rinsed substrates were then blown dry with pressurized nitrogen gas. These etched substrates were then annealed in a clean furnace at 950 ˚C in oxygen flow for 90 minutes. To confirm the completion of the etch process the surface topography of a few selected substrates were characterized with an Atomic Force Microscope (AFM). An Asylum Research MFP-3D AFM in the non-contact mode was used for this purpose. Figure 2.3 (b) shows the as recorded AFM micrograph of the surface of a chemically etched STO surface indicating a stepped terraces like topography. These surfaces are single terminated (Ti-O_2 layers). The reason such a stepped surface is formed is due to the crystal miscut angle. Hence from such an AFM micrograph, the miscut anle of the substrate

can be estimated by measuring the dimensions of the step. Figure 2.3 (c) shows a z height plot of a line scan across terraces plotted on a nanometer scale. From the figure, it can be seen that the steps are observed to have a width of ~ 200 nm. Each step height is identical and uniform and equal by and large to 0.39 nm which is close to the known unit cell constant for STO = 3.905 Å. From these values the approximate angle of miscut can be estimated to be ~ 0.11˚. A 3-dimensional illustration of the measured area is shown in Fig 2.3 (d) for illustration purpose.

2.1.2. Target synthesis

This section is based on reading from Ref. [72,57] and also from diverse collective inputs from experienced colleagues over the years. Targets form a vital component of the PLD process. Ceramic pellets, single crystals and metals/metal alloys are the most commonly used types of targets. In case of oxide thin films as is within this study, bulk polycrystalline ceramics are often used as targets because they are non-transparent/poorly reflective and thus can better absorb the energy of the laser pulses. Density, stoichiometry, chemical homogeneity and smooth-planar surface are some of the critical aspects that qualify ceramic pellets to be used as targets for PLD.

Density: As a thumb rule, the ceramic pellet is required to have a density which is at-least 80% of the bulk single crystal density of the material being studied. This is important to avoid the formation of large macroscopic target material fragments in the ablated flux. These larger chunks/fragments of particles can bombard the substrate surface causing defects and hindering film growth.

Stoichiometry: In case of simple oxides and compounds which are energetically stable in bulk form so that bulk pellets of them can be synthesized with relative ease, it is commonly preferred to have the targets in the pure single phase form. This ensures chemical homogeneity of the target and stoichiometry. Phase pure targets whose phase is same as the intended films, may also remove the complexity of changing oxidation states of the species during the deposition process. However, in case of the compounds in this study and also in the case of many complex oxides being studied currently, it often turns out that they are either energetically meta-stable or unstable in bulk. In such cases it is commonly accepted that, it is sufficient to have a stoichiometric phase mixture of the elemental species sintered into a pellet with sufficient overall density in a way that the stoichiometry is homogeneous over length scales much smaller than the laser spot size. This is because of the fact that the

ablation process (as described further in section 2.1.3. ensures a stoichiometric transfer of the ablated flux of material from the target to the film.

Homogeneity: Chemical or stoichiometric inhomogeneity either across the plane of the target surface or through the depth can have detrimental consequences on the film growth. This can lead to off-stoichiometry in films, defects in structure and in severe cases lead to polycrystallinity or amorphous growth.

Surface Plane: Studies on the target-laser interactions have established that the direction of the plume is dependent on the surface normal of the target plane. Thus unevenness of the target plane may change the direction of the plume with respect to the position of the substrate, thereby causing dynamic changes in the material arriving at the substrate-consequently leading to stoichiometric changes or defects in the film.

In this study, several different methods were used to synthesize the PLD targets. Conventional solid state synthesis which was used for the case of the 3*d*-3*d* compound Bi_2FeCrO_6 (BFCO) and a sealed quartz tube process was employed in the case of the 3*d*-5*d* compounds La_2MnReO_6 (LMRO) and La_2NiReO_6 (LNRO). Spark Plasma Sintering was used in the case of $BiLaMnReO_6$ (BLMRO).

Conventional solid state synthesis: As illustrated in Fig. 2.4 (left) the conventional solid state synthesis procedure started with mixing and thorough grinding of the oxide powders in stoichiometric quantities. The well-mixed powders are subjected to calcination in a muffle furnace. Partly reacted calcined powders are then reground to attain homogeneity and inter-mixing. In the usual solid state synthesis method, this process of calcining and re-grinding of powders is repeated until the reaction of all oxide species is fully or nearly complete. These powders were then pressed into a pellet using a uniaxial press. The pressed pellet was then subjected to sintering to form a hard, stable and dense ceramic.

Solid state synthesis in sealed quartz tubes: As displayed in Fig 2.4 (right), a relatively more complicated process was adopted in the case of the 3*d*-5*d* compounds LMRO and LNRO. The process allows for almost complete isolation of the reaction mixture from air or atmosphere. This is done in order to counteract the instability or meta-stability of the Rhenium oxides. Under this method, all precursor powders were stored inside an Argon glove box. Mixing and grinding of the oxide powders was performed within the glove box. Well mixed powders of the component oxides were then transferred into one side closed quartz

tubes. Following this, series of steps were undertaken within and outside the glove box to evacuate the tube and finally seal it under a vacuum of about 10^{-2} mbar.

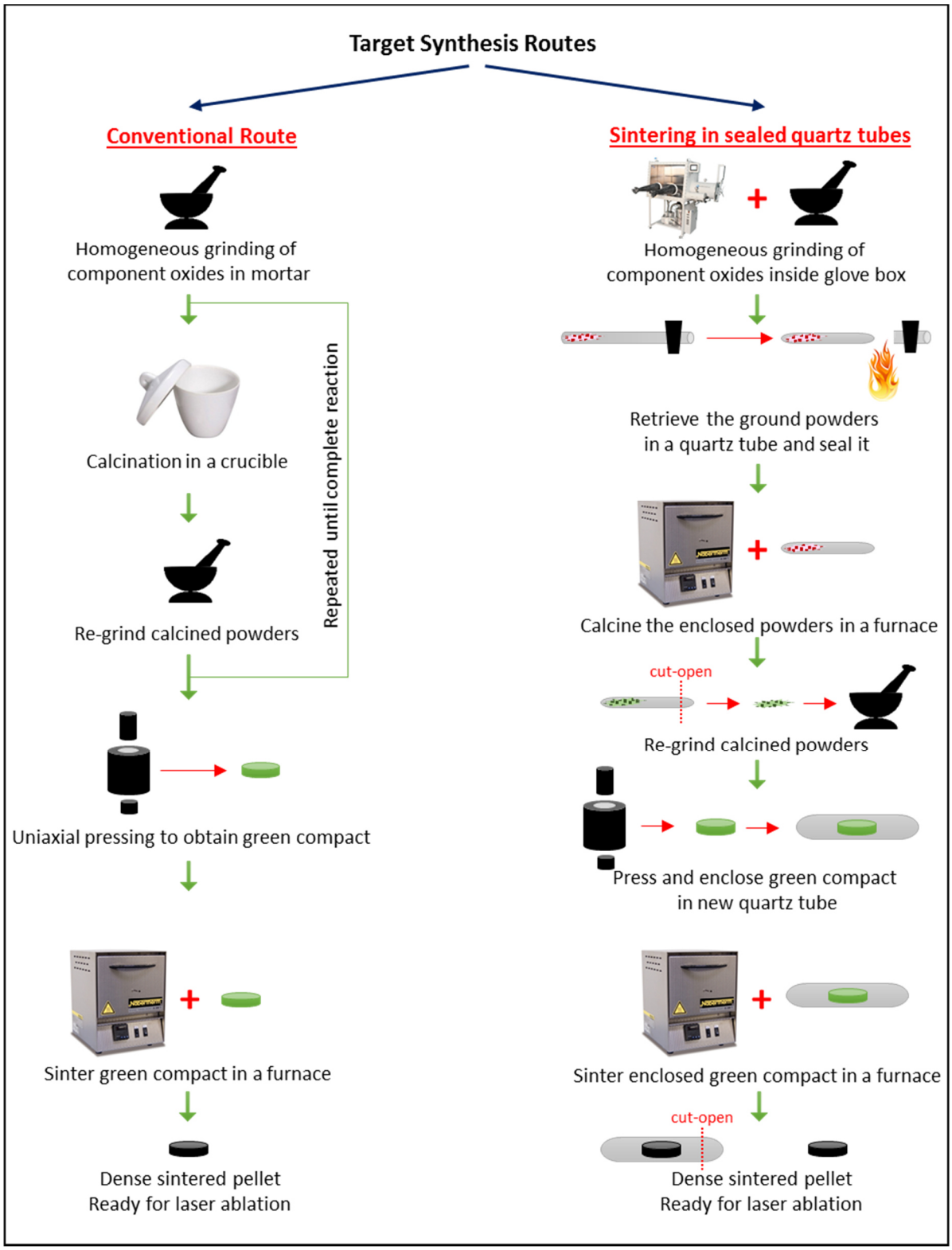

Fig. 2.4 (left) Sequence of steps undertaken in conventional solid-state synthesis of BFCO target; (right) Sequence of steps adopted in the sealed tube process for LMRO/LNRO targets.

All glass blowing and related quartz tube working was self-done using a mixed oxygen-propane gas burner. This required significant amount of self-handling practice over weeks/months and some valuable inputs from expert glass blowers of our neighboring chemistry department. Once initial reaction was complete, powders in intermediary phases were then stable in atmosphere and were further handled outside the glove box. Once again for sintering, powders were pressed in a uniaxial hydraulic press. Pressed pellets were placed in evacuated sealed quartz tubes which were furnace sintered to form the required dense pellets. As the temperatures used were always below 1000˚C, there was no indication of reaction between the quartz tube and the powders. It may thus be noted that for such sintering temperatures (<1000˚C), additional inert isolation (Eg: Platnium/tungsten foils) may not be required.

Spark Plasma Sintering: Final sintering of in some target synthesis trails was also undertaken by Spark Plasma Sintering (SPS), also sometimes known as Field Assisted Sintering Technique (FAST). For this purpose, a Dr. SinterLab system from Fuji Electronics Industrial Co. Japan, belonging to the group of Prof. Dr. Barbara Albert was used. SPS is a high pressure sintering technique where the powders to be sintered are heating by a large electric discharge through the powder mixture. The discharge between the particles creates a spark plasma that allows for reaching extremely high temperatures within a short time period. As a consequence, the elements in the mixture undergo an electrically assisted diffusion process leading to a high density sintered pellet within considerably shorter time as compared to conventional sintering techniques.

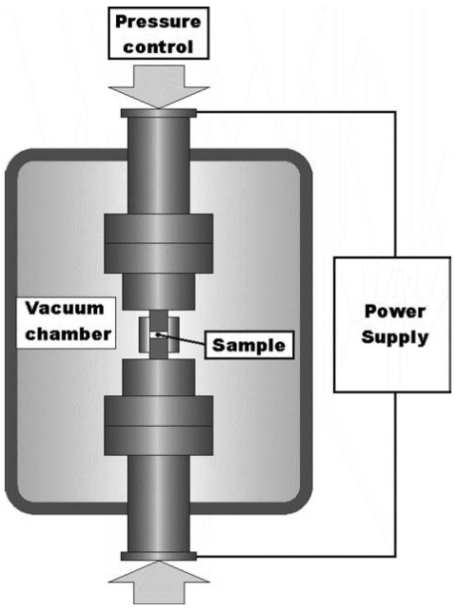

Fig. 2.5 Schematic construction of a Spark Plasma Sintering system (Taken from Ref. [73]).

A schematic drawing of a typical SPS system is shown in Fig. 2.5. The powders to be sintered are externally grinded in a mortar and then filled into a graphite dye. The inner sides of the dye is lined with an additional graphite foil in order to prevent the reaction mixture from fusing with the dye. The filled dye along with the two pistons is then placed on the sample stage. The sample stage is fitted with a pressure control unit that is capable of providing a uniaxial compression. In this system, forces upto 20 kN could be generated by the pressure control system. The whole set up is placed within a vacuum chamber. It is important to have the chamber devoid of oxygen in order to prevent burning of the graphite at elevated process temperatures. The pressing unit is provided with an external power supply that provides the DC source for the spark plasma process. Further information on SPS/FAST can be found in Ref. [73].

2.1.3. Pulsed laser deposition

This section is written based on concepts found in Ref. [72,57] and also from diverse collective inputs from experienced colleagues over the years. Pulsed laser deposition – commonly abbreviated as PLD is a Physical Vapor Deposition technique (PVD), which has been popularly used to grow high quality thin films of a wide range of materials. The process is relatively simple and involves shooting of high energy laser pulses onto a surface of a target. This leads to ionization/ablation of the target material into a plasma plume. A substrate is placed at a suitable position in the vicinity of the target with its surface exposed to the plume. Charged species from the plume collect at the surface of the substrate usually held at elevated temperatures. Nucleation and growth processes at the surface of the substrate leads to growth of a thin film. The entire process is carried out within a clean ultra-high vacuum (UHV) chamber with base pressures of 10^{-6} Torr or lesser.

Although historically laser assisted film growth has been known since the 60s using the early commercial ruby lasers back then, the real emergence of the PLD process as we know it today, was in the late 80's when a team of scientists at Bell Labs, USA demonstrated the use of laser ablation to grow good crystalline quality thin films of $YBa_2Cu_3O_7$ (YBCO) high temperature superconductor.[9] Since then the technique has been widely used to fabricate thin films of a large range of materials including oxides, nitrides, metals and superlattices. The technique has been particularly very successful for the case of ceramic oxides due to its unique capability of being effective for both simple and complex stoichiometries. Parallel improvements also in laser technologies which can now produce lasers with high repetition rate and short duration pulses has further bolstered the capabilities of the PLD process.

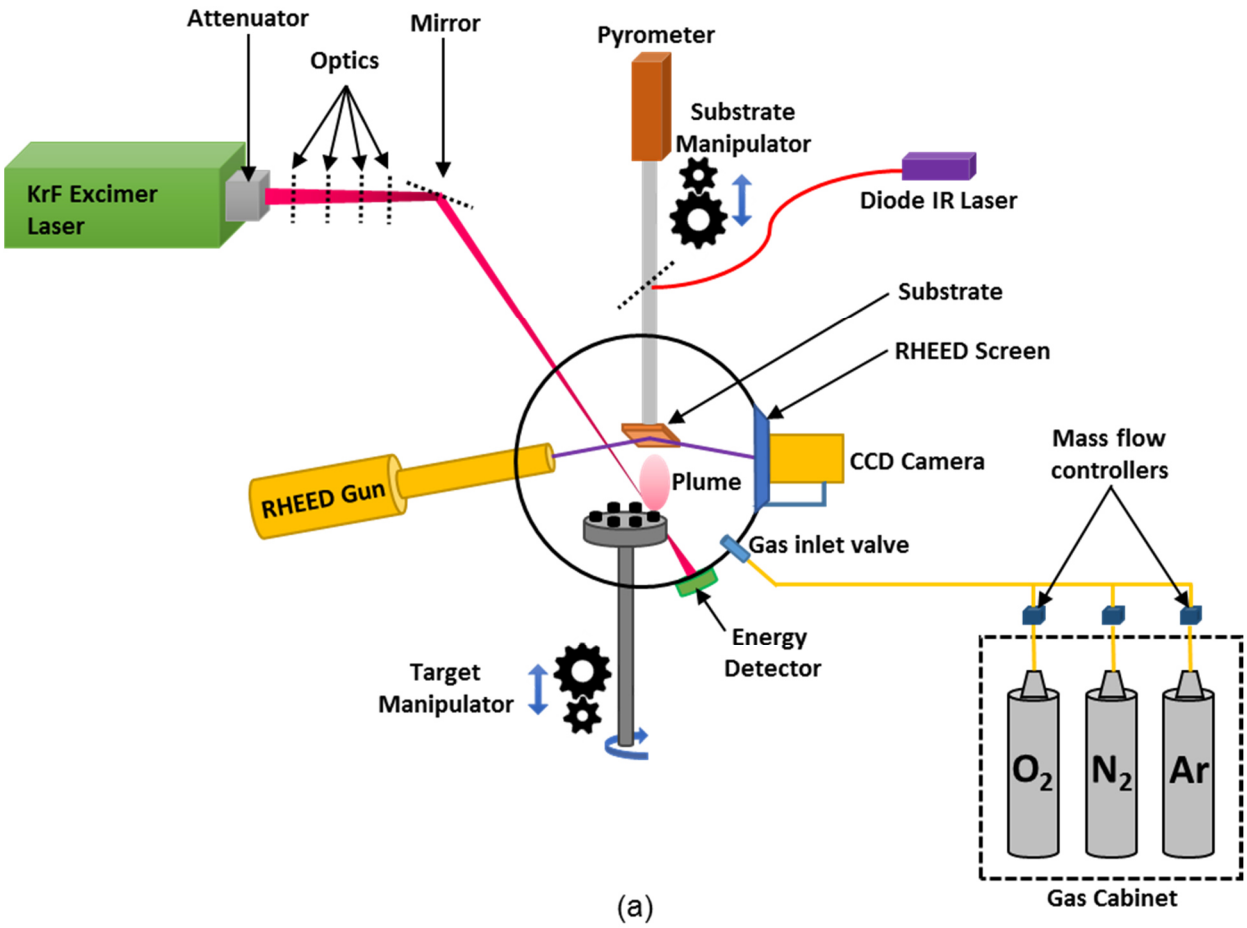

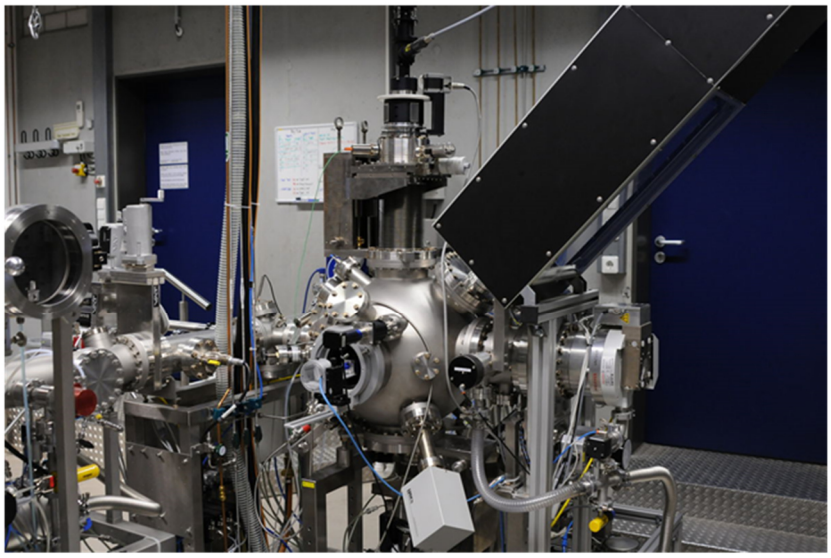

Fig. 2.6 (a) Schematic construction of the DCA Instruments PLD 500 system; (b) Actual photograph of the DCA Instruments PLD 500 System (Photo credits: Gabi Haindl).

System Construction: Fig. 2.6 (a) shows a schematic diagram of the PLD set up used for all experiments in this work. It is a custom built system based on the PLD 500 sourced from DCA Instruments, Finland. An KrF excimer laser from Lambda Physik LEXtra at 248 nm wavelength is used for the ablation. The pulsed beam of the laser is directed through a series of custom designed optics (lenses & mirrors) that ensure a homogenous beam with a small well defined spot. Laser energy densities up to a maximum of 5 J/cm^2 at average spot sizes of 3 mm^2 were achievable. A UV transparent window lets the laser beam into the vacuum chamber directed on to the target carousal. The target carousal can hold 6 targets, each of which have both rotation and sweep movements. Energy measurement is done outside of the chamber along the beam path by moving the target carousal away from the beam path. Substrate manipulator is suspended from top and the holder is positioned vertically above the target. Target substrate distance can be varied by moving the height of the substrate manipulator. Substrate heating is achieved by a 140 W infrared diode laser at 938 nm wavelength and temperature is read out by an infrared pyrometer. Monitoring of surface structure of substrate and the growing film is made possible by an in-situ Reflection High Energy Electron Diffraction (RHEED) system which consists of a 50 keV electron gun pointed at grazing incidence to the substrate surface. High purity process gases can be introduced into the chamber via mass flow controllers and the chamber pressure can be controlled by pumps, standard valves and also an electronic gate valve. Available software allows for remote control of most of the process parameters involved. Furthermore, a load-lock is available for transferring samples in and out of the chamber without breaking the vacuum.

Key Physical Aspects: Some key physical aspects of the PLD process is described below:

a. Laser Target Interactions: For a target material having an optical absorption coefficient a, the Beer's law provides for the calculation of the penetration depth t, at which the incident laser energy is lowered by a factor of the Euler's number ($e = 2.718$). The formula being:

$$t = a^{-1} \ln\left(\frac{\varepsilon}{\varepsilon_0}\right)$$

Where ε is the incident laser energy fluence and ε_0 is the ablation threshold of the target material. During the laser pulse interaction however, some energy is lost to the target by heat diffusion which has a characteristic length of ξ. Excessive target heating is to be avoided as it may lead to thermal evaporation which is undesirable. Thus, for favoring ablation the condition has to be $t < \xi$. This is achieved by the use of lasers capable of delivering high energy densities such as the KrF excimer laser (248 nm) with pulse

widths below 30 ns. It is due to the purposeful use of ablation as against evaporation that one is able to achieve stoichiometric transfer of the target species[74].

b. Plume Dynamics: There are several important points to consider when discussing the plume plasma dynamics. Some of them are – the laser absorption characteristics of the target involved, target surface morphology, interactions of the charged plasma species with the background gases. As the laser pulse hits the target surface, the ablated material is ejected into a plasma containing charged ions, electrons and molecules. The plasma that is created at the target surface then expands and propagates away from the target. The inter-particle collisions are known to cause an anisotropic expansion of the plasma plume. Therefore a preferential forward direction, i.e. normal to the target surface is observed for the plasma particles. Particles in the plasma typically have high velocities (in range of 10^4 m/s). Process gases such as Ar, O_2 or N_2 are thus often used to reduce the kinetic energies of the plasma species. In addition, process gases may also influence oxidation/reduction chemistry at the growing film[72].

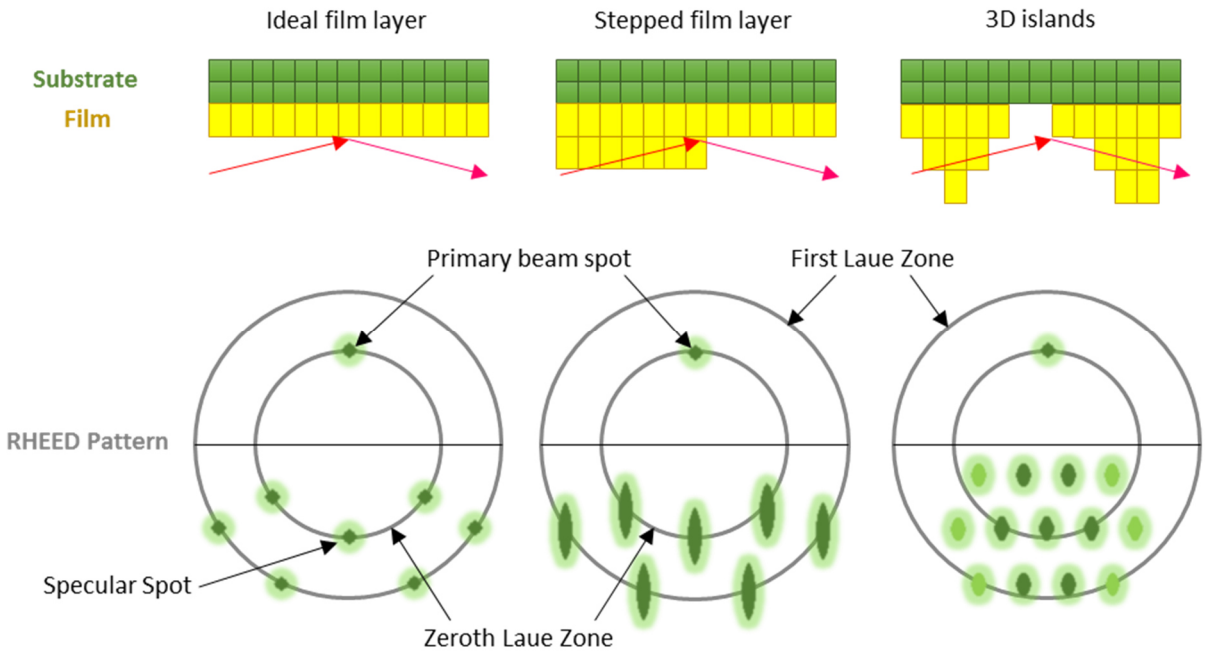

Fig. 2.7 Common trends of observed RHEED inference pattern for different surface morphologies. (Adapted from Ref. [75] - unpublished report)

c. Film growth and in-situ RHEED monitoring: The arriving ionic species from the plume are assimilated on to the substrate surface during film deposition. Film formation takes place by nucleation and growth processes that were described in section 1.3.2. Substrates are often held at elevated temperatures (in range of 500 – 1000 ˚C). This provides atoms

arriving at the surface with the thermal energy to distribute across the surface, which can lead to crystalline films. Use of cold substrate surfaces may lead to the formation of amorphous films. In-situ monitoring of the substrate surface prior to growth and the surface structure of film layer during growth can be monitored by RHEED. A high energy electron beam is diffracted by the surface lattice mesh and the diffracted beam illuminates a phosphor screen at the other end. The observed beam pattern can provide valuable real-time information about the surface structure. The crystallography of the surface mesh determines the type of the diffraction pattern observed. As the film grows, the pattern may remain same or change with time. This time evolution of the diffraction pattern sheds light on the actual mode of the film growth. In case of a 2-D layer-by-layer growth, the intensity of the diffraction spots show a periodic oscillation that corresponds to constructive and destructive interferences at each added full monolayer and half monolayer of the growing film. Thus by counting the oscillations, one can determine the thickness of the film. This is particularly useful in case of growing superlattices. However, not all materials may grow in a layer-by-layer fashion thereby restricting such an in-situ monitoring of film thickness. Fig. 2.7 shows the different surface morphologies and their corresponding RHEED patterns. Ideal 2D surface produces well defined spots along the Laue Zones. A stepped surface has a similar pattern, however the spots appear elongated. A surface with 3D islands results in a spotty pattern.

Laser Pulse Control Software: A small, yet important system upgrade was undertaken within the scope of this doctoral work. This was concerned with coding a customized software to control the pulsed emissions of the KrF excimer laser used for the experiments.

Fig. 2.8 An image of the National Instruments NI PCI 6601 Card (Ref.: National Instruments®. Retrieved 16.11.2016, from http://sine.ni.com/nips/cds/view/p/lang/de/nid/3589)

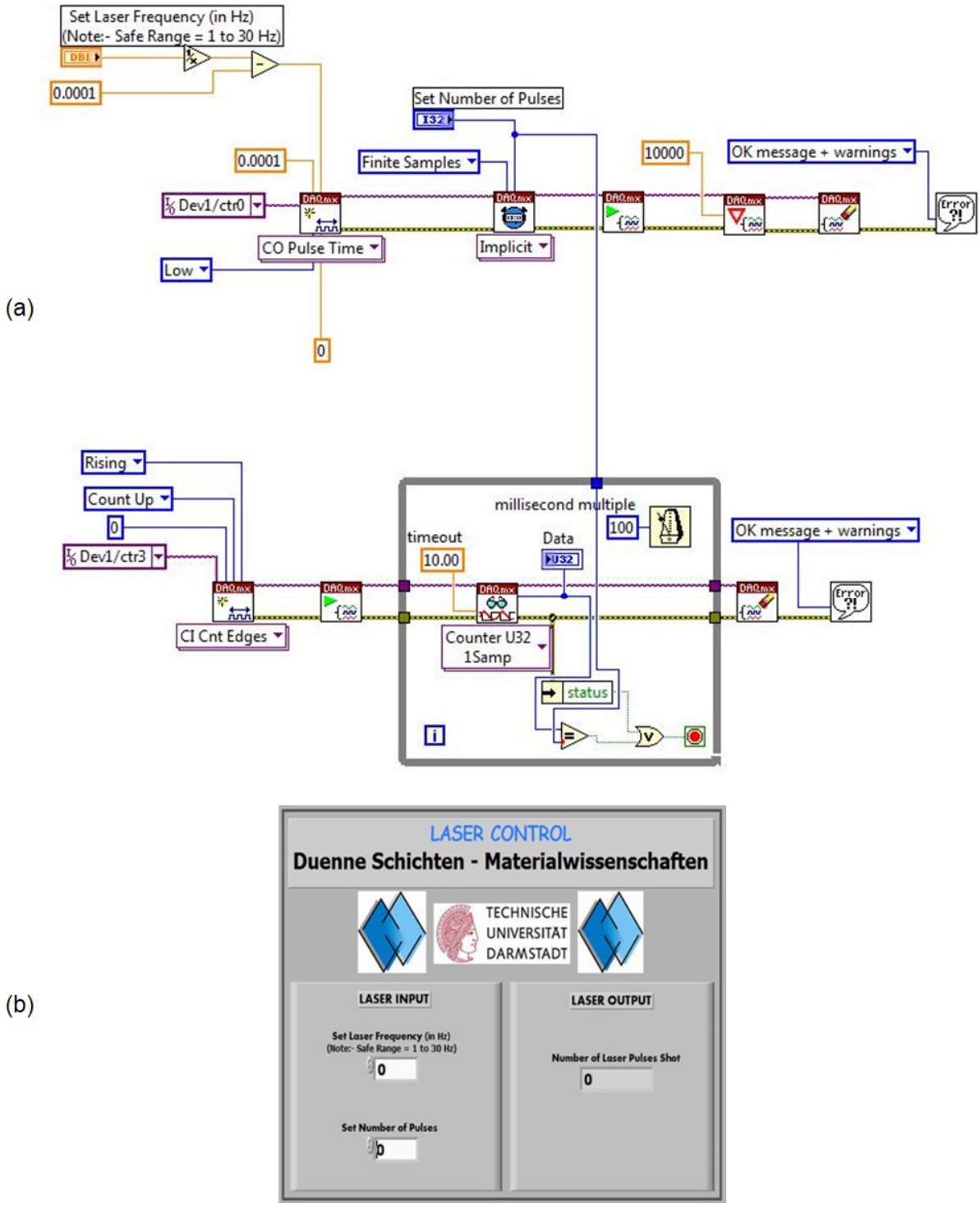

Fig. 2.9 (a) Block diagram of the as coded program for the Laser control software; (b) Graphical User Interface of the Laser control program.

The objective of the software was to generate an external pulse to trigger each pulsed laser shot while the laser remained passively switched-on in remote control mode. By doing so, one is capable of accurately counting the number of laser pulses to be shot and consequently pre-set required number of laser shots for each experimental run. Another aspect of the software

was to be able to pre-set the laser pulse frequency for each experiment. This way, one is capable of varying frequency of the laser pulses ranging from 1 Hz to 30 Hz. Laser pulse frequency is one of the crucial film growth parameters that often needs to be optimized for different materials. Thus this software has been an inevitable component of routine PLD usage not just for this research work but also all other studies that have been carried out in above mentioned DCA-PLD-500 system.

This task was realized by using a National Instruments PCI 6601 card which is a timing and digital Input/Output board for PCI computers (Shown in Fig. 2.8). The card was inserted into a PCI slot available on a regular Windows PC. The card was then connected to the hardware input of the laser via a NI CB-68LP terminal block and a R-6868 connector cable. The software for the required functions was coded using National Instruments LabVIEW 8.2. Fig. 2.9 (a) shows a block diagram for the as written code for the laser control functions and the corresponding graphical user interface is shown in Fig. 2.9 (b).

2.2. Structural characterization

This research work was aimed at fabricating epitaxial thin films of the materials concerned. Fundamentals of epitaxy were discussed previously in section 1.3.2, from which one can infer that crystallography is an important aspect of establishing epitaxy. Besides it also provides useful information about the phases, phase purity, crystallinity, strain, crystal structure and lattice parameters. Hence detailed crystallographic / crystal structure studies were undertaken in this work using various methods of X-ray diffraction.

2.2.1. X-ray diffraction

This section is drafted based on Ref. [76–81]. X-rays are a type of electromagnetic radiation whose energies lie in the range of 100 eV – 100 keV and were first discovered by Wilhelm Röntgen 1895. Since then X-rays have been widely studied and technologically applied. To condensed matter physicists, particularly of interest is the interaction of X-rays with matter where scattering is one the most dominant effects. Two types of scattering may occur: inelastic and elastic. Inelastic scattering or Compton scattering occurs when part of energy of the X-rays is transferred to the scattering electron thereby changing its wavelength. When the wavelength of the X-ray before and after a scattering event remains, unchanged, it is said to have undergone an elastic scattering. When regular array of such scattering centers cause elastic scattering of a beam of incident X-rays, the scattered rays can interact with each other thereby allowing for the possibility for diffraction. X-ray diffraction (XRD) is a physical

phenomenon where a crystal containing uniformly spaced atoms can cause an interference pattern of a monochromatic beam of X-rays directed at the crystal. The phenomenon is governed by the Bragg's law which is depicted in Fig. 2.10. For a crystal with a given family of planes (hkl), whose planes are placed at a repeating distance of d_{hkl}, the Bragg's law states that a constructive interference will be observed when the incident angle θ, is such that the path difference between two waves is a multiple of the wavelength of the incident X-ray radiation. Mathematically, it is written as:

$$2d_{hkl}\sin\theta = n \cdot \lambda$$

Where n is the order of the diffraction and λ is the wavelength of the incident radiation. For most experiments in this work, Copper $K\alpha_1$ was used which has $\lambda = 1.5406$ Å

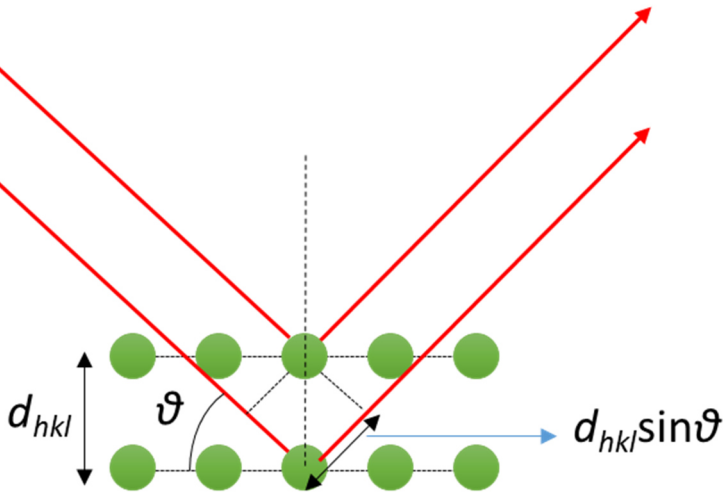

Fig. 2.10 (a) Illustration of conditions for satisfying Bragg's law.

Thus X-ray diffraction can be used to get valuable dimensional and structure pattern information of crystals and materials.

In order to conveniently analyze the observed diffraction effects and also to address various measurement techniques, the concept of reciprocal lattice is widely used in XRD methods. Under this convention, each family of lattice planes with equal d-spacing is represented by a vector $\mathbf{g}_{hkl}$ whose direction is identical to the plane normal and length is identical to the inverse of the interplanar spacing d_{hkl}. This vector is called the reciprocal lattice vector, whose starting point is called the origin and the end point is a reciprocal lattice point. A collection of the reciprocal lattice points the reciprocal lattice. The space in which the actual lattice and

actual lattice planes exist is known as the real space and conversely the space containing the reciprocal lattice is known as the reciprocal space. In order to define the Bragg condition under this convention, the incident and the scattered X-ray beams are represented by wave vectors $\mathbf{k}_i$ and $\mathbf{k}_s$ respectively whose directions are same as the direction of propagation of the X-rays and whose lengths are given by $\frac{1}{\lambda}$. The scattering of the $\mathbf{k}_i$ and $\mathbf{k}_s$ is defined by the scattering vector K which is a sum of the incident and scattering wave vector as follows:

$$\mathbf{k_i} - \mathbf{k_s} = \mathbf{K}$$

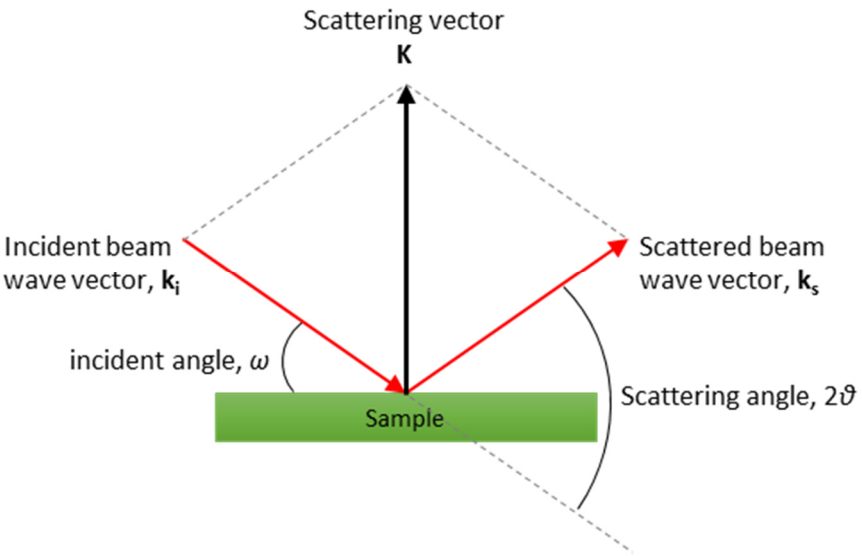

Fig. 2.11 (a) Relationship of the incident beam vector k_i, scattered beam vector k_s and the scattering vector K.

For a given family of lattice planes (*hkl*) each time the scattering vector K coincides with the reciprocal lattice vector $\mathbf{g}_{hkl}$, the diffraction condition or the Bragg's law is said to be met.

System Description: Most of the XRD experiments undertaken in this work were carried out on a Rigaku SmartLab four – circle diffractometer with a rotating anode Cu $K\alpha_1$ X-ray source (λ = 1.5406 Å). Figure 2.12 (a) Å shows an image of the front view of the diffractometer and a schematic construction of the sample stage of the horizontal sample mount goniometer is shown in 2.12 (b). In the standard configuration, on the incident beam side, we used a 2-bounce Ge-monochromator and a slit to direct the divergent beam of X-rays to a parallel beam mode. Additionally horizontal and vertical length limiting slits were used to cut the dimensions of the incident beam in accordance with the sample under investigation. Thin film samples were grown on 5 X 5 mm substrates and hence in most cases vertical and horizontal slits of 1 mm and 2 mm respectively were used to tailor the beam to a 1 X 2 mm spot on the

sample. The beam was once again narrowed with slits also on the reflected beam side using two 0.5 mm slits. The various axes of possible movements have been depicted in Figure 2.12 (b). In addition the sample stage also has automated movement along the z-axis.

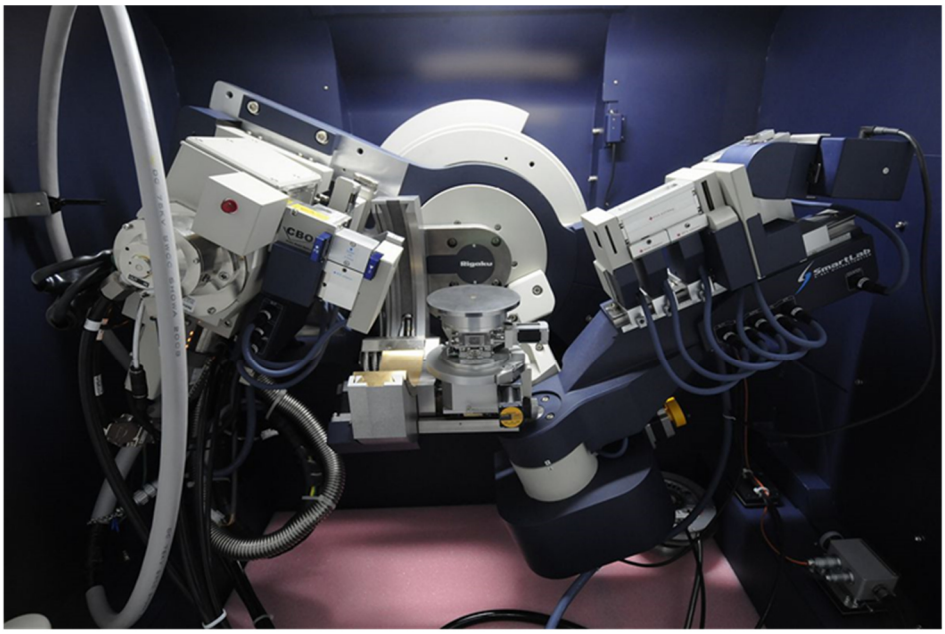

(a)

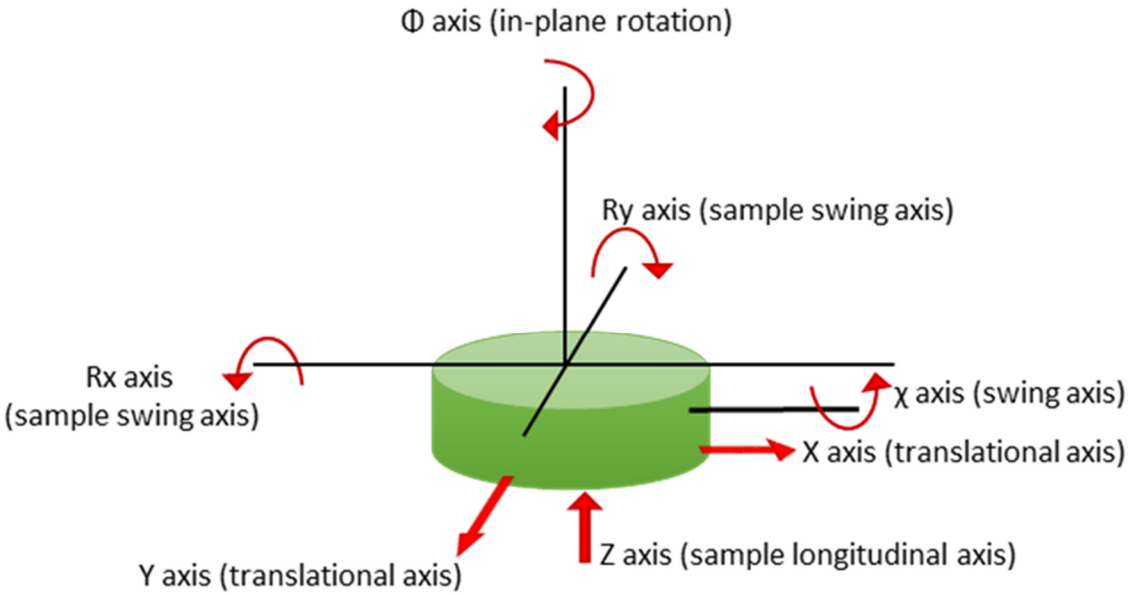

(b)

Fig. 2.12 (a) Photographic front view of the Rigaku SmartLab four-circle diffractometer (Picture Credits: Gabi Haindl); (b) Sample stage of the horizontal sample mount goniometer (Adapted from Rigaku SmartLab Training Textbook[79]).

Several different XRD measurement techniques used in this study are described in the following sections:

Coupled $2\theta - \omega$ Scan:

This type of measurement can be realized by the movement of both the source and the detector, while the sample is held stationary. As the name suggests, in spite of both movements of the detector and the source, a constant angular relation between the two is maintained namely – the diffraction angle (2θ) is always held to be twice the incident angle (ω). Thus the direction of the scattering vector remains unchanged during the measurements. This method is used for the investigation of crystal planes that are parallel to the measurement/surface plane. Interplanar spacings of these parallel planes can be estimated. In case of epitaxial thin films this method is used to determine the out-of-plane lattice parameter of the thin films. Besides, it can also help in identifying impurity phases, if present.

ω – Scan or Rocking Curve Measurement:

This type of measurement can be realized by holding both source and detector at fixed angle corresponding to a particular Bragg reflection and then rocking the sample about the Bragg peak slightly. Such a measurement enables the variation of the scattering vector along a circular path centered at the origin. A plot of the detected intensity of such a measurement as a function of ω is known as the rocking curve. In reality, the as-grown thin films even though epitaxial, are different from ideal crystals. They may consist of crystallites that have small differences in their orientation which leads to a mosiacity. Besides the measured samples may also contain defects such as point defects and/or also dislocations. These crystal imperfections can be effectively characterized by the ω – scan. A lower mosiacity leads to a smaller full width at half maximum (FWHM) of the measured Bragg peak and relates to better crystallinity. On the other hand, a high mosiacity leads to observation of a peak with a larger FWHM.

X-ray reflectivity

An X-ray reflectivity measurement is performed similar to the $2\theta - \omega$ scan in terms of the movement of the source and detector, however it is performed at much lower incidence angles. Another important difference is that – for a reflectivity measurement, the alignment is done with respect to the surface normal of the sample and not the lattice plane normal. X-ray reflectivity is based on the principle of total external reflection where a beam of X-rays incident at low angles on a surface of a film such that the incident angle is smaller than a

critical angle θ_c, the beam is fully reflected back from the surface. θ_c is a function of the electron density of the film media and thus indirectly related to its density.

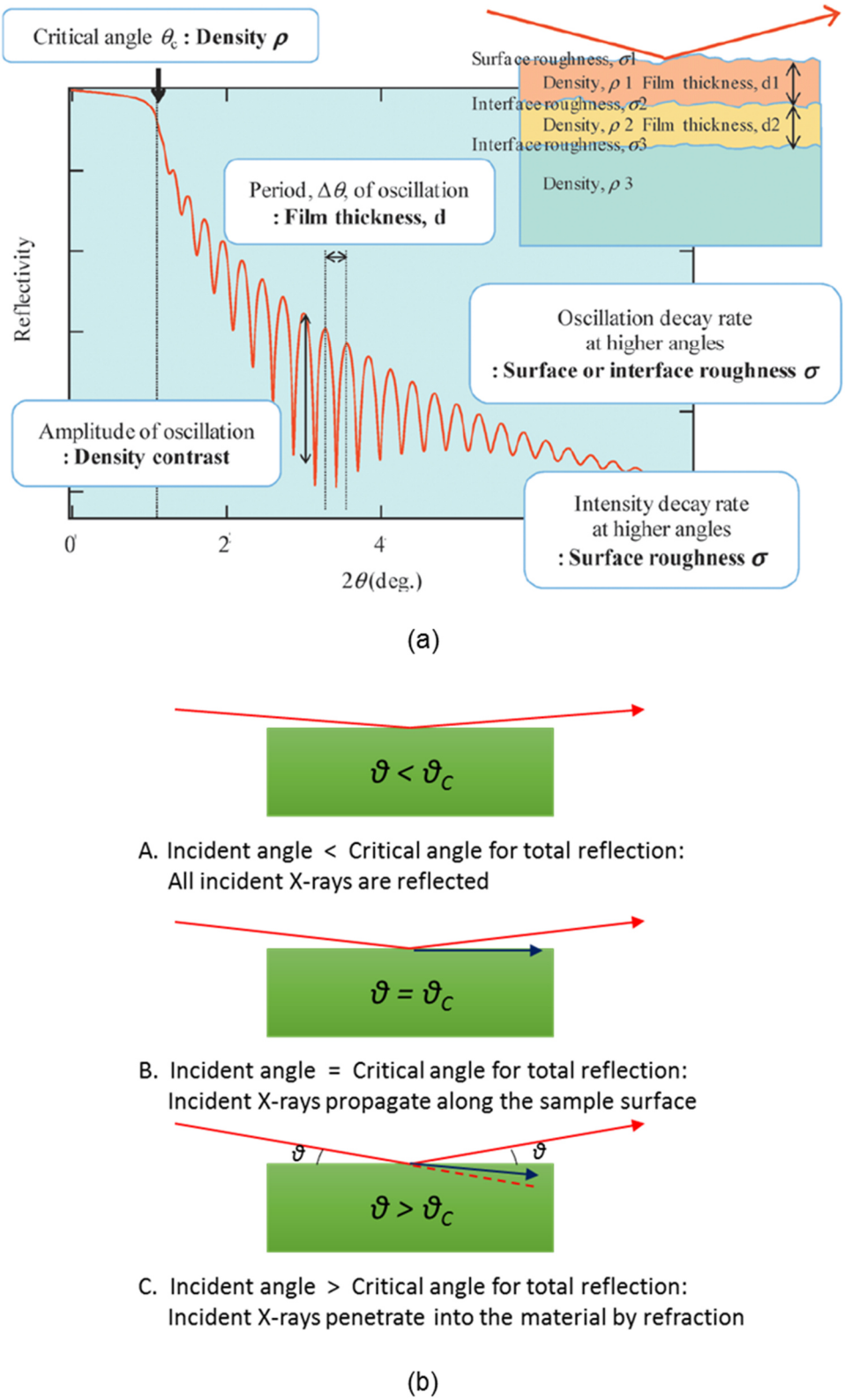

Fig. 2.13 (a) Various features of an XRR profile and the information they can provide (Taken from Ref. [80]); (b) Reflection and Refraction of a beam of X-rays directed at a material (Adapted from Ref. [80]).

Beyond the critical angle, a part of the beam can penetrate into the film and get reflected from interface of the film and the substrate. Interference occurs between the X-rays reflected from film surface and the film-substrate interface which shows up as oscillations in the measured intensity. These are known as Kiessig fringes. The period of the oscillations bear a relationship with the thickness of the film, its amplitude with film-substrate interface roughness and its damping with roughness at film surface. Figure 2.13 demonstrates various features of a typical XRR curve and the corresponding valuable information they contain. The measurement data can be analyzed by fitting the curve using standard reflectivity fitting programs from where all the crucial film parameters such as density, film thickness, surface and interface roughness can be extracted.

Skew-symmetric scans

In some cases, it may be of experimental interest to characterize a set of planes that are not parallel to the sample surface or whose plane normal has an in-plane component. One such case has to do with regard to characterization of 'rock-salt' type chemical ordering of the *B*-site cations in double perovskite thin films studied within this work. Here, ordering of the *B*-site cations causes doubling of the unit cell along the (111) direction. Detection of such a superstructure may be possible by a skew-symmetric scan which is possible in a 4 circle diffractometer such as the Rigaku SmartLab. In the skew geometry, the sample is tilted with respect to its surface normal by the lattice plane inclination χ, which makes the required (*hkl*) family of planes parallel to the measurement plane. Once the χ tilt is fixed, measurement is completed similar to a coupled $2\theta - \omega$ Scan**.** The value of the skew-symmetric inclination χ, used for measuring the (111) family of planes in the case of the cubic $SrTiO_3$ substrates used in this study was 54.7˚.

Reciprocal space mapping

Reciprocal space mapping (RSM) is a type of measurement used to extract intensity distribution maps around a particular crystal reflection (*hkl*). Here one of the Miller indices – say k, is fixed in the reciprocal lattice, and other two indices h and l are scanned in the vicinity $\pm\delta h$ and $\pm\delta l$. Such a contour map can be realized by measuring either several $2\theta - \omega$ scans for different ω offsets, or conversely by performing several ω scans for different 2θ offsets. It is particularly of interest for epitaxial layers, as it provides information on substrate-film epitaxial relation, strain state of the film and lattice parameters in- and out-of- the layer plane. The measurement is analyzed in a two dimensional plot of the intensity contour plotted across perpendicular (q_z or $Q_\perp$) and parallel (q_x or $Q_\parallel$) components in reciprocal lattice units. The lattice

parameters of the layer out-of- and in-plane are each inversely related to the peak positions along $Q_{\perp}$ and $Q_{\parallel}$ respectively. Fig. 2.14 (top) shows a schematic of a RSM scan for symmetric reflection [$h0l$]. Fig. 2.14 (bottom) shows variations in the reciprocal lattice for a strained and an unstrained epitaxial layer.

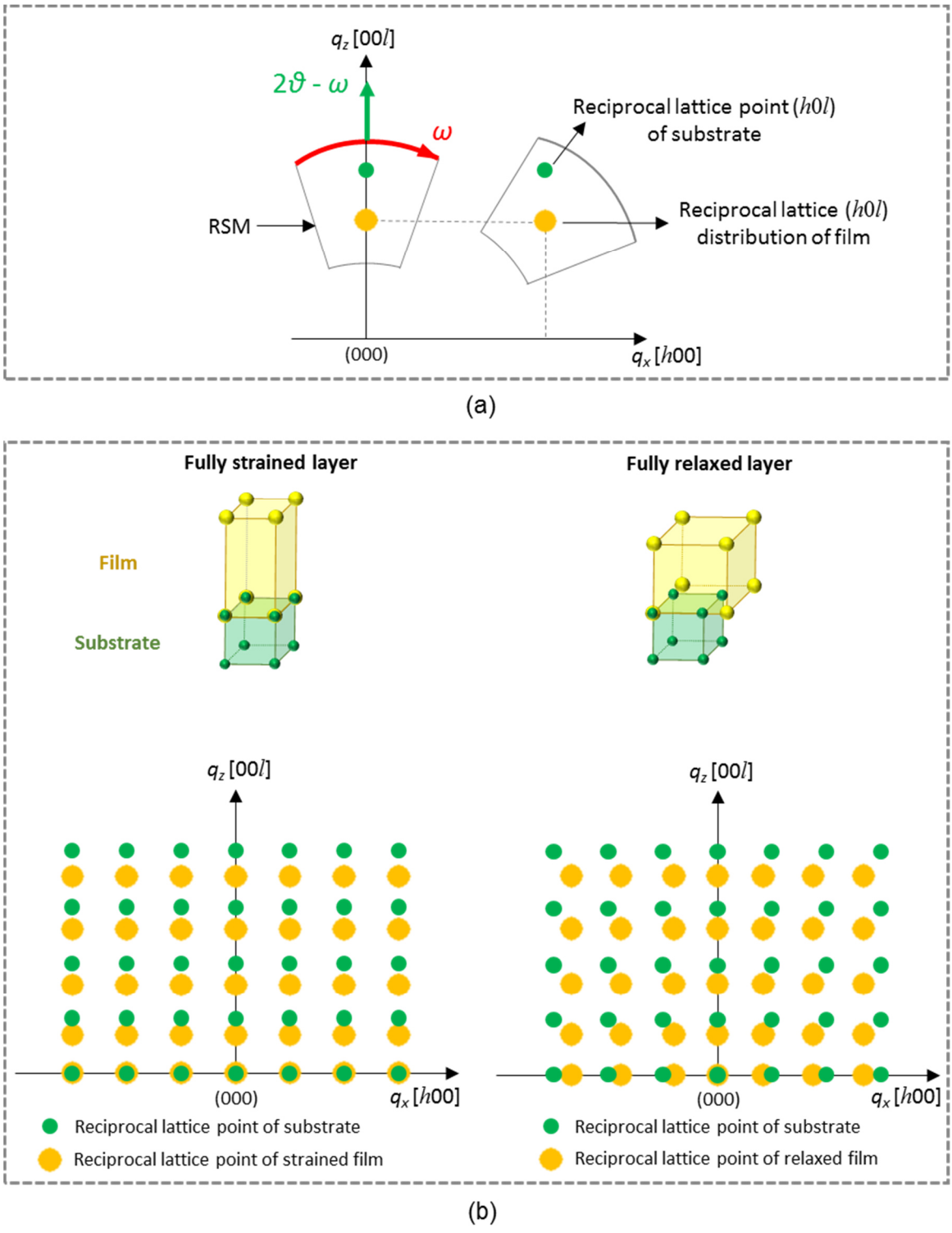

Fig. 2.14 (a) Schematic representation of an RSM scan (Adapted from Rigaku SmartLab Training Textbook-Ref. [79]); (b) Variations in reciprocal lattice for a strained and relaxed film.

Energy dependent measurements

Often synchrotron facilities are sought after when X-rays at different energies are required for a particular study. In this work a similar goal was accomplished by simply making use of various separate X-ray sources and laboratory diffractometers. As discussed further in section 3.4, this was primarily done to vary the structure factor of a particular reflection (F_{hkl}) as a function of the incident X-ray energy. Measurements were performed at 4 different characteristic X-ray energies namely Co-K_α (6930 eV), Co-K_β (7649 eV), Cu-K_α (8047 eV) and Mo-K_α (17,497 eV). Diffraction experiments under a Co source was performed on an Enraf-Nonius CAD-4 four-circle diffractometer while a home/built six-circle diffractometer was used for experiments under a Mo source. For measurements at Cu- K_α energies, the same Rigaku SmartLab 4-circle diffractometer, as described in above sections was used.

2.3. Surface topography, microstructrual characterization and imaging

2.3.1. Atomic force microscopy

Atomic Force Microscopy (or AFM) is a type of Scanning Probe Microscope (SPM) which was developed as an extension of the Scanning Tunneling Microscopy for the sake of applying to non-conductive samples. Since its development, AFM has been widely used to perform high-resolution (of the order of a fractions of nanometer in best case) topography imaging of a wide range of materials.

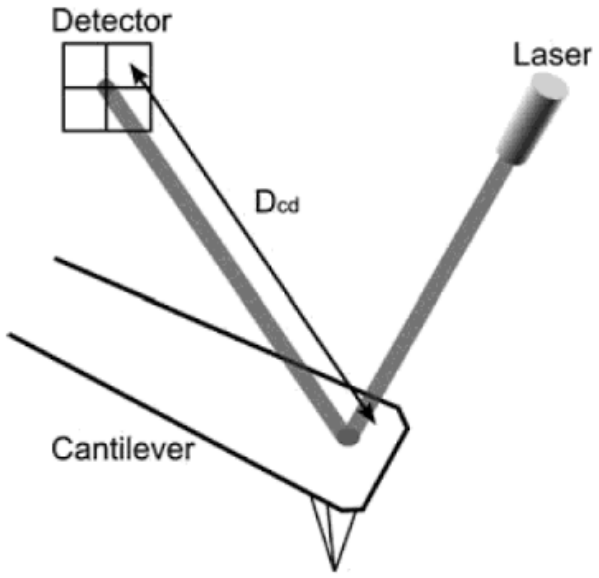

Fig. 2.15 Schematic drawing of an optical lever mechanism used in an AFM. (Taken from Ref. [82])

AFM is realized by scanning a probe with a sharp tip (tip radius ~ 5 to 20 nm) across the surface of the sample while delicately maintaining the force between the tip and the sample surface. A laser beam is directed at the back side of the cantilever probe, which reflects off of the probe and falls on to a distant highly sensitive photodetector. This is known as an optical lever. As the tip is scanned across the sample surface by precise position controlling piezoelectric mechanism, interatomic forces between the tip and the sample surface induces displacement of the tip and corresponding bending of the cantilever. These small bending movements of the tip due to the sample topography are recorded exaggeratedly by the photodetector due to the changing reflected beam positions. This feedback is thus electrically processed and used to build a high resolution topography image.[82,83]

There are several modes in which an AFM is operated. These are namely: contact mode, tapping mode and the non-contact mode. The contact mode is a static mode where the tip is literally dragged across the sample surface. Tapping and non-contact modes are considered to be dynamic modes since in these modes, an additional piezoelectric element is used to induce a high-frequency (in the range: 10 – 300 kHz). In the tapping mode, the tip actually comes in contact with sample surface and goes back away from the surface with each oscillation. In the non-contact mode, the cantilever remains close to the sample surface but not really in contact. Post the success of the AFM, the basic technique was adapted to achieve various kinds of functional characterization. Some examples are Piezoresponse Force Microscopy (PFM) which can be used to characterize ferroelectric materials; Magnetic Force Microscopy (MFM) which can be used to map magnetic domains at the sample surface; Kelvin Probe Microscopy (KPM) which can be used to measure work function and contact potential differences across the sample surface. Details of each of these advanced SPM techniques is beyond the scope of this work.

2.3.2. Scanning electron microscopy

Scanning Electron Microscopy (SEM) or High Resolution Electron Microscopy (HREM) is a surface topography, microstructure and chemical composition analysis technique where a focused beam of electrons is used to illuminate a sample in a high vacuum chamber. In this work, a Philips XL30 with a field emission gun (FEG) was used. Electrons emitted from the field emission gun is accelerated by a positively charged anode. Focusing of the beam is achieved by magnetic lenses and scanning coils are used to raster the focused electron beam across the surface of the sample. Interaction of the electron beam with the sample results in the ejection of secondary electrons, Auger electrons, X-rays and primary backscattered electrons. The system used in this work consisted of two individual detectors for secondary

and backscattered electrons which gather the ejected electrons to form the image. Secondary electrons are emitted from the atoms close to the surface top and provides a direct visualization of the surface topography. Often with secondary electron imaging, high resolutions can be achieved. With most standard SEMs topographic features under a magnification of up to 100,000 X, spatial resolutions of the order of 5 nm can be achieved. Backscattered electrons are the incident electrons that are directly reflected back by the atoms in the sample. In this type of imaging, the resulting contrast is determined by the atomic number of the sample elements. This technique can thus be used to detect chemical phase distributions in the sample. Samples can be observed live under the electron illumination, images of the relevant features are then digitally recorded and saved using the provided microscope control software.[84]

2.3.3. High angle annular dark field – Scanning transmission electron microscopy

Scanning Transmission Electron Microscopy (STEM) was used in this work to observe the microstructure of the thin film cross-section. STEM sample preparation and measurements were performed by the collaborating group of Prof. Dr. Joke Hadermann at the University of Antwerp, Belgium. Measurements were carried out on a FEI Titan 80-300 "cubed" microscope equipped with a Super-X detector and operated at 300 kV.

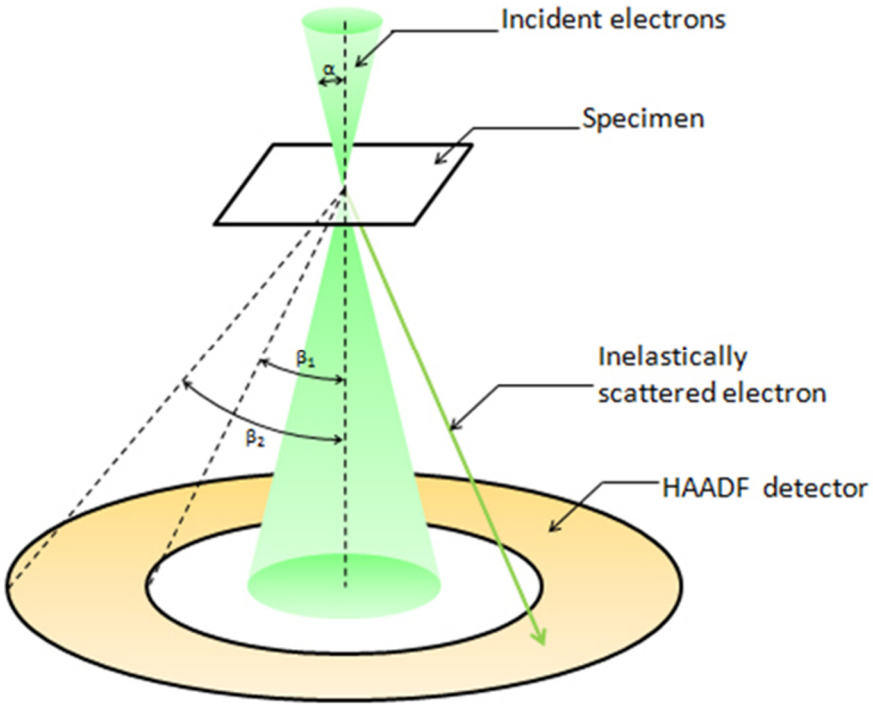

Fig. 2.16 An illustration of the HAADF detector in a STEM setup. (Ref.: JEOL Limited. Retrieved 17.11.2016, from http://www.jeol.co.jp/en/words/emterms/search_result.html?keyword=HAADF-STEM)

High-angle annular dark-field scanning transmission electron microscopy (HAADF-STEM) is a one of the STEM methods where an annular dark field detector is used to receive inelastically scattered electrons at high angles. As indicated in Fig 2.16 below the detector is in the form of a disc with a hole. The STEM image is then constructed by integrating the intensities of the electrons with respect to the incident probe position. It has been noted that the HAADF image intensities are proportional to a power of the atomic number, Z ($I \sim Z^n$, $1.5 < n < 2.0$), hence heavier atoms are observed brighter than the lighter ones.[85,86]

2.4. Chemical analysis methods

2.4.1. Energy dispersive X-ray spectroscopy

Energy dispersive X-ray spectroscopy (EDX or EDS) is an analytical technique used for elemental analysis where both qualitative and quantitative chemical characterization can be performed. The basic principle of EDX is as follows: when a focused beam of high energy electrons is directed at the sample, inelastic collisions may occur leading to ejection of the core shells of the atoms in the sample. This is followed by de-excitation where an electron from an outer shells falls down to the vacant inner shell. The difference in the energy of the electron leads to the emission of an X-ray photon. The energies of the emitted photons due to the excitation - de-excitation process are characteristic of the elements involved. Thus the energies of the emitted characteristic X-rays contain qualitative information of the elements present in the sample. Besides the characteristic X-rays, there is also the Bremsstrahlung radiation observed as a background which basically results from the energy loss of the incident electrons by the Coloumb field of sample atoms. The EDS setup consists of a semiconducting silicon/germanium detector that collects the incoming X-ray photons and processes their energies to finally provide a plot of intensity of signal as a function of energy of the photon. Integral area of the peak intensites in an EDS spectrum contains quantitative information of the elements involved. EDS detectors are often coupled with electron beam based microscopy techniques such as SEM and TEM. Combining with the imaging capabilities of these tools, one can perform spatially resolved elemental analysis from areas in range of few nanometers. In this work, EDS was mainly used to estimate stoichiometries of various samples involved.[84]

2.4.2. X-ray photoelectron spectroscopy

X-ray Photoelectron Spectroscopy (XPS) or sometimes also referred to as Electron Spectroscopy for Chemical Analysis (ESCA) is a surface analysis technique that can provide valuable quantitative and chemical environment/state information of the elements present on the sample surface. The measurement depth is usually about 5 nm. XPS is based on the principle of the photoelectric effect, where a sample illuminated by soft X-ray radiation leads to the emission of photoelectrons from the bound states of surface atoms leaving them behind in an excited state. Since the energy of the X-ray photons used is known, the kinetic energy of the photoelectrons can be mathematically described as follows:

$$E_K = h\upsilon - (BE + \phi)$$

Where hυ, BE and ϕ are the photon energy, binding energy of the ejected electron and the work function of the material respectively.

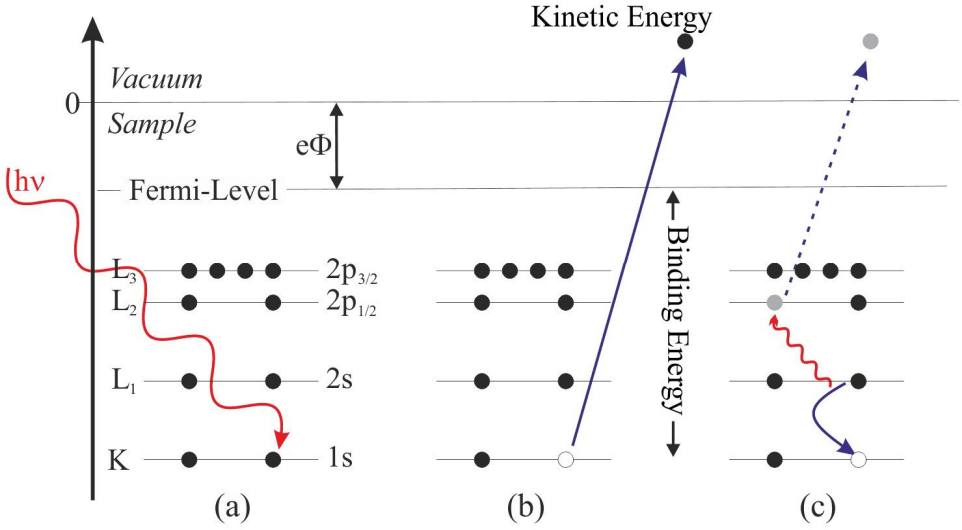

Fig. 2.17 Principle of photoelectron emission and Auger relaxation. (Ref.: Eagle Lab – Polish Academy of Sciences, Retrieved 17.11.2016, from http://www.eagle-regpot.eu/EAgLE-Equipment_XPS.html)

The ejected electrons are collected by an electron analyzer that records their kinetic energy. Based on the equation above, a plot of the energy spectrum of intensity versus binding energy is taken for analysis. Each peak on the obtained plot corresponds to a specific element thus allowing to qualitatively identify the elements present in the sample. In addition to that, the integral intensities of the peaks contain quantitative information and can thus be used to determine the chemical composition of the sample. In addition to the ideal photoemission as described above, additional phenomena may often occur that show up as features on the

obtained energy spectrum and need to be considered in the analysis process. One example is the Auger electron emission which basically results when a core hole recombines with an outer electron by transferring the recombination energy to another outer electron leading to its emission. In this work, XPS measurements were performed on a PHI Versaprobe 500 spectrometer using a monochromatic Al-K_α X-ray radiation source (1486.6 eV). Measurements were performed at room temperature under ultra-high vacuum ($<10^{-9}$ Torr). Samples for measurement were fabricated ex-situ. Measurements were performed at high sample-inclination angles (75˚) in order to secure maximum depth of analysis.[87,88]

2.5. Functional characterization

2.5.1. Superconducting quantum interference device – Magnetic property measurement system

Magnetic response of the as-fabricated thin films in this work was characterized by using a dc-Superconducting Quantum Interference Device (dc-SQUID) – Magnetic Property Measurement System (MPMS) from quantum device. Mainly two types of measurements were performed – magnetic response of the sample as a function of the applied field and secondly the magnetic response as function of temperature. The available MPMS system allowed for field measurements up to ±7 Tesla and temperature variation between liquid Helium temperature of 4.2 K to 330 K. SQUID Magnetometry is currently one of the most effective and sensitive ways to measure the overall magnetic moment of a sample. The set-up of the dc-SQUID-MPMS used in this work primarily consists of a superconducting coil with two Josephson junctions connected in parallel. A Josephson junction is a thin insulating layer separating two superconductors that can allow the electron Cooper pairs to steadily tunnel through them when a biasing current is applied across the junction. In addition to the SQUID coil, the MPMS also consists of a superconducting electromagnet, a superconducting pick-up coil which is inductively coupled to the SQUID coil, Helium dewar and pumping unit and also most importantly a set-up of voltage amplification electronics. In order to perform a measurement, the sample is fixed within a clean commercially available non-magnetic straw and placed inside the helium Dewar within the pick-up coils. When the sample is moved up and down within the pick-coils, it produces an alternating magnetic flux, whose signals are transmitted to the inductively coupled SQUID coil which is located away from the sample in an isolated liquid helium bath.

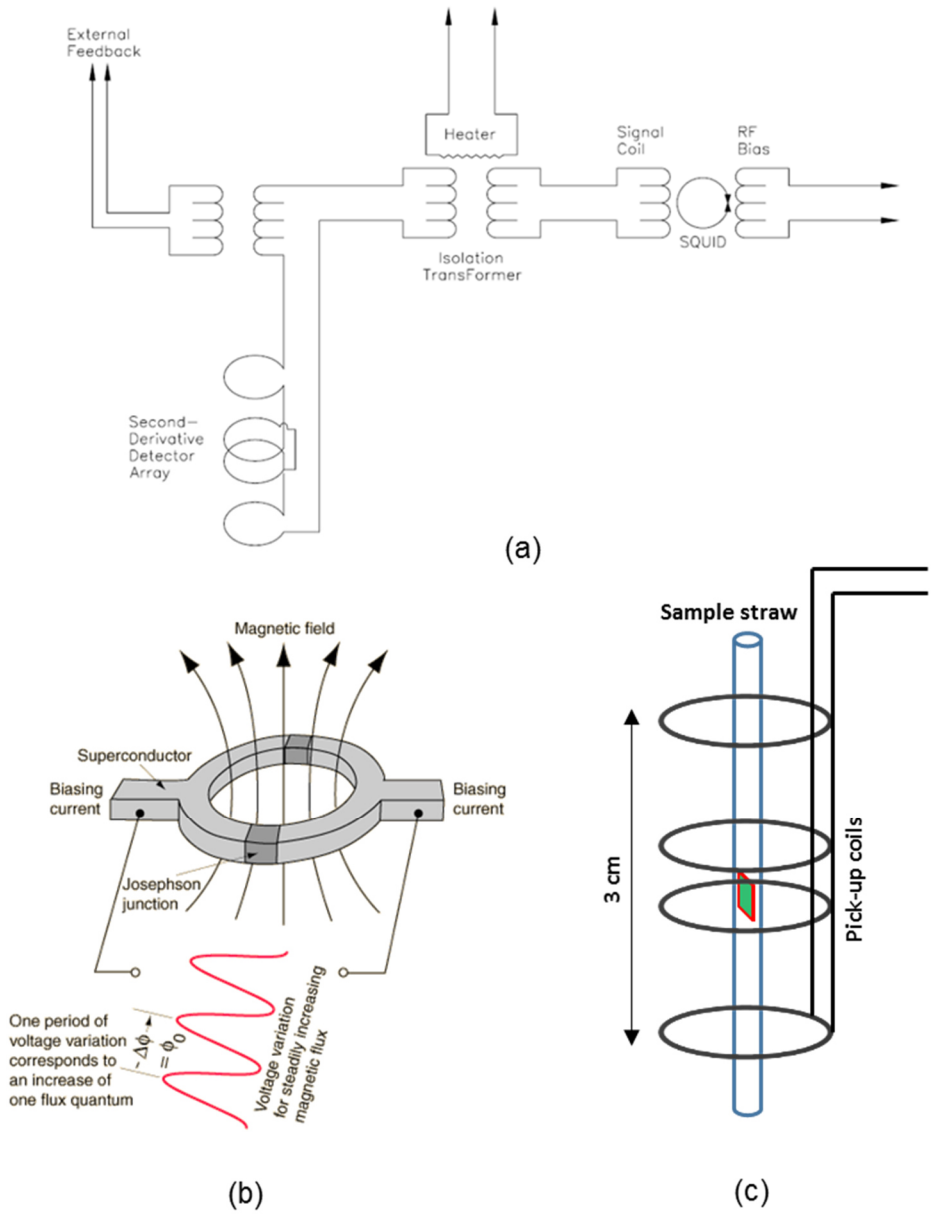

Fig. 2.18 (a) Schematic circuitry of a SQUID magnetometer (Taken from Quantum Design MPMS manuals) (b) Construction of a dc-SQUID coil with two Josephson junctions (Ref.: University of Wuppertal, Retrieved 19.11.2016, from http://hydrogen. Physic. uni- wuppertal.de/hyperphysics /hyperphysics /hbase /solids /squid.html); (c) Schematic view of pick-up coils in the MPMS and the standard sample positioning.

Thus the change in magnetic flux caused by the sample causes a change in the voltage drop across the SQUID coil which is read out by locking in the read out frequency. Thus the SQUID primarily acts as a magnetic flux-to-voltage converter. What is fundamentally important to note here is that the discovery that magnetic flux is quantized and each single flux quanta unit has an extremely small value of $\phi_o = h/(2e) = 2.07 \times 10^{-15}$ Wb. This allows for the SQUID to be extremely sensitive where magnetic moments of the order of 10^{-8} emu can be

detected. The measured changes in voltage drop are then amplified by the MPMS electronics and provided as an output. Furthermore the MPMS used in this study is equipped with a Reciprocating Sample Option which allows for sensing of magnetic moments as low as 5×10^{-9} emu. Further elaboration on SQUID-Magnetometry can be found in Ref. [89–91]

2.5.2. X-ray absorption spectroscopy

This section is outlined based on Ref. [92–96]. All matter absorb X-rays to a certain degree. When a beam of X-rays is directed at a material medium, they interact with the electrons present in the atoms. Interactions of the X-rays with the electrons leads to various processes like scattering, excitation, fluorescence or just transmission. As per the Beer's law when a parallel beam of X-rays of intensity I_o passes through a material medium of thickness t, results in a transmitted intensity I as per the following relation:

$$\ln\left(\frac{I_o}{I}\right) = \mu t$$

Where μ is the linear absorption coefficient of the material medium.

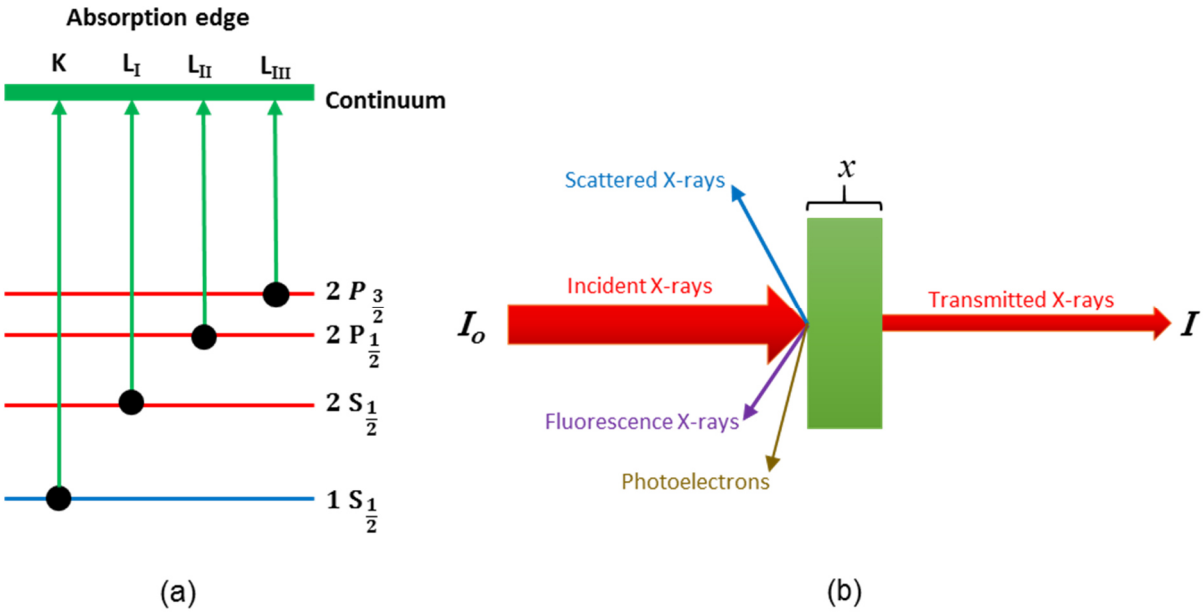

Fig. 2.19 (a) Standard nomenclature for absorption edges; (b) Interaction of a beam of X-rays with a material block of width *x*.

At particular energies of X-rays, the absorption is observed to have a large peak which is referred to as the Absorption edge. Similar to the case as explained in the section on XPS above, these edges occur when the X-ray energy is just sufficient to excite the core electrons

from their bound state to vacuum continuum. The nomenclature of the absorption edges are based on the core-atomic shells from which they were excited – Eg: K, L, M and so on. An integer sub-script is added for edges resulting out of L shell and above. For example, excitation of electrons from the 2s orbital results in an L_1 edge. Further more, since the p-orbitals are split into two energy levels (total angular momentum $j = \frac{1}{2}$ and $\frac{3}{2}$) due to spin-orbit coupling, excitations from the 2p shell are further classified into causing the L_2 and L_3 absorption edges respectively.

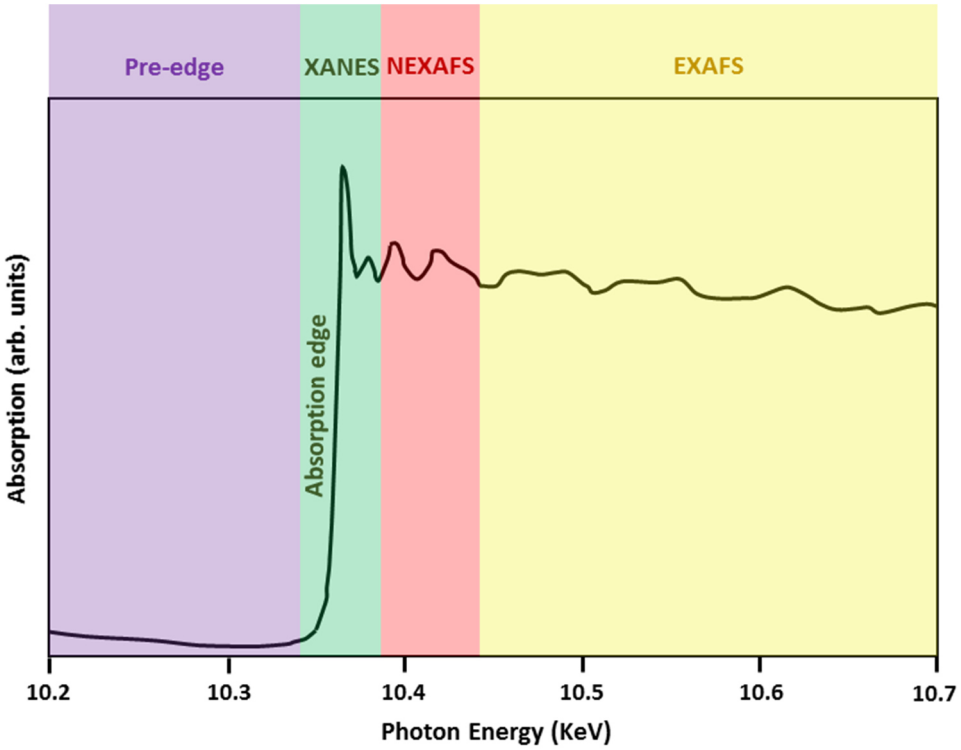

Fig. 2.20 Illustration of a typical absorption edge and its various sections of interest.

Fig. 2.20 shows an illustration of a typical absorption edge which generally has four characteristic sections namely (i) Pre-edge; (ii) X-ray absorption near edge structure (XANES); (iii) Near edge X-ray absorption fine structure (NEXAFS) and (iv) Extended X-ray absorption fine structure (EXAFS). Pre-edge corresponds to energies lower than the binding energy ($E < E_o$). Features in this region are commonly due to electron transitions from the core levels to the higher unfilled/partly-filled shells. XANES refers to the region in the immediate vicinity of the absorption edge ($E = E_o \pm 10 - 12\ eV$). In this region electron transitions from the core levels to the immediate non-bound levels takes place. Since such a transition is highly probably, a large change in the absorption is observed here which marks the edge. NEXAFS and EXAFS refer to the region of energies greater than 10 eV above the absorption edge. Studies on these extended regions are beyond the scope of this work,

however it may be noted that these regions correspond to low and high energy photoelectrons respectively that undergo scattering from nearby atoms and hence contain valuable information of the chemical and structural information of the near vicinity of the excited species.

X-ray magnetic circular dichroism:

X-ray magnetic circular dichroism (or XMCD) is an extended method of XAS that can be used for element specific magnetic characterization of materials. Dichroism is a phenomenon that refers to the difference in the absorption of electromagnetic radiation by a material medium when two differently polarized light is used. In XMCD, circular polarized light (left- and right-circular polarized) light is used to measure the resulting difference in X-ray absorption.

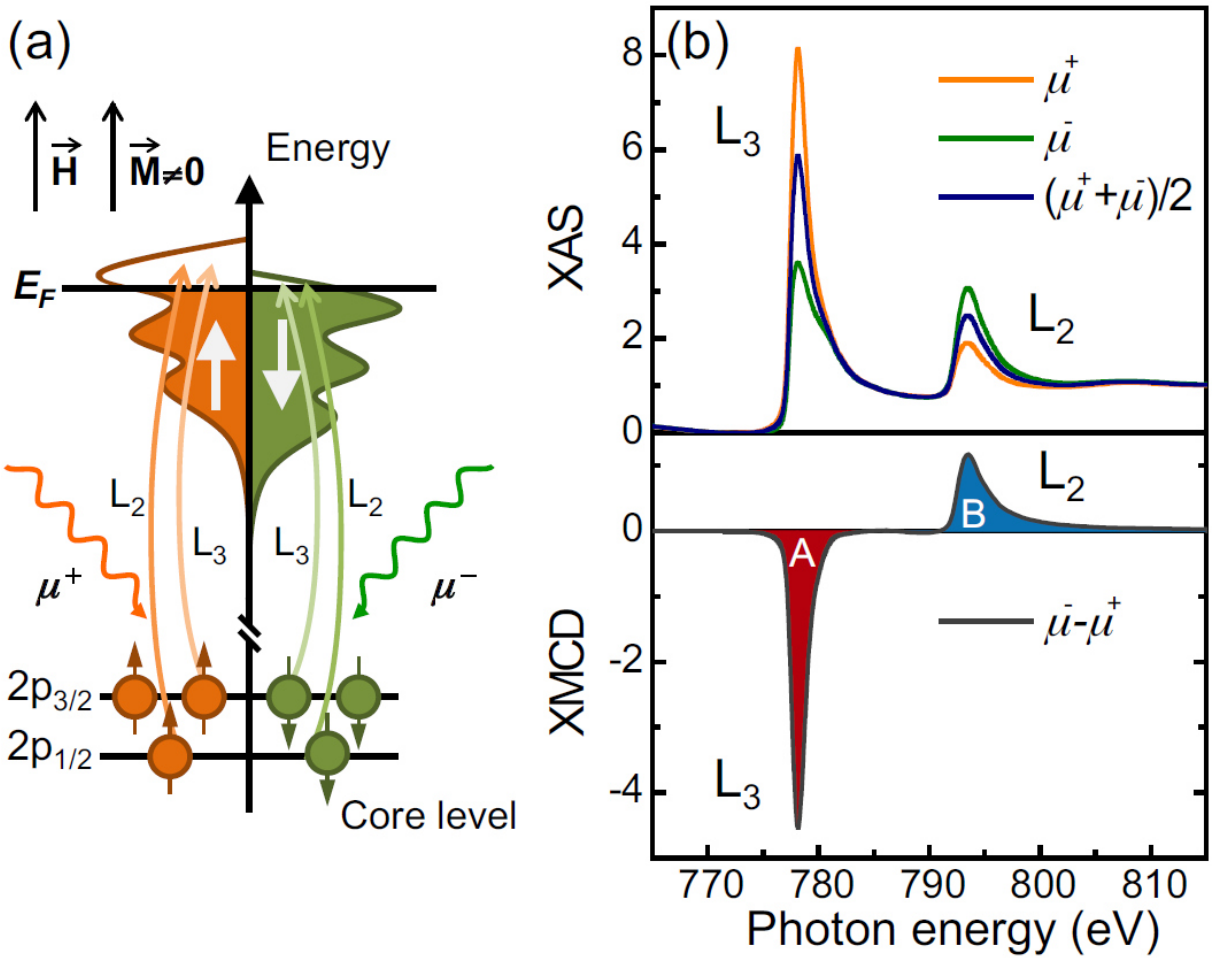

Fig. 2.21 (a) Illustration of the spin-dependent excitation process used in an XMCD measurement; (b) X-absorption spectra at the Co $L_{2,3}$ edges for right (μ^+) and left (μ^-) circular polarized light and the difference spectrum – XMCD. (Taken from Ref. [93])

Pioneering work on XMCD was presented by Gisela Schütz *et al.* in 1987 where they studied the difference in absorption of left- and right-circular polarized light by iron. Since then, development and access to synchrotron radiation has led to XMCD being a widely used technique for element specific magnetic characterization for bulk materials, thin films, single crystals and powders.

During an XMCD experiment, electrons are excited from a core shell to the partially filled valence shells of *d*-block transition metals. These electron excitations are governed by the dipole selection rules which state that only transitions involving a change in angular momentum $\Delta l = \pm 1$ are allowed and also the electrons are not allowed to change their spin during the excitation. When right and left circular polarized light is used, transitions corresponding to $\Delta l = +1$ and $\Delta l = -1$ are allowed respectively. These conditions lead to the difference in absorption of the left and right circular polarized light depending upon the available empty valence *d*-shell of the element probed. The difference in absorption can be caused either by using the oppositely polarized light as mentioned above or also by changing the direction of magnetization of the sample. An illustration of the excitation process in XMCD is shown in Fig. 2.21 (a). As can be seen in the figure, the above selection rules allow for spin dependent excitation of *p*-electrons allows us to probe the available empty states in the valence d-shell of the transition metal. As the magnetic properties of *d*-block elements arise from an imbalance in the number of occupied-up and down-spin electrons in the *d*-shell, spin dependent excitation allows us to quantitatively probe this imbalance and thereby characterize the magnetic state of the element under consideration. As shown in Fig 2.21 (b), XMCD spectra is then obtained by taking difference of the absorption spectra for the excitations under the two polarized lights. From this obtained XMCD spectra quantitative estimations of the spin and orbital moment can be estimated by using the so-called sum-rules.[95,96] If the integrated area under the XMCD spectra for the L_3 edge is I_{L3} and similarly I_{L2} for the L_2 edge, then as per the sum rules, the orbital moment is proportional to $I_{L2}+I_{L3}$ and the spin moment is proportional to $I_{L2}-2I_{L3}$.

The XMCD measurements performed in this work were undertaken at the ID12 circular polarization beamline at European Synchrotron Radiation Facility (ESRF), Grenoble – France. ID12 beamline provides for measurements with hard X-rays in the energy range $2.0 < \hbar\upsilon < 20$ keV. Fig 2.22 (b) shows a schematic view of the ESRF synchrotron and Fig 2.22 (a) shows the measurement set-up at the ID12 beamline where the high-field superconducting electromagnet can be seen. This magnet allows for applying fields up to 17 Tesla. XANES spectra were recorded using the total fluorescence yield detection mode. Measurements were

performed with both helicities of the incident X-rays. In order to check for any measurement artefacts, spectra were also recorded for both directions of applied magnetic field. In order to have comparable results measurements were performed at same low temperatures of pre-existing SQUID Magnetometry measurements of the samples concerned. The monochromatic beam of X-rays have a high degree of circular polarization (in excess of 95 %).

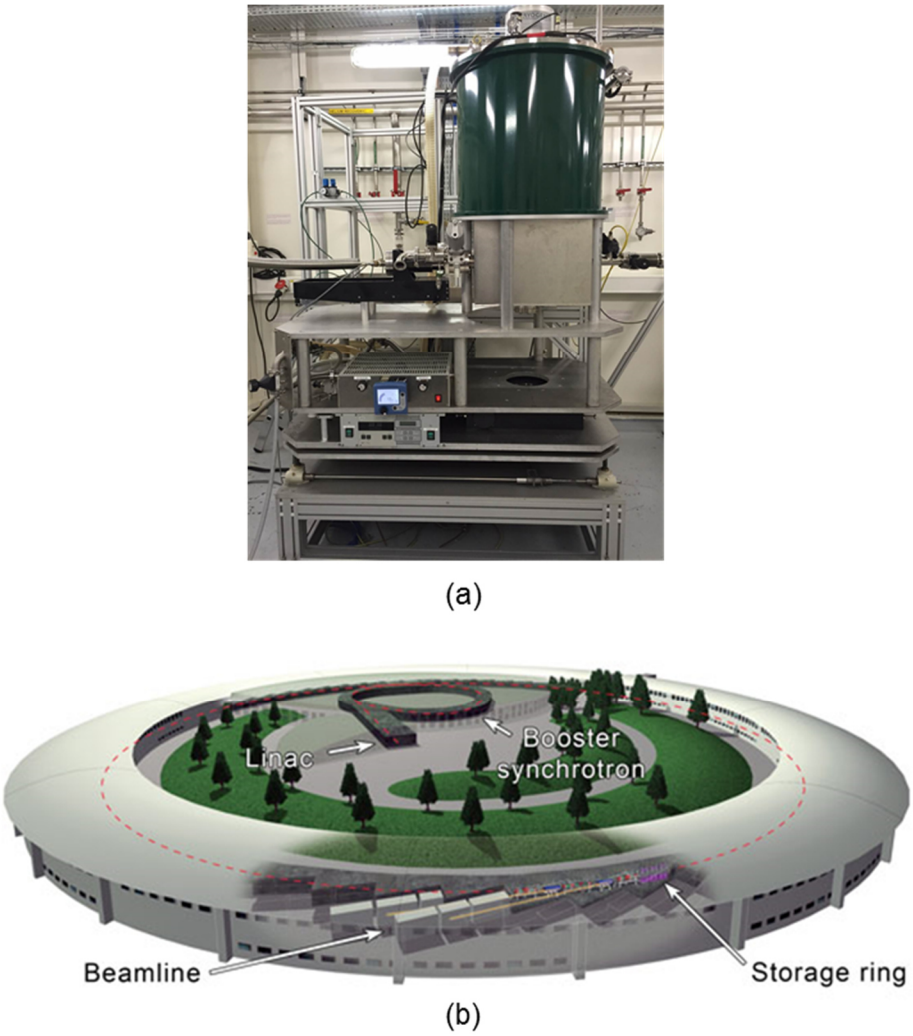

Fig. 2.22 (a) Front view of the 17 Tesla superconducting electromagnet used for XMCD measurements at the end-station of the ID12 beamline at ESRF; (b) Schematic view of the European Synchrotron Radiation Facility showing all of its major components such as the linear accelerator, booster ring, storage ring and the beamline end-stations. (Ref.: ESRF Grenoble, Retrieved 19.11.2016, from http://www.esrf.eu/about/synchrotron-science/synchrotron)

2.5.3. Electrical characterization

In order to characterize the temperature dependence of resistivity of the double perovskite films, the four-probe measurement method was used. As fabricated thin film samples were taken onto which four gold electrodes were sputtered through a mask using a Quorum QD500 DC-sputtering unit under an applied current of 30 mA over a deposition duration of 200

seconds. The geometry of the gold contacts was in the form of stripe pads as shown in Fig. 2.23.

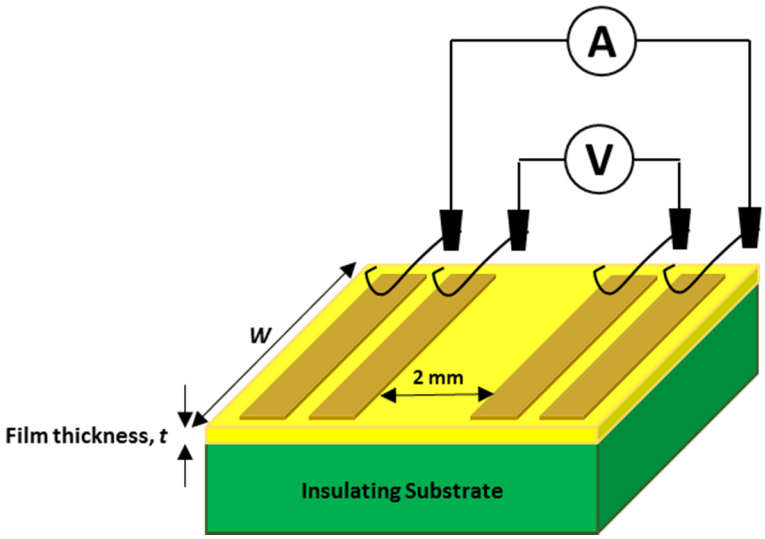

Fig. 2.23 Schematic drawing of the 4-probe electrical resistivity measurement setup.

For the measurement, a constant current (10 – 100 nA) was applied through the two outer electrodes using Keithley current source model 6621. By measuring the voltage drop (V) between the two inner gold contacts (using a Keithley nanovoltmeter model 2182A, resistivity (ρ) of the film could be estimated as:

$$\rho = \frac{tw}{l} \times \frac{V}{I}$$

Where t is the film thickness, w is the width of the substrate (5mm used), l is the length between the two inner electrodes (2 mm as per mask design) and I is the sourced current. Temperature of the unit is measured by a LakeShore calibrated silicon diode model DT-670D-SD. The above contacting procedure is in-fact realized on a custom built dip-Stick stage. For the measurement, the dip-stick which bears the sample stage at its lower end is introduced vertically into a liquid helium dewar. Temperature variations were realized by moving the dip-stick vertically up and down the dewar. A custom LabView program was used to record the measurement data.

3. 3*d* – 3*d* double perovskite : Bi_2FeCrO_6

In chapter 1, the requirements for a full-multiferroic functionality in double perovskite compounds were established. Ideally a robust ferroelectric-ferromagnetic compound with room temperature functionality is desired. Possibility to stabilize such compounds in a thin film form is a further advantage towards possible device applications. From literatures, one can note that the adopted strategy for ferroelectricity has been to introduce a lone-pair ferroelectric cation such as Bi^{3+} at the *A*-site. Consequently, a combination of two transition metals coupled via exchange interactions have been used at the *B*-sites which are a source of the intended magnetic response in the compound. The explored *B*-site cation combinations can further be widely classified into three groups namely 3*d*-3*d*, 3*d*-4*d* and 3*d*-5*d* systems. Following the literature on these systems, 3*d*-3*d* compounds are comparatively the most explored among the three systems. The reason behind this is the comparatively simple chemistries of the constituent 3*d* transition metal oxides and their well-documented synthesis routes. Based on this thought, our first line of approach in this work on ferrimagnetic double perovskites, was to go for an *A*-site bismuth based 3*d*-3*d* double perovskite.

Some notable early thin film studies on 3*d*-3*d* double perovskites include the work of Ueda *et al.* as published in the Science journal in 1998[60], where ordered $LaFeO_3$-$LaCrO_3$ layers were reported to show a strong magnetic order. Further work was based on idea to explore possibilities of using other magnetic 3*d* elements (such as Co,Ni,Mn) at the *B*-sites to promote strong ferri-/ferromagnetism. Consequently interesting magnetoelectric effects were found in other *A*-site Lanthanum based double perovskites such as La_2MnNiO_6 and La_2MnCoO_6.[97,98] In the meantime, the turn of the millennium saw the surge in pursuit of $BiFeO_3$ and other similar compound with ferroelectric+magnetic functionalities.[50] Taking a lead from above the Ueda *et al.*[60] findings in 1998, Baettig and Spaldin proposed using density functional calculations the compound Bi_2FeCrO_6(BFCO), as one of the first Bismuth based 3*d*-3*d* double perovskite compounds foreseen for multiferroic functionality.[36,99] The compound was actively pursued by experimentalists in the following years. With similar motivations analogous compounds such as Bi_2NiMnO_6,[100] Bi_2FeMnO_6,[101] Bi_2CoMnO_6,[102] etc. were all extensively explored. Table 3.1 shows a list of such 3*d*-3*d* compounds which have been studied in the thin film form for an intended ferro-/ferrimagnetic and or multiferroic functionality.

Table 3.1 Non-exhaustive list of various ferri-/ferromagnetic 3*d*-3*d* double perovskites studied in the thin-film form as potential templates for multiferroic functionality; included along is a list of the observed low temperature saturation magnetizations and magnetic ordering temperatures for the corresponding compounds.

Compound	Reference	Magnetization (M) at low Temp. (~5 K)	Magnetic ordering temperature (T_C)
La_2FeCrO_6	Ueda *et al.* (1998)[60]	6 μ_B/f.u.	375 K
	Chakraverty *et al.* (2011)[61]	2 μ_B/f.u.	50 K
La_2FeMnO_6	Ueda *et al.* (1999)[103]	2.6 μ_B/f.u.	230 K
	Yoshimatsu *et al.* (2015)[104]	1.3 μ_B/f.u.	--
La_2MnNiO_6	Guo *et al.* (2006)[105]	4.63 μ_B/f.u.	270 K
	Hashisaka *et al.* (2006)[106]	4.6 μ_B/f.u.	280 K
La_2MnCoO_6	Singh *et al.* (2007)[107]	5.8 μ_B/f.u.	245 K
	Guo *et al.* (2006)[108]	5.8 μ_B/f.u.	230 K
Bi_2FeCrO_6	Nechache *et al.* (2009)[109]	1.91 μ_B/f.u.	**> 400 K**
	Ichikawa *et al.* (2008)[110]	3.4 μ_B/f.u.	**> 300 K**
Bi_2FeMnO_6	Bi *et al.* (2008)[101]	0.06 μ_B/f.u.	--
	Zhao *et al.* (2010)[111]	0.6 μ_B/f.u.	--
Bi_2MnNiO_6	Sakai *et al.* (2007)[100]	4.5 μ_B/f.u.	100 K
	Padhan *et al.* (2008)[112]	4.3 μ_B/f.u.	130 K
Bi_2MnCoO_6	Singh *et al.* (2008)[102]	3.1 μ_B/f.u.	800 K (not-reproduced)

As is evident from Table 3.1, the compound Bi_2FeCrO_6 stands out particularly because of its reported room temperature magnetic ordering. In-addition having the ferroelectrically active Bismuth at the *A*-site is an advantage towards full multiferroic functionality. In-spite of these advantages, diverse literature on BFCO highlight some unexplored challenges and inconsistencies (as explained in following sections). This was the source of our motivation to take BFCO as a 3*d*-3*d* compound of choice for the first line of study in this research work.

3.1. Theory and background

As discussed above, first scientific findings on the compound BFCO were reported in the theoretical studies of Baettig and Spaldin in 2005.[99] At a time when the interest in $BiFeO_3$ as a multiferroic material was at its peak, it was realized that the compound owing to its inherent antiferromagnetic nature had only a very small magnetic moment which came from the canting of the spins. A solution to this drawback was suggested by Spaldin *et al.* who drew motivation from a study by Ueda *et al.* in 1998 showing a strong magnetic coupling in thin films with alternating layers containing Fe^{3+} and Cr^{3+}.[60] Starting from the parent compound $BiFeO_3$, Spaldin *et al.* suggested that replacing every second $3d^5$-Fe^{3+} with a trivalent $3d^3$-Cr^{3+} leading to an ordered double perovskite can yield a compound with an effective non-zero magnetization. The non-zero magnetism is said to be achieved as a consequence of ferrimagnetism. In ferrimagnetism, the coupling between the two magnetic species is strongly antiferromagnetic, but since the sub-lattices of the two magnetic species have different magnetizations, an effective net magnetization occurs. And since antiferrmagnetic superexchange is strong, the authors expected Curie temperatures above room temperature.

Based on the pre-selected *B*-site cations, Spaldin *et al.* then used density functional theory within the LDA+U framework to determine the ground state functionalities of the compound BFCO. For the rock-salt ordered double perovskite BFCO, they found that the ground state structure of the compound stabilized with an *R*3 symmetry (spacegroup 146). A schematic crystal structure of the calculated *R*3 symmetric BFCO is shown in Fig. 3.1 (a) (constructed using VESTA visualization program[14]). A strong ferroelectric polarization of ~80 $\mu C/cm^2$ was estimated to arise from the stereochemical activity of the Bi lone pair. Furthermore a stable magnetic order was found to exist where ferromagnetic planes of Fe and Cr coupled antiferromagnetically with each other to give rise to a magnetization of 2 μ_B/f.u. or 160 emu/cm^3. Based on these values of magnetization and polarization, the theoreticians predicted the compound to be more robust than any other single phase system with coexisting magnetism and ferroelectricity. Their calculated density of states for BFCO is shown in Fig. 3.1 (d) where the top of the valence band is was set to 0 eV. Here it was noted that the dark and light shaded regions include contributions from the Fe 3*d* and Cr 3*d* states, respectively. States at -10 eV were noted to be that of the Bi 6*s*. Unshaded states in the broad band below Fermi have largely O 2*p* character. The so predicted compound was clearly found to be insulating. Besides the calculated density of states also indicated that top of the valence band and the bottom of the conduction band are 100 % spin polarized.[36,99]

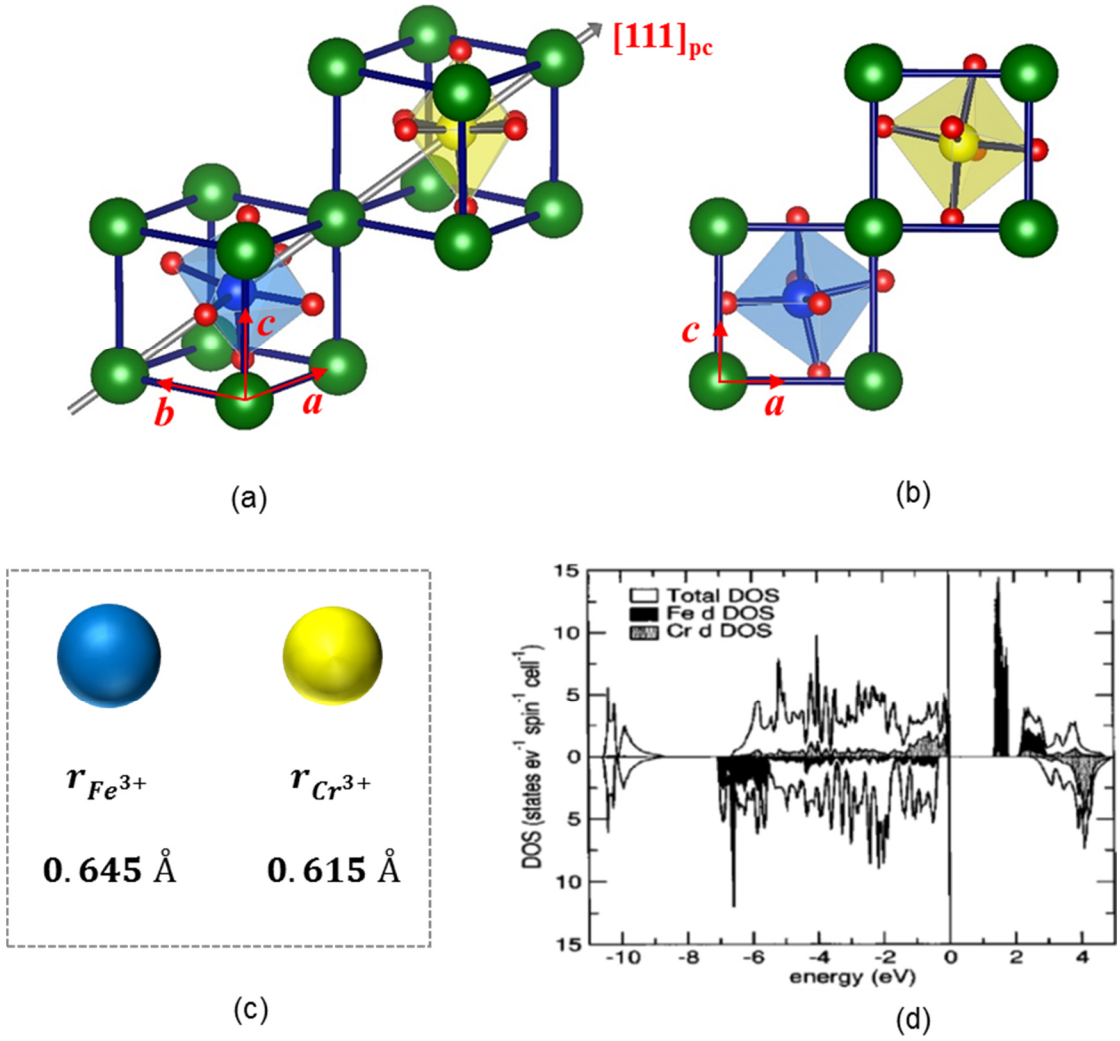

Fig. 3.1 (a) 3-dimensional schematic of the theoretically predicted crystal structure for Bi_2FeCrO_6 (BFCO)[99] constructed using the VESTA visualization program[14]; (b) Crystal structure of the *B*-site ordered BFCO looking down along the *b*-axis; (c) Schematic comparison of ionic radii for Fe^{3+} and Cr^{3+} cations; (d) Calculated ground state density of states for BFCO (Taken from Ref. [99])

The above theoretical findings of Baettig and Spaldin generated significant interest among both bulk and thin film experimentalists to synthesize the compound. However, one of the fundamental concerns with regard to synthesis of 3*d*-3*d* double perovskites is the challenge in achieving the required *B*-site chemical order.

As was discussed in section 1.2.2, it is known that a larger difference in the ionic radii of the two *B*-site cations and also a different formal valance state makes the ordered state more energetically favorable. In the case of BFCO, both Fe and Cr are in their 3+ oxidation state having no charge difference; furthermore, their ionic radii of 0.645 Å and 0.615 Å for Fe and Cr respectively, are also rather similar. This makes achieving fully ordered BFCO sample a challenging task experimentally. A report by Chakraverty *et al.* showed for the analogous *A*-

site La based double perovskite system, that the Fe-Cr ordering can be forcibly induced by growing films via PLD at very high temperatures (~900 - 1000˚C) followed by quenching and subsequent annealing.[61] However, it should be noted such a high temperature process and post-annealing techniques are unsuitable for BFCO due to the high volatility of the Bismuth at elevated temperatures.

Nevertheless, following the theoretical findings of 2005, several independent experimental efforts towards synthesizing the double perovskite BFCO were undertaken which can be found in Ref. [28,109,110,113–120]. A collective analysis of these literature shows that a consistent picture of ferroelectricity was observed by most studies (with remnant polarizations in range: 50 to 60 $\mu C/cm^2$). Contrastingly, large discrepancies in the observed magnetic moment ranging from nearly zero to as high as 5.2 μ_B/f.u. were reported. Table 3.2 shows a summary of various experimental efforts of BFCO synthesis and their reported magnetic moments.

First report on an attempted bulk synthesis of BFCO was published by Suchomel *et al.* where they had to go for a high pressure furnace synthesis method under pressures of the order ~ 6 GPa to achieve a phase pure product. Their crystallographic analysis showed a BFO like polar structure however, there was no evidence of *B*-site chemical order. Consequently, no magnetic order corresponding to the expected d^3-d^5 superexchange was found, instead the antiferromagnetic d^3-d^3 (Cr^{3+}-Cr^{3+}) and d^5-d^5 (Fe^{3+}-Fe^{3+}) were found to be dominating.[114] This result highlights the meta-stable nature of the ordered double perovskite BFCO. Thin-film approach which allows for synthesizing also meta-stable compounds was simultaneously pursued by other groups. In a publication in 2006, Nechache *et al.* reported for the first time an attempt to grow epitaxial BFCO thin films via PLD on single crystalline $SrTiO_3$ substrates from a single stoichiometric target. A small magnetic moment of 0.26 μ_B/f.u. was observed.[113] In a follow-up paper by the same group in 2009, a much larger magnetic moment of 1.91 μ_B/f.u. (almost close to theoretical value) was reported in thin films grown by similar method as in the previous attempt. They attributed this magnetic moment to be resulting from the spontaneous ordering of Fe-Cr.[109] Contrastingly, PLD grown BFCO thin films of Kim *et al.* were reported to have a random distribution of Fe and Cr cations. No significant magnetic moment was recorded in their samples.[115] Furthermore, a much larger magnetization of 3.4 μ_B/f.u. was reported in the $BiFeO_3$-$BiCrO_3$ epitaxial thin film superlattices grown by Ichikawa *et al.* which is larger than the theoretically expected moment for a ferrimagnetic coupling of Fe-Cr sub-lattices.[110] Contrastingly a meager 0.1 μ_B/f.u. were reported for polycrystalline thin films of BFCO. Also more recent studies using advanced element specific magnetic

characterization technique of XMCD, found no evidence of a strong magnetic coupling in the compound.[120]

Table 3.2 List summarizing various independent experimental efforts towards synthesizing ferrimagnetic BFCO and their corresponding saturation magnetizations as reported.

Reference	Synthesis/fabrication method/ sample details	Magnetization (*M*) at low Temp. (~5 K)
Nechache *et al.* (2006)[113]	Epitaxial BFCO thin films grown via PLD using single stoichiometric target	**0.26 μ_B/f.u.**
Suchomel *et al.* (2007)[114]	High-pressure synthesis of ceramic powders at 6 GPa and 1000 °C	**0.015 μ_B/f.u.**
Kim *et al.* (2007)[115]	$BiFeO_3$-$BiCrO_3$ superlattices grown by PLD	**~ 0.1 μ_B/f.u.**
Ichikawa *et al.* (2008)[110]	$BiFeO_3$-$BiCrO_3$ superlattices grown by PLD	**3.4 μ_B/f.u.**
Nechache *et al.* (2009)[109]	Epitaxial BFCO thin films grown via PLD using single stoichiometric target	**1.91 μ_B/f.u.**
Bai *et al.* (2012)[116]	Ceramic BFCO by high pressure synthesis at ~5 GPa and 1100 °C	**No hysteresis**
Nechache *et al.* (2012)[117]	BFCO thin film nanostructures by patterning via masked growth by PLD.	**5.2 μ_B/f.u.**
Sha *et al.* (2013)[118]	Polycrystalline BFCO thin films by PLD	**~ 0.1 μ_B/f.u.**
Zhu *et al.* (2013)[119]	Polycrystalline BFCO ceramics by high pressure synthesis at 4 GPa and 900 °C	**No hysteresis**
Shabadi *et al.* (2014)[28]	Epitaxial BFCO thin films grown via PLD using single stoichiometric target	**0.06 μ_B/f.u.**
Vinai *et al.* (2015)[120]	Epitaxial BFCO thin films grown via PLD using single stoichiometric target	**0.1 μ_B/f.u.**

Clearly there is a large divergence in the literature concerning the magnetic properties of BFCO. By following the literature, one can note that a major source of these inconsistencies lies in the difficulty in ordering of Fe and Cr which is a crucial requirement for the magnetic functionality. Also the possibility of existence of magnetic impurity phases of Fe may lead to erroneous observations of magnetism in some cases. Another difficulty with regard to ordered Fe-Cr structures, is detecting the chemical order itself. For instance, direct imaging techniques at atomic resolution such as HAADF-STEM cannot distinctly aid in detecting the ordering in this case, due to insufficient Z contrast between Fe and Cr. For the studies that observed large

magnetic moment such as by Nechache *et al.*, the resulting magnetism was attributed to a spontaneously achieved Fe-Cr order. As a proof of the existing chemical order, half-order reflections or superstructure peaks in X-ray diffractograms along the pseudo-cubic [111] directions were cited which are rather unusually intense in BFCO when compared to other similar 3*d*-3*d* compounds.[109]

These diverse findings in the literature on BFCO present a peculiar challenge that concerns double perovskite compounds in general. The question concerning difficulty in spontaneously ordering two *B*-site cations of similar ionic radii/charge and also subsequently finding suitable methods to characterize this order presents an interesting technological challenge. This motivates the work undertaken as reported in the following sections of this chapter. We grew high quality epitaxial BFCO thin films via pulsed laser deposition. Detailed structural studies followed by magnetic characterization were carried out on the films. We establish a crucial finding with respect to the Fe-Cr ordering and the observed superstructure in BFCO film which helps in explaining the diverse findings on magnetic properties. Our work reveals crucial understanding on the evaluation of chemical ordering in double perovskite thin films and consequently helps to better engineer similar functional compounds in the future.

3.2. Target preparation

As discussed in the preceding section, it is inferred from study of Suchomel *et al.*,[114] that phase pure synthesis of bulk BFCO was realized only via high pressure synthesis (>5 GPa). Different set-ups commonly used for such high pressure synthesis are capable of processing only small amounts of ceramic – often in the milligram range. In addition it was also noted that the high pressure synthesis did not yield an Fe-Cr ordering, instead a disordered $Bi(Fe,Cr)O_3$ was produced. Ceramics to be used as PLD targets require minimum mass in the range of 3 – 5 grams. Since PLD involves a laser assisted ablation process, where the stoichiometry of the target is transferred to the substrate irrespective of which phase/several phases that exist in the ablated target[72], it is not strictly essential to have a phase pure pellet of the intended compound. Conventional solid state synthesis as elaborated in section 2.1.2 was undertaken to fabricate homogeneous flat stoichiometric ceramic pellets of BFCO. Following chemical reaction was used as the basis for the stoichiometric calculations:

$$2\,Bi_2O_3 + Fe_2O_3 + Cr_2O_3 \longrightarrow 2\,Bi_2FeCrO_6$$

Bi_2O_3 is known to be a volatile oxide (Melting point - 817˚C), hence a 20 % stoichiometric excess was taken to start with in order to make up for the losses during the sintering process. In addition, a two-step process was adopted to minimize the Bi loss during the target synthesis:

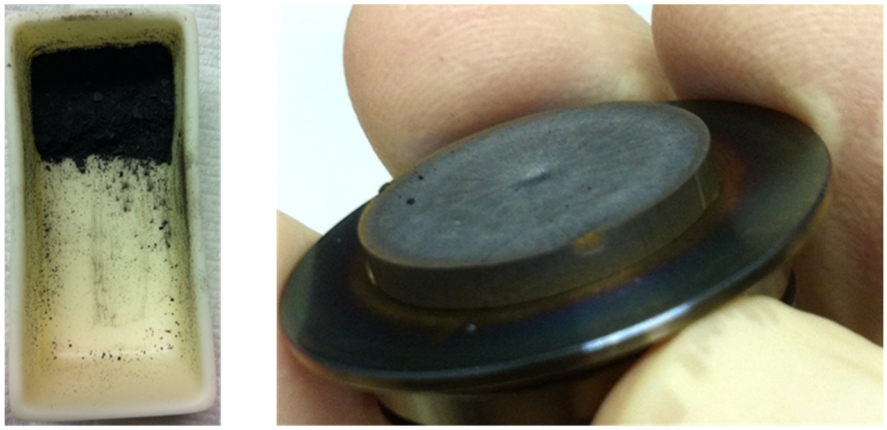

(a) (b)

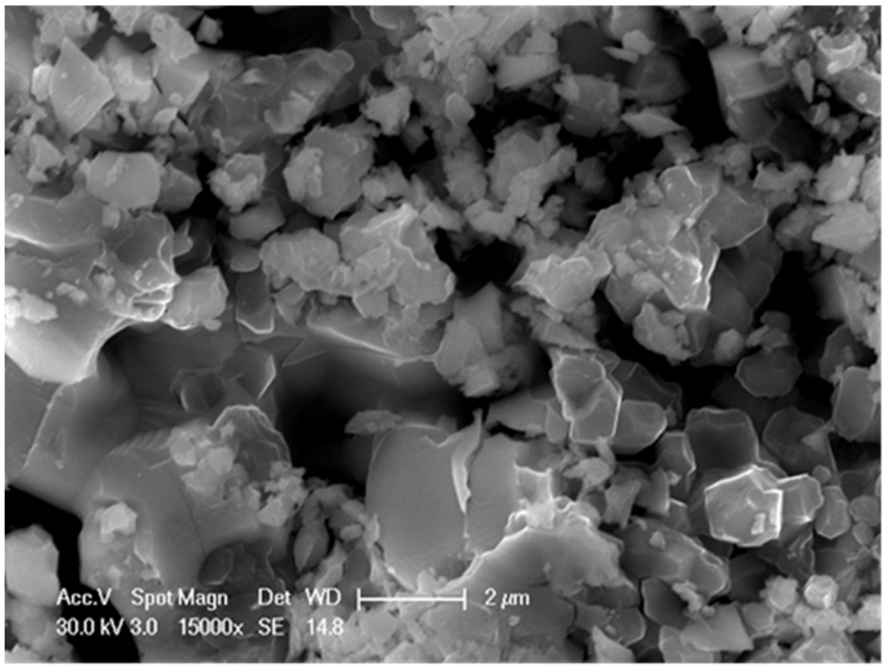

(c)

Fig. 3.2 (a) Photograph of an alumina crucible containing a reacted mixture of Fe_2O_3 and Cr_2O_3 powders corresponding to Step 1; (b) Photograph of as-prepared BFCO target glued on to a standard metallic target holder for use in DCA-500 PLD system; (c) SEM image of the polished top surface of the sintered BFCO target.

Step 1: In the first calcination step, stoichiometric amounts of Fe_2O_3 (Purity: 99.998 %; Source: Alfa Aesar) and Cr_2O_3 (Purity: 99.97 %; Source: Alfa Aesar) were weighed and

transferred into a mortar. The powders were subjected to grinding for upto 45 minutes in order to obtain a homogenous mixture. Mixed powders were then transferred to an Alumina crucible and calcined at 1150˚C for 10 hours and then cooled down to room temperature. A photo visual of the alumina cruicible with the reacted mixture of Fe_2O_3 and Cr_2O_3 is shown in Fig 3.2 (a)

Step 2: The calcined powders containing an intermediate reaction mixture of Fe_2O_3 and Cr_2O_3 were retrieved from the crucible and once again homogeneously grinded in a mortar. To this intermediate mixture, pre-weighed powder (with 20% excess) of Bi_2O_3 (Purity: 99.999 %; Source: Sigma-Aldrich) was added and further ground for upto 1.5 hours to obtain a high level of homogeneity. The homogeneous mixture was then pressed into a green-pellet using a uniaxial press under 6 Tonnes of load. The pressed cylindrical pellet with a diameter of ∼18 mm was then weighed and placed into a crucible. The green compact was then sintered in a furnace at 790˚C for a duration of 20 hours and then slowly cooled to room temperature (∼5˚ / min).

This resulted in a stable, crack-free pellet with a density of 87% of the theoretical single crystal density of BFCO. Stability of the target was tested by ablation carried out in a separate custom-design PLD chamber (Baby-PLD) in order to avoid possible contamination of the main DCA-Instruments PLD500 system. No indications of target disintegration or particle ejection confirmed the stability of the stoichiometric target for further experimental use.

Pre-characterization of the so prepared target was carried out by XRD, SEM and EDS. As expected in the preceding text, XRD pattern of the pellet (not shown) indicated existence of several intermediary and primary phases of the three component oxides used. Microstructure of the sintered target after polishing off the top surface with a sand paper was studied under the Philips XL-30 FEG SEM. Fig 3.2 (c) shows an SEM image of the polished top surface of the sintered target. Observed grains have sizes in the range of 0.2 to 2 μm. Besides the target appears to be moderately dense. A crucial aspect for a successful PLD process is the stoichiometry of the target. This was probed using an EDS detector fitted to the above Philips XL-30 FEG SEM. Acceleration voltage of 30 kV was used for experiment. The collected EDS spectra (not shown) did not show indications of any impurities. All peaks were identified to be coming only from Bi, Fe, Cr or O. Intensity of the peaks in an EDS spectrum contains quantitative information of the corresponding elements. The provided software of the EDS detector contains an in-built algorithm to extract the atomic concentrations of the species involved. After subtracting the background due to the Bremsstrahlung radiation, the EDS spectra was quantitatively analyzed using the system software. The results of the EDS analysis

is outlined in table 3.3. The algorithm of the software performs internally intensity corrections due to the atomic number (*Z*), the absorption factor (A) and fluorescence (F) which are indicated in the same table. The column marked in red shows the atomic concentrations of Cr, Fe and Bi to be 25.44%, 24.32 and 50.24 respectively. Considering a 5% error bar in EDS analysis, the target under consideration here contains Bi:Fe:Cr concentration as per the intended ratio for BFCO and hence the target was taken to be suitable for growth of BFCO films via PLD. For use in PLD, the ceramic pellet is glued onto a standard metallic target holder with the help of commercially available silver glue as shown in Fig. 3.2 (b)

Table 3.3 Summary of the quantitative EDS analyses performed using the EDS Genesys software.

Element/Peak	Wt. %	At. %	Z	A	F
Cr-K	10.04	**25.44**	1.1229	0.6779	1.0201
Fe-K	10.30	**24.32**	1.1287	0.7575	1.0202
Bi-L	79.66	**50.24**	0.9414	0.9992	1.0000

3.3. Thin film growth and characterization

As inferred from the sections above, the motivation to use the thin film approach towards stabilizing the BFCO phase form came from the successful story its parent compound $BiFeO_3$ (BFO). Pioneering work that established the possibility of growing high quality epitaxial thin films of BFO was undertaken by Wang *et al.* in 2003[121]. This success generated an unprecedented interest in the compound, leading to numerous independent studies across the world in the years that followed[122–124]. By virtue of this widespread interest, the process parameters for achieving high quality BFO thin films via PLD were soon well established. Besides, explorations for immediate alternative compounds with similar functionalities extended the thin film growth capabilities also to other analogous compounds such as $BiCrO_3$ and $BiMnO_3$ among others[125,126]. These available reports provided a good starting point for early growers of BFCO thin films. Detailed studies on the growth optimization of BFCO thin films via PLD was undertaken in Ref. [109]. In addition, several other PLD growth studies of BFCO thin films were independently undertaken (Ref. [110,113,115,127]). Today the growth

window for stabilizing BFCO thin films is rather well established across several studies which are largely in agreement with one another.

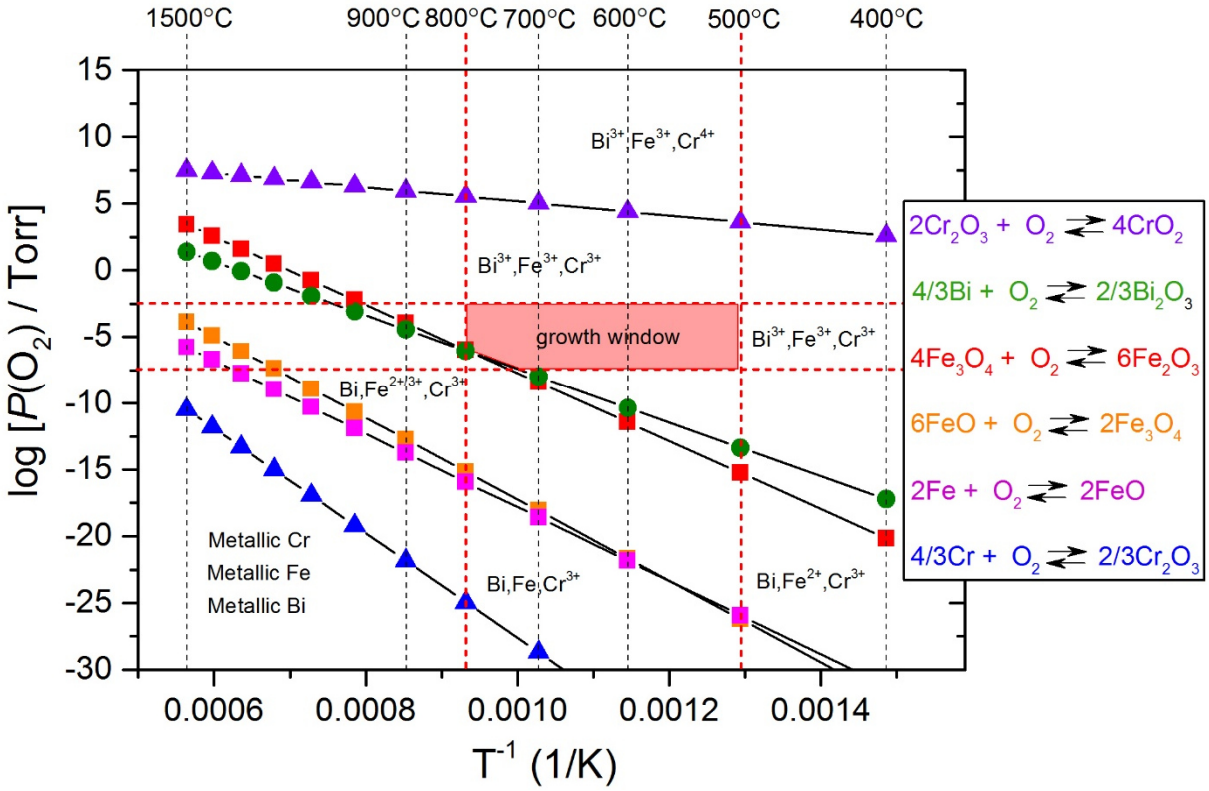

Fig. 3.3 Thermodynamic phase stability diagram for different oxidation states of bismuth, iron and chromium. (Derived based on inputs from Ref. [128])

In general, for any multi-cationic system, a thermodynamic *P-T* (pressure vs temperature) phase diagram can be plotted for the various redox reactions of the species in thermodynamic equilibrium in accordance with the following equation[128]:

$$\log P(O_2) = \alpha - \beta T^{-1}$$

Where the factors α and β are calculated from the standard enthalpy and entropy of compound formation. The factors α and β for different redox systems of all cations involved in this study as taken from Ref. [128] are listed in Appendix 1. Such a phase diagram can serve as a good starting point to choose suitable *P* and *T*, which are the two important deposition process parameters. Figure 3.3 shows one such phase diagram as plotted for the different cationic species in the BFCO system. The straight lines mark the thermodynamic redox equilibrium points in a Temperature-Pressure space between various oxidized and

reduced states of the three constituent cations in BFCO. As indicated the suitable region to stabilize Bi, Fe and Cr all in their 3+ state as desired for BFCO, is shown by the red shaded region. It should be noted that, besides the thermodynamic stability constraints, the growth window is also restricted by the limitations for possible growth temperature/pressure with respect to Bismuth based compounds and the PLD system in general have also been considered.

Although the above *P-T* phase diagram can be used to roughly identify broad range of process parameters, one must also consider that the PLD is a kinetically driven process which may cause the actual growth windows to be shifted from the thermodynamically derived growth windows. Besides small variations in the growth parameters may also exist between one PLD system to another.

Based on the thermodynamic phase diagram and the inputs from established growth routines in Ref. [109], a short optimization study was undertaken in this study to achieve best growth conditions. This is done to account for the small variations in growth conditions that may exist in different PLD system. The three more important parameters namely pressure, temperature and fluence were each individually varied in the vicinity of the established literature values while optimizing for crystalline quality (monitored via XRD ω-scans) and for phase purity (monitored via XRD $\theta - 2\theta$ scans). It was found that the pressure and temperature windows were indeed narrow as expected. Oxygen pressures beyond ~40 mTorr lead to the formation of Bismuth oxide impurity phases in addition to the perovskite phase. This is consistent with observations in the literature - Ref. [109,124]. Oxygen pressures lower than 1 mTorr led to films with low crystallinity since at such lower pressures, reduction to metallic bismuth becomes prevalent as also indicated by the phase diagram. Growth temperatures were scanned in the range of 600 to 740˚C. Temperatures higher than that resulted in loss of the volatile bismuth from the film. In general, very high-temperature synthesis and post annealing strategies to further promote chemical ordering, as suggested in Ref. [61,63] cannot be adopted in case of BFCO thin films due the high volatility of the *A*-site Bismuth.

Following the optimization process, phase pure BFCO thin films of best crystalline quality (based on analysis of various XRD measurements) as grown in the DCA-Instruments PLD500 system were obtained under conditions outlined in Table 3.4.

Table 3.4 Optimized parameters for PLD growth of epitaxial BFCO thin films on STO single crystal substrates.

Growth Parameter	Optimum value
Background pressure	8 mTorr of Oxygen
Substrate temperature	680˚C
Laser fluence	1.3 J cm^{-2}
Laser pulse frequency	5 Hz
Excimer laser used	248 nm KrF laser
Laser spot size	3 mm^2

Structural Characterization: BFCO films were grown on single crystalline (001) and (111) oriented $SrTiO_3$ (STO) substrates. Commercially available STO substrates were pre-treated with buffered-HF in accordance with the process highlighted in section 2.1.1 in order to obtain atomically smooth surfaces. Bulk single crystalline STO has a cubic structure with lattice parameter a = 3.905 Å. Figure 3.4 (a) shows an out-of-plane XRD pattern of a BFCO thin film deposited on to a (001) oriented STO substrate grown under the above listed optimized conditions. The film is seen to grow with a single preferential (00l) orientation. Besides the (00l) oriented perovskite phase, there are no indications of any impurity phases or second orientation as observed from the diffraction pattern. Since the (00l) peaks of the BFCO film lie at smaller 2ϑ values as compared to the substrate (00l) reflections, BFCO is found to have a higher *c*-axis lattice parameter in comparison with the STO substrate. Using the Nelson-Riley extrapolation function, the out-of-plane lattice parameter of the BFCO film was found to be 3.95 Å. This value is consistent with the observed *c*-axis lattice parameters in the literature[113,129]. An enlarged view of the out-of-plane diffraction pattern around the BFCO (002) reflection is shown in Fig. 3.4 (c). The observation of symmetric Laue oscillations indicate a coherently grown, high crystalline and smooth film. The periodicity of the Laue oscillation contains quantitative information on the thickness of the coherent film. Hence the thickness t can be calculated using the following formula:

$$t(\text{Å}) = \frac{\lambda(\text{Å})}{2 \cdot [\sin\theta_n - \sin\theta_{n+1}]}$$

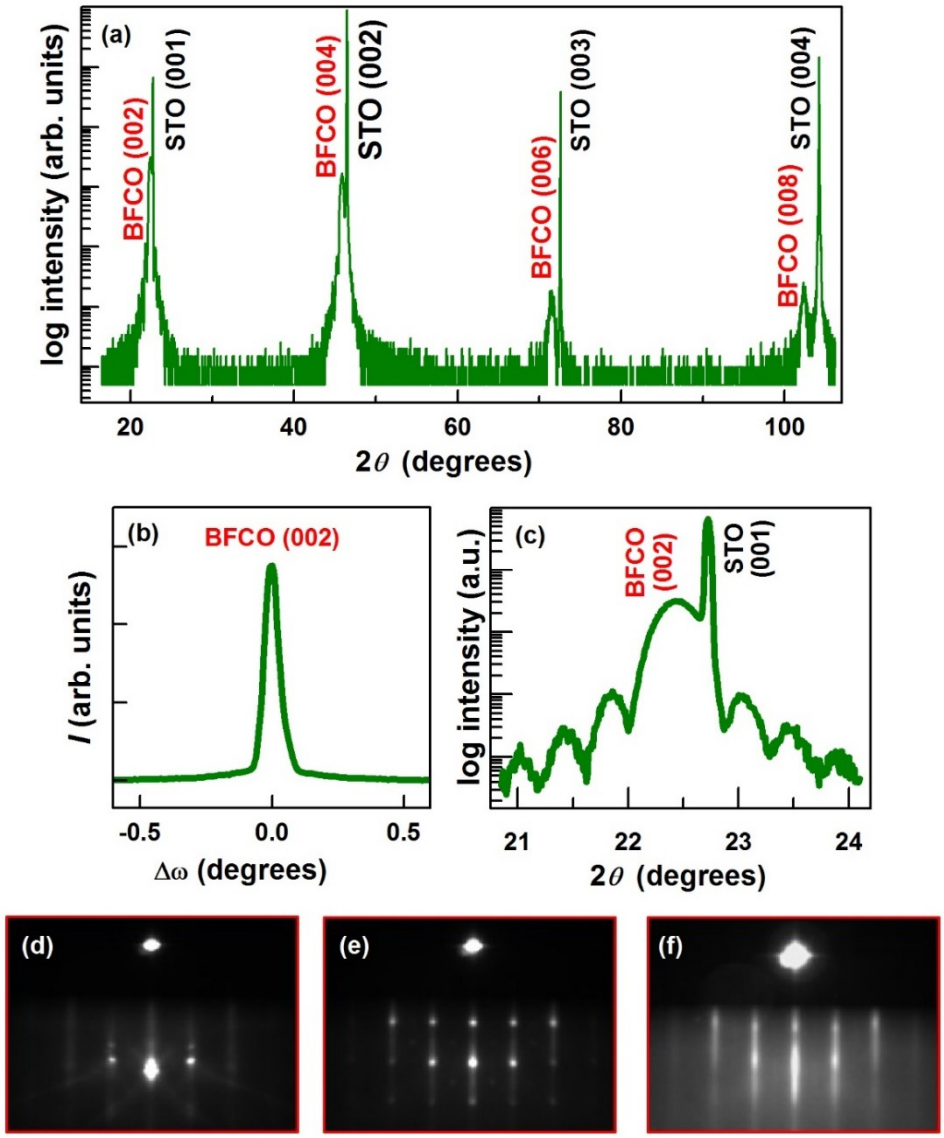

Fig. 3.4 (a) $\theta - 2\theta$ XRD pattern of the 25 nm think BFCO film grown on STO (001) substrate as measured with a Cu K_α source; (b) Rocking-curve (ω-scan) of the BFCO (002) reflection; (c) Enlarged view of the XRD pattern around the STO (001) reflection; (d) – (f) RHEED patterns recorded during the growth sequence showing the bare substrate just before start of growth (d), intermediary island growth phase (e), streaky stepped terrace surface towards the end of film growth (f).

Where λ is the wavelength of the X-ray radiation. θ_n and θ_{n+1} correspond to two consecutive Laue oscillation peaks, which are to be taken in radians. Using the above formula, the BFCO film shown here is found to have a thickness of 25 nm. This thickness value was found to be consistent with the thickness determined by analysis of an X-ray reflectivity curve of the same sample. Fig. 3.4 (b) shows a rocking-curve scan of the BFCO (002) out-of-plane reflection which has a full-width at half maximum (FWHM) of 0.07°. Such a small value of the FWHM indicates low degree of mosiacity in the film. Fig. 3.4 (d) to (f) show the surface RHEED patterns recorded for the bare STO substrate prior to deposition and that of the growing

BFCO film. The RHEED pattern of the bare STO substrate (Fig. 3.4 (d)) indicates a well-defined crystalline surface. The specular spot and diffraction spots corresponding to the 0th Laue zone are clearly seen. As observed in Fig. 3.4 (e), the BFCO film had a characteristic spotty RHEED pattern at the start indicating a Volmer-Weber type growth which is growth by forming 3D islands. As the growth progresses the 3D islands grow and coalesce forming a complete layer, after which a 2D like growth prevails as indicated by the streaky RHEED pattern in Fig. 3.4 (f).

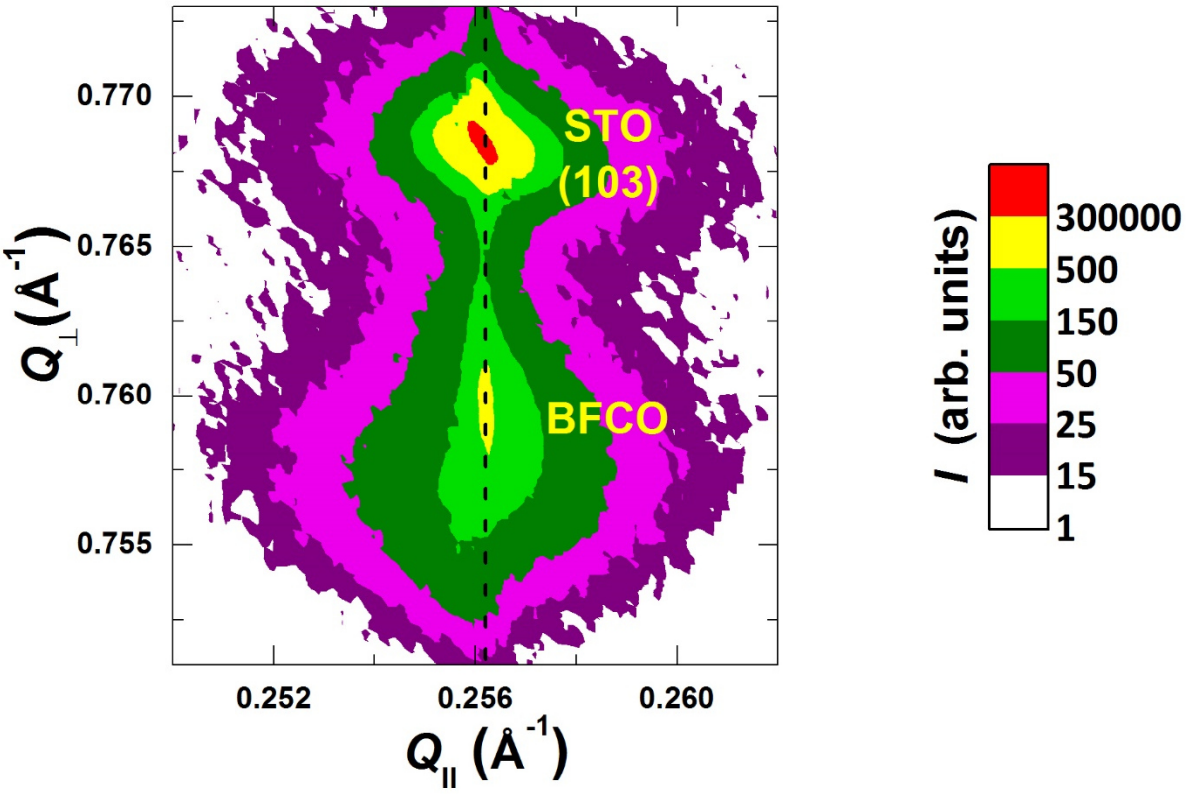

Fig. 3.5 Reciprocal Space Map (RSM) recorded in the vicinity of the STO (103) reflection. $Q_{||}$ and $Q_\perp$ stand for directions along the STO [010] and STO [001] respectively.

X-ray reciprocal space mapping (RSM) was carried out in order to characterize the in-plane lattice parameters and the strain state of the film. Fig. 3.5 shows an RSM intensity contour map recorded in the vicinity of the STO (103) reflection. As is evident in the plot, the substrate and the BFCO film peaks are aligned along the vertical axis at $Q_{||} = 0.2561$ Å^{-1}. The corresponding in place *d*-spacing obtained by taking a reciprocal was found to be ~3.905 Å which is the cubic lattice parameter of STO. For the same sample other RSMs were also recorded around the STO ($\bar{1}03$), (013) and ($0\bar{1}3$) reflections (not shown). Similar patterns were observed in all cases thereby ruling out presence of any orthorhombic distortions. Thus from the collective structural analysis, it can be inferred that the BFCO films grown on the (00*l*) oriented substrates are fully strained across the thickness of the film with in-plane lattice

parameters locked-in to that of the cubic STO lattice parameter. The out-of-plane lattice parameter is larger as compared to that of STO thereby yielding a tetragonal like structure of the BFCO phase. The epitaxy of the BFCO film can thus be concluded to be cube-on-cube type with no in-plane rotations thereby giving an epitaxial relationship of: (001)[100]BFCO || (001)[100]STO.

Chemical analysis: Chemical analysis of the as-grown films was done by X-ray photoelectron spectroscopy (XPS) in an ex-situ on a PHI Versaprobe 500 spectrometer using a monochromatic Al-K_α X-ray radiation source (1486.6 eV). Measurements were performed at room temperature under ultra-high vacuum ($<10^{-9}$ Torr). Qualitative and quantitative chemical information of the thin films were extracted from the measurements. While the spectral features such as peak positions, peak widths, satellite features, etc. contain qualitative information on the chemical environment and the oxidation state of the species, the integrated intensity areas under the peaks are quantitatively proportional to the abundance of that particular species in the probing zone. However, it is important to note that XPS is a surface sensitive technique whose probing depth is about 5 nm. So, in cases of some materials which have active surface effects or instabilities, measurement information may deviate from the bulk of the sample away from the surface. It is therefore customary to perform XPS measurements in-situ, soon after fabrication. An in-situ vacuum transfer of sample was not done in this case due to the existing device facility at the time of the measurement. However, excess care was taken to minimize the duration of sample exposure to atmosphere. During the measurement, an integrated Argon ion neutralizer was used to prevent charging on the surface of the samples.

Fig. 3.6 shows a survey spectrum recorded for the optimized BFCO thin film grown on STO substrate. All the observed peaks corresponded to the various binding energies of the core-states of the constituent atoms Bi, Fe, Cr or O. Some of the unmarked peaks correspond to satellite peaks of the core levels. Peaks corresponding to no other elements could be found in the survey spectrum thereby confirming the chemical purity of the BFCO film. Next, individual core-level spectra corresponding to the four component elements Bi, Cr, Fe and O were each collected separately and analyzed in the following text.

Fig 3.7 (a) shows the core level spectra recorded for bismuth where the detected electrons originate from the Bi 4*f* orbital. The spectra shows a doublet peak which arises as a consequence of the energy splitting due to spin orbit coupling. The angular momentum l (l = 0,1,2,3..n-1, where n is the principal quantum number), and the spin quantum s $\left(s = \pm\frac{1}{2}\right)$,

couple as per $j = l + s$ which characterizes the spin orbit coupling. Therefore, the Bi 4*f* orbital doublets are correspondingly referred to as the Bi $4f_{7/2}$ and Bi $4f_{5/2}$. The two peaks also have specific area rations that arises from the degeneracy of each spin state. In this case there exists a ratio of 3:4 for the areas of the 5/2 and the 7/2 peaks. In oxide materials, spectral features of bismuth as a cation have been well documented in literature.[130–133] The '3+' state is a rather stable oxidation state for bismuth. Bi 4*f* spectra for the BFCO film as displayed in Fig. 3.7 (a) shows the 4*f* doublets at 158.4 and 163.7 eV for the 7/2 and 5/2 peaks respectively. These values are in good agreement with similar values recorded for Bi^{3+} in the literature. As documented in the Perkin-Elmer Handbook of XPS (Ref. [133]), the binding energies corresponding to metallic bismuth are clearly lower at 157 eV and 162.31 eV. Possible presence of metallic bismuth in the sample, which might arise due to more reductive atmosphere than required, would clearly indicate additional peak features at the corresponding lower binding energy as was observed in Ref. [132] and Ref. [131]. Since we do not find any such features or shoulders corresponding to metallic bismuth, we can confirm the 3+ state for the *A*-site bismuth cations in BFCO.

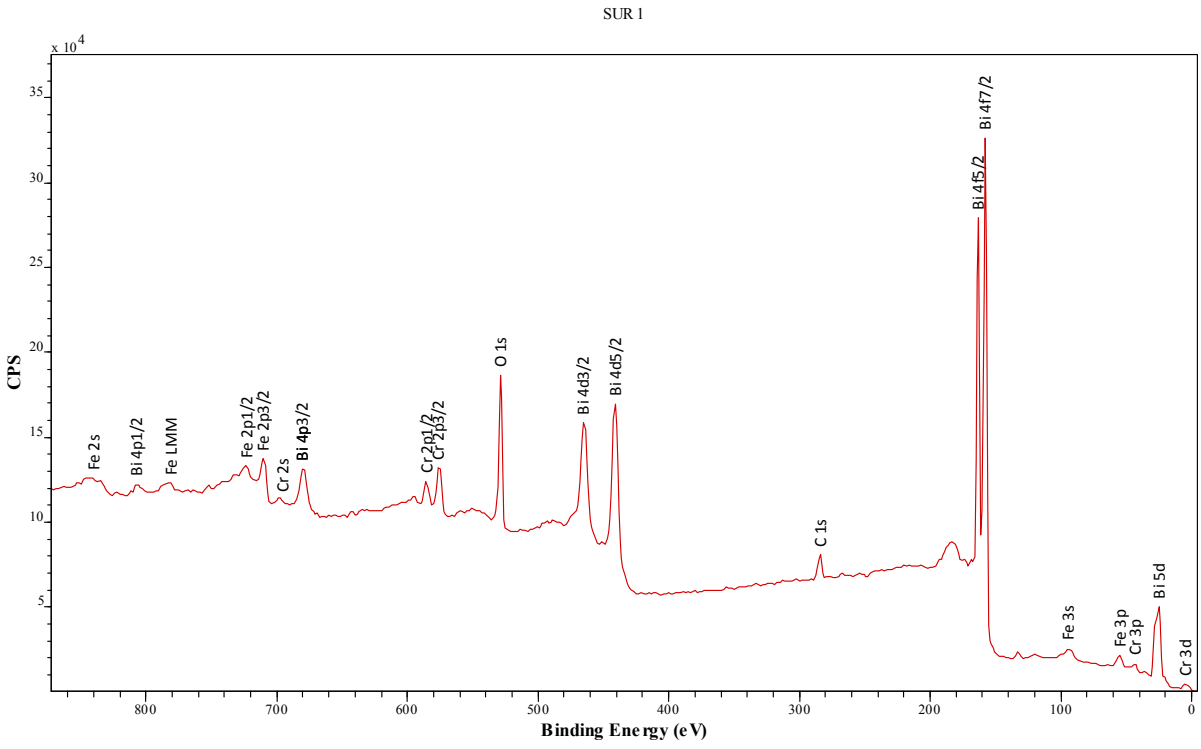

Fig. 3.6 X-ray photoemission survey spectrum recorded using the PHI Versaprobe 500 spectrometer with a monochromatic Al-K_α X-ray source on an optimized BFCO thin film

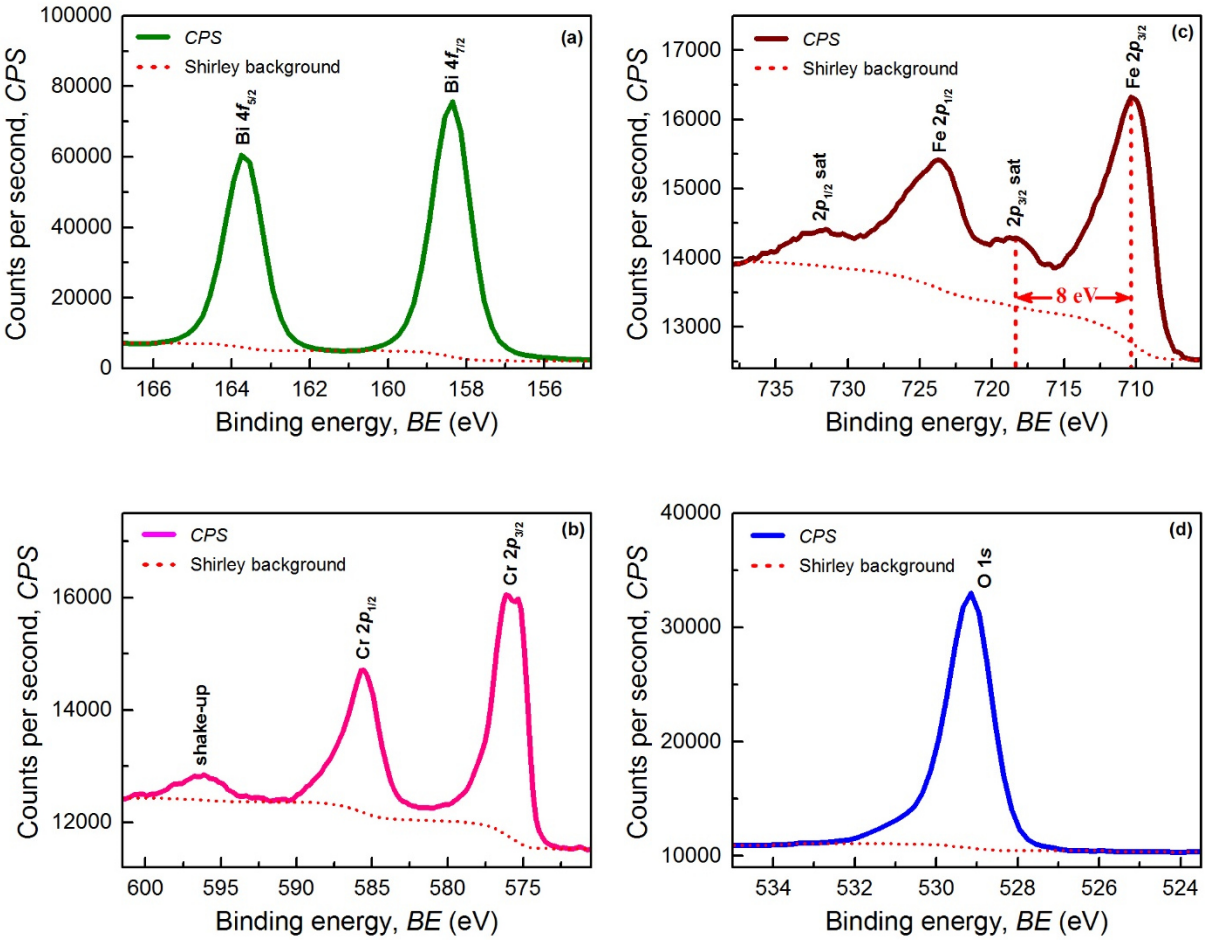

Fig. 3.7 (a) – (d) X-ray photoemission spectra recorded using a PHI Versaprobe 500 spectrometer with a monochromatic Al-K_α X-ray source on optimized BFCO film at binding energies corresponding to Bi 4*f* (a), Cr 2*p* (b), Fe 2*p* (c) and O 1*s* (d) core levels.

The recorded core-level spectra for chromium is displayed in Fig. 3.7 (b), where the detected electrons are originating from the Cr 2*p* orbital. Similar to the 4*f* spectra of bismuth, the Cr 2*p* spectra also shows a doublet splitting. Here the doublets have a nomenclature of $2p_{1/2}$ and $2p_{3/2}$ due to the spin-orbit coupling involving the electrons of the *p*-orbital which have an angular momentum quantum number, $l=1$. Peak areas corresponding to the $2p_{1/2}$ and $2p_{3/2}$ peaks have standard ratio of 1:2 as opposed to a previously mentioned 3:4 ratio for the 4*f* core peaks of bismuth. In order to characterize the fingerprint features of the Cr 2*p* spectra we referred to the literature in Ref. [134–136], which together provide a systematic spectroscopic overview of various oxidation states of chromium in different chemical coordination environments. Cr metal (0), Cr^{3+}, Cr^{5+} and Cr^{6+} are the commonly known stable oxidation states for chromium. For a metallic chromium, the binding energy for the $2p_{3/2}$ as per the Handbook of XPS is documented to be 574.4 eV.[133] It is noted in the literature that going from the metallic to the 3+ state, the BE of the $2p_{3/2}$ shifts by ~1 eV. This appears to be the case

also for the 2*p* spectra of BFCO. The shift in BE of the $2p_{3/2}$ is much higher for the other stable oxidation states of 5+ and 6+ (4 eV and 5 eV respectively). It has been noted in the literature that going from metallic Cr to the 3+ state, a rather smooth spectra for the metallic state changes into a more complex form because of multiplet splitting and shake up.[134] The line shapes are noted to become again simpler for the higher oxidation states of 5+ and 6+. The split feature of the Cr $2p_{3/2}$ spectra in BFCO is a common feature which was also recorded for the analogous $LaCrO_3$ compound and is known to arise from the coupling interactions of the three unpaired electrons in the $3d^3$ chromium with the photoemission driven 2*p* holes as accounted for by Ref. [134]. In addition, the shake-up peak seen at ~597 eV in Fig 3.7 (b) is also found to be a characteristic feature of 3+ chromium as found in compounds such as Cr_2O_3 and $LaCrO_3$. Such a shake-up peak was not found either for metallic Cr or for the higher oxidation states. The above observations unambiguously confirm the desired 3+ oxidation state for chromium in the BFCO film.

On a similar note, we now discuss the spectral features of the 2*p* core-level spectra of the iron in BFCO film as show in Fig. 3.7 (c). Iron as cation in perovskite and other oxides is once again a system that is widely studied and documented in the literature.[101,136–138] 2+ and 3+ are the most common oxidation states of iron. From the literature, it can be noted the spectra of the Fe 2*p* for the different oxidation states and in several coordination environments have by far similar components. However, now there are distinct fingerprint features which enable to clearly distinguish between the two stable oxidation states of iron. The recorded spectrum for the BFCO film shows two main peaks at 710.40 eV and 723.75 eV for the spin-orbit split $2p_{3/2}$ and $2p_{1/2}$ respectively. Our observed binding energy of the $2p_{3/2}$ (710.40) compares closely with those reported for Fe^{3+} in PLD grown thin films of $BiFeO_3$ (710.57) as in Ref. [101] and also with other comparable compounds in literature. Furthermore, no shoulder peaks to the $2p_{3/2}$ were observed, which are commonly present when sample may contain iron in the 2+ state. In addition to the principal peaks, the iron 2*p* spectra often also show the presence of distinct satellite peaks. In particular, the $2p_{3/2}$ satellite (718.40 eV) which in our case is found at ~8 eV above the $2p_{3/2}$ main peak is considered to be a characteristic of the oxidation state of iron in the literature. Based on Ref. [101,139,140], it is known that, due to their different d-orbital configurations, Fe^{2+} and Fe^{3+} during relaxation will show satellite peaks at 6 eV or 8 eV above the principal $2p_{3/2}$ peak respectively. Thus the recorded 2*p* spectra for iron in our BFCO films indicate that the iron is mainly in its 3+ state. Finally Fig. 3.7 (d) shows a core-spectrum of the oxygen 1*s* peak. The peak seems to be rather symmetric without any distinct shoulders, therefore indicating presence of a single oxide phase of the BFCO thin

film. Small shoulder like asymmetry to the left of the peak are attributed to the C=O bonds due to the adsorbed carbon at the surface after exposure to atmosphere.

In the next step a quantitative analysis was performed on the collected core-level spectra for the BFCO film. As was noted in the preceding sections, the area integral of the spectra can be used to determine relative concentrations of the various elements at the surface of the sample. In order to do this, we first subtracted the measured background from the spectra. To do this we used the Shirley algorithm within the software program CasaXPS to apply the background to the spectra. The raw areas under the spectra were then individually collected for each of the elements. The raw area for each element is then corrected for elemental sensitivity by dividing each area with its corresponding element specific Relative Sensitivity Factor (RSF). The corrected areas are then each proportional to the atomic concentration of the corresponding element at the surface. The resulting atomic concentrations of Bi, Fe and Cr were thus found to be 49±5%, 25±2% and 26±2% respectively. Within the known limits of error of the XPS technique calculated relative concentrations of the cations are consistent with the required nominal composition for the BFCO double perovskite.

3.4. Investigation of chemical order

From the preceding sections, we know that one of the key structural requirement for the intended functionality in BFCO is the chemical ordering of Fe^{3+} and Cr^{3+} cations. As per the theoretical calculations, a rock-salt ordering is expected where-in the *B*-site occupation of Fe and Cr ions alternate along all three directions. Such an order allows for exchange interactions along the Fe-O-Cr coupling systems which is the source of the expected ferrimagnetic ordering as per theoretical calculations. Structurally speaking, a rock-salt order in a pseudo-cubically grown thin film with a (00l) orientation implies that the (111) family of planes are alternately occupied by either Fe or Cr atoms. This therefore creates a doubling of the unit cell along the (111) direction. In order to check for such an ordering in our BFCO films we performed θ-2θ scans along the [111] as out-of-plane direction. Fig. 3.8 (a) shows XRD θ-2θ scan of the (00l) oriented BFCO film measured in a skew-symmetric geometry where the sample is tilted along the χ axis by an angle 54.7°. It can be observed that the fundamental reflections of the BFCO perovskite sub-cell namely $(222)_{\mathrm{dpc}}$ and $(444)_{\mathrm{dpc}}$ are found in the vicinity of the STO substrate (111) and (222) reflections respectively ('dpc' denotes double-perovskite cell). For convention, we define the BFCO dpc lattice parameter (a_{dpc}) is twice as large as its perovskite sub-cell lattice parameter (a_{pc}), namely $a_{dpc} = 2 \cdot a_{pc}$. Interestingly again in Fig. 3.8 (a), two additional peaks at 2ϑ values of ~19.5° and 61.1° are

also observed which are indicative of a superstructure. We name these superstructure peaks as 'SP'. We also attempted growth of the BFCO films on the (111) oriented STO substrate. Fig. 3.8 (b) shows an out-of-plane/ θ-2θ scan of the (111) oriented BFCO film. Also here, similar superstructure peaks are found in addition to the fundamental perovskite reflections. Such SPs are common to ordered double perovskite films as a consequence of the above discussed rock-salt order. For double perovskite films, these SPs are normally indexed as $(111)_{dpc}$ and $(333)_{dpc}$.

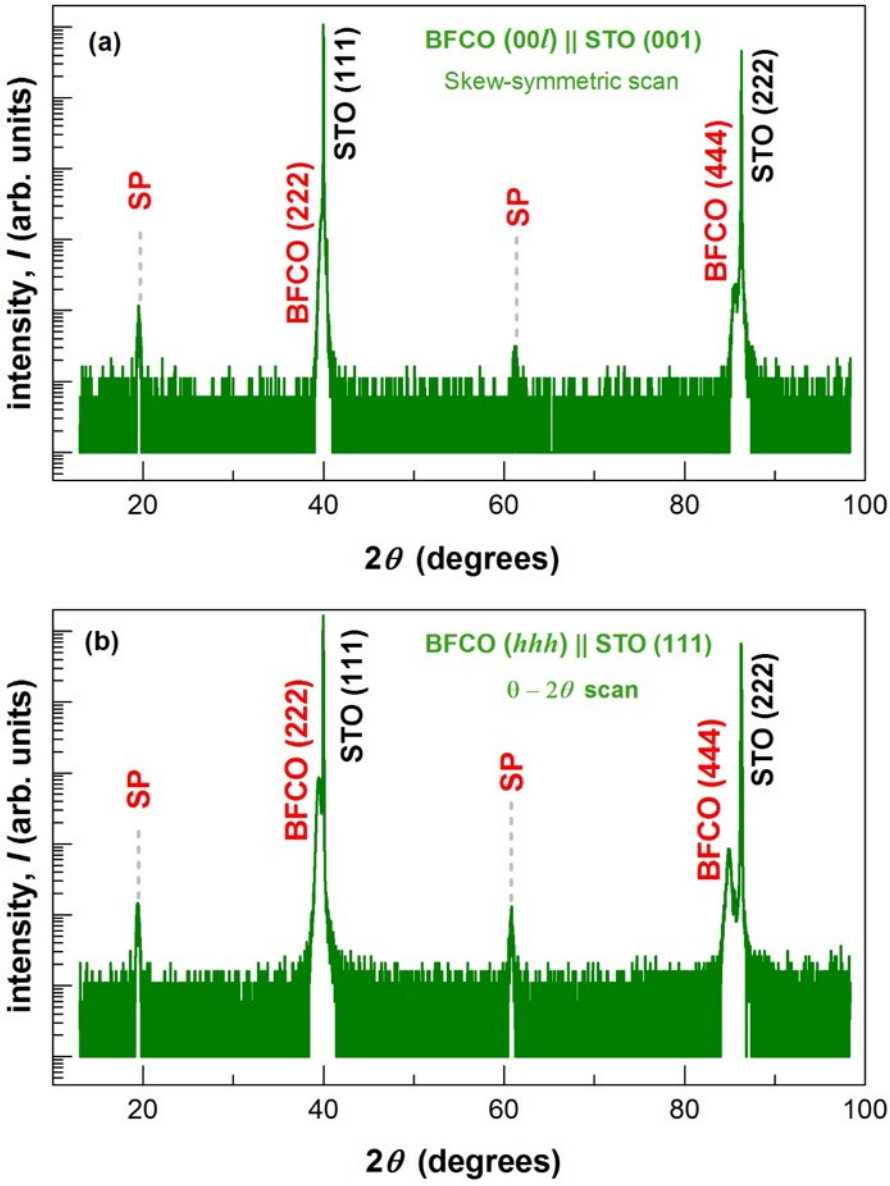

Fig. 3.8 (a) $\theta - 2\theta$ XRD pattern of a 25 nm thick BFCO film grown on a STO (001) substrate measured along the pseudo-cubic [111] direction; (b) $\theta - 2\theta$ XRD pattern of BFCO thin film grown on a (111) oriented STO single crystal substrate. Both measurements were performed using a Cu K_α source.

From crystallography and diffraction point of view, it is to be noted that the intensity of an SP that arises due to pure chemical ordering has to be proportional to the square of the contrast in the atomic form factor (a.k.a. atomic scattering factor) of the two *B*-site cations.[141] Fe and Cr are almost next neighbours in the periodic table. Furthermore, the scattering contrast between them is rather low and one would expect difficulty in detecting their order. For example, in a similar bismuth based double perovskite in Ref. [142] with similar low scattering contrast of the B-site cations, high brilliance synchrotron radiation had to be employed to observe and characterize the SPs coming from chemical order. Therefore, the intensities of the observed SPs in our BFCO films appears to be suspiciously high. This motivates a deeper study into the reason behind the high SP intensities and in general also the source of the observed superstructure in our BFCO films.

From the fundamentals of diffraction, it can be noted that the intensity relations between various reflections can be analyzed by determining the structure factor. The general formula of the structure factor is given by:

$$F_{hkl} = \sum_{j=1}^{N} f_j e^{i2\pi(hx_j+ky_j+lz_j)} \tag{1}$$

Where the summation is performed over all *N* atoms in a unit cell. The atomic form factor for atom *j* is given by f_j. The fractional coordinates of the j^{th} atom (x_j,y_j,z_j) are derived from the experimentally determined lattice parameters. The experimentally observed tetragonal like structure of BFCO in contrast to the theoretically predicted rhombohedral, causes only a small difference in the peak intensities due to the *Q*-dependence of the atomic form factors. The extinction rules also do not change and remain as for a face-centered BFCO lattice, where only $(ooo)_{dpc}$ and $(eee)_{dpc}$ ['o' and 'e' are odd and even numbers respectively] are allowed. In some double perovskite literatures, SPs and the sub-cell peaks are referred in the half cell notation as $\frac{1}{2}(ooo)_{pc}$ and $\frac{1}{2}(eee)_{pc}$ respectively.

We constructed an ideal BFCO crystal without any additional structural distortions (no octahedral tilts/cation shifts). For such a crystal in a completely B-site disordered state, no superstructure peaks are present, only the $(eee)_{dpc}$ peaks are present whose structure factor can be formulated as:

$$F_{hkl}^{dpc} = 8\left[f_{\mathrm{Bi}} + \frac{1}{2}(f_{\mathrm{Fe}} + f_{\mathrm{Cr}})\mathrm{e}^{\frac{i\pi}{2}(h+k+l)} + f_{\mathrm{O}}\left(\mathrm{e}^{\frac{i\pi}{2}(h+k)} + \mathrm{e}^{\frac{i\pi}{2}(k+l)} + \mathrm{e}^{\frac{i\pi}{2}(l+h)}\right)\right] \quad (2)$$

On the other hand for a fully rock-salt ordered case, we can write:

$$F_{hkl}^{dpc} = D_1\left[F_0\left(1 + \mathrm{e}^{i\pi(h+k+l)}\right) + F_1 + F_2\mathrm{e}^{i\pi(h+k+l)}\right] \quad (3)$$

Where the face centering is described by $D_1 = 1 + \exp^{i\pi(h+k)} + \exp^{i\pi(k+l)} + \exp^{i\pi(l+h)}$; for the allowed peaks $D_1 = 4$. Bi and I contributions to F_0 has the same terms as from Eq. (2) and $F_1 = f_{\mathrm{Fe}}\mathrm{e}^{\frac{i\pi}{2}(h+k+l)}$ and $F_2 = f_{\mathrm{Cr}}\mathrm{e}^{\frac{i\pi}{2}(h+k+l)}$ are the contributions from the ordering of Fe and Cr respectively. The structure factor for the $(111)_{\mathrm{dpc}}$ SP (F_{111}^{dpc}) is therefore:

$$F_{111}^{dpc} = -4i(f_{\mathrm{Fe}} - f_{\mathrm{Cr}}) \quad (4)$$

It is seen that the above structure factor for the SPs is a function only of the ordered *B*-site atoms Fe and Cr. Contrastingly the structure factor for the sub-cell $(222)_{\mathrm{dpc}}$ refelection (F_{222}^{dpc}), is given by:

$$F_{222}^{dpc} = 8\left(f_{\mathrm{Bi}} + 3f_{\mathrm{O}} - \frac{1}{2}(f_{\mathrm{Fe}} + f_{\mathrm{Cr}})\right) \quad (5)$$

Which includes contributions from all atoms and is independent of the degree of *B*-site order. The thus resulting structure factors were estimated using PowderCell[143] for an ideal BFCO crystal for various cases of irradiation under different X-ray sources used in this study. These are shown in Table 3.5 below.

Table 3.5 Calculated structure factors ($|F_{hkl}|$) values using Powder Cell at different X-ray energies used in this study. Amplitude of the $(222)_{dpc}$ peak (and the STO (111) peak) is seen to be almost constant, whereas maximum contrast for the $(111)_{dpc}$ peak occurs between the Co K_α and Co K_β radiation (emphasized). Peak intensities are proportional to $|F_{hkl}|^2$.

	$BFCO_{dpc}$		$SrTiO_3$
	222	111	111
$d - hkl$ (Å)	2.265	4.53	2.255
Cu K_α	64.02	2.54	30.78
Mo K_α	63.22	4.07	29.52
Co K_α	66.11	5.30	31.31
Co K_β	65.62	1.98	31.04

Synthesis of double perovskites may also yield partially ordered compound. In such case, a long range order parameter S can be defined, such that for a complete disordered case, $S = 0$; and for a fully ordered case, $S = 1$. The amplitude of the $(ooo)_{dpc}$ SP is proportional to S and to the contrast in the form factors, $C = |f_{Fe} - f_{Cr}|$, whereas the integrated intensity of the SP (which scales with square of the form factor, $|F|^2$ in the kinematic limit) is proportional to S^2 and C^2. Therefore, it can be noted that the integrated intensity of the SPs that arise purely due to chemical ordering contain quantitative information of the B-site ordering. Complete calculative estimations of peak intensities requires considerations of corrections due to several factors such as beam polarization, temperature, Lorentz-polarization factor, film absorption and irradiation volume.[144] The corresponding relationship between the order parameter and the superstructure peak intensities is:

$$S^2 = \frac{(I_{111}/I_{222})^{\text{sample}}}{(I_{111}/I_{222})^{\text{fully ordered}}} = \frac{NI^{\text{sample}}}{NI^{\text{fully ordered}}} \tag{6}$$

where $(I_{111}/I_{222})^{\text{sample}}$ and $(I_{111}/I_{222})^{\text{fully ordered}}$ are intensity rations of the (111) to (222) reflections of a partially ordered and fully ordered sample.

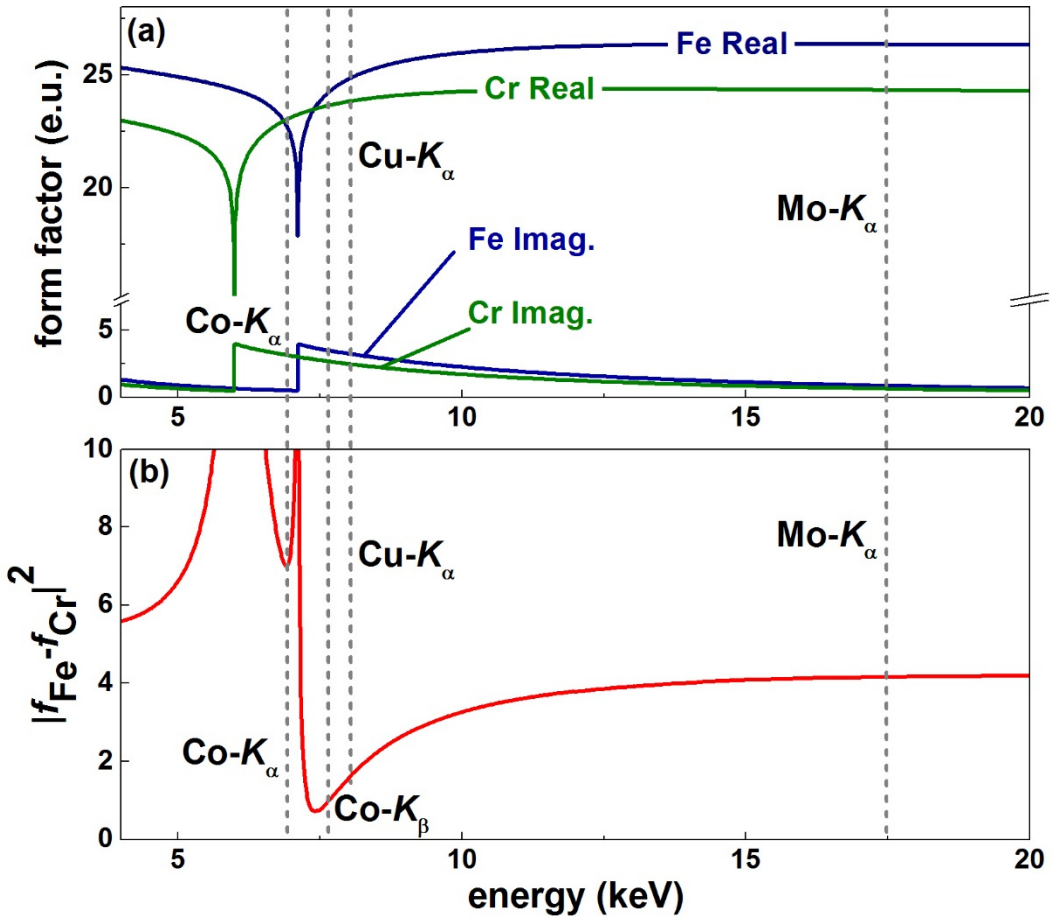

Fig. 3.9 (a) Real and imaginary components of the atomic form factors for Fe and Cr atoms plotted as a function of radiation energy; (b) calculated value of the contrast, $C = |f_{Fe} - f_{Cr}|^2$ also plotted as a function of same scale of radiation energy.

The real and imaginary parts of the atomic form factors for Fe and Cr plotted as a function of energy of X-ray radiation is shown in Fig. 3.9 (a). What is particularly of interest to us here is the contrast (C) between the form factors for Fe and Cr which is also consequently a function of the radiation energy. Based on the preceding sections we have established that if the $(111)_{dpc}$ SP originates purely due to B-cation ordering, its integral intensity should be proportional to C^2. We have therefore, plotted a graph of C^2 versus energy in Fig. 3.9 (b). All form factors were taken from the program Hephaestus,[145] which is based on the Cromer-Liberman tables for calculations of the anomalous scattering (note that the calculations omit the Q-dependance of the atomic form factors. In Ref. [141], Reinhard *et al.* showed for an Fe-Cr system that it is possible to sweep the C^2 (using a tunable energy synchrotron radiation source) from almost zero to about 35 $(e.u.)^2$ (e.u. stands for electron units) in vicinities of energies close to the Cr absorption edge (see Fig. 3.9 (b)). Motivated by this idea, we realized that a smaller but sufficiently significant contrast change can also be created by using

different laboratory X-ray sources. For example, from Fig 3.9 (b) it can be seen that by using Co K_β we can cause a smallest contrast between Fe and Cr among the available X-ray sources marked on the graph. Such a situation should lead to the least intense SPs. On the other hand, largest contrast can be caused by using a Co K_α radiation which should result in the highest intensity of SPs. Similarly also an intermediate contrast change can be caused when going from Cu K_α to Mo K_α.

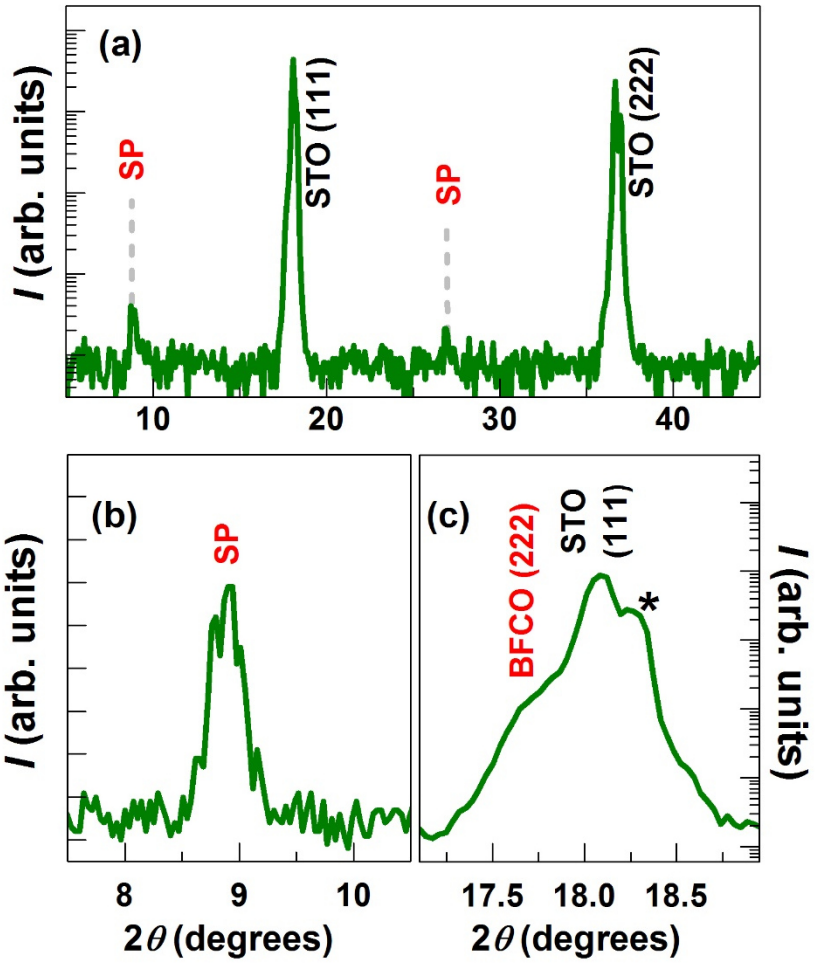

Fig. 3.10 (a) $\theta - 2\theta$ XRD pattern of the 25 nm thick BFCO film on (001) oriented STO substrate measured along pseudo-cubic [111] direction with a Mo K_α source; (b) Enlarged view of the $(111)_{dpc}$ superstructure peak; (c) Enlarged view of the $\theta - 2\theta$ XRD pattern in the vicinity of the STO (111) reflection. The splitting of the STO (111) peak (as marked with star) arises due to the polychromatic Mo $K_{\alpha 1}$ and Mo $K_{\alpha 2}$ radiation.

Thus, in order to investigate the presence of *B*-site cation ordering in the BFCO films, we performed diffraction experiments under various available laboratory X-ray radiation sources (Cu K_α, Co K_α, Co K_β and Mo K_α). Subsequently we analyzed the changes in the SP intensities with corresponding changes in the irradiation source. Fig. 3.10 (a) shows an XRD pattern of a (00l) oriented BFCO film measured along the pseudo-cubic [111] direction using Mo K_α

radiation. Detailed view of the SP and the sub-cell peak are shown in Fig. 3.10 (b) and (c). From preceding discussion, we said that the intensity change of the sub-cell $(222)_{dpc}$ peak with energy is small as it depends on the form factor of all BFCO atoms (Bi, Fe, Cr and O). From structure factor estimations in Table 3.5, we know that the SPs due to chemical order measured under Mo K_α radiation should have a normalized intensity $NI^{\text{sample}}_{\text{Mo}K\alpha}$ larger than the $NI^{\text{sample}}_{\text{Cu}K\alpha}$ measured under a Cu K_α source by a factor of 2.63. However, we found that both quantities were equal, there was no significant increase in the normalized intensity.,

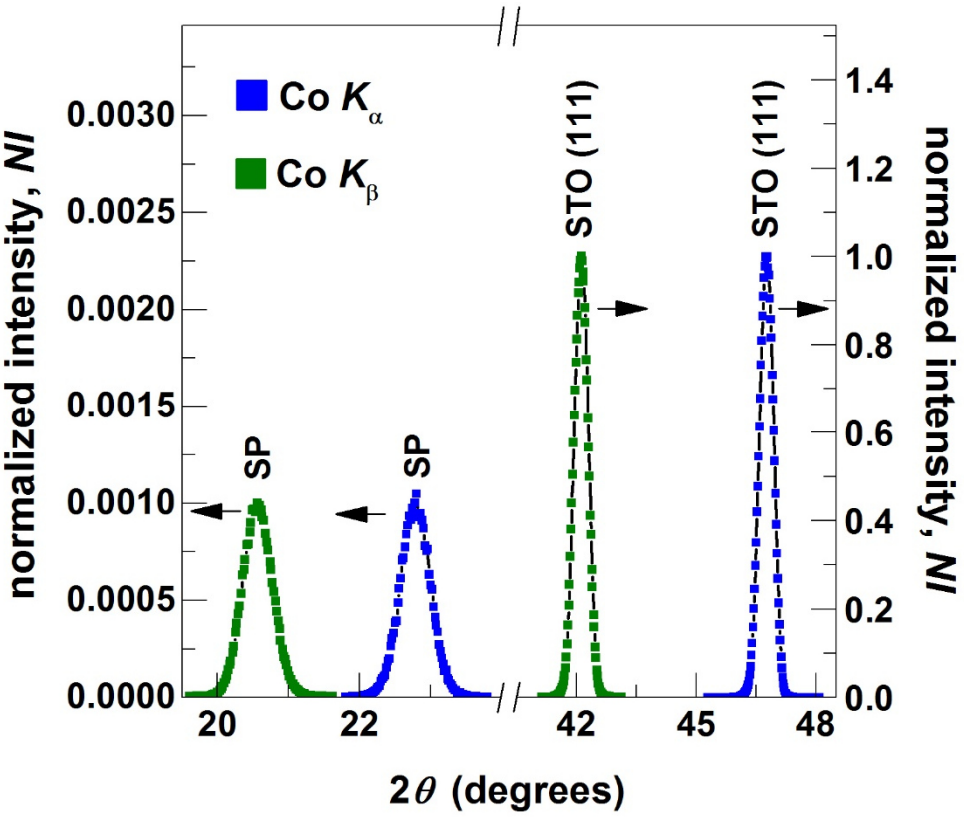

Fig. 3.11 $\theta - 2\theta$ XRD patterns of the (001) oriented BFCO film measured along the pseudo-cubic [111] direction using Co K_α and Co K_β radiation. Superstructure peaks have been normalized to the STO (111) peaks.

Furthermore, the same BFCO sample was measured using a Co source tuned to Co K_α and Co K_β lines at 6930 and 7649 eV respectively. Except the source energy, no other parameters were changed between the two scans in order to rule out any systematic errors contributing to peak intensities. As established in above paragraphs, using both the Co lines, we can measure: (a) at the lowest accessible contrast (at Co K_β); and (b) the largest possible contrast ratio ($NI^{\text{sample}}_{\text{Cu}K\alpha}/NI^{\text{sample}}_{\text{Cu}K\alpha} \approx 7$) as derived from Table 3.5. XRD scans from these two measurements are shown in Fig. 3.11. Here, due to the lower angular resolution of the diffractometer, we

were unable to separate film and substrate peaks, and therefore used the STO (111) for normalization of SPs. As evident in the figure, we did not see the expected seven fold change in the normalized intensities of the SPs. Here, we were unable to normalize the intensity of the SP to the BFCO sub-cell $(222)_{\mathrm{dpc}}$ peak, which would be more accurate approach. Nevertheless, it should be noted that the X-ray wavelength change between the two scans (with Co K_α and Co K_β) is small, across which the substrate (111) structure factor does not change significantly as seen from Table 3.5, but importantly a significant change for BFCO $(111)_{\mathrm{dpc}}$ SP exists due to the scattering contrast jump near the Co absorption edge. From the calculations of structure factor, the substrate peak intensity change should be approximately 1.75 % which is small compared to the expected seven fold contrast caused change to the SP. A consistent observation for recorded also by considering the absolute reflected intensities by correcting Bragg peak intensities relative to direct beam intensity.

As per our ideally constructed BFCO cell in the fully ordered case, the intensity ratio $I_{(111)\mathrm{dpc}}/I_{(222)\mathrm{dpc}}$ when measured with Cu K_α radiation, must be approximately 0.36 % (including geometrical corrections and negletting illumination and absorption corrections). However, $I_{(111)\mathrm{dpc}}/I_{(222)\mathrm{dpc}} \approx 1.76 \pm 0.10\%$ is observed, which is much larger than expected. The above analysis thus suggests that the normalized intensity of the observed BFCO SPs are large and independent of changes in the scattering contrast. This cannot be explained by pure ordering of the Fe-Cr cations. Therefore, other possible origins of the SPs were investigated in the following sections.

3.5. Origin of superstructure

In preceding sections we discussed at length cation ordering in perovskite structures which causes doubling of the fundamental perovskite unit-cell. In addition to cation ordering, other structural features such as cation shifts and tilts of the oxygen octahedral can also lead to doubling of the perovskite unit cell.[146] In 2007, Suchomel *et al.* attempted synthesis of bulk BFCO using high pressure reaction methods. They were unable to achieve ordering of the B-site cations Fe and Cr, however obtained a disordered BFCO powders that crystalized in the rhombohedral space group *R*3*c*. Here the $(hhh)_{\mathrm{dpc}}$ ('*h*' is odd) SPs are forbidden (Fig 3.12 (a)). Since in our films, we observe a strong $(111)_{\mathrm{dpc}}$ SP, the symmetry of the unit cell must deviate from the *R*3*c* substantially. If this symmetry lowering was caused by cation ordering alone without other distortions (as shown in Fig. 3.12 (b)), then the $(111)_{\mathrm{dpc}}$ SP would have been ideally suited for characterization of chemical order. But in fact, the *R*3 symmetry of the

theoretically predicted full ordered BFCO unit cell (Fig. 3.12 (c)) does not only have a cation-order related symmetry lowering but also due to shifts of different magnitudes of Bi, Fe and Cr cations along the polarization axis (the pseudo-cubic [111] direction), and also distortions of the oxygen octahedral.[99]

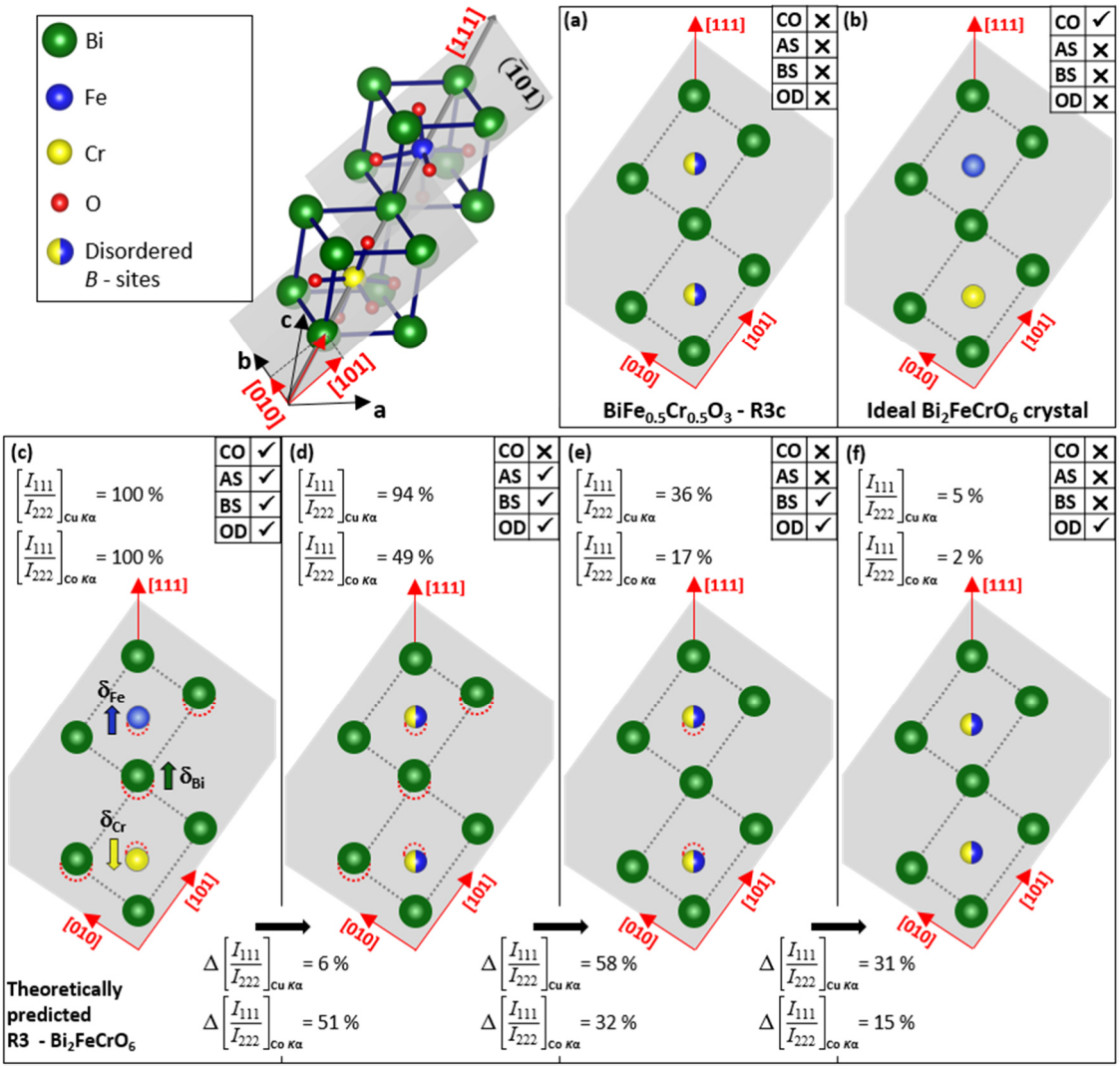

Fig. 3.12 (a) – (f) Schematic figures (not drawn to scale) showing positions of *A* and *B*-site cations on the pseudo-cubic ($\bar{1}01$) plane of BFCO under the following various conditions of structural order/distortions: CO – chemical order; AS – *A*-site cation shifts; BS – *B*-site cation shifts and OD – oxygen octahedral distortions. (As published in Ref. [28])

To mutually compare the influence of the each of the symmetry lowering structural changes on the SP, we calculated their relative contributions to the $NI = I_{111}/I_{222}$ intensity ratio using the crystal visualization software Vesta for Cu K_α (and Co K_α) radiation, starting from the theoretically predicted *R*3-symmetric BFCO.[14] In the first step, a Fe-Cr 50% - 50% random distribution (as shown in Fig. 3.12 (d)) results in a 6% decrease of the intensity ratio (51%

for Co K_α). Second, a shift of every alternating Bismuth ion located at (x,y,z) = (0.503,0.503,0.503) in *R*3 to the highest symmetry positions of $\left(\frac{1}{2},\frac{1}{2},\frac{1}{2}\right)$ in *R*3*c* (Fig. 3.12 (e)) leads to a major 58% drop of *NI* (32% for Co K_α). Subsequent movement of the B-site cations to their symmetric *R*3*c* postions leads to a significant 31% (15% for Co K_α) decrease in the *NI*. The left over, considerably small 5% change of *NI* (2% for Co K_α) is due to the oxygen octahedral distortions. Thus, the SPs can be caused by any electron density modulations which are compatible with the face-centered lattice of BFCO. Based on the above analysis, the contribution of the octahedral distortions is negligible and due to selection rules, there is no contributions due to oxygen octahedral tilts to the $(111)_{dpc}$ SP.[18] In addition to that, based on the analysis in the preceding section, we can explicitly exclude *B*-site cation ordering as the origin of the SPs as their intensities do not follow the energy dependence of anomalous scattering. As is evident from the above analysis, it turns out that the theoretically predicted displacements of the *A*- and *B*-site cations along the [111] pseudo-cubic directions have the largest contribution and are the only structural modulations that are commensurate to the magnitude of the observed SP intensities. In ferroelectric perovskites with lone-pair active cations such as Bismuth, such shifts of cations along the polarization axis are common and have been established also in other studies in the literature.[147,148] Therefore by systematically ruling out all other contributions, the only plausible origin of the observed doubling of the unit cell here are the unequal displacements of Bi^{3+}, Fe^{3+} and Cr^{3+} cations along the $[111]_{pc}$ direction, which are compatible with the face-centering of the double pseudo-cubic unit cell. Similar SPs were also reported by Kannan *et al*. in epitaxial $BiCrO_3$ thin films grown by PLD where only one *B*-site cation – Cr^{3+} exists. Here, the SPs were attributed to structural modulations arising from substrate induced strain.

3.6. Magnetic characterization

In the introductory sections of this chapter, the existing large discrepancies concerning magnetic properties of as grown BFCO thin films was discussed. Although theoretical calculations on bulk ideally ordered BFCO predict ferrimagnetic coupling of the Fe – Cr sub-lattices resulting in a magnetization of 2 μ_B/f.u., varied observations of magnetic responses ranging from almost zero to higher than predicted moment were reported. However, in light of the detailed structural investigations in preceding sections, background of the existing discrepancies can be understood. In our case with negligible chemical ordering, no significant magnetic moment is expected. Magnetic characterization of the BFCO films were carried out using a SQUID magnetometer.

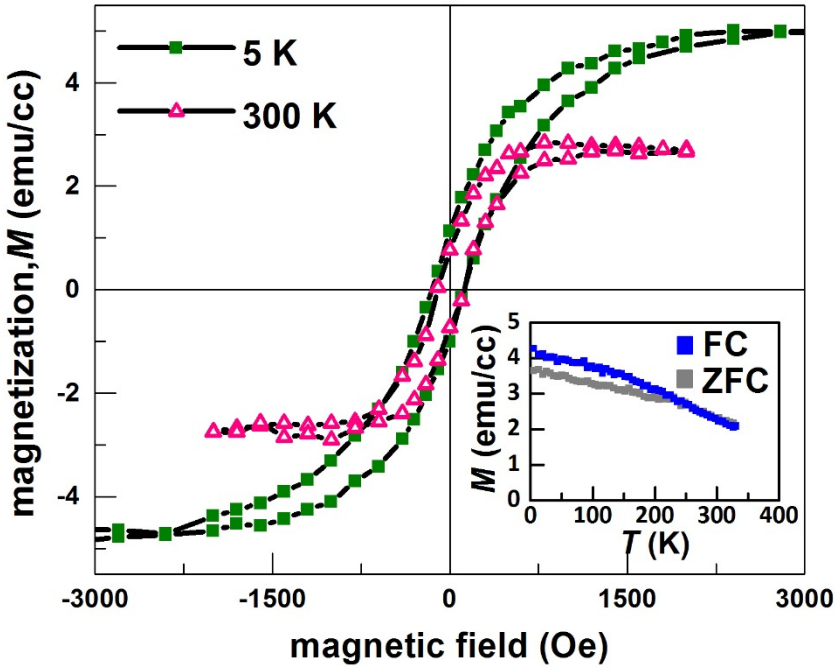

Fig. 3.13 Magnetization *vs.* field curves measured for the 25 nm thick BFCO film at 5 K and 300 K. Applied field was in-plane with respect to the sample surface and the diamagnetic contribution of the STO substrate was subtracted. Inset shows magnetization *vs.* temperature curves recorded for the same sample.

The magnetization *vs.* field curves for the (00l) oriented BFCO sample 5 K and 300 K are shown in Fig. 3.13. Substrate contribution of the diamagnetic STO was subtracted. At temperature of 5 K, only a meagre 5 emu/cc (0.06 μ_B/f.u.) is observed as the saturation magnetization. This low value of magnetization suggests a predominant antiferromagnetic order resulting from the lack of *B*-site cation order. Inset in Fig. 3.13 shows the field cooled and zero field cooled magnetization curves for the BFCO film measured as a function of temperature in range 5 to 330 K. The curves show a persistent small magnetization up to room-temperature without any indications of a magnetic transition. This low residual magnetization can arise either from a small degree of the ordered phase in the sample or due to some magnetic nano-clusters that are beyond the resolution of the performed XRD measurements. Therefore, it can be noted that the $(111)_{dpc}$ SP alone is not a sufficient indicator of the Fe-Cr ordering. Study of energy-dependence of the X-ray intensities can clarify origin of the SPs and allow for an unambiguous determination of chemical order. Resolving all cation displacements and determining precise atomic positions for the BFCO films would require more extensive analysis and use of high intensity synchrotron facilities. Our analysis method can be applied to any ordered double perovskite, however double perovskites containing ferroelectrically active species like Bi^{3+} are more prone to cation displacements

that can mimic a chemically ordered state. Also more recent studies by Vinai *et al.* and Rout *et al.* have used various advanced experimental an theoretical approaches to study the magnetic response of epitaxial BFCO thin films.[120,149] Both studies found lack of strong magnetic ordering in the as grown films. In fact, the density functional calculations of Rout *et al.*[149] established that the *B*-site disordered structure is more stable in coherently strained epitaxial films which is consistent with the findings in this study.

Chapter 3 - Acknowledgements

The author acknowledges following collaborative works in Chapter 3:

- Advanced structural analysis of the superstructure peaks were done in collaboration with M. Major and W. Donner.
- The work was conducted under advisory supervision of P. Komissinsskiy, W. Donner and L. Alff.

4. 3*d* – 5*d* double perovskites : La_2MnReO_6 and La_2NiReO_6

In chapter 3, a first line of approach in this work on finding suitable ferrimagnetic double perovskites as templates for room temperature multiferroism was discussed. This study on the *A*-site bisumuth based 3*d*-3*d* double perovskite Bi_2FeCrO_6 provided some valuable insights in to epitaxial stabilization and characterization of double perovskite thin films. A fundamental understanding of challenges concerned with achieving spontaneous *B*-site cation ordering in as-grown double perovskite thin films and also concerning subsequent detection of the order was developed. Although a weak magnetic response was observed, as opposed to the desired robust ferrimagnetic order, the work on BFCO highlights the importance of choosing the right combination of *B*-site cations to achieve the desired magnetic functionality. Leveraging on these findings, we extended our work to 3*d*-5*d* double perovskites, results of which have been elaborated in the following sections of this chapter.

4.1. Introduction and background

Combining a 3*d* transition metal with one from the 5*d* series as the two *B*-site cations in double perovskites of the type $A_2BB'O_6$ can have several advantages when compared to their 3*d*-3*d* counterparts. For instance, there can be significant differences in the two *B*-site ionic radii which in accordance to the discussions in section 1.2.2 acts as a strong driving force for spontaneous chemical ordering. In addition to that, many 5*d* elements owing to their several stable high oxidation states can be suitably coupled with appropriate 3*d* cations in combinations having a difference in oxidation states of 2 or more, thereby also promoting their spontaneous chemical ordering. Many 5*d* elements are by themselves often non-magnetic metals. So the idea of employing them for magnetic double perovskites is to combine them with appropriate magnetic 3*d* species which in-turn induce a magnetic moment in them as a consequence of the exchange interactions along the – *B* – O – *B'* – O – *B* – chains.[2] As a matter of fact, if you look back at the history of double perovskites in general (as documented by D Serrate *et al.* in Ref. [22]), some of the earliest reports which date back to the 1950 – 60s were indeed works on 5*d* Rhenium based double perovskites. These works were reported by Longo and Ward in 1961, who at the time were probing room temperature ferromagnetism in Rhenium based double perovskites.[23]

Table 4.1 Non-exhaustive list of prominent 3*d*-5*d* double perovskites explored for room temperature magnetism in either bulk, thin film or theory; included along is a list of the observed low temperature saturation magnetizations and magnetic ordering temperatures for the corresponding compounds.

Compound	References	Magnetization, M at low T (~5 K)	Magnetic ordering temperature, T_C	Type of study
Sr_2CrWO_6	J. B. Philipp, L. Alff *et al.*[150]	1 μ_B/f.u.	390 K	Bulk
	J. B. Philipp, L. Alff *et al.*[151]	1.9 μ_B/f.u.	> 400 K	Thin film
Sr_2CrReO_6	S. Geprägs, L. Alff *et al.*[38]	0.8 μ_B/f.u.	635 K	Thin film
	A. J. Hauser *et al.*[152]	1.29 μ_B/f.u.	508 K	Thin film
Sr_2CrOsO_6	Y. Kockenberger, L. Alff *et al.*[2]	2 μ_B/f.u.	725 K	Bulk
	R. Morrow *et al.*[153]	0.4 μ_B/f.u.	660 K	Bulk
Sr_2CrIrO_6	T. K. Mandal *et al.*[154]	1 μ_B/f.u.	884 K	Theory
	S. Dasgupta *et al.*, (unpubl.)	~0.8 μ_B/f.u.	> 330 K	Thin film
Ca_2FeReO_6	T. Alamelu *et al.*[155]	2.37 μ_B/f.u.	539	Bulk
Sr_2FeReO_6	K. –I. Kobayashi *et al.*[156]	2.7 μ_B/f.u.	400 K	Bulk
Ba_2FeReO_6	W. Prellier *et al.*[157]	3.04 μ_B/f.u.	315 K	Bulk
Bi_2MnReO_6	M. Ležaić & N. A. Spaldin[4]	2.34 μ_B/f.u.	330 K	Theory
Bi_2NiReO_6	M. Ležaić & N. A. Spaldin[4]	0.58 μ_B/f.u.	360 K	Theory

Most 5*d* transition elements, owing to their high Z (atomic number) values, are associated with an enhanced spin-orbit coupling. This introduces energy interactions in the scales comparable to coulomb correlation and bandwidth.[158] As a consequence several compounds containing 5*d* elements exhibit exotic functionalities such as topological insulators, metal-insulator transitions and complex magnetic order.[159–161] In-spite of these advantages, double perovskites with 3*d*-5*d* combinations of *B*-site cations have been less explored as compared to the 3*d*-3*d* compounds. Furthermore, even fewer 3*d*-5*d* double perovskites have been stabilized

in the thin film form. Primary reason for this is the relative chemical complexity of epitaxially stabilizing 5*d* compounds as compared to the 3*d* ones. For some elements such as Osmium, toxicity is also a further hindrance that calls for complex synthesis procedures. Table 4.1 shows a list of few prominent 3*d*-5*d* double perovskites that have been explored for room temperature magnetism. At first look, one can note that almost all of the compounds experimentally realized have shown magnetic ordering temperatures above room temperature. This is primarily a great advantage as compared to the prominent 3*d*-3*d* compounds listed in Table 3.1, where a majority of the double perovskites were ferri-/ferromagnetic only below room temperature. Also notable is the fact that only a few compounds have been explored via the thin film approach as compared to the extensive 3*d*-3*d* list in Table 3.1. 3*d*-5*d* compounds thus provide a large test ground for discovering new functionalities in unexplored compounds using the thin film approach.

Some trends in Table 4.1 are particularly interesting to note. For example consider the series of compounds of type $Sr_2CrB'O_6$ as enclosed in the blue-dashed box where we substitute *B'* with various cations along the period of the 5*d* elements. All of these compounds exhibit very high Curie temperature and appear to contain a trend. In the case of the popular and widely studied 3*d*-4*d* double perovskite Sr_2FeMoO_6, modulation of the magnetic critical temperature with electron doping up to an order of ~100 K for added electron was achieved. In this case the electron doping was realized by partially substituting the *A*-site strontium with the trivalent lanthanum in the $Sr_{2-x}La_xFeMoO_6$ system.[162] Motivated by these results, the works on the $Sr_2CrB'O_6$ used a different approach to electron doping. Instead of *A*-site substitution, the *B'* site was sequentially replaced with the series of 5*d* elements W, Re and Os thereby allowing for studying the direct effect of 5*d* band filling on the magnetic properties of the series.[2,37,38,163] As was expected, a large curie temperature of ~725 K was observed for the compound Sr_2CrOsO_6 sequentially higher than its two predecessors Sr_2CrReO_6 (635 K) and Sr_2CrWO_6 (400 K).[2] Thus an erroneous previous report that concluded Sr_2CrOsO_6 to be not ferromagnetic at room temperature stood corrected.[164] What was also an interesting outcome of the findings of Y. Krockenberger *et al.* was the electrical state of the compound. The fully spin polarized half-metallicity observed in Sr_2CrWO_6 and Sr_2CrReO_6 could be changed to a ferrimagnetic insulating state in the case of Sr_2CrOsO_6. This was possible since, in the case of Sr_2CrOsO_6, the Os 5*d* t_{2g} minority-spin orbital is completely filled, while the majority-spin channel is split by a gap, thereby rendering an insulating state for the compound.

Prior to the observation of insulating ferrimagnetism in Sr_2CrOsO_6, the use of 3*d*-5*d* double perovskites in the design and search for single phase multiferroics was neglected as it was

believed that most 3*d*-5*d* compounds, owing to the delocalized nature of the 5*d* bands are largely metallic in nature. This metallicity can be contraindicative to the need for an insulating state to achieve ferroelectric multiferroics. However, the reported insulating ferrimagnetism in Sr_2CrOsO_6 with high transition temperatures upto 700 K changed that perspective. Consequently in 2011, Ležaić and Spaldin by theoretical design proposed two 3*d*-5*d* cationic systems that could provide potential ferrimagnetic insulating templates for achieving room temperature multiferroicity (highlighted within the red-dashed box in Table 4.1).[4] As per the commonly used approach for single phase type I multiferroics as discussed in Section 1.2.4, the ferroelectrically active trivalent cation - Bi^{3+} was chosen as the *A*-site cation, thereby predicting two compounds Bi_2MnReO_6 (BMRO) and Bi_2NiReO_6 (BNRO) as prospective multiferroic compounds. However, experimental works on 3*d*-5*d* double perovskites with *A*-site bismuth have so far been seldom reported in the literature.

As reported in Ref. [4], Ležaić and Spaldin used first principles density functional theory to calculate the ground state structure and the magnetic ordering of BMRO and BNRO. Their structural optimizations using the Vienna ab initio Simulation Package (VASP) yielded a monoclinic, centrosymmetric $P2_1/n$ symmetry as the lowest energy structure for both compounds in their ferrimagnetic insulating state. The authors noted that a slightly higher energy ferroelectric structure with rhombohedral *R*3 symmetry could be achieved if two in-plane lattice parameters are constrained to be equal in length. Such a constraint can be achieved via coherent heteroepitaxy on a substrate with square in-plane lattice. Consequently, their calculated values (incl. spin-orbit coupling) for the functional responses of polarization and magnetization have been listed in Table 4.2. Non-integer values of the total magnetization arise due to the inclusion of the spin-orbit coupling.

Table 4.2 Calculated properties for bulk ferroelectric *R*3 phase of Bi_2MnReO_6 and Bi_2NiReO_6 as calculated by Ležaić and Spaldin (Taken from Ref. [4])

Compound	Polarization, P ($\mu C/cm^2$)	Magnetization, M (μ_B/f.u.)	Curie Temp. T_C (K)
Bi_2MnReO_6	86	2.34	330
Bi_2NiReO_6	80	0.58	360

The magnetic ordering temperatures were estimated using finite-temperature Monte-Carlo scheme and the lowest energy magnetic ordering was ferrimagnetic corresponding to the anti-alignment of the 3*d* and 5*d* spins. Oxidation states of 2+ was desired for the manganese ($3d^5$:$t_{2g}^3e_g^2$) and nickel ($3d^8$:$t_{2g}^6e_g^2$) and 4+ for rhenium ($5d^3$:$t_{2g}^3e_g^0$). As a consequence of these configurations, a 150˚ bond angle between Mn-O-Re was found to stabilize an aniferromagnetic coupling of Mn/Ni with Re via the superexchange mechanism.

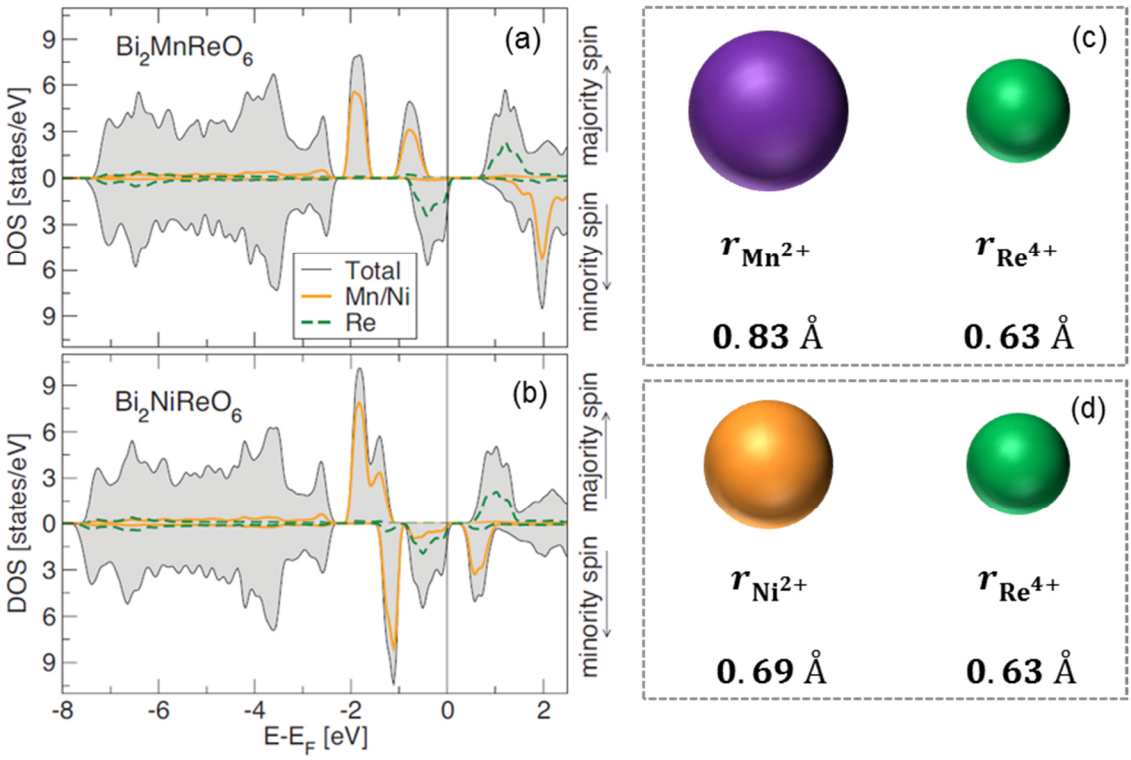

Fig. 4.1 Theoretically calculated Density of States (DOS) for the ferroelectric phase of Bi_2MnReO_6 (a) and Bi_2NiReO_6 (b) (Taken from Ref. [4]); Schematic comparison of the ionic radii of Mn^{2+} and Re^{4+} (c) and Ni^{2+} and Re^{4+} (d) in a 6 coordinate octahedral environment (Shannon ionic radii – Ref. [27]).

Fig. 4.1 shows the calculated density of states for the two compounds where an insulating gap above the 5*d* t_{2g} band is clearly found in both compounds similar to the case of Sr_2CrOsO_6. In spite of these interesting theoretical findings on the Mn^{2+}-Re^{4+}/$Ni^{2+}Re^{4+}$ combinations, there are as yet no reports in the literature on their experimental realization. One of the primary reasons for this being the general difficulty of stabilizing 3*d*-5*d* compounds which is made further complex by the presence of the volatile bismuth at the *A*-site. One way to overcome this challenge is to establish synthesis routes to analogous compounds. For instance, one

could replace Bi^{3+} at the *A*-site in part or full with an alternative, less-volatile trivalent cation such as La^{3+} (e.g.: Bi_2MnReO_6 – $Bi_xLa_{1-x}MnReO_6$ – La_2MnReO_6). *A*-site lanthanum based perovskites have been extensively studied in the thin film form and a technique such as PLD offers good possibility to stabilize such meta-stable compounds via non-equilibrium growth conditions and strain. Although La^{3+} cation lacks the stereochemically active lone pair as in Bi^{3+}, ferroelectricity may still be achieved non-conventionally also in Lanthanum based double perovskite thin films as shown by Takahashi *et al.* in Ref. [165].

Motivated by these findings, we undertook a combined theoretical and thin film approach to study two less explored double perovskites La_2MnReO_6 (LMRO) and La_2NiReO_6 (LNRO) for possible room temperature ferrimagnetic functionality. The two compounds were treated within density functional theory as well as dynamic mean field theory to identify the stable ground state structural parameters, their electronic structures and magnetic ordering. Based on the structural relaxations that yielded a monoclinic $P2_1/n$ lowest energy phase, a ferrimagnetic ordering of the Mn^{2+}/Ni^{2+} and Re^{4+} is expected similar to the case of BMRO and BNRO. Encouraged by these theoretical findings, we synthesized epitaxial LMRO and LNRO thin films by pulsed laser deposition on single crystalline (001) and (111) $SrTiO_3$ substrates. Ionic radii comparisons for the two 3*d*-5*d* cation combinations Mn-Re and Ni-Re has been schematically shown in Fig. 4.1 (c) and (d) respectively. In contrast to a similar schematic observed for Fe and Cr in Fig. 3.1 (c), a much larger and significant difference in ionic radii is observed for Mn-Re and Ni-Re. This is expected to more readily promote the spontaneously ordered state in LMRO and LNRO. Detailed structural investigations established phase purity, fully strained epitaxy and a high crystalline quality of the films. Microstructure was studied via advanced composition sensitive high resolution transmission electron microscopy imaging techniques. This was followed by an analysis of the functional properties of the two compounds. Collective evaluation of the results from structural, microstructural and functional characterizations confirmed the ordering of the *B*-site cations and consequently the desired stable and sizeable magnetization was attained.

4.2. Theory

Theoretical calculations in this chapter are an outcome of joint collaborative work between ATFT Division, TU Darmstadt and three other research groups/individuals namely: group of Prof. Dr. Marjana Ležaić (FZ Jülich), Prof. Dr. Hongbin Zhang (TU Darmstadt) and Dr. Adam Jakobsson (Formerly at FZ Jülich). Their individual contributions have been noted and acknowledged in the Preface section. As a starting point for the study of two 3*d*-5*d* double

perovskites La_2MnReO_6 (LMRO) and La_2NiReO_6 (LNRO), density functional theory was used to obtain the crystal and electronic structures of the two compounds. Structural optimizations were performed using the Vienna ab initio Simulation Package (VASP)[166–171], using projector augmented wave (PAW) potentials and PBEsol exchange-correlation functional.[172,173] The semicore *p*-states of Mn, Re and La were treated as the valence. An energy cutoff of 500 eV, and 6×6×6, 4×4×6 and 4×4×4 Γ-centered k-points meshes were used for the unit cells of 10, 20 and 40 atoms, correspondingly. Relativistic effects were not taken into account during the calculations. The relative stability of ferro- and ferrimagnetic states in the ground state structure was investigated within the full-potential augmented planewave code FLEUR [www.flapw.de]. For this purpose, a planewave cutoff of 4.2 bohr-1 and a 4×4×3 k-points mesh was employed.

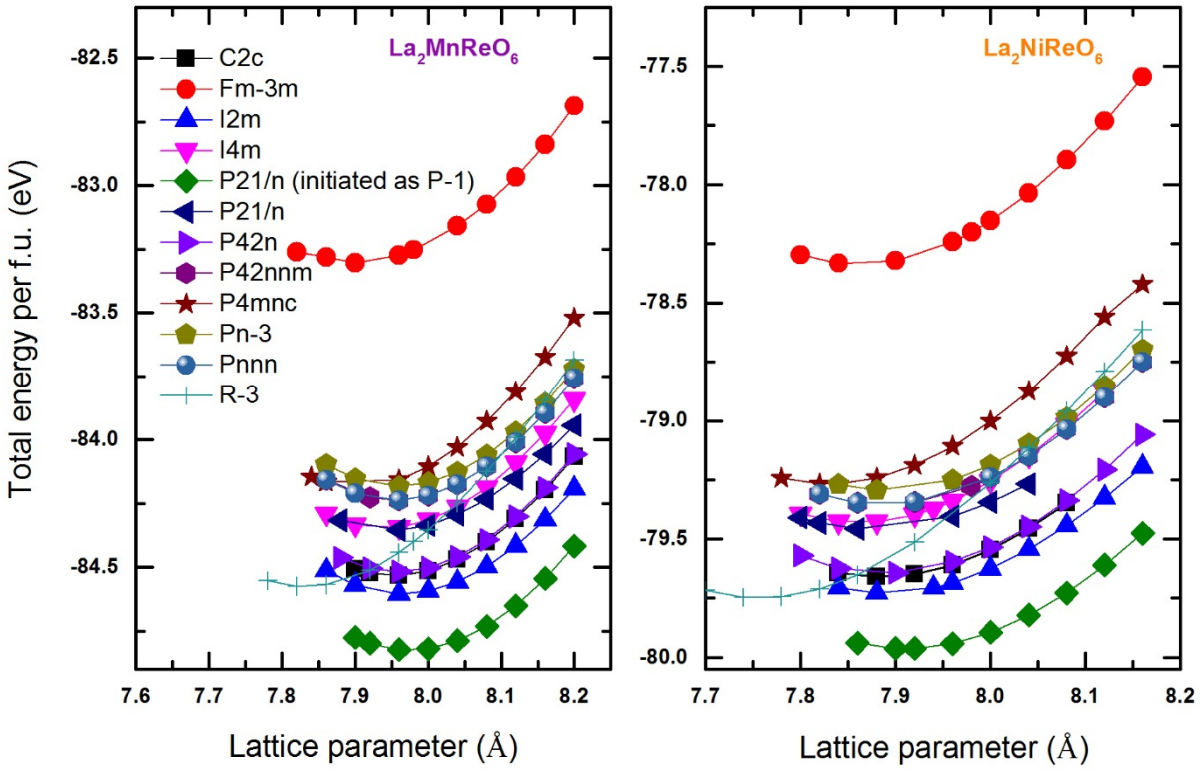

Fig. 4.2 Total energies of the centrosymmetric structures with different combinations of oxygen octahedra tilts in La_2MnReO_6 (a) and La_2NiReO_6 (b).

To find the ground-state structure for LMRO & LNRO we optimized 12 centrosymmetric unit cells with different combinations of tilts and rotations of the oxygen octahedra, which can

occur in double perovskites.[174] The results of these calculations, depicted in Fig. 4.2 (a) and (b), clearly show that the lowest-energy structure for both compounds is the monoclinic one with $P2_1/n$ symmetry (we note that a calculation initiated with P-1 symmetry also converged to the $P2_1/n$ structure and is therefore not shown separately in the figure). Only the total energies for the assumed ferrimagnetic ordering of Mn and Re moments are shown in this figure, since the ferromagnetic ordering was calculated to have essentially higher total energies, by 433 meV per formula unit (f.u.) in the ground-state structure. The ground-state structure is characterized by $a^- b^- c^+$ oxygen tilts, in Glazer notation,[8] and a 3-dimensional checkerboard or rock-salt type arrangement of Mn^{2+}/Ni^{2+} and Re^{4+} cations. The significant difference in the ionic size of the B-site elements and also the difference in their formal charge is expected to help stabilize their ordering at the B-site.

Table 4.3 Ground-state structural parameters for the LMRO and LNRO double perovskites as calculated with VASP. Lattice constants are in Å.

		LMRO $a = 5.512$; $b = 5.796$; $c = 7.894$ $\beta = 90.04^\circ$			**LNRO** $a = 5.489$; $b = 5.782$; $c = 7.826$ $\beta = 90.63^\circ$		
Atom	Wyckoff Position	***x***	***y***	***z***	***x***	***y***	***z***
La	4e	0.4858	0.9426	0.2513	0.4843	0.9374	0.2510
Mn/Ni	2d	0.0	0.0	0.0	0.0	0.0	0.0
Re	2b	0.0	0.0	0.5	0.0	0.0	0.5
O1	4e	0.9067	0.0302	0.2532	0.9064	0.0261	0.2518
O2	4e	0.3090	0.2077	0.0503	0.3118	0.2095	0.0501
O3	4e	0.7032	0.8023	0.5474	0.7016	0.8062	0.5465

Tthe optimized bulk structural parameters for the two compounds have been listed in table 4.3. The VESTA visualization program was used to create 3-dimensional illustrations of the as calculated crystal structures for the two compounds. A pseudo-cubic view of these structures has been displayed in Fig. 4.3 (a) and (b). Structural illustrations of the as calculated monoclinic unit-cells are provided in Appendix B.

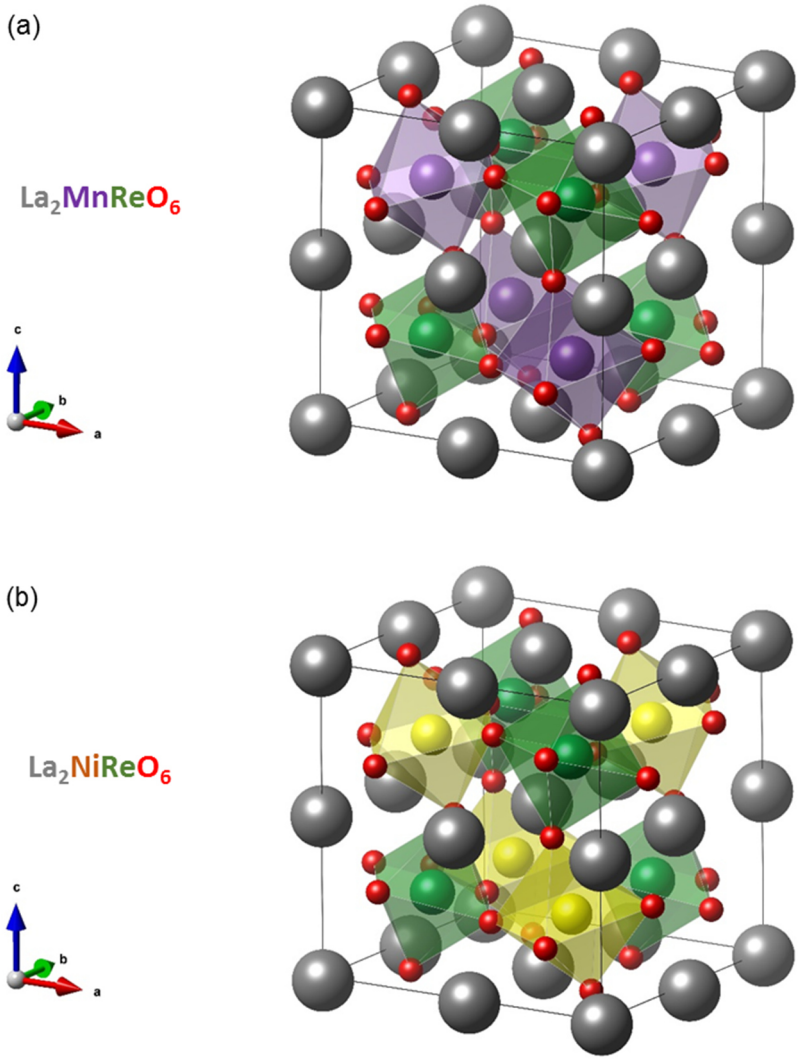

Fig. 4.3 Schematic crystal structures of the theoretically derived lowest energy P21/n configuration for LMRO (a) and LNRO (b) constructed using the VESTA visualization program[14] (shown in a pseudo-cubic representation).

The as calculated zero Kelvin density of states for LMRO and LNRO are shown in Fig. 4.4 (a) and (b) respectively. As it is commonly known, in an octahedral environment, the *d*-manifold splits into three-fold degenerate t_{2g} states with lower energy and two-fold degenerate e_g states with higher energy. Therefore, the highest occupied states of the majority (minority) spin are the e_g states of Mn (t_{2g} states of Re) in LMRO and e_g states of Ni (t_{2g} states of Re) in LNRO. A crystal-field induced gap with a width of $\sim$ 1 eV was clearly observed for both compounds. Thus the prospect of an insulating ground state appears promising for possible multiferroic functionalties. In LMRO, a ferrimagnetic spin arrangement of the Mn^{2+} ($3d^5$:$t_{2g}^3 e_g^2$) and Re^{4+}

($5d^3$:$t_{2g}^3 e_g^0$) sub-lattices should yield a spin-only magnetic moment of 2 μ_B/f.u. (Fig. 4.4 (c)). Similarly 1 μ_B/f.u. as is the expected spin only moment in LNRO by again an anti-parallel spin arrangement of the Ni^{2+} ($3d^8$:$t_{2g}^6 e_g^2$) and Re^{4+} ($5d^3$:$t_{2g}^3 e_g^0$) sub-lattices (Fig. 4.4 (d)). Treatment of the compounds within the dynamical mean field theory (DMFT) also showed a consistent picture of the electronic structures for both LMRO and LNRO. Precise estimations of the total magnetic moment for a ferrimagnetic order including spin-orbit coupling yielded 2.9 μ_B/f.u. and 0.80 μ_B/f.u. for LMRO and LNRO respectively.

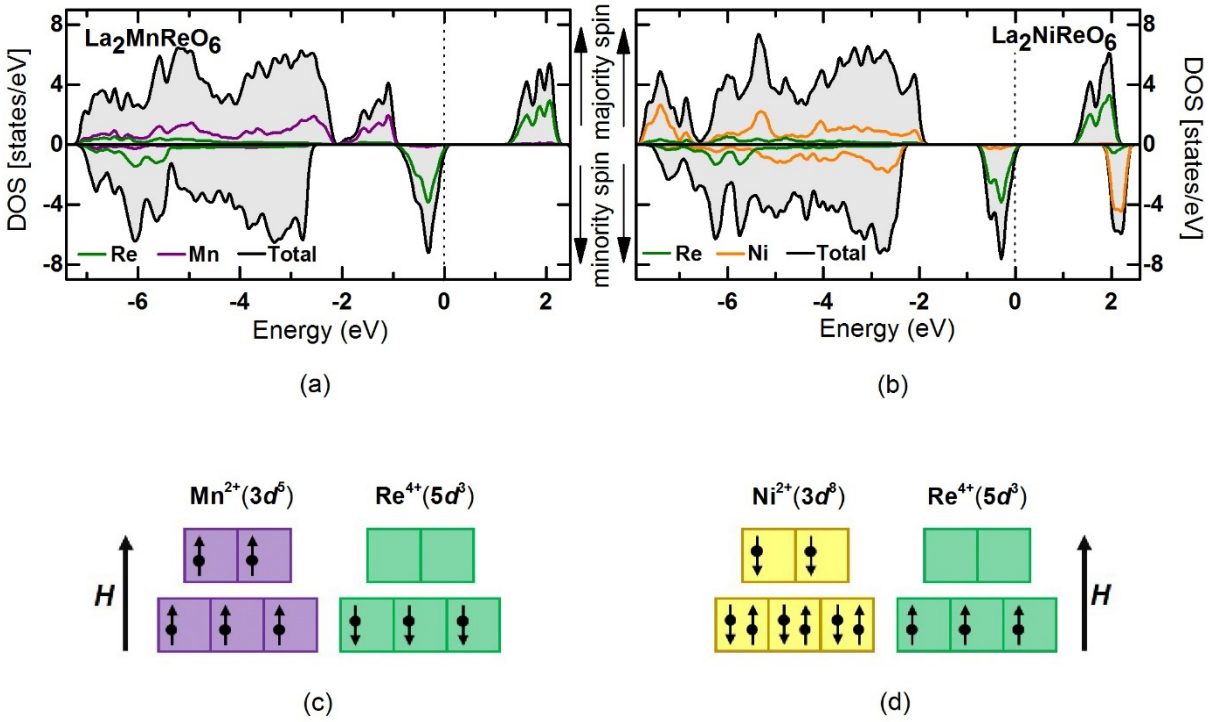

Fig. 4.4 Ground state spin-polarized density of states plots for bulk (a) LMRO and (b) LNRO, both compounds behaving as insulating phases with ferrimagnetic ordering; The *d*-shell spin alignment of Mn^{2+} ($3d^5$) – Re^{4+} ($5d^3$) in LMRO (c) and Ni^{2+} ($3d^8$) – Re^{4+} ($5d^3$) in LNRO (d).

4.3. Target preparation

Similar to the case of BFCO in chapter 3, the goal of the target preparation here was to obtain dense ceramic pellets to be used as PLD targets for growth of LMRO and LNRO films. A similar *A*:*B*:*B'* stoichiometry of La:Mn:Re = La:Ni:Re = 2:1:1 was desired for both targets. However, inclusion of rhenium as one of the cations presents a specific challenge. Although metallic Rhenium has quite a high melting point (>3180 K), in the presence of oxygen at

elevated temperature, it undergoes oxidation quite easily.[175] Apart from its stable oxidation state of 4+ (corresponding oxide: ReO_2), Rhenium can also get to higher oxidation states of 6+ and 7+ (corresponding to ReO_3 and Re_2O_7) quite easily in the presence of oxygen at elevated temperatures. Once it forms the Re_2O_7 oxide, it becomes difficult to handle as Re_2O_7 sublimes at relatively low temperatures (~300˚C).[176] Thus a suitable method had to be chosen to avoid the oxidation of rhenium to its 7+ state. Consequently an oxygen-exposure free method as elaborated in section 2.1.2 was adopted where powder handing was done inside a glove box and calcination/sintering were performed within self-prepared evacuated quartz tube enclosures. It is to be noted that significant time/efforts and repeated attempts were made via a trial and error route to identify best practices and conditions to obtain dense-stable and stoichiometric PLD targets in this case.

In the first step, commercially purchased powder of lanthanum oxide (La_2O_3 99.99 %, Alfa Aesar) was dried overnight in a muffle furnace at 1000 ˚C in a standard muffle furnace in air. This ensures removal of absorbed moisture which La_2O_3 was found to be highly prone to. The dried La_2O_3 powder was then taken in to the glove box. Powders of Manganese oxide (MnO, 99.99% Alfa Aesar), nickel oxide (NiO, 99.99 % Alfa Aesar) and rhenium oxide (ReO_2, 99.9% Alfa Aesar) were also commercially purchased and stored within the glove box. Stoichiometric amounts of the powders were weighed individually in accordance with the following equations:

$$La_2O_3 + MnO + ReO_2 \longrightarrow La_2MnReO_6$$

$$La_2O_3 + NiO + ReO_2 \longrightarrow La_2NiReO_6$$

The powders were then grinded in a mortar within the glove-box by hand for up-to 1 hour to obtain a homogeneous mixture. The mixed powders were then pressed in a cylindrical dye to form the green compact of the pellet. The green compact is then carefully inserted into a one side sealed quartz tube. The quartz tube is then evacuated and sealed at the other end by melting under a laboratory oxy-propane torch (Fig. 4.5 (a)). A photograph of the pressed pellet in the quartz tube after evacuation and sealing is shown in Fig. 4.5 (b).

(a)

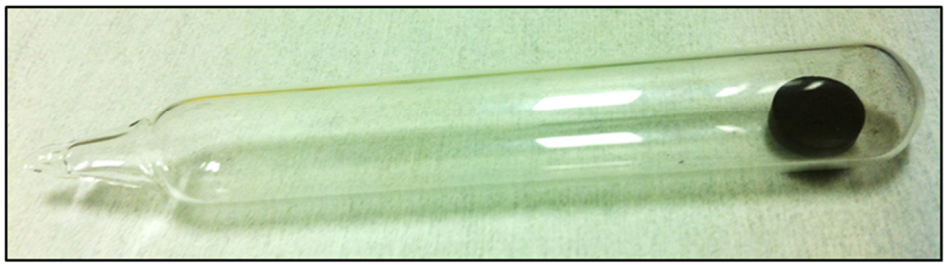

(b)

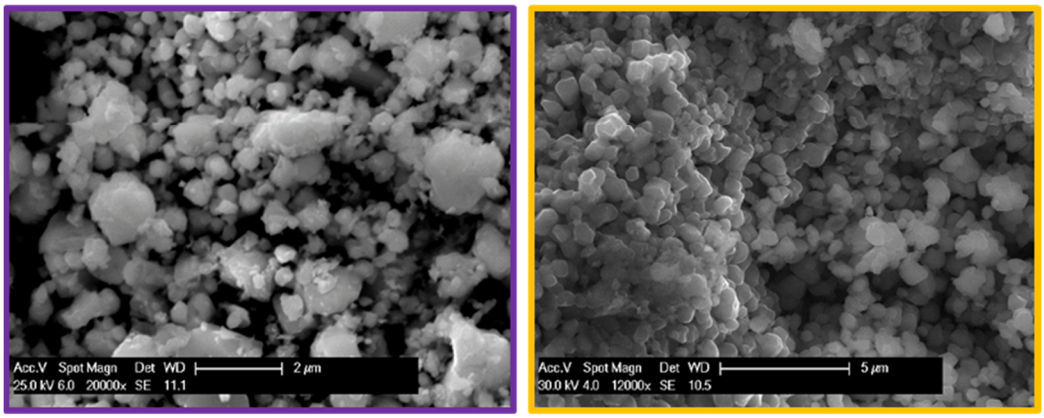

(c) (d)

Fig. 4.5 (a) Photograph showing use of a laboratory based Oxy-Propane Torch used for sealing of the quartz tubes; (b) Photograph showing evacuated sealed quartz tube with a pressed pellet; SEM images of the top surface of the sintered LMRO pellet (c) and LNRO pellet (d).

The quartz tube and the enclosed pellet were then placed in a muffle furnace and fired at 800˚C for a duration of 24 hours and cooled back to room temperature. The sealed quartz tube was once again opened by melting a hole at one end of the tube and the now darker coloured partially reacted pellet was withdrawn. The pellet was once again crushed and

grinded in a mortar to form a homogenous powder. The above process of sintering in a sealed quartz tube was repeated for a second time once again for 24 hours at 800˚C to achieve a further reaction of the powder particles. At the end of the second sintering, the pellet was extracted out of the tube and observed to be dark in appearance, mechanically stable, hard and visually free from any macroscopic cracks. Similar procedure was performed to obtain pellets for both LMRO and LNRO targets.

The so obtained pellets were then subjected to characterization via XRD and SEM-EDS. XRD measurements (not-shown) showed the presence of a mixture of several phases. Considering the metastable nature of the two compounds, ambient pressure synthesis is not expected to yield phase pure LMRO and LNRO in bulk. Nevertheless, as was in the previous case of BFCO in chapter 3, the goal of the PLD target fabrication process was to create mechanically stable and dense pellets with a definite stoichiometry or elemental ratio of the component cations and not necessarily to obtain a pure phase. SEM images of the surface of the as prepared LMRO and LNRO pellets recorded using a secondary electron detector is shown in Fig. 4.5 (c) and (d) respectively. In LMRO, a larger spread of grain sizes can be observed in the range of 0.5 microns to 2. 0 microns in diameter. On the other hand, a more homogenous grain sizes with an average diameter in range of 1.0 micron was observed in LNRO. These differences might arise due to differences in grinding and handling procedures during the synthesis steps. Most importantly the pellets appeared to be reasonably dense and no observable cracks were found on the surface.

Table 4.4 Summary of the quantitative EDS analyses performed on the as prepared LMRO target using the EDS Genesys software.

Element/Peak	Wt. %	At. %	Z	A	F
Mn-K	10.32	**24.33**	1.1168	0.6504	1.0126
Re-L	33.61	**23.38**	0.9659	0.9197	1.0000
La-L	56.07	**52.29**	0.9873	0.8845	1.0135

Table 4.5 Summary of the quantitative EDS analyses performed on the as prepared LNRO target using the EDS Genesys software.

Element/Peak	Wt. %	At. %	Z	A	F
Ni-K	12.39	**27.02**	1.1606	0.7772	1.0341
Re-L	33.19	**23.82**	0.9564	0.9124	1.0000
La-L	54.42	**50.16**	0.9778	0.8834	1.0116

Qualitative and quantitative chemical analysis of the two pellets were performed using an in-situ EDS detector fitted to the in-house XL-30 FEG SEM. Using an acceleration voltage of 30 kV, EDS spectrums were collected for both compounds. The collected EDS spectra (not shown) did not show indications of any chemical impurities. All peaks could be identified to be coming only from La, Mn, Ni, Re or O. It is known that the intensity of the peaks in the EDS spectrum contain quantitative information of the corresponding elements. An in-built software algorithm of the EDS system was used to first subtract a background intensity arising due to the Bremsstrahlung radiation. Thereafter the algorithm performs a fitting analysis of the peaks and uses the integrated area of the peaks to internally calculate the concentrations of the individual elements.

The output of the quantitative analysis for LMRO and LNRO are shown in Table 4.4 and 4.5 respectively. The columns marked in red show the atomic concentrations for Mn, Re, La and Ni, Re, La in the two pellets to be 24.33 %, 23.38 %, 52.29 % and 27.02 %, 23.82 % and 50.16 % respectively. Considering that the EDS analysis contains an error bar of up to 5 %, the two prepared targets for LMRO and LNRO growth are both found to have the intended 2:1:1 stoichiometric ratio for the *A*:*B*:*B'* cations within the limits of error of EDS analysis.

The pellets were then cleaned under a stream of pressurized air to remove any dust particles and later glued onto a standard metallic target holder for further use in PLD using a commercially available organic based silver glue.

4.4. Thin film growth and characterization

Over the past decade, pulsed laser deposition has been well established as an effective technique for thin film growth and a way to stabilize also those materials that have been previously inaccessible in bulk due to their meta-stable nature. The key advantage of the PLD process is its ability to provide a stoichiometric transfer of elements from the target on to the substrate. It is thus a best suited technique to epitaxially stabilize multi-cation systems such as La_2MnReO_6 and La_2NiReO_6. In order to roughly identify the good range of parameters that would be suitable for the growth of LMRO and LNRO film, one can construct a pressure-temperature phase diagram in accordance with the equation:

$$\log P(O_2) = \alpha - \beta T^{-1}$$

Where α and β are calculated constants from the standard enthalpy and entropy of formation of compounds. We plot the points for various accessible pressures and temperatures for all possible oxidation states of the component cations. The curves so obtained are effectively the boundaries of stability between higher and lower oxidation states across a redox equilibrium. The factors α and β for different redox systems of all cations involved in this study as taken from Ref. [128] are listed in Appendix 1. Such a pressure temperature stability diagram can provide good indications on whether an oxidizing or reducing atmosphere is suited for a particular cationic system and if so, how strongly oxidizing or reducing. Besides an approximate idea of the good growth temperature range can also be extracted. Fig. 4.6 (a) and (b) show the as constructed *P-T* phase diagrams for LMRO and LNRO respectively. Both cases show a rather similar range of thermodynamic stability (shaded in Red) which in terms of oxygen partial pressure is mainly governed by boundaries of reduction of Re^{4+} to metallic state and its oxidation to the 6+ state. In spite of these limits, what is promising to note is the possible co-existence of a stable 2+ region for both Mn and Ni overlapping with the Re^{4+} region. This is primarily a promising sign that the 2+ - 4+ states for the two 3*d*-5*d* cationic systems is thermodynamically favorable and achievable. In addition to the thermodynamic equilibrium boundaries, what further narrows down the possible P-T region is the general limits of standard working pressures and temperatures accessible in the PLD system. Following the PLD growth literatures for similar material systems where there is greater tendency of a cation (such as Re^{4+}) to go to multiple higher oxidation states, reductive oxygen pressure regimes have been successfully employed. These regimes often lie in range of 10^{-2} Torr at the upper limit and vacuum growth or base pressure limit around 10^{-8} Torr for the lower boundary (marked by horizontal red-dashed lines). Standard temperature boundaries for high quality crystalline growth in PLD often lie between 500˚C and 900˚C (or higher).

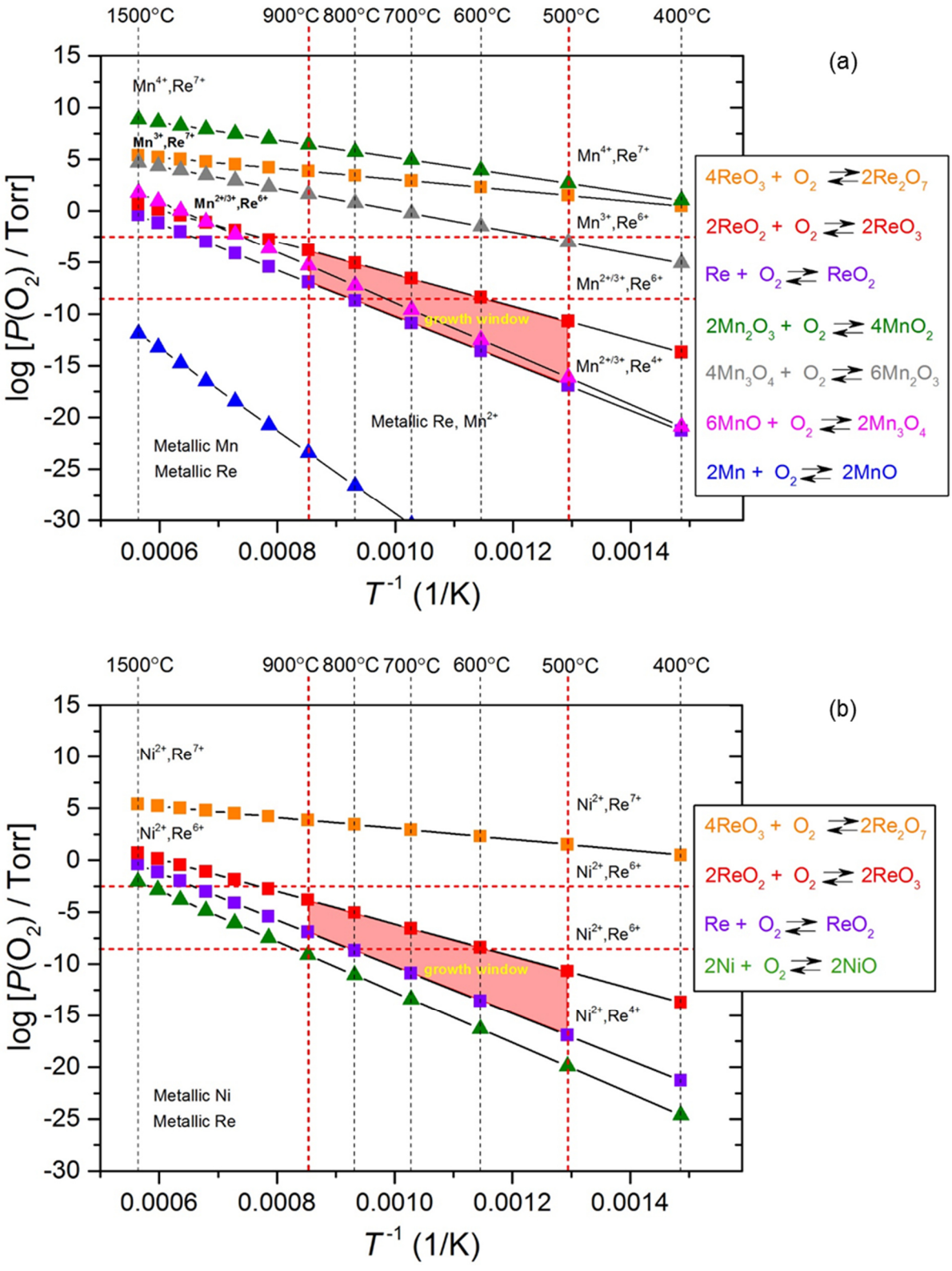

Fig. 4.6 Thermodynamic phase stability diagram for different oxidation states of Mn-Re (a) and Ni-Re (b) (Derived based on inputs from Ref. [128]).

This has been marked by the vertical red-dashed lines. Based on these theromodynamic and technical boundary condition, we were able to narrow down the growth window for experimental trails. However, one needs to keep in mind the fact that PLD involves a kinetically dominant process due to which optimum conditions may eventually be slightly shifted from the thermodynamically determined values.

After approximately identifying the growth window from the above phase diagrams, individual sets of studies were undertaken towards the thin film growth of LMRO and LNRO. In case of LMRO, film growth was performed by A. Kulkarni as part of a Master thesis project supervised within this work (Ref. [177]). For both LMRO and LNRO, several films were grown spanning across the identified growth window (Pressure range: 10^{-2} to 10^{-6} Torr; Temperature range: 500 - 900˚C. Optimization of growth parameters were done based on phase purity and crystalline quality of the films. Single crystalline cubic strontium titanate (a = 3.905 Å) was chosen as a substrate. From the theoretically derived monoclinic structures for bulk LMRO and LNRO (Fig. 4.3 (a) and (b)), their pseudocubic Mn-Re and Ni-Re lattice parameters were found to be in the range of 3.94 to 3.99 Å along the in-plane axes. Considering these lattice parameters, a lattice mismatch ranging up to 2.1 % can be expected. Thus an in-plane compressive strain is expected for the heteroepitaxy of both LMRO and LNRO on STO. Other commercially available substrates such as $DyScO_3$ (~3.95 Å), $GdScO_3$ (~3.97 Å) and $SmScO_3$ (~3.98 Å) have comparatively closer in-plane lattice parameters to the calculated bulk LMRO and LNRO parameters. However, due to their paramagnetic nature, magnetic characterization of the film with laboratory techniques such as SQUID magnetometry becomes difficult as the large paramagnetic moment overshadows the small magnitude magnetic signal coming from the film material. This is one of the important reasons behind choosing the diamagnetic STO substrate, where the diamagnetic moment arising from the substrate can be easily subtracted from the film signal. Growth of LMRO and LNRO films on alternative substrate materials was not performed within the scope of this work and is certainly an interesting topic for future studies. In addition to pressure and temperature another important PLD parameter namely fluence or the laser energy density was also varied in the range of 0.5 to 2 J/cm^2 during the optimization runs. At the end, a fluence of 0.8 J/cm^2, a repetition rate of 2 Hz, substrate temperature of ~750 ˚C and an oxygen background pressure 10^{-5} Torr were found to be the most optimum growth conditions for both LMRO and LNRO (Table. 4.6). Based on the observations made from the phase diagrams in Fig. 4.6 (a) and (b), it is not unusual that films of both materials grow best at similar pressure-temperature conditions. Besides, the only differing factor between LMRO and LNRO is the *B*-site cation: Mn or Ni. Since both these belong to the same 3*d* period with only a small difference in their atomic

masses, will have similar ablation characteristics, and therefore does not greatly differ in terms of their required optimum fluences.

Table 4.6 Optimized parameters for PLD growth of epitaxial LMRO - LNRO thin films on single crystalline STO substrates.

Optimized growth parameters for LMRO & LNRO thin films	
PLD Parameter	Optimum value
Background pressure	1 x 10^{-5} Torr of Oxygen
Oxygen Flow	1 sccm
Substrate temperature	750˚C
Laser fluence	0.8 J cm^{-2}
Laser pulse frequency	2 Hz
Excimer laser used	248 nm KrF laser
Laser spot size	3 mm^2

Fig. 4.7 shows results of basic structural characterization performed on a representative LMRO thin film grown on (001) oriented STO substrate grown under the optimized growth conditions. The STO substrates used for the depositions were subjected to the established buffered-HF acid etching and subsequent annealing procedure as discussed in section 2.1.1. in order to obtain an atomically smooth single terminated surface. Fig. 4.7 (a) corresponds to an XRD out-of-plane $2\theta - \omega$ scan of the LMRO film. From the graph, it can be noted that the peaks corresponding to the LMRO film appear at lower 2θ values than the corresponding substrate peaks. This indicates a larger out-of-plane lattice constant for the LMRO film as compared to the substrate. This is consistent with the in-plane compressive strain expected for the heteroepitaxy on STO. For the film, only peaks corresponding to the (00l) family are seen, thereby indicating that the LMRO films grow with a preferential (00l) orientation on the (001) oriented STO substrate. Within the resolution limit of the diffractometer, no other peaks corresponding parasitic phases or mixed orientations were observed in the films. From the 2θ values of the LMRO (00l) reflections, an out-of-plane pseudo-cubic lattice parameter (c_{pc}) of the LMRO film was found to be 4.02 Å. Fig. 4.7 (b) shows a RHEED pattern recorded from the surface of the LMRO film at the end of the growth process. A streaky pattern was observed from the start of the growth till end.

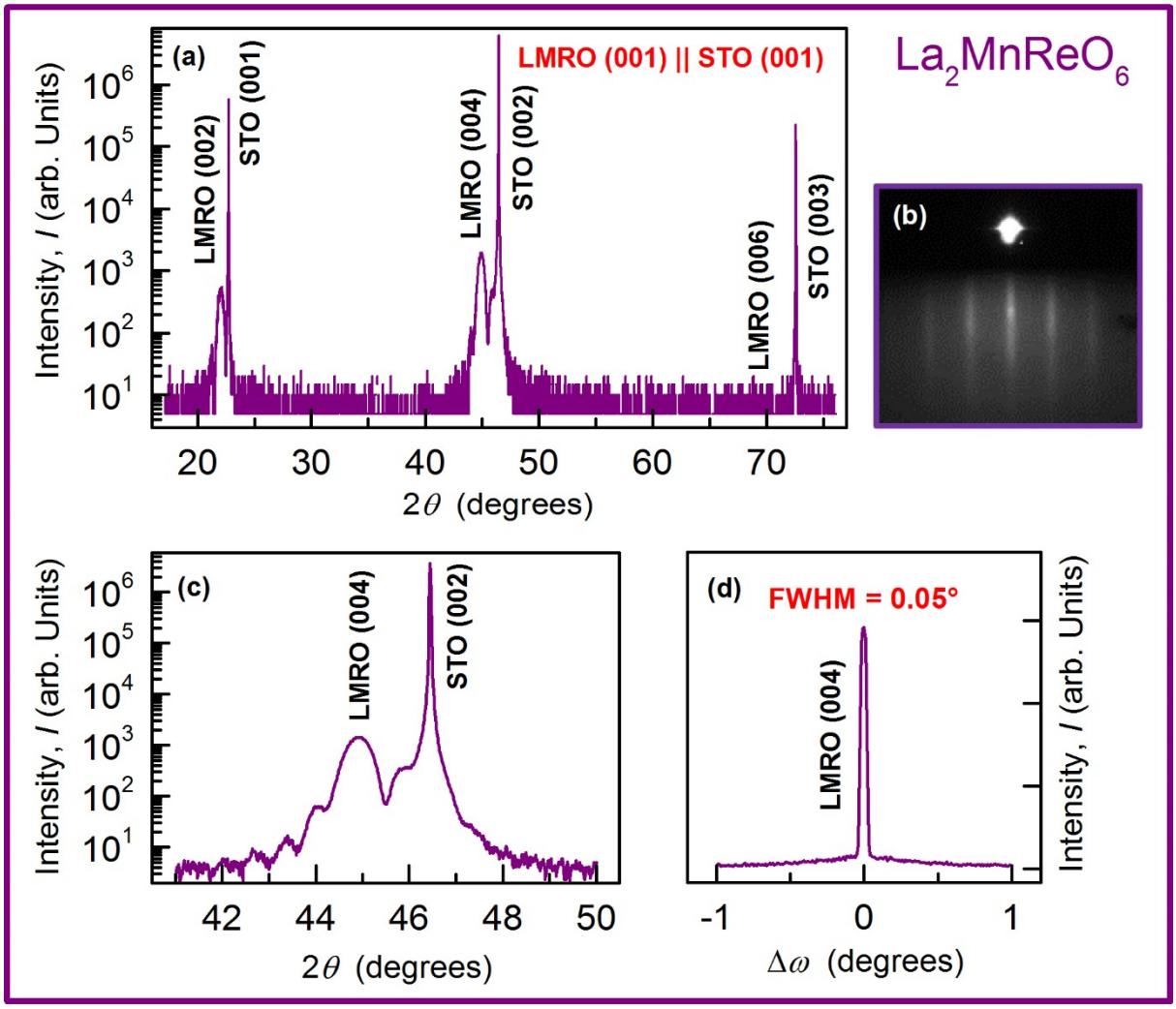

Fig. 4.7 (a) $\theta - 2\theta$ XRD pattern of a 16 nm think LMRO film grown on STO (001) substrate as measured with a Cu K_α source; (b) RHEED pattern recorded for the surface of the as grown LMRO thin film towards the end of the deposition sequence; (c) Enlarged view of the $\theta - 2\theta$ XRD pattern around the LMRO (004) reflection; (d) Rocking-curve (ω-scan) of the LMRO (004) reflection which has a FWHM of 0.05°.[i]

This indicates a stepped-flow growth mode for the LMRO films. An enlarged view of the LMRO (004) peak (Fig. 4.7 (c)) indicates the presence of Laue oscillations in the vicinity of the main peak suggesting a coherently grown film. From the periodicity of the oscillations, thickness of the film could be estimated according to the equation:

$$t(\text{Å}) = \frac{\lambda(\text{Å})}{2 \cdot [\sin\theta_n - \sin\theta_{n+1}]}$$

[i] Fabrication of LMRO films and some LMRO measurements (XRD, SQUID magnetometry, R-T) were performed by A. Kulkarni – a Masters student supervised under this project during WiSe: 2014-15.

Where λ is the wavelength of the X-ray radiation. θ_n and θ_{n+1} correspond to two consecutive Laue oscillation peaks, which are to be taken in radians. A calculated thickness value of 16 nm was consistent with the thickness calculated from the Fourier transform of the oscillations in an X-ray reflectivity measurements (XRR) on the same film. The XRR determined density of the film was found to be 7.05 g/cc which is close to the estimated theoretical density of 7.73 g/cc for LMRO. Fig. 4.7 (d) shows a rocking curve scan performed on the LMRO (004) reflection which had a narrow full-width at half maximum (FWHM) = 0.05˚. Thus the film can be noted to have a low mosiacity.

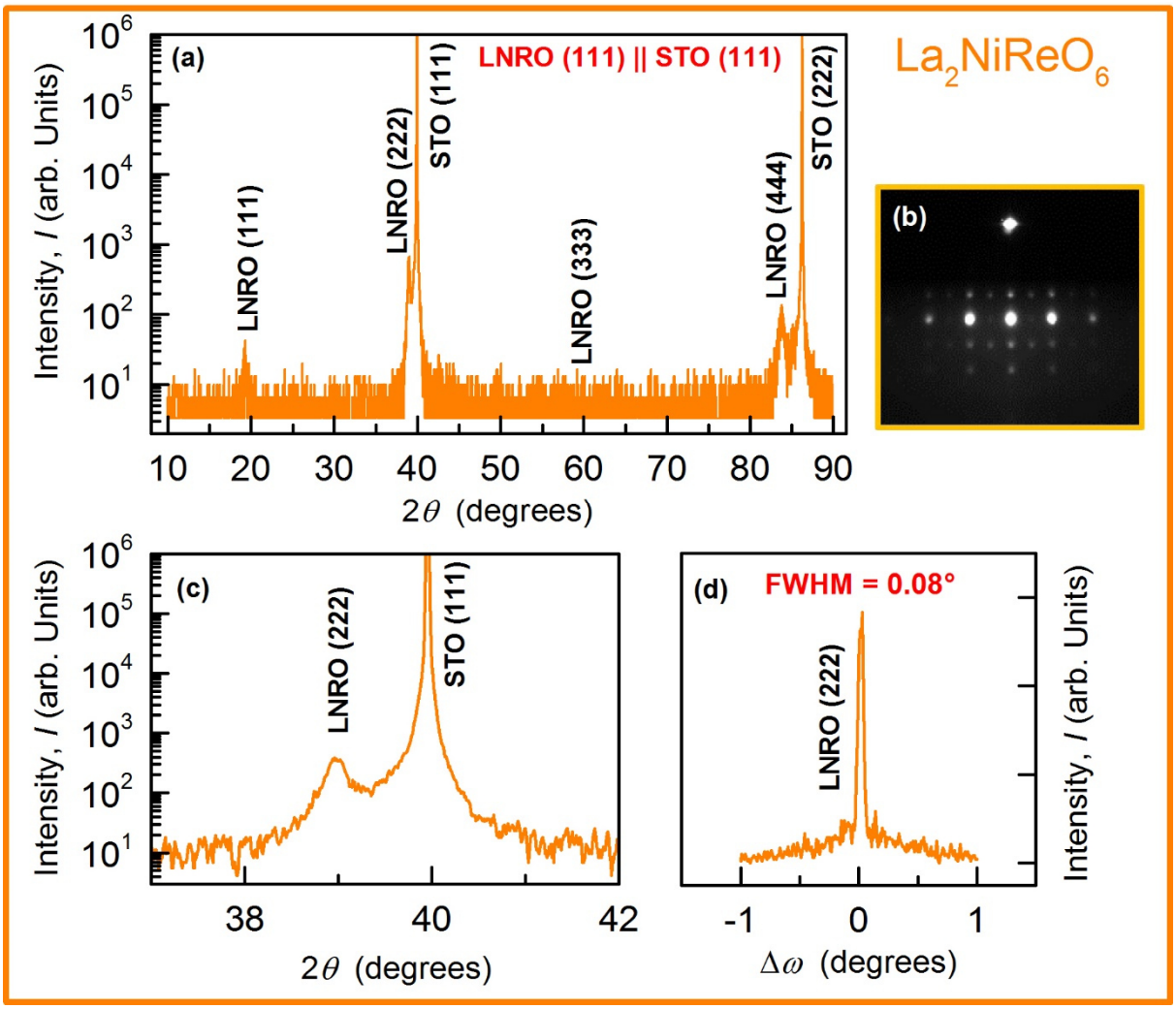

Fig. 4.8 (a) $\theta - 2\theta$ XRD pattern of a 40 nm think LNRO film grown on STO (111) substrate as measured with a Cu K_α source; (b) RHEED pattern recorded for the surface of the as grown LNRO thin film towards the end of the deposition sequence; (c) Enlarged view of the $\theta - 2\theta$ XRD pattern around the LNRO (222) reflection; (d) Rocking-curve (ω-scan) of the LNRO (222) reflection which has a FWHM of 0.08˚.

Similarly Fig. 4.8 shows set of basic structural characterization performed on an LNRO thin film deposited at the optimized growth conditions. An XRD $2\theta - \omega$ scan of the LNRO film on a (111) oriented single crystalline $SrTiO_3$ (STO) substrate is shown in Fig. 4.8 (a). Only peaks corresponding to the (111) orientation of the LNRO film can be seen which confirms a single oriented growth. The LNRO film was found to have a $d_{(222)} = 2.31$ Å in comparison to the corresponding $d_{(111)} = 2.25$ Å of the STO substrate. Thickness of the film as calculated from XRR was found to be 40 nm. From the critical angle for total reflection in the XRR scan, the density of the LNRO was found to be 7.18 g/cc in comparison to the calculated theoretical density of 8.12 g/cc. Within the resolution limit of the XRD system, there were no stray peaks or reflections observed, thereby indicating a phase purity of the thin film. A RHEED pattern recorded by directing an intense focused electron beam on the LNRO film surface during the PLD growth of the film, showed a spotty pattern all though the growth process. This indicates that the Volmer-Weber type or the growth by island formation is the active growth mechanism in this case. In comparison to LMRO, a (111) oriented STO substrate was preferred to stabilize epitaxial LNRO thin films instead of the using (001) substrate. This is because repeated attempts to grow LNRO on (001) oriented STO led to multiple orientations or textured films. A magnified view of the LNRO (222) reflection is shown in Fig.4.8 (c). In comparison to LMRO films, LNRO films did not show any Laue oscillations indicating a comparatively inferior crystalline quality of the film. This is also corroborated by the rocking curve scan (Fig. 4.8 (d)) performed on the LNRO (222) reflection which showed a comparatively higher FWHM of 0.08˚ indicating higher mosiacity as compared to LMRO films. It is also observed that the rocking curve scan for LNRO has a comparatively larger diffuse background intensity which corresponds to a higher defect / dislocation density in the film which can be expected as an ideal 2D layer-by-layer growth mode was not achieved in the case of LNRO. From the literature on heteroepitaxy of various perovskite materials, it is noted that growth of very high quality epitaxial films on (111) oriented STO substrates is essentially challenging due to the polar nature of its surface.[178,179] In this context, the achieved LNRO film quality via heteroepitaxy on STO (111) surface can be considered fair.

In addition to the above basic structural characterization, XRD reciprocal space mapping (RSM) was carried out to investigate in-plane lattice parameters and strain state of the LMRO and LNRO films. A schematic crystal structure of the La_2BReO_6 (B = Mn/Ni) compounds in a pseudocubic form is displayed in Fig. 4.9 (b) for visualization, wherein the MnO_3^{4-} (Lavender) or NiO_3^{4-} (Yellow) octahedra are arranged alternatingly with the ReO_3^{2-} (Green) octahedra in a checkerboard fashion resulting in the rock-salt type of ordering. Fig. 4.9 (a) shows an RSM intensity contour map recorded in the vicinity of the STO (103) reflection. As is evident in the

plot, the substrate and the LMRO film peaks are aligned along the vertical axis at Q_x = 0.2561 Å^{-1}. The corresponding in place d-spacing obtained from the reciprocal lattice was found to be ~3.905 Å which is the cubic lattice parameter of STO. Thus the LMRO film appears to be have an in-plane lattice fixed to that of STO. RSMs were also recorded around the STO ($\bar{1}03$), (013) and ($0\bar{1}3$) reflections (not shown). All 4 measurements showed a similar contour pattern with equivalent peak positions on both the parallel and perpendicular axes, thereby ruling out any orthorhombic distortions in the film. Thus from the collective structural analysis, it can be inferred that the LMRO films grown on the (00l) oriented substrates are fully strained across the thickness of the film with in-plane lattice parameters locked-in to that of the cubic STO lattice parameter. The out-of-plane lattice parameter is larger as compared to that of STO thereby yielding a tetragonal like structure of the LMRO thin films. The epitaxy of the LMRO film can thus be concluded to be cube-on-cube type with no in-plane rotations thereby giving an epitaxial relationship of: (001)[100]LMRO || (001)[100]STO.

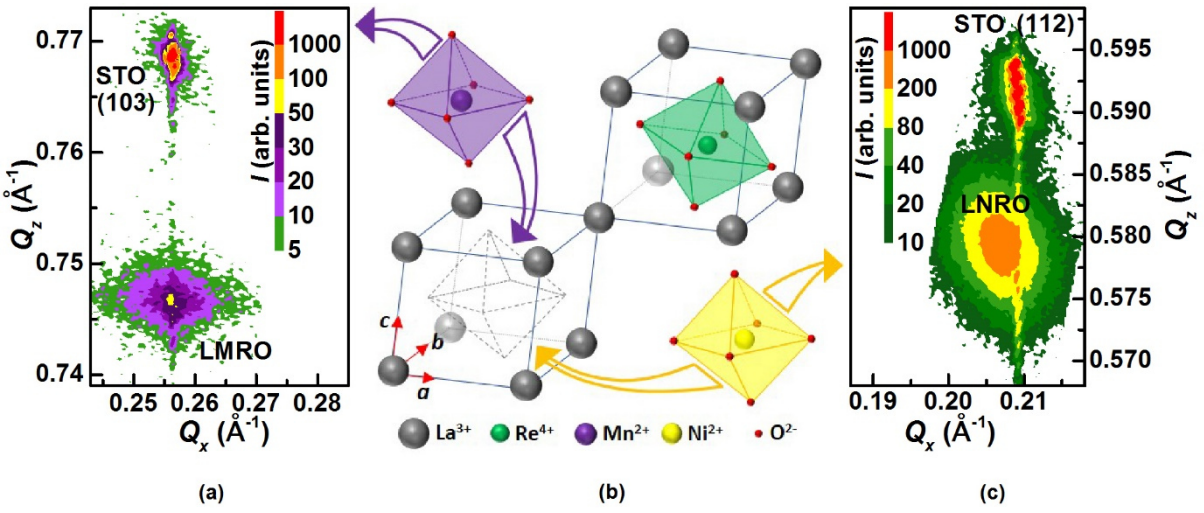

Fig. 4.9 (a) An XRD-reciprocal space map (RSM) recorded around the (103) reflection of the (001) oriented STO substrate with an epitaxial LMRO film; (b) Pseudocubic representation of double perovskite La_2MReO_6 (M = Mn or Ni), wherein the MnO_3^{4-} (Lavender) or NiO_3^{4-} (Yellow) octahedra are arranged alternatingly with the ReO_3^{2-} (Green) octahedra in a checkerboard fashion resulting in the rock-salt type of ordering; (c) XRD-RSM recorded around the (112) reflection of the (111) oriented STO substrate with an epitaxial LNRO film.

Similarly a reciprocal space map recorded for the 40 nm thick LNRO film grown on a [111] oriented STO substrate is shown in Fig. 4.9 (c). The intensity contour map was recorded in the vicinity of the STO (112) reflection. The LNRO film peak was observed to be more diffuse and stretched across a range of Q_x values that can be indicative of more defects and a possible

gradient in the strain state of the film. The LNRO film peak and the STO substrate peak also do not appear to be aligned along the vertical axis. Taking the centered value of the LNRO film peak, the film was found to have a smaller $Q_x = 0.2068\,\text{Å}^{-1}$ as compared to the STO substrate $Q_x = 0.2091\,\text{Å}^{-1}$. This can be indicative of a partially relaxed state of LNRO films on the (111) STO substrate.

Collectively from the above structural characterizations, it is encouraging to note that: in spite of their meta-stable nature, an epitaxial phase stabilization could be achieved for both LMRO and LNRO using the thin film approach. Among the two, it was observed from the optimization studies that, a reproducible 2D growth and higher crystalline quality could be better achieved in LMRO than in LNRO.

4.5. Investigation of chemical order

In the preceding chapters, we have established the importance of the *B*-site chemical ordering in double perovskite thin films in order to achieve functionalities such as magnetism. Magnetism in double perovskites is commonly achieved by the coupling of the *B* and *B'* cation via exchange interactions along the *B*-O-*B'* chains. Rock-salt type of ordering where the *B* and *B'* cations occupy their octahedrally coordinated sites in a alternating fashion in all three directions allows for such a type of *B*-O-*B'* interactions. As it was observed in chapter 3, such a type of B-site order creates alternating pattern of planes along pseudo-cubic [111] direction which leads to creation of a superstructure or doubling of the unit cell. In order to check for the presence of such a superstructure we grew a film of LMRO on [111] oriented STO substrate via PLD. Figure 4.10 (a) shows $2\theta - \omega$ scan of the [111] oriented LMRO film. In addition to the (*hhh*) peaks of the STO substrate, we also observed the (*hhh*) peaks corresponding to the LMRO film. In addition to the fundamental perovskite sub-cell (222) reflection, a distinct peak corresponding to the expected super-structure or unit-cell doubling was also observed. The superstructure peak was found at a 2θ value of 19.27° which as per Bragg's condition, corresponds to a d – spacing of 4.60 Å, which is twice the d – spacing corresponding to the fundamental (222) peak of 2.30 Å. Similarly $2\theta - \omega$ scan of the (111) oriented LNRO film (same sample as in section 1.4) is once again plotted together in Fig. 4.10 (b) for comparison. As in the case of LMRO, the [111] scan of the LNRO film also shows presence of a distinct superstructure peak at a nearly similar 2θ value of 19.24 °. Apart from the odd and even (*hhh*) peaks, no other peaks were found for both LMRO and LNRO indicating the absence of any stray impurity phases.

Observation of a distinct superstructure reflection along the [111] direction in both LMRO and LNRO could be taken as a first fingerprint of a spontaneously achieved *B*-site ordering.

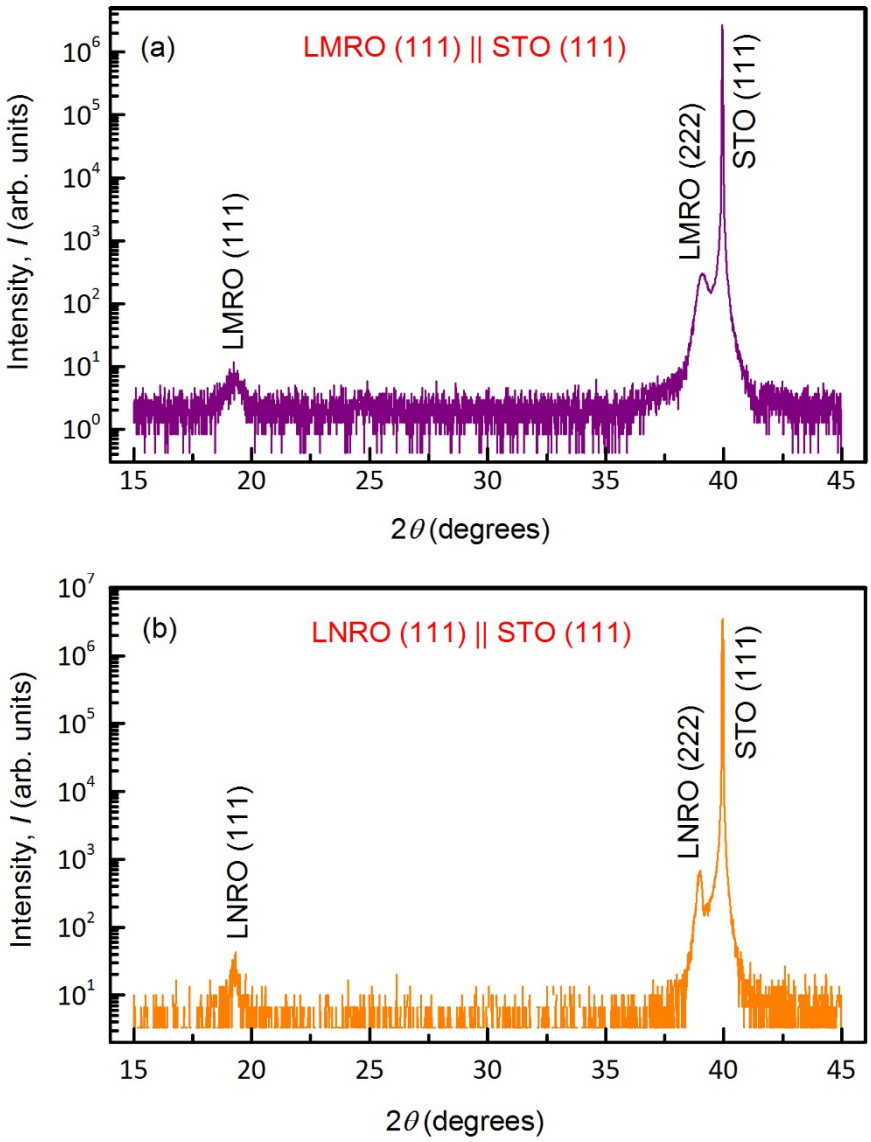

Fig. 4.10 $\theta - 2\theta$ XRD patterns of (a) LMRO and (b) LNRO thin films deposited on (111) oriented STO substrates, depicting the observation of a (111) superstructure peak in addition to the fundamental perovskite (222) reflection.

However, one of the important findings of chapter 3 must be taken into consideration here. Through systematic evaluations on a representative system such as BFCO, it was shown that a mere observation of the superstructure peaks may not be a sufficient proof of chemical order, particularly in systems where structural distortions such as cation shifts can also cause a similar doubling of the unit cell. Thus evaluation of chemical order particularly in the thin films of double perovskite needs a holistic or collective experimental approach to confirm the presence of the chemical ordering. The unit cell in systems such as BFCO, are more prone to

distortions such as cation shifts because of the presence of a lone-pair active species such as the Bi^{3+} cation. Absence of such a stereochemically active species in both cases of LMRO and LNRO reduces the tendency of this complication. Besides existence of a larger difference/contrast in the ionic radii and *Z* (atomic number) of the two *B*-site cations, allows us to use other direct visualization techniques such as high resolution electron microscopy to detect the chemical ordering at an atomic level. As it has been observed in case of BFCO and other similar double perovskites, characterization of functionalities such as magnetism and magnetic coupling also shed valuable light on the state of the *B*-site ordering. Based on these considerations, a multi-sided experimental approach has been used in the case of LMRO and LNRO to establish the presence of a spontaneously achieved chemical ordering in the thin films. These have been elaborated in the following sections.

In the case of LMRO, there is larger difference in ionic radii of the two *B*-site cations: 0.83 and 0.63 Å for Mn^{2+} and Re^{4+} respectively. This in addition with the *Z* contrast (Mn-25 and Re-75) makes it a suitable system to investigate chemical ordering via a *Z* sensitive imaging technique such as the high angle annular dark field – scanning transmission electron microscopy (HAADF-STEM). Also the higher crystalline quality of the LMRO films is expected to provide for better quality imaging at the atomic resolution. Figure 4.11 shows a set of images obtained from the atomic resolution HAADF-STEM and STEM-EDS imaging performed on the [00*l*] oriented LMRO film grown on the (001) STO substrate. Sample preparation and imaging were performed within the electron microscopy group of Prof. Joke Hadermann at the University of Antwerpen, Belgium. A cross-sectional lamina of the LMRO sample was cut along the [110] zone was taken for the imaging.

Figure 4.11 (a) shows a HAADF-STEM image of the LMRO film and its interface with the STO substrate. The hetero-epitaxial interface between LMRO and STO was mostly found to be smooth and sharp through most parts of the sample. At the interface, the substrate is found to end with a Ti-O_2 layer and the film is found to start with an La-O layer. This is expected, as the STO substrate, prior to deposition, was subjected to a buffered – HF etch process in order to create an atomically smooth single terminated surface. Fig. 4.11 (b) shows a magnified view of a portion of the LMRO film away from the interface. Since the brightness of the intensities of the atomic columns on HAADF-STEM images are proportional to the average atomic number along the columns ($I \sim Z^n$, $1.5 < n < 2.0$), the (*B*, *B'*), columns with Re atoms will be brighter than the columns with Mn atoms. The layers of La-cations will have a constant brightness. Using this knowledge, one can easily recognize the layers with (*B, B'*)

cations in the image. A portion of the magnified image is further enlarged and shown as an inset on the left side of Fig. 4.11 (b).

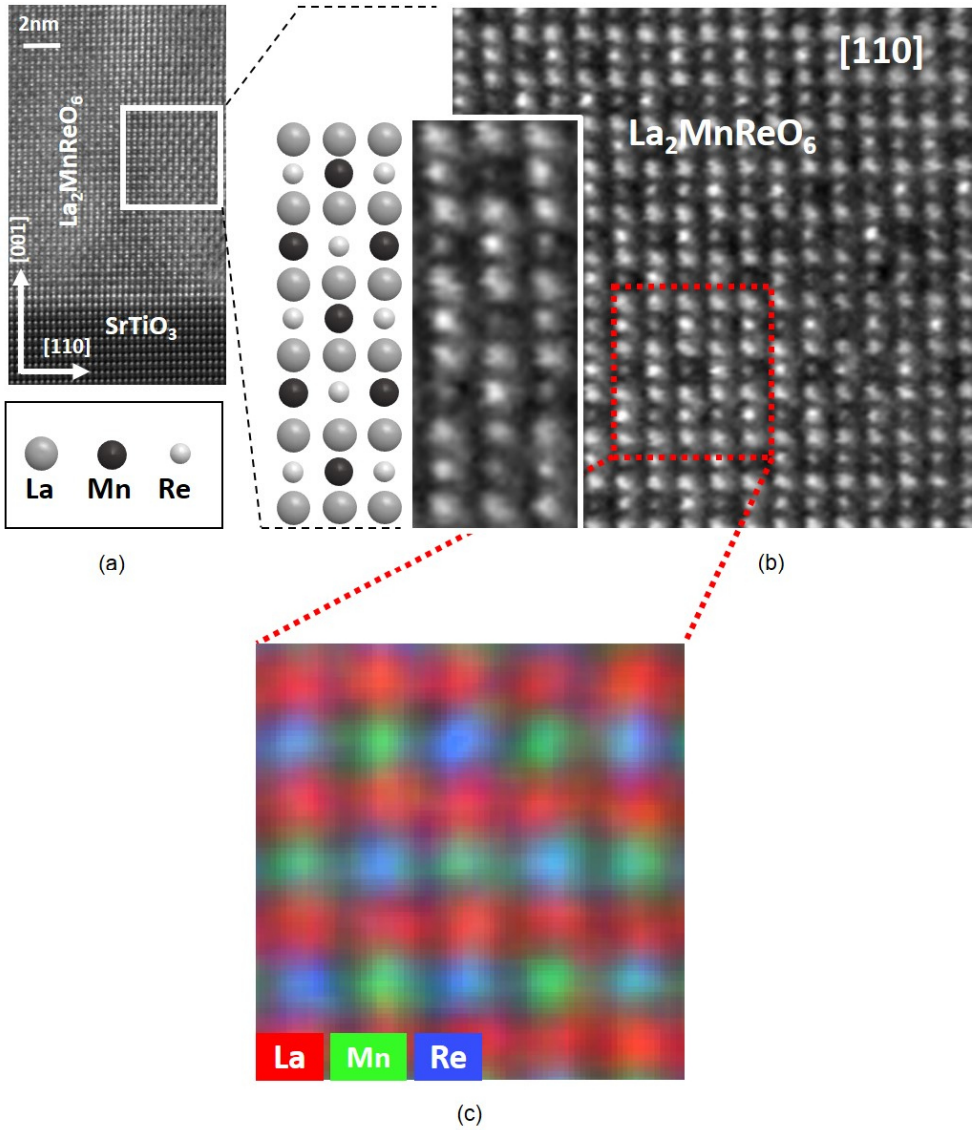

Fig. 4.11 (a) A HAADF-STEM cross-sectional image of an LMRO film grown on a (001) oriented STO substrate depicting a sharp and atomically smooth interface of the film with the substrate; (b) A magnified view of the [110] zone of the LMRO thin film away from the interface, (inset) – enlarged view of atomic columns depicting the expected intensity/brightness variation pattern corresponding to the *B* - site chemical order; (c) STEM-EDS mapping of the [110] zone, visually demonstrates the expected checkerboard pattern of the Mn-Re rock-salt ordering. [STEM-EDS cation colour code: La (Red), Mn (Green) and Re (Blue)].

A repeating pattern of varying atomic image intensities can be distinctly seen along both [001] and [110] directions. A schematic pattern of La, Mn and Re atoms, displayed next to the inset demonstrates the observed arrangement of the atoms in the LMRO film. As the

images show the [110] zone, this alternation pattern is in agreement with rock-salt order of the *B* (Mn^{2+}, Re^{4+}) cations in the film. Close to the interface, and stretching up to two monolayers of the LMRO film, such an alternation was not observed which indicates a *B*-site disorder in the initial monolayers of the film. The disorder of the *B* cations close to the interface has been commonly observed in independent studies of epitaxial thin films of various (3*d*-3*d* / 3*d*-4*d* / 3*d*-5*d*) double perovskites.[61,63,180,181] So far, it is believed to be caused by complex interactions of competing surface energies of the species and/or due to surface defects/mixed terminations at the substrate surface. Setting aside the two initial monolayers, the ordered pattern of atoms in the majority bulk of the film was observed in similar imaging performed at multiple locations in the film confirming a long range ordering of the Mn-Re cations.

Qualitative identification of the atomic columns was further probed via atomic resolution STEM-EDS mapping. Red, green and blue colours were chosen for the individual EDS maps of La, Mn and Re respectively. The image as obtained from the cumulative EDS mapping is shown in Fig. 4.11 (c). A checker-board type alternating arrangement of the green and blue colours corresponding to Mn and Re atoms respectively, can be clearly seen in this atomic resolution image. This pattern unambiguously confirms the desired rock-salt type ordering of the Mn-Re cations. Continuous rows of atoms in red correspond to the *A*-site lanthanum atoms. Among the green and blue columns, some green columns appear to be a duller green or little bluish and some blue columns appear to be dull blue or a tad greenish. This effect arises from the possible presence of anti-site defects along that atomic column where a rhenium atom is misplaced at a manganese site and vice-versa. But considering that the expected original colours for the atomic columns is largely retained in the pattern and a similar observation recorded at several measurement locations in the sample, the overall amount of anti-sites can be confirmed to be low.

The STEM-EDS analysis was also used to determine the stoichiometry of the LMRO films. The chemical composition was quantified on 50 different regions of a LMRO film at low magnification and out of [110] zone axis, by using Sprit 1.9 BRUKER software. The overall composition of the film according to STEM-EDX is $La_{2.00}Mn_{0.99}Re_{1.02}O_x$ which is in good agreement with the nominal composition of the double perovskite La_2MnReO_6.

4.6. Functional characterization

The most important functionality of interest in this study of LMRO and LNRO double perovskites is their magnetic properties. Coupling of the uncompensated spins of the two *B*-site transition metal cations is expected to yield a sizeable magnetization in both the compounds. In LMRO, Mn^{2+} with a $3d^5$ configuration couples with the $5d^3$ Re^{4+}. If we consider a *B*-site spin only moment, a total magnetization of 8 μ_B/f.u. can be expected for a ferromagnetic coupling of the Mn-Re spins, and 2 μ_B/f.u. is expected for the case of ferrimagnetic order. Similarly in the case of LNRO, $3d^8$ Ni^{2+} can couple with the $5d^3$ Re^{4+} to result in a spin only moment of either 5 μ_B/f.u. or 1 μ_B/f.u. for a ferromagnetic or ferrimagnetic ordering respectively. A more precise theoretical estimation of the overall magnetization (including spin-orbit coupling) for the ferrimagnetic case yielded 2.90 μ_B/f.u. and 0.80 μ_B/f.u. for LMRO and LNRO respectively.

In order to characterize the overall magnetization of the LMRO and LNRO thin films, we used a Quantum Design MPMS system which via SQUID magnetometry is capable of measuring magnetization as a function of applied field and temperature. The system allows for applying field up to a maximum of 6 Tesla and the measurable temperature range is between liquid helium temperature of 4 K and little above room temperature (~330 K). Fig. 4.12 (a) shows a plot of the overall magnetization measured as a function of the field (applied in the plane of the samples) at low temperature (20 K) for both LMRO and LNRO. Both compounds show a well-defined hysteresis loop and indicate the presence of a finite magnetization. As evident from the hysteresis curves, LMRO was found to have a harder magnetic state as compared to LNRO with a high coercive field ~ 6200 Oe. After subtracting the diamagnetic contributions of the STO substrates, saturation magnetizations of 2.2 μ_B/f.u. and 0.38 μ_B/f.u. was recorded for LMRO and LNRO respectively.

Comparing these magnetizations with the theory, it is evident that the observed values clearly deviate from the expected magnetizations for a parallel alignment of the *B*-site spin sub-lattices and hence ferromagnetic order can be ruled out. The magnetizations rather match well with the ferrimagnetic order including spin-orbit coupling as estimated by theory. This can be noted as an experimental confirmation of the DFT calculations which found ferrimagnetism to be the more stable ground state magnetic order for both compounds with lower total energies of the order of ~ 433 meV/f.u. as compared to their ferromagnetic counterparts.

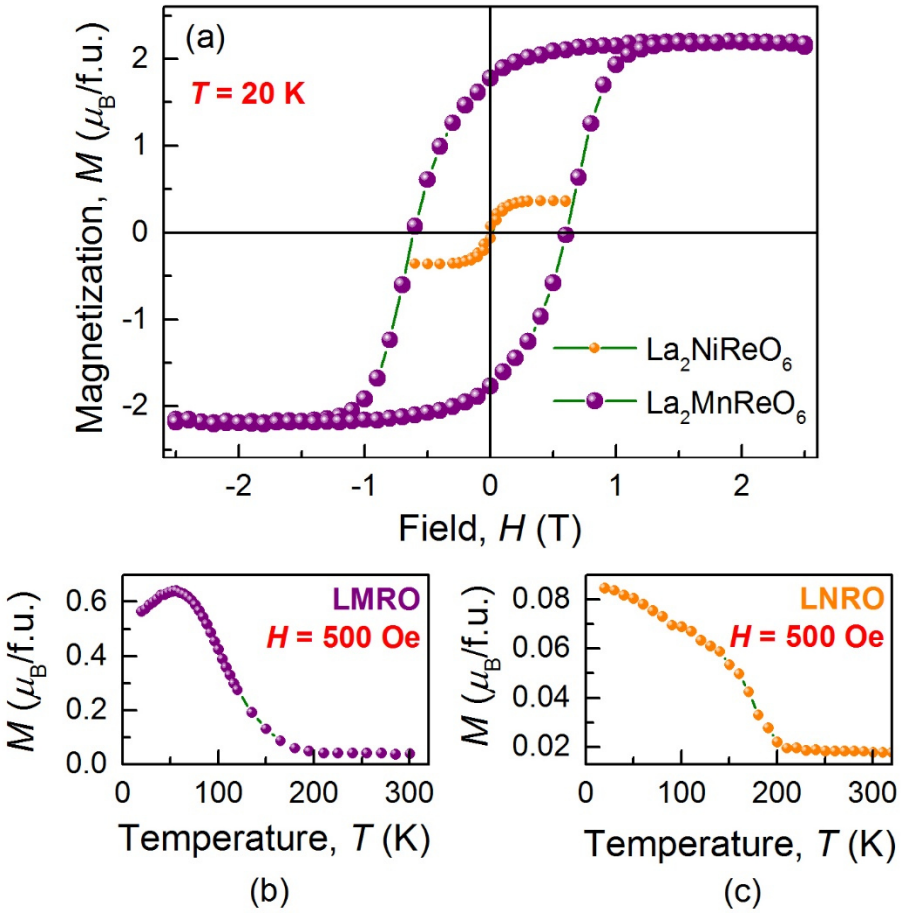

Fig. 4.12 (a) Magnetization *vs.* field curves measured via SQUID magnetometry for LMRO and LNRO thin films at T = 20 K, showing well-defined hysteresis loops for both; (b) Field cooled magnetization *vs.* temperature curve (measured under an applied in-plane field of 0.05 T) of an LMRO thin film with a transition temperature of 180 K; (c) Field cooled magnetization *vs.* temperature curve (measured under an applied in-plane field of 0.05 T) of an LNRO thin film with a transition temperature of 200 K.

In comparison to the negligible magnetic response observed for the *B*-site disordered 3*d*-3*d* double perovskite BFCO in chapter 3, the magnetizations observed in both LMRO and LNRO are stable and significant. This is a promising prospect and further confirms the 3*d*-5*d* cation ordering discussed in section 4.5. Now, considering the theoretical values for the ferrimagnetically ordered LMRO (2.90 μ_B/f.u.) and LNRO (0.80 μ_B/f.u.), the experimentally observed values are comparatively smaller for both compounds. This difference can either arise due to an overestimation by theory (which is likely, as nonlocal correlations are not considered in our DMFT calculations) and/or also due to some degree of *B*-site cation disorder or anti-site defects.

As discussed in the introductory sections of this dissertation, anti-site defects are deviations from the ideal rock-salt order of the *B* / *B*' cations and result when a *B* cation is misplaced at a

B' site or vice-versa. The anti-site defect concentration in a double perovskite sample can vary from zero to 50 %. A zero anti-site defect concentration refers to an ideal fully ordered double perovskite. Starting from a fully ordered double perovskite misplacing every one *B*-site cation creates two defect sites and thus 50 % anti-site defect concentration corresponds to a fully disordered case. Existence of direct correlations between anti-site defects and properties such as magnetization have been reported in a large number of studies on double perovskites. In fact, several studies, both experimental as well as theoretical modelling on similar ferrimagnetic double perovskite systems have concluded presence of a near linear relationship between the anti-site defect concentration and magnetization.[29,182–184] By applying a similar model to this study, we found the anti-site defect concentrations in LMRO and LNRO thin films to be 12 % and 26 % respectively. Here it is important to note that these defect concentrations were calculated with respect to an overestimated theoretical value of total magnetization (derived from DMFT) and in reality the defect concentrations in our films should to be smaller (for example, performing a similar calculation with respect to the theoretical magnetization reported for analogous compounds BMRO and BNRO (Table 4.2) yields lower anti-site defect concentrations of 4 % and 17 % for LMRO and LNRO respectively).[4] Based on above evaluation, the degree of ordering in our LMRO and LNRO films is estimated to be > 76 % and > 48 % respectively. However, it is to be noted that this approximate evaluation provides a lower limit and the degree of ordering should be larger in reality. A more precise estimation of the degree of ordering could be done if a fully ordered thin film sample or single crystals were available as a reference.

The temperature dependences of magnetization for LMRO and LNRO are shown in Fig. 4.12 (b) & (c). Both curves show a distinct transition to the paramagnetic state. Transition temperatures of 180 K and 200 K were recorded for LMRO and LNRO respectively. Comparing the observed magnetic transition temperatures to the theoretically estimated values by Ležaić and Spaldin for the analogous compounds BMRO (330 K) and BNRO (360 K) as listed in Table 4.2[4], it is seen that the observed values follow a similar mutual trend as the theoretical values for the Mn-Re and Ni-Re compounds.

Theoretical calculations also indicated a possibility of a significant orbital contribution to the overall magnetization, considering the presence of heavy transition cation like rhenium. Quantitative estimations and disentanglement of spin and orbital moment can be realised via advanced synchrotron based and element sensitive magnetic characterization technique such as X-ray magnetic circular dichroism (XMCD). We thus performed XMCD measurements on both the LMRO and LNRO samples in order to qualitatively and quantitatively characterize

the magnetic state of the Rhenium in the two compounds. Since the element sensitive XMCD measurements on the 5*d* metal Rhenium uses excitation at the $L_{2,3}$-edges for analysis, which lie in the energy range of 10 to 12 KeV, we had to use hard X-rays for the experiment. Thus all the XMCD measurements on both samples were performed at the hard X-ray circular polarization beam line at the European Synchrotron Radiation Facility (ESRF) in Grenoble. Measurements were performed at 20 K within a superconducting electromagnet capable of producing magnetic fields up to 17 Tesla.

For the measurements, the energy of the intense incident beam of X-rays was scanned across the absorption edge, while the spectra were recorded using the total fluorescence yield detection mode. The corresponding XMCD signals at the edges were generated by taking the direct difference between two consecutive absorption spectra scanned with opposite helicities of the incident X-rays. Data were also collected for both directions of the applied magnetic field in order to free the XMCD spectra of any artefacts. The obtained spectra were normalized, and the edge jump ratio was corrected to 2.20/1, as per Ref. [185].

Fig. 4.13 (a) and (c) show plots of the normalized X-Ray absorption spectra recorded at the Re $L_{2,3}$-edges for the LMRO & LNRO films respectively. As observed, for both the edges and also for both cases of LMRO and LNRO, the measurement range could not be extended much beyond the edges, due to the detection of extremely intense diffraction peaks of the STO substrate in the spectra, which greatly hindered our measurements. The L_2 and L_3 edges correspond to the transitions $2p_{1/2} \rightarrow 5d$ and $2p_{3/2} \rightarrow 5d$ transitions respectively. The normalised spectra of the recorded XMCD is also correspondingly plotted (black-red) for the L_2 and L_3 absorption edges in Fig. 4.13 (a) & (c).

In case of LMRO (Fig. 4.13 (a)), a clear and sizeable XMCD signal is recorded at both the absorption edges which indicates presence of a significant local magnetic moment at the Re site. The recorded XMCD signals showed consistent features with other similar measurements at 5*d* $L_{2,3}$ edges in double perovskite compounds.[2,163] The XMCD signal at the L_3 edge was small and positive, where as a relatively large negative signal was recorded at the L_2 edge. The overall XMCD thus clearly indicated that the magnetic moment at the Re site aligns opposite to the net magnetization of the compound consistent with the expected theory as elaborated previously in Fig. 4.4 (c). Thus the negative magnetic moment at the Rhenium site once again confirms the anti-parallel or ferrimagnetic coupling between the Mn and Re moments, which is a favoured magnetic order arising from the Mn-O-Re exchange.[186,187] Variation of XMCD signal as a function of the applied field was also measured at both L_2 and L_3 edges for the LMRO film (Fig. 4.13 (b)). A distinct hysteretic curve as expected was

observed at both the edges which are consistent with the magnetization curves measured with the SQUID MPMS. Both the hysteresis loops showed a remarkably large coercive field up to 0.5 T.

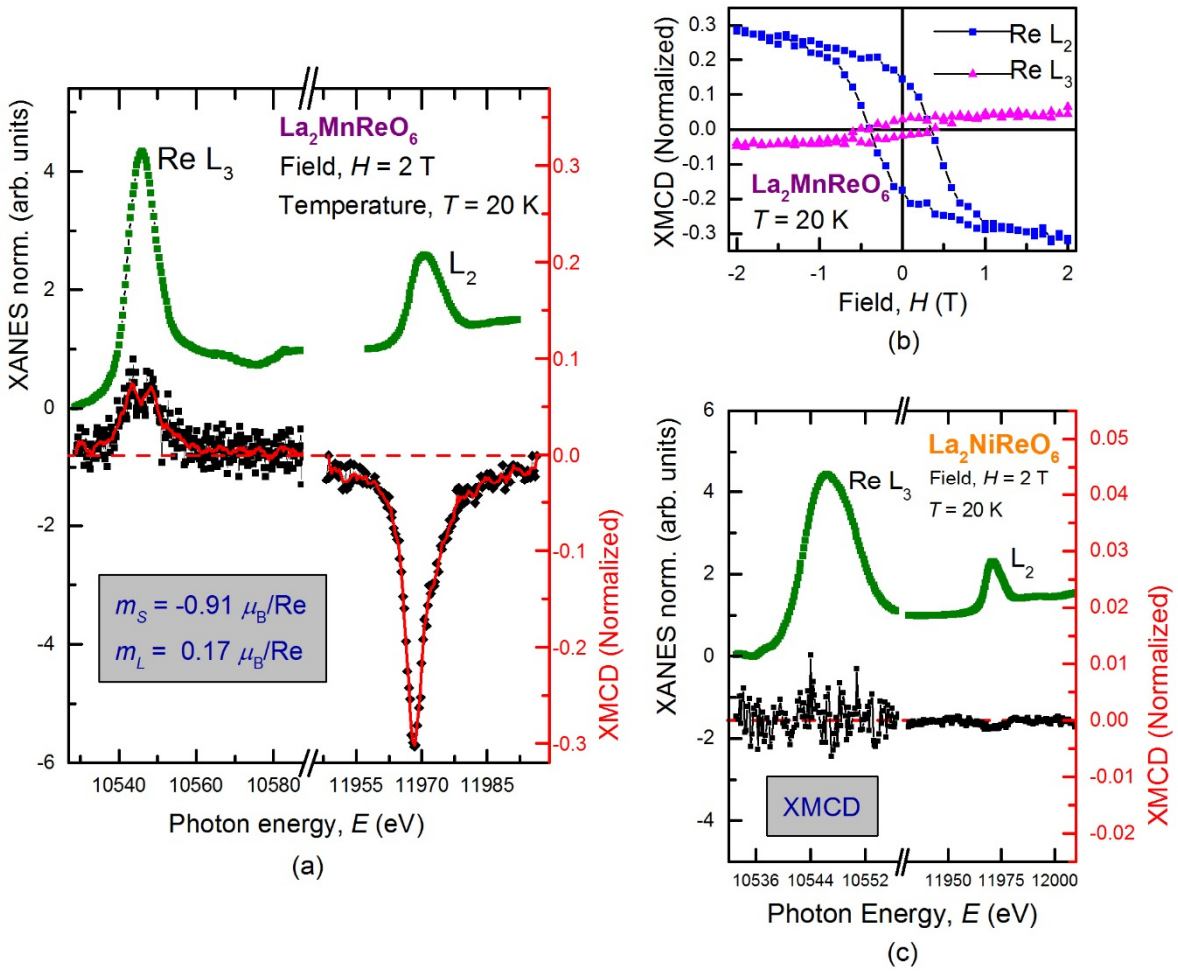

Fig. 4.13 (a) Normalized XANES and XMCD spectra recorded for the LMRO film at the Re-$L_{2,3}$ edges under an applied in-plane field of 2 T measured at T = 20 K; (b) Normalized XMCD at the Re-$L_{2,3}$ edges measured as a function of the applied field at T = 20 K, showing a clear hysteretic behavior; (c) Normalized XANES and XMCD spectra recorded for the LNRO film at the Re-$L_{2,3}$ edges under applied in-plane field of 2 T measured at T = 20 K.

The area integral of the intensities under the XMCD curves contain quantitative information on the spin, orbital and total local magnetic moment of the specific element which can be deduced via the so called 'Sum Rules'.[95,96] The sum rules established that the sum of the integrated intensities under the XMCD spectra at both L_2 and L_3 edges is proportional to the orbital moment (m_L), and the difference between the integrated intensities at the L_3 and twice

the L_2 edge is proportional to the spin moment (m_S). Final values of the spin and orbital moments are obtained by normalizing the integrated spectra to the White Line (peaks of the absorption spectra) intensity and the number of 5*d* holes (n_h). The 5*d* holes (n_h) simply refers to the number of unoccupied electron states in the 5*d* shell of the cation, in our case its Re^{4+}. Although in some experiments in literature, the n_h value is theoretically derived by simulation, its value can be approximately estimated to range across 7 (for Re^{4+}) and 9 (for Re^{6+}), derived simply as (10 – number of electrons in *d*-shell). Taking the value of $n_h = 7$ for the Re^{4+} in LMRO and by applying the sum rules, we estimated the total magnetic moment to be -0.73 μ_B/Re corresponding to a spin moment $m_S = 0.90$ μ_B/Re and an orbital moment of $m_L = +0.17$ μ_B/Re. Thus it is observed that there is a clear evidence of a significant and unquenched orbital moment in Rhenium. Now, assuming a *B*-site only model, the magnetic moment of the Mn-atom was deduced from the values of total magneitization as measured by SQUID and the derived total moment of the Re atom. This was found to be 2.93 μ_B/Mn atom.

XMCD at the Re $L_{2,3}$-edges were also recorded for the LNRO film under similar measurement conditions as in the case of LMRO (Fig. 4.13 (c)). In comparison to LMRO, the recorded XMCD signals were very weak. As observed in the plot, no significant XMCD was recorded at the L_3 edge. At the L_2 edge, indications of a small negative peak similar to the L_2 XMCD in LMRO was observed. However the recorded XMCD signal in the case of LNRO is in the order of $2 \cdot 10^{-3}$ or smaller (about 100 times weaker than in the case of LMRO), thus rendering it unfit for quantitative estimations. Reasons behind the noisy and a weak measured XMCD could be several. In some cases, insufficient sample quality or noisy measurements due to the very intense and unsystematic Bragg peaks in the vicinity can be an issue yielding an unfavourable signal to noise ratios. Variations in incident beam intensity on a particular measurement day and occurrence of a beam refill in the middle of a measurement sequence were also found to affect the measured signals. Besides these, there could also be other intrinsic reasons such as competing magnetic interactions, which were reported for some other nickel based 3*d*-5*d* double perovskites in the literature.[188] However, further investigations and additional synchrotron measurements may be required to more extensively characterize the rhenium magnetism in LNRO.

A cumulative list of all theoretically calculated and experimentally observed magnetic moments for LMRO and LNRO have been listed in Table 4.7 below.

Table 4.7 Overview of theoretical and experimental recorded element specific and overall magnetic moments for LMRO and LNRO.

	Theoretical (DMFT)				Experimental			
	Total Magnetization, $\|M\|$ (μ_B/f.u.)	Re		Mn or Ni	Total M, (SQUID measured) (μ_B/f.u.)	Re XMCD		Mn or Ni ($M_{Tot} - m_{Re}$)
		m_{spin} (μ_B/Re)	$m_{orbital}$ (μ_B/Re)	$m_{Mn/Ni}$ (μ_B/Mn or Ni)		m_{spin} (μ_B/Re)	$m_{orbital}$ (μ_B/Re)	$m_{Mn/Ni}$ (μ_B/Mn or Ni)
La_2MnReO_6	2.90	-0.96	0.30	3.56	2.20	-0.91	0.17	2.93
La_2NiReO_6	0.80	1.11	-0.45	-1.46	0.38	-	-	-

Besides the magnetic investigations, X-ray absorption spectra are also commonly used to extract other qualitative information such as the chemical environment or the oxidation state of the particular element. Particularly for determining the oxidation state, often either the *K*-edges or the L_1 edges are analysed. It is known that these edges shift to higher energies with increasing oxidation state. This happens due to the fact that the core shells become more bounded due to oxidation because of which its energy becomes lower. Correspondingly the final unlocalized states are not shifted much, therefore the energy gap for transition is more which shifts the edge. Thus the position of the absorption edges can often be used as a fingerprinting technique to determine the oxidation states. Although such shifts in the case of the $L_{2,3}$ edges are comparatively smaller, Tougerti *et al.*[189] performed a systematic experimental and simulation study on a series of Rhenium oxides in its different oxidation states going from metallic to 7+. By comparing the features of the experimental and simulated curves of the L_1 and L_3 edges, they documented the differences in the features of the various spectra. By comparing with the outlined features of all the rhenium oxides in the study, it is observed that our measured L_3 spectra of both LMRO and LNRO is more in agreement with that of ReO_2. The absorption edge White Line characteristics of the higher oxidation state such as 7+ appear significantly different and are positioned 2 eV higher in energy. The 7+ state can thus be ruled out unambiguously. In terms of the edge position, the L_3 edge for both 4+ and 6+ have been noted to occur at similar energy. However, it is not readily feasible for Rhenium to go into a higher oxidation state like 6+ within a stoichiometric double perovskite environment of LMRO and LNRO. Since, Lanthanum has a very stable 3+ state, Rhenium shifting to a higher oxidation state of 6+ would require

Manganese/Nickel to go to a lower oxidation state than 2+ in order to maintain the electrical neutrality. Now considering both Mn and Ni have no lower stable oxidation state (except for going in to metallic state), and since no metallic Mn or Ni was detected, we consider 6+ as an unlikely state for Rhenium here. Also worth noting is the fact that for a double perovskite with a trivalent *A*-cation (like $La_2BB'O_6$), there can only be three different combinations for charge states of *B/B'* cations in order to maintain electrical neutrality of the compound, namely – (a): 1+/5+; (b) 2+/4+; and (c) 3+/3+. Considering that 1+ and 5+/3+ are not stable states of oxidation for Mn/Ni and Re respectively, options (a) and (c) can be ruled out for a stoichiometric, electrically neutral double perovskite. Thus from the overall evaluation derived above from multiple characterizations performed on the LMRO and LNRO films which established stoichiometric films of fair crystalline quality, we consider 2+ & 4+ to be the dominant oxidation state in our samples for Mn/Ni and Re respectively.

We next looked at the electrical properties of the films. The as measured electrical resistivity as a function of temperature for LMRO and LNRO are shown in Fig. 4.14 (a) and (b) respectively. The corresponding magnetization *vs.* temperature curves for both the samples have also been overlaid in the plots for illustration purpose. In the case of LMRO, the resistivity was measured under a standard 4-bar probe setting built with a Keithley 6221 Current source & Keithley 2182A Nanovoltmeter. We unexpectedly observed a sharp and distinct metal-to-insulator transition at a temperature which appears to coincide with the magnetic ordering temperature of the compound. In the paramagnetic regime (>180 K), the LMRO film was found to clearly show a metal like variation in the resistivity. Below the magnetic ordering temperature (180 K), the resistivity curve was observed to sharply rise up to >1000 mΩ cm beyond which the resistivity values remained higher than the measurable limit of the unit suggesting a stable insulating state. The film continued to be in an insulating state all the way up to liquid Helium temperature. The observed behavior was reproducible in LMRO thin films grown at the optimized conditions.

On the contrary the LNRO film was found to be insulating at room temperature, also with a simple multimeter test. Due to its higher values resistivity, a two probe set-up using the Keithley 6717B Electrometer was used to once again measure the resistivity as a function of temperature. In comparison to the LMRO film, the insulating state was stable across the magnetic ordering temperature and remained insulating in the entire measured range up to room temperature.

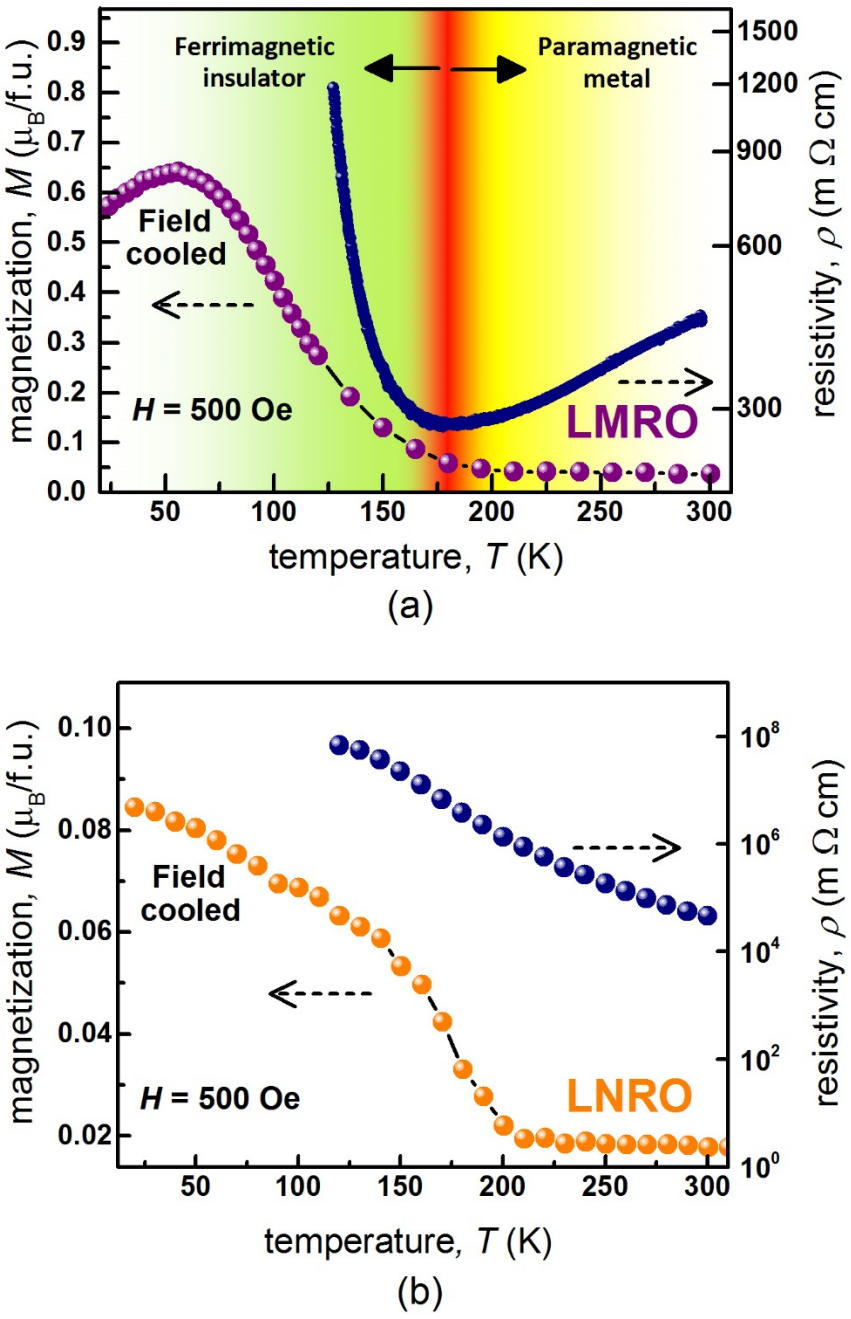

Fig. 4.14 (a) As measured temperature dependent resistivity for the LMRO film overlaid on an *M vs. T* plot of the same film, depicting the a transition (red shaded region) from ferrimagnetic insulating to paramagnetic metal state at a transition temperature ~180 K; (b) As measured temperature dependent resistivity for the LNRO film overlaid on an *M vs. T* plot of the same film, depicting a persistent insulating behavior of the film up to the measured temperature of 300 K.

To understand the origin of the observed differences in the electrical properties of these two compounds, we take a look at the differences in their electronic configurations. Schematic illustrations of the individual band structures of LMRO and LNRO under conditions below and above the magnetic ordering temperature are shown in Fig. 4.15 (b) – (e). In general, the *5d* transition element - rhenium is known to be a non-magnetic metal (Fig. 4.15 (a)). When such

a cation is placed in a double perovskite framework, under the influence of an exchange interaction with the neighbouring magnetic *3d* cations, the *B*-O-*B'* superexchange leads to an exchange split ferrimagnetic insulating state (Fig. 4.15 (b) & (d)).[2] Now, in the case of LMRO as shown in Fig. 4.15 (c), if we were to have a condition where the interactions due to the magnetic order are broken (for instance when $T > T_C$), The induced moment at the rhenium site is expected to vanish, the rhenium t_{2g} will no longer be exchange split and return to a condition similar in Fig. 4.15 (a). In this state, should there be sufficient thermal activation energy, the rhenium t_{2g} states could hybridize with the like symmetry and empty t_{2g} states of the nearest neighbours, namely manganese and thereby lead to metallicity.

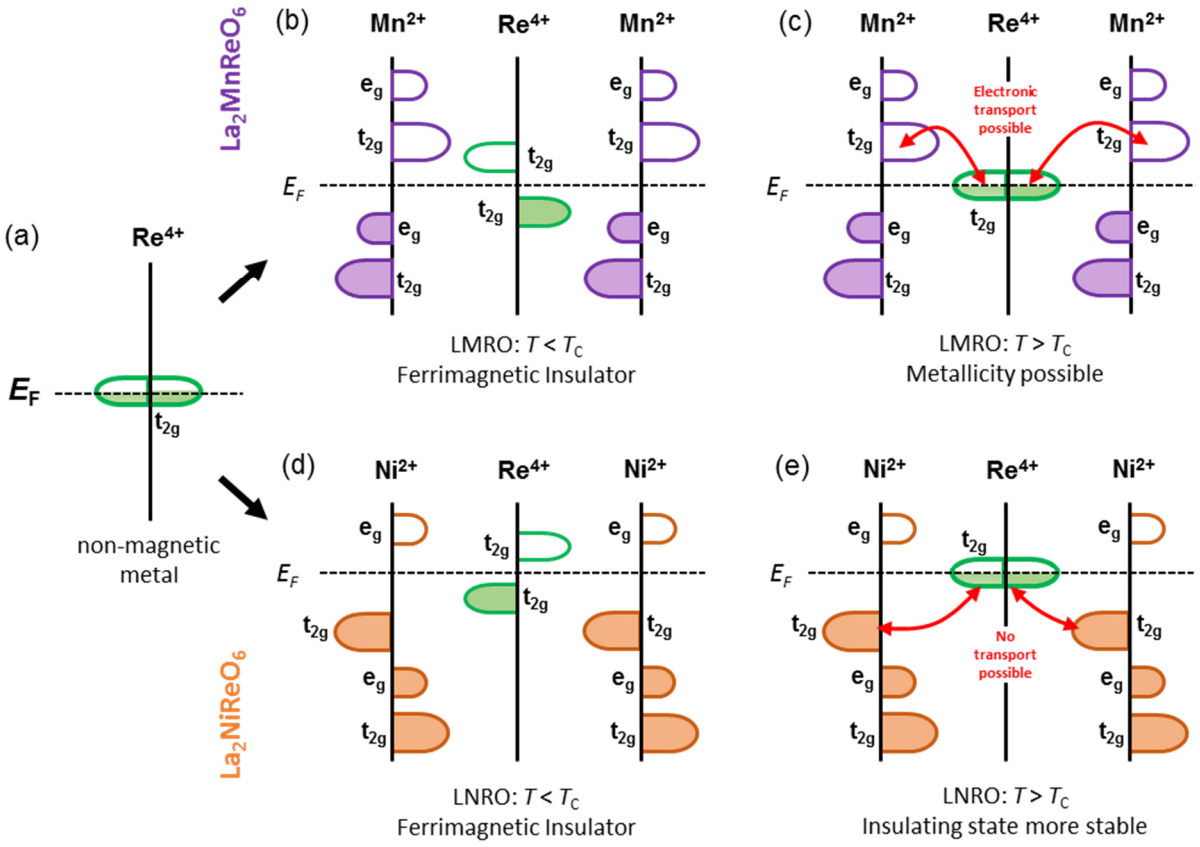

Fig. 4.15 Schematic band-structure sketches for (a) A free-standing Re^{4+} as a non-magnetic metal; (b) Mn^{2+}-Re^{4+} in LMRO in its ground state as a ferrimagnetic insulator; (c) Mn^{2+}-Re^{4+} in LMRO above the magnetic ordering temperature; (c) Ni^{2+}-Re^{4+} in LNRO in its ground state as a ferrimagnetic insulator; (c) Ni^{2+}-Re^{4+} in LNRO above the magnetic ordering temperature.

On the other hand, looking at a similar condition ($T > T_C$) in the case of LNRO (Fig. 4.15 (e)), the nearest neighbours Ni^{2+} owing to their $3d^8$ configuration, do not have empty states in the t_{2g}, due to which hopping of rhenium t_{2g} electrons may not be as readily feasible as compared to LMRO (or may require higher thermal activation energies). The nearest neighbours Ni^{2+}

have empty states in their e_g levels, however hybridization of the rhenium t_{2g} with the e_g states is forbidden by symmetry. Thus, LNRO can be expected to have a more stable insulating state. On the other hand, a symmetry selective orbital hybridization above the magnetic ordering temperature can lead to a metal-insulator transition as observed in LMRO.

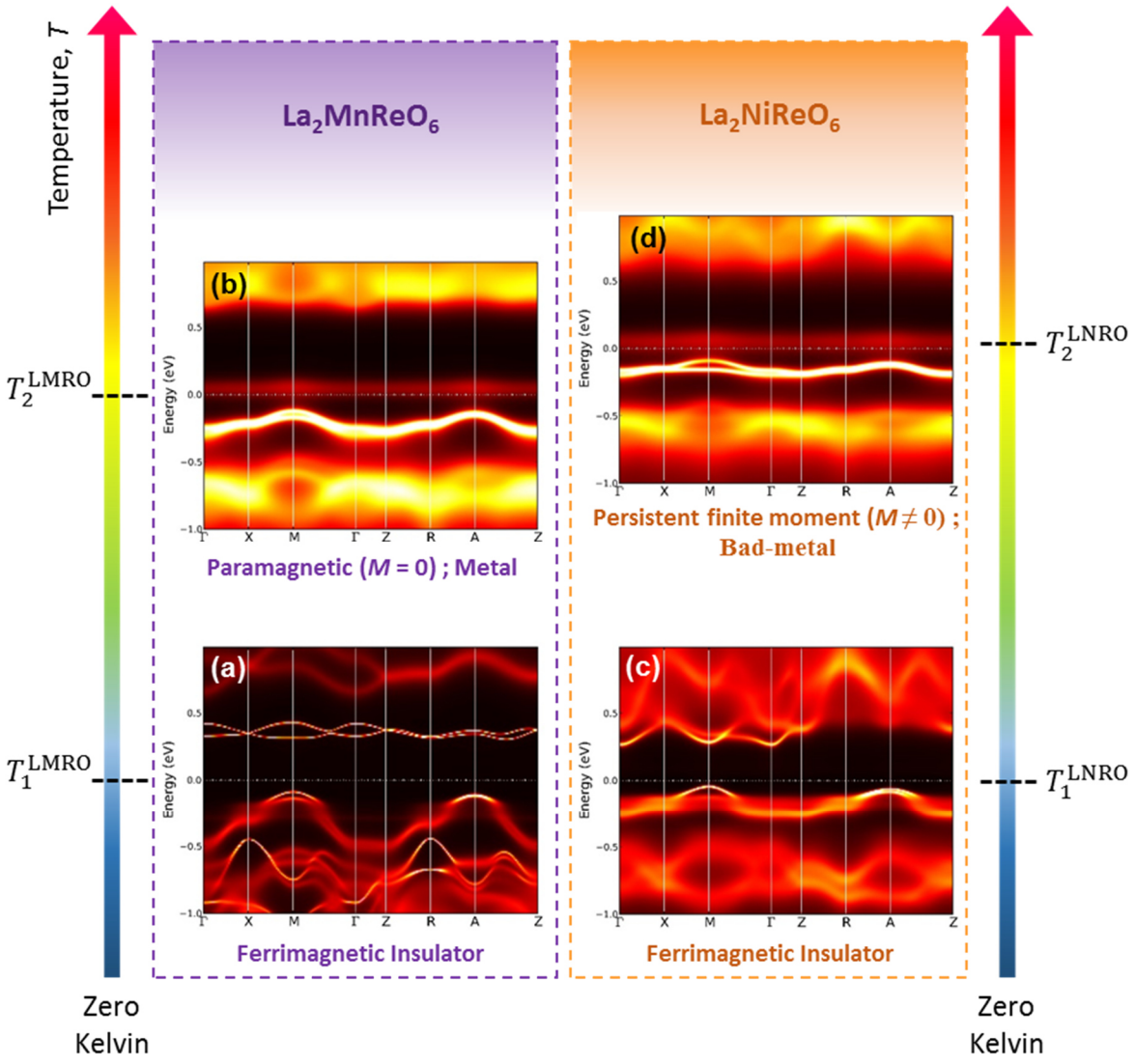

Fig. 4.16 DMFT derived spectral functions for LMRO at low temperature - T_1^{LMRO} (a) and elevated temperature T_2^{LMRO} (b); Corresponding spectral functions derived for LNRO at low temperature T_1^{LNRO} (c) and at elevated tempearature T_2^{LNRO} (d).

In order to confirm these observations, LMRO and LNRO were treated within the dynamical mean filed theory (DMFT), which has been established as a successful method to study the electronic structure and properties of correlated materials. Here, we studied the variations in the electronic structure of LMRO and LNRO as a function of temperature, particularly observing the changes below and above the expected magnetic transition. Consequently Fig.

4.16 (a) and (b) show respectively the representative images of the calculated electronic band structures below and above the transition temperature. The observed low temperature calculations for LMRO (Fig. 4.16 (a)) shows a consistent picture of the bands as expected for its ferrimagnetic ground state. An observed band gap close to ~0.6 - 0.8 eV is of similar magnitude as derived with DFT estimations of the DOS. When sweeping the conditions from lower temperatures (T_1^{LMRO} <400 K) to higher temperatures (T_2^{LMRO} <500 K), we observed a clear magnetic transition from a ferrimagnetic to a paramagnetic state. Interestingly, this transition was also accompanied by a closing of the bandgap and appearance of finite bands at the Fermi level leading to a metallic state (Fig. 4.16 (b)). This is consistent with the experimentally observed metal insulator transition in LMRO.

Similarly, DMFT calculations performed on LNRO also showed at lower temperatures (T_1^{LNRO} <400 K), a consistent ferrimagnetic state with a commensurate band-gap as observed from the DFT calculations (Fig. 4.16 (c)). However, in contrast to LMRO, no magnetic transition was observed in LNRO by increasing the temperature up to 500 K. Upon going further higher in temperature (T_2^{LNRO} >500 K), we see that states similar to the case of LMRO begin to appear at the Fermi level (Fig. 4.16 (c)). However, in contrast to LMRO, we observed that at this state LNRO had not undergone a complete transition to a paramagnetic state. The state had a persistent finite moment and thus bore characteristics of a magnetic bad metal.

Thus, several observations and inferences can be drawn from the findings of the DMFT calculations. Firstly, the theoretical estimations of the magnetic transition temperatures were found to be between 400 - 500 K for LMRO and above 500 K for LNRO. The mutual trend of these theoretical values are consistent with the experimental observations which showed $T_C^{LNRO} > T_C^{LMRO}$. The T_C trend is also consistent with theoretical estimations reported for analogous compounds BMRO and BNRO in Ref. [4]. However, we find that the theoretical values are higher as compared to experimental values. This is to be expected with our DMFT treatment and is a consequence of not considering non-local correlations in the calculations.

The second important observation from the DMFT calculations is that it accurately captures the observed insulator to metal transition observed in the case of LMRO. This transition accompanies the magnetic transition of the compound to a paramagnetic state. Furthermore there is also a collective indication from the DMFT calculations that the insulating state in LNRO is comparatively more persistent with temperature in comparison to LMRO, consistent with our inference from Fig. 4.15. Thus, from the overall analysis, there seems to be a good agreement of the theoretical calculations with the experimental findings on LMRO and LNRO.

Chapter 4 - Acknowledgements

The author acknowledges following collaborative works in Chapter 4:

- DTF calculations & crystal structure optimizations were done in collaboration with I. Slipukhina, A. Jakobsson and M. Ležaić.
- Fabrication of samples and characterizations were done jointly by the author and A. Kulkarni (A Masters student supervised within this project).
- HAADF-STEM & STEM-EDS measurements were performed by R. Paria Sena and J. Hadermann.
- XAS & XMCD – Experiments and analysis were assisted by F. Guillou, F. Wilhelm, A. Rogalev.
- DMFT calculations were done in collaboration with H. Zhang.
- This work was conducted under advisory supervision of P. Komissinsskiy and L. Alff.

5. Summary and outlook

- This study was conducted with purpose of identifying ferrimagnetic insulating phases among double perovskite compounds and using the thin film approach to epitaxially stabilize them as pure phases.

- Double perovskites of type $A_2BB'O_6$ have been noted as valuable framework for engineering functionalities such as half-metallicity and high T_C magnetism.[1,2] Room-temperature ferrimagnetic insulating double perovskites are few, but particularly interesting as viable templates to achieve single phase multiferroism. Stabilizing these functionalities in thin film form can find large scale device applications.

- The flexibility of the $A_2BB'O_6$ structure allows for several thousands of structurally feasible double perovskite compounds. However, particular challenges have so far withheld a wide-scale exploration, namely (i) meta-stable nature of some compounds, (ii) requirement of chemical ordering.

- With recent advancements in thin film technology, Pulsed Laser Deposition (PLD) has emerged as technique of choice to grow thin layers of multi-cation oxides. It offers unique possibilities of creating non-equilibrium material growth conditions and epitaxial strain induced phase stabilization.

- Thus the PLD process can be an effective alternative route to overcome the synthesis challenges associated with meta-stable double perovskites which may be bulk-inaccessible. Recent studies have also reported the ability of spontaneous chemical ordering of the *B*-*B*' cations in epitaxial layers grown by PLD.

- In spite of the advances, only small fraction of all experimentally realized double perovskites have been adapted to thin films, while many others remain unexplored by both bulk and thin film methods.

- Each double perovskite system is different from another; their constituting cationic species can have mutually competing chemical and physical interactions which can complicate the synthesis. Thus, significant simultaneous efforts involving large amounts trial and error attempts as well as systematic study are required to uncover the potential of double perovskites.

Table 5.1 Summary of the theoretically predicted and experimentally realized magnetic properties for the three double perovskites studied under this work.

	Material System	Oxidation state & ionic radii of *B*-site cations	*M* Theory	*M* Exp.	T_C Theory	T_C Exp.
3*d*-3*d*	Bi_2FeCrO_6	$3d^5$ $r_{Fe^{3+}}$ 0.645 Å; $3d^3$ $r_{Cr^{3+}}$ 0.615 Å	2.00 μ_B/f.u.	0.06 μ_B/f.u.	100 K	–
3*d*-5*d*	La_2NiReO_6	$3d^8$ $r_{Ni^{2+}}$ 0.69 Å; $5d^3$ $r_{Re^{4+}}$ 0.63 Å	0.80 μ_B/f.u.	0.38 μ_B/f.u.	>500 K	200 K
	La_2MnReO_6	$3d^5$ $r_{Mn^{2+}}$ 0.83 Å; $5d^3$ $r_{Re^{4+}}$ 0.63 Å	2.90 μ_B/f.u.	2.20 μ_B/f.u.	~ 400 - 500 K	180 K

- At start of this work, existing literature was surveyed to identify particular material systems that held promising potential for a room temperature functionality among two families of double perovskite compounds: 3*d*-3*d* and 3*d*-5*d* (the nomenclature refers to the elemental periods from which the *B* and *B'* cations are chosen)

- Electronic structure and the resulting functionalities of double perovskites are driven by the coupling interactions of the *B* and *B'* cations. Thus by systematically choosing the right cation combinations, one can indeed engineer functionalities on demand in this framework.

- Subsequent to material selection, thin film approach via PLD along with theoretical evaluation methods was used to undertake individual studies.

- Each of the work-lines (as elaborated below) yielded results that collectively help in developing crucial insights concerning growth and characterization of double perovskite thin films; in due process, interesting material systems and functionalities were discovered.

5.1. 3*d* – 3*d* double perovskites

- Literatures showed: 3*d*-3*d* systems are comparatively more studied among double perovskite compounds; reason being the well documented and relatively simpler synthesis chemistries involving 3*d* cations. Handling and processing of 3*d* compounds is also less complex (compared to 5*d* counterparts)

- Magnetism in double perovskites - coupling interactions of the *B*-site cations along the the *B*-O-*B*' chains resulting in either a ferri-or ferromagnetic order. For multiferroic functionality (ferroelectric+ferromagnet), common approach is to introduce stereochemical lone-pair active cation such as Bi^{3+} at the *A*-site; resulting in type I multiferroism where polarization and magnetization have individual sources.

- Based on the literature review: common drawback with most 3*d*-3*d* double perovskites is low magnetic ordering tempearatures; curtailed room-tempearature functionality. Particular exception to this was reported for compound Bi_2FeCrO_6 (BFCO)

- Although ab-initio density functional theory predicted T_C < 100 K for BFCO, some experiments reported stable magnetic order above room temperature; generating significant interest. However, subsequent independent studies reported divergent observations: ranging from negligible or no magnetization to as high as 5.2 μ_B/f.u.

- Drawing interest from above, BFCO was selected as system of choice - for study under 3*d*-3*d* regime. Theoretical predictions for BFCO: ferrimagnetic ground state resulting from the anti-parallel coupling of the $3d^5$ Fe^{3+} with the $3d^3$ Cr^{3+}. Magnetization of 2 μ_B/f.u. Stable ground state structure - *R*3 symmetry with rock-salt ordering of Fe^{3+} and Cr^{3+}.[36]

- Preparation of a stoichiometric PLD target – possible via standard solid synthesis – sintering in muffle furnace at 790˚C. Required stoichiometry Bi:Fe:Cr = 2:1:1 confirmed by EDS. Subsequently thin films of BFCO, grown via PLD on single crystalline STO substrates.

- Optimized thin films of BFCO: epitaxial, phase pure, fully strained with stretched *c*-axis lattice parameter = 3.95 Å; Preferential (00*l*) growth on (001) oriented STO substrates; no in-plane rotations; epitaxial relationship: (001)[100]BFCO || (001)[100]STO.

- XRD investigation of *B*-site chemical ordering: Distinct superstructure peaks (SPs) corresponding to unit-cell doubling observed for both the (00*l*) and (*hhh*) oriented BFCO films. However, upon careful examination: intensity of the $(111)_{dpc}$ SPs - found to be suspiciously high, considering low electronic scattering contrast between Fe and Cr.

- From structure factor calculations: Intensity of SPs (I_{111}) are function of *B*-site ordering and the corresponding contrast in Fe-Cr scattering factors; whereas intensity of the sub-cell peaks (I_{222}) - independent of the order. Thus scattering contrast between Fe and Cr was intentionally varied (i.e. by measuring under various accessible X-ray sources), while analyzing corresponding changes to intensity of SPs.

- **Key Finding 1:** In spite of large changes in scattering contrasts (For Eg.: between Co-K_α and Co-K_β – estimated to cause seven fold jump in the SP intensity), no corresponding change in intensity of SP. This confirmed presence of other possible origins of unit cell doubling.

- **Key Finding 2:** Systematic structural analysis undertaken to evaluate influence of different crystal distortions on SPs. It was found that theoretically predicted distortions in BFCO - cation shifts and octahedral distortions indeed have significant and larger contribution to intensity of SP.

- **Key Finding 3:** As intensity of observed SPs did not follow the energy dependence of anomalous scattering, ordering of Fe-Cr explicitly excluded as origin for observed superstructure. Systematically ruling out each possibility, structural modulations involving cationic displacements found to be most plausible origin of superstructure.

- **Key Finding 4:** In light of these findings, experimental discrepancies concerning magnetic properties of BFCO was better understood. In this case, due to no or negligible *B*-site order, extremely low magnetic moment of 0.06 μ_B/f.u. was recorded. Source of this residual moment can be small amount of ordered phase or undetectable impurities.

Conclusions:

Epitaxy and phase purity were achieved for the chosen 3*d*-3*d* double perovskite BFCO in the thin films grown via PLD. The films were fully strained and had a good crystalline quality. By

means of a detailed structural analysis, it was found that Fe and Cr were not spontaneously ordered; highlighting the need for ensuring larger contrast (of size and charge) in the selection of *B*-site cations. Other types of structural distortion were found to cause unit cell doubling in BFCO – observation of SP alone may not be a sufficient indicator of chemical ordering. Thus an approach of using multiple experimental methods/tools for a holistic confirmation of chemical order is recommendable for double perovskite thin films. As a consequence of the Fe-Cr disorder, a small magnetic moment was observed for the BFCO thin film.

5.2. 3*d* – 5*d* double perovskites

- 5*d* elements based compounds - more complex synthesis and handling procedures, due to meta-stable/toxic nature of some. On the other hand, there are several advantages: using 3*d*-5*d* cations allows having larger contrast (in size and charge) of *B*-site cations; enhanced spin-orbit coupling in 5*d* elements - noted to result in exotic physical functionalities.

- Several 3*d*-5*d* double perovskites: $Sr_2CrB'O_6$ (*B'* = W, Re, Os) or A_2FeReO_6 (*A* = Ca, Sr, Ba), among others, have been synthesized and known to have high magnetic ordering temperatures. However, only few - realized in thin film form.

- For case of multiferroism, 3*d*-5*d* compounds were mostly neglected, due to rarity of insulating phases among 5*d* compounds. Consequently, combination of 3*d*-5*d* DPs with ferroelectric cations like Bi^{3+} at *A*-sites have been seldom studied.

- Motivated by finding of insulating ferrimagnetic state in Sr_2CrOsO_6, Ležaić and Spaldin proposed by first principles density functional calculations, a prospective room temperature multiferroic state in two compounds Bi_2MnReO_6 and Bi_2NiReO_6.[4] These compounds have so far evaded synthesis; 3*d*-5*d* combinations of Mn-Re and Ni-Re have been seldom reported in literature.

- Drawing motivation from this, we chose Mn-Re and Ni-Re as our combinations of choice for study under 3*d*-5*d* system. We chose the more stable trivalent La^{3+} as *A*-site cation. No existing reports were found in literature. Understanding these elemental combinations and establishing synthesis routes can further enable realization of full multiferroic functionality along prospective series of La_2BReO_6 – $La_xBi_{1-x}MnReO_6$ – Bi_2MnReO_6 (B = Mn/Ni).

- Theory: Structural optimizations and density functional calculations were performed. Stable lowest energy structure: monoclinic; $P2_1/n$ symmetry. Ground state: stable ferrimagnetic insulating phase. In La_2MnReO_6 (LMRO): ferrimagnetic coupling of Mn^{2+} ($3d^5$:$t_{2g}^3e_g^2$) and Re^{4+} ($5d^3$:$t_{2g}^3e_g^0$) – expected spin only moment: 2 μ_B/f.u. In La_2NiReO_6 (LNRO): ferrimagnetic coupling of Ni^{2+} ($3d^8$:$t_{2g}^6e_g^2$) and Re^{4+} ($5d^3$:$t_{2g}^3e_g^0$), expected spin only moment: 1 μ_B/f.u.

- Ground state structure involves rock salt ordering of Mn^{2+}/Ni^{2+} and Re^{4+} cations in both LMRO and LNRO. Larger differences in ionic sizes of *B*-site elements (Mn^{2+}: 0.83 Å; Ni^{2+}: 0.69 Å; Re^{4+}: 0.63 Å) and also the difference in their formal charge, are expected to promote spontaneous ordering at the *B*-site.

- PLD targets for both LMRO and LNRO synthesized via evacuated sealed quartz tube sintering method. Sintering temperature 800˚C yielded dense pellets. Required La:Mn:Re = La:Ni:Re = 2:1:1 stoichiometry confirmed via EDS analysis.

- PLD grown thin films of LMRO on STO (001) substrates: epitaxial, phase-pure and good crystalline quality. Films fully strained with stretched *c*-axis lattice parameter = 4.02 Å; Preferential (00*l*) growth on (001) oriented STO substrates. Thin films of LNRO grown via PLD on STO (111) substrates: epitaxial, phase pure and fair crystalline quality.

- $(111)_{dpc}$ superstructure peaks corresponding to unit-cell doubling distinctly observed for both LMRO and LNRO. This is indicative of chemical ordering, provided no other unit cell doubling distortions exist in accordance with Ref. [28]. Such distortions – more prevalent and observed for systems involving ferroelectrically active cations like Bi^{3+}.

- Since an unambiguous confirmation of chemical ordering demands holistic approach; using multiple experimental tools and analyzing functional properties; atomic resolution imaging via HAADF-STEM used to characterize a LMRO film. Observed intensity pattern was consistent with atomic arrangement corresponding to rock-salt order. STEM-EDS mapping at atomic resolution - a further confirmation of Mn-Re rock-salt order. Similar images recorded at multiple locations: show consistent pattern – confirms long-range / high degree of ordering.

- **Key finding 1:** Magnetic characterizations showed both LMRO and LNRO films have a stable magnetic ground state as predicted in theory. Clear hysteretic behavior observed for both films from measured magnetization *vs.* field curves at low tempearatures.

- **Key Finding 2:** Saturation magnetizations of 2.20 μ_B/f.u. and 0.38 μ_B/f.u. recorded for LMRO and LNRO – suggestive of a ferrimagnetic order. X-ray absorption spectroscopy showed presence of a significant XMCD signal at the Re-$L_{2,3}$ for LMRO confirming a definite induced moment at the Re-site. Quantitative evaluation via sum-rules showed an unquenched orbital moment on Re – site. Overall moment at the Re-site aligned opposite to the external field, consistent with spin alignments for ferrimagnetic order. Based on established empirical relationship between saturation magnetization and anti-site disorder for ferrimagnetic double perovskites, the degree of ordering was approximately estimated to be >76 % in LMRO and >48 % in LNRO.

- **Key Finding 3:** Magnetic ordering temperatures for LMRO and LNRO – recorded at 180 K and 200 K respectively. In LMRO, an unexpected metal-insulator transition was observed at the magnetic ordering temperature, while an insulating state prevailed in LNRO within the measured range. A schematic comparative analysis of the electronic band structures showed that a symmetry selective orbital hybridization as possible source of the metal-insulator transition in LMRO. Corresponding differences in the band structure for LNRO suggested a more stable insulating state.

- **Key Finding 4:** To confirm above findings, the two compounds were treated within DMFT theoretical methods. A clear transition from a ferrimagnetic insulating to a paramagnetic metallic state was found in case of LMRO consistent with the experiment. Similarly, the DMFT observations were also suggestive of a more stable insulating state in LNRO, thereby confirming the model and experimental findings.

Conclusions:

Motivated by the theoretical findings, 3*d*-5*d* double perovskites La_2MnReO_6 (LMRO) and La_2NiReO_6 (LNRO) were epitaxially stabilized in thin film form via PLD. In contrast to 3*d*-3*d* case of BFCO, *B*-site cations in both compounds ensured larger contrast in size and charge. Thin films showed crystallographic as well as functional indications of a spontaneously achieved *B*-site order, which was unambiguously confirmed also microstructurally in case of LMRO via HAADF-STEM imaging and STEM-EDS analysis. Both films showed a stable magnetic order in ground state as theoretically expected. XMCD analysis confirmed the desired ferrimagnetic order. Magnetic ordering temperatures of 180 K and 200 K were recorded for LMRO an LNRO, thereby curtailing their room temperature functionality. Nevertheless, a metal-to-insulator transition at the magnetic ordering temperature discovered in LMRO, adds a unique additional functionality to the compound.

Table 5.1 provides a summary of the overall magnetizations and ordering temperatures recorded for the three double perovskite compounds studied in this work. By comparing among them their film growth dynamics, crystalline quality and functionality that could be achieved, it is noted that the desired ferrimagnetic double perovskite state could be best realized in the case of LMRO. This established possibility of stabilizing the La_2MnReO_6 phase as thin films, opens up few avenues for future scientific investigations (as discussed in Section 5.2 below). This work highlights the opportunities and challenges associated with thin film approach towards synthesizing functional double perovskites.

5.3. Outlook and future prospects

Based on the outcomes of this work, following topics are suggested as possible research lines that can extend the findings contained in this thesis:

1. The promising functional qualities of the Mn-Re double perovskite can be extended by *A*-site substitution with a ferroelectrically active cation such as Bi^{3+}. Realization of compounds of the $La_{2-x}Bi_xMnReO_6$ (LBMRO) system could lead to achieving type I multiferroism. The established synthesis methods for the LMRO thin films in this work can serve as a good starting point to realize the bismuth substituted compounds. However, one must take into consideration the tendency of bismuth oxides to reduce to metallic bismuth at low oxygen partial pressures as used in the target synthesis and film growth of LMRO. Use of fast sintering methods such as spark plasma sintering could be an effective alternative route to produce the required LBMRO PLD targets. Film growth may also require use of comparatively higher oxygen partial pressures at which tendency of bismuth to undergo reduction can be chemically balanced with the tendency of rhenium oxidation.

2. Effect of substrate-strain on the growth and functional responses of LMRO and LNRO films is also a promising direction for future work. Considering, both LMRO and LNRO films have larger lattice constants than STO, use of substrates such as Scandates ($DyScO_3$ and $GdScO_3$) with larger lattice constants can change the strain state in the LMRO/LNRO films. Reduction in the compressive strain with these substrates could yield higher film qualities, at the same time, functional responses such as magnetization and magnetic ordering temperature may also vary owing to the changing *B*-O-*B'* bond angles by strain. However, due to paramagnetic nature of the Scandate substrates, the element specific techniques such as XMCD will be required for magnetic characterization.

3. In case of the $Sr_2CrB'O_6$ series of compounds, electron doping via sequential *B'* substitution by the series of 5*d* elements along the period (W, Re, Os, Ir) was found to have a remarkable effect on their magnetic ordering temperatures. Starting from around 400 K for the Cr-W compound, magnetic critical temperatures above 700 K was achieved for the Cr-Os case.[2] Consistent with the trend, the Cr-Ir compound was theoretically predicted to have a still larger ordering temperature (~800 K), however the compound has so far evaded synthesis. Of course, use of the thin film approach to realize the meta-stable phase Sr_2CrIrO_6 (SICO) can itself be an interesting prospect for future research (Ref.: Unpublished work of S. Dasgupta on SICO films). But more importantly in this context, one could use the established La_2MnReO_6 framework, to substitute Re with subsequent elements of the 5*d* period namely Os and Ir to probe if a similar electron doping effect could yield magnetic ordering above room-temperature. A combined theoretical and thin film approach, as was used in this work, can enable one to efficiently uncover the prospects of these compounds.

Appendix A

List of factors α and β used for the plotting of the thermodynamic *P-T* valence state diagrams in this work. The factors were taken from Ref. [128], where they have been derived from the standard thermodynamic data for condensed phases:

Oxidized Form		Reduced Form	α	β
2/3 Bi_2O_3	↔	4/3 Bi + O_2	9.9	20200
2/3 Cr_2O_3	↔	4/3 Cr + O_2	8.8	39300
4 CrO_2	↔	2 Cr_2O_3 + O_2	7.6	5300
2 FeO	↔	2 Fe + O_2	6.9	27600
2 Fe_3O_4	↔	6 FeO + O_2	10.5	30600
6 Fe_2O_3	↔	4 Fe_3O_4 + O_2	15.0	25600
2/3 La_2O_3	↔	4/3 La + O_2	9.5	62000
2 MnO	↔	2 Mn + O_2	7.8	40000
2 Mn_3O_4	↔	6 MnO + O_2	12.8	24600
6 Mn_2O_3	↔	4 Mn_3O_4 + O_2	7.8	10600
4 MnO_2	↔	2 Mn_2O_3 + O_2	10.8	8500
2 NiO	↔	2 Ni + O_2	8.9	24500
ReO_2	↔	Re + O_2	9.5	22650
2 ReO_3	↔	2 ReO_2 + O_2	6.6	15600
2 Re_2O_7	↔	4 ReO_3 + O_2	5.5	5300

Appendix B

Unit-cells of the theoretically calculated $P2_1/n$ structure of La_2MnReO_6 and La_2NiReO_6 constructed using VESTA visualization program[14]:

La_2MnReO_6					
a	b	c	α	β	γ
5.512 Å	5.796 Å	7.894 Å	90˚	90.04˚	90˚

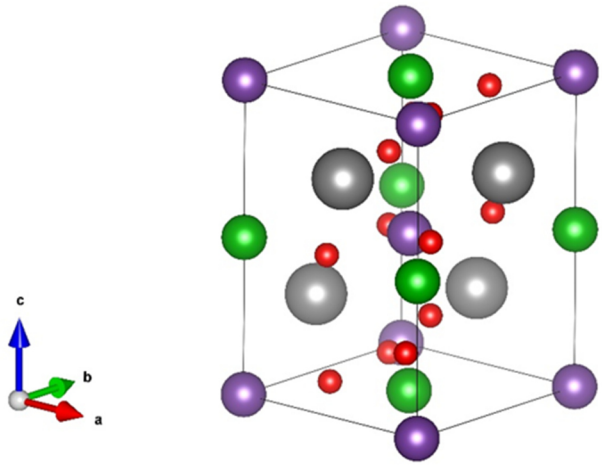

La_2NiReO_6					
a	b	c	α	β	γ
5.489 Å	5.782 Å	7.826 Å	90˚	90.63˚	90˚

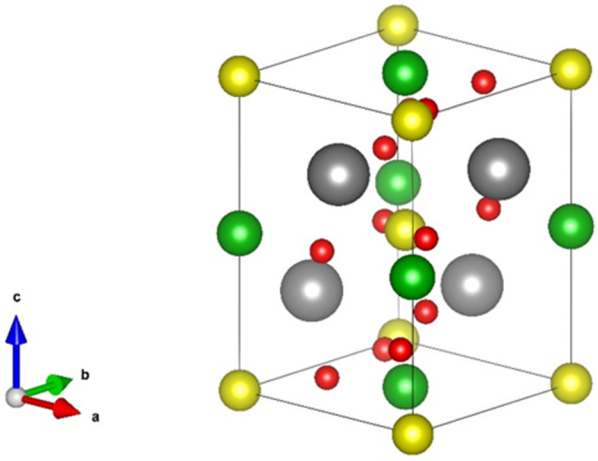

List of abbreviations

μ_B	Bohr magneton
2D / 3D	Two dimensional / three dimensional
AFM	Atomic force microscopy
BFCO	Bismuth iron chromium oxide
BFO	Bismuth ferrite
BHF	Buffered hydrofluoric acid
BOE	Buffered oxide etch
DAAD	Deutscher Akademischer Austauch Dienst
DFT	Density functional theory
DI	Deionized
DMFT	Dynamic mean field theory
DP	Double perovskite
dpc	Double pseudo-cubic
EDS/EDX	Energy dispersive spectroscopy by X-rays
Eg.	Exempli gratia
emu	Electromagnetic unit
Eq.	Equation
ESCA	Electron spectroscopy for chemical analysis
ESRF	European synchrotron radiation facility
EXAFS	Extended X-ray absorption fine structure
f.u.	Formula unit
FAST	Field assisted sintering technique
FEG	Field emission gun
Fig.	Figure
FWHM	Full width at half maximum
HAADF	High angle annular dark field
HF	Hydrofluoric acid
HREM	High resolution electron microscope
KPM	Kelvin probe miscroscopy
LBMRO	Lanthanum bismuth manganese rhenium oxide
LMRO	Lanthanum manganese rhenium oxide
LNRO	Lanthanum nickel rhenium oxide
MBE	Molecular beam epitaxy
MFM	Magnetic force microscopy
MPMS	Magnetic property measurement system
NEXAFS	Near edge X-ray absorption fine structure
NI	Normalized intensity
PAW	Projected augmented wave
pc	Pseudo-cubic
PFM	Piezoresponse force microscopy
PLD	Pulsed laser deposition
Ref.	Reference
RF	Radio frequency
RHEED	Reflection high energy electron diffraction
RSM	Reciprocal space mapping
sccm	Standard cubic centimeters per minute
SEM	Scanning electron microscopy
SP	Superstructure peak
SPS	Spark plasma sintering
SQUID	Superconducting quantum interference device
STEM	Scanning transmission electron microscopy
STO	Strontium titanate
TEM	Transmission electron microscopy
UHV	Ultra-high vacuum
UV	Ultraviolet
VASP	Vienna ab initio simulation package
XANES	X-ray absorption near edge spectra
XAS	X-ray absorption spectroscopy
XMCD	X-ray magnetic circular dichroism
XPS	X-ray photoelectron spectroscopy
XRD	X-ray diffraction
XRR	X-ray reflectivity

List of figures

List of tables

References

[1] K.-I. Kobayashi, T. Kimura, H. Sawada, K. Terakura, and Y. Tokura, Nature **395**, 677 (1998).

[2] Y. Krockenberger, K. Mogare, M. Reehuis, M. Tovar, M. Jansen, G. Vaitheeswaran, V. Kanchana, F. Bultmark, A. Delin, F. Wilhelm, A. Rogalev, A. Winkler, and L. Alff, Phys. Rev. B **75**, 020404(R) (2007).

[3] S. Vasala and M. Karppinen, Prog. Solid State Chem. **43**, 1 (2015).

[4] M. Ležai and N.A. Spaldin, Phys. Rev. B **83**, 24410 (2011).

[5] M.G. Blamire, J.L. MacManus-Driscoll, N.D. Mathur, and Z.H. Barber, Adv. Mater. **21**, 3827 (2009).

[6] M. Opel, J. Phys. D. Appl. Phys. **45**, 33001 (2012).

[7] A.M. Glazer and H.D. Megaw, Acta Crystallogr. Sect. A **29**, 489 (1973).

[8] A.M. Glazer, Acta Crystallogr. Sect. B **28**, 3384 (1972).

[9] D. Dijkkamp, T. Venkatesan, X.D. Wu, S.A. Shaheen, N. Jisrawi, Y.H. Min-Lee, W.L. McLean, and M. Croft, Appl. Phys. Lett. **51**, 619 (1987).

[10] M.K. Wu, J.R. Ashburn, C.J. Torng, P.H. Hor, R.L. Meng, L. Gao, Z.J. Huang, Y.Q. Wang, and C.W. Chu, Phys. Rev. Lett. **58**, 908 (1987).

[11] J.B. Goodenough, Prog. Solid State Chem. **5**, 145 (1971).

[12] C. Rao and B. Raveau, *Transition Metal Oxides* (New York: Wiley- VCH, 1998).

[13] M. Johnsson and P. Lemmens, in *Handb. Magn. Adv. Magn. Mater.* (John Wiley & Sons, Ltd, Chichester, UK, 2007).

[14] K. Momma and F. Izumi, J. Appl. Crystallogr. **44**, 1272 (2011).

[15] Y.A. Abramov, V.G. Tsirelson, V.E. Zavodnik, S.A. Ivanov, and I.D. Brown, Acta Crystallogr. Sect. B **51**, 942 (1995).

[16] V.M. Goldschmidt, Naturwissenschaften **14**, 477 (1926).

[17] A.F. Wells, *Structural Inorganic Chemistry* (Oxford Science Publications, London, 1993).

[18] A.M. Glazer, Acta Crystallogr. Sect. A **A31**, 756 (1975).

[19] T. Wolfram and S. Ellialtioglu, *Electronic and Optical Properties of D-Band Perovskites* (Cambridge University Press, 2006).

[20] L. Chen, N. Dai, X. Jiang, K. Jin, H. Liu, H. Zhao, and S.J.T.U. Press, *Advances in Condensed Matter Optics* (Walter de Gruyter GmbH & Co KG, 2015).

[21] K. Van Benthem, C. Elsässer, and R.H. French, J. Appl. Phys. **90**, 6156 (2001).

[22] D. Serrate, J.M. De Teresa, and M.R. Ibarra, J. Phys. Condens. Matter **19**, 23201 (2007).

[23] J. Longo and R. Ward, J. Am. Chem. Soc. **83**, 2816 (1961).

[24] P.M. Woodward, Acta Crystallogr. Sect. B Struct. Sci. **53**, 32 (1997).

[25] G. King and P.M. Woodward, J. Mater. Chem. **20**, 5785 (2010).

[26] D. Serrate, J.M. De Teresa, and M.R. Ibarra, J. Phys. Condens. Matter **19**, 23201 (2007).

[27] R.D. Shannon, Acta Crystallogr. Sect. A **32**, 751 (1976).

[28] V. Shabadi, M. Major, P. Komissinskiy, M. Vafaee, A. Radetinac, M. Baghaie Yazdi, W. Donner, and L.

Alff, J. Appl. Phys. **116**, 114901 (2014).

[29] L.I. Balcells, J. Navarro, M. Bibes, A. Roig, B. Martínez, and J. Fontcuberta, Appl. Phys. Lett. **78**, 781 (2001).

[30] M.T. Anderson, K.B. Greenwood, G.A. Taylor, and K.R. Poeppelmeier, Prog. Solid State Chem. **22**, 197 (1993).

[31] S. Blundell, *Magnetism in Condensed Matter* (Oxford University Press Inc., New York, 2001).

[32] J. Kanamori, J. Phys. Chem. Solids **10**, 87 (1959).

[33] P.W. Anderson, in *Magnetism*, edited by G.T. Rado and H. Suhl (Academic Press, New York, 1963), pp. 25–83.

[34] J.B. Goodenough, *Magnetism and the Chemical Bond* (Interscience Publisher, New York, 1963).

[35] J.-S. Zhou and J. Goodenough, Phys. Rev. B **66**, 9 (2002).

[36] P. Baettig, C. Ederer, and N.A. Spaldin, Phys. Rev. B **72**, 214105 (2005).

[37] J.B. Philipp, P. Majewski, L. Alff, A. Erb, R. Gross, T. Graf, M.S. Brandt, J. Simon, T. Walther, W. Mader, D. Topwal, and D.D. Sarma, 14 (2003).

[38] S. Geprägs, F.D. Czeschka, M. Opel, S.T.B. Goennenwein, W. Yu, W. Mader, and R. Gross, J. Magn. Magn. Mater. **321**, 2001 (2009).

[39] H. Schmid, Ferroelectrics **162**, 317 (1994).

[40] W. Eerenstein, N.D. Mathur, and J.F. Scott, Nature **442**, 759 (2006).

[41] M. Fiebig, J. Phys. D Appl. Physics. **38**, R123 (2005).

[42] J.F. Scott, Nat. Mater. **6**, 256 (2007).

[43] M. Gajek, M. Bibes, S. Fusil, K. Bouzehouane, J. Fontcuberta, A. Barthélémy, and A. Fert, Nat. Mater. **6**, 296 (2007).

[44] A. Lyle, J. Harms, S. Patil, X. Yao, D.J. Lilja, and J.-P. Wang, Appl. Phys. Lett. **97**, 152504 (2010).

[45] N.A. Hill, J. Phys. Chem. B **104**, 6694 (2000).

[46] N.A. Spaldin, S. Cheong, and R. Ramesh, Phys. Today 38 (2010).

[47] D. Khomskii, Phys. 2 **20**, (2009).

[48] L.W. Martin, S.P. Crane, Y.-H. Chu, M.B. Holcomb, M. Gajek, M. Huijben, C.-H. Yang, N. Balke, and R. Ramesh, J. Phys. Condens. Matter **20**, 434220 (2008).

[49] L.W. Martin and R. Ramesh, Acta Mater. **60**, 2449 (2012).

[50] J. Wang, J.B. Neaton, H. Zheng, V. Nagarajan, and S.B. Ogale, Science **299**, 1719 (2003).

[51] W. Eerenstein, F.D. Morrison, J. Dho, M.G. Blamire, J.F. Scott, and N.D. Mathur, Science **307**, 1203a (2005).

[52] H. Béa, M. Bibes, S. Fusil, K. Bouzehouane, E. Jacquet, K. Rode, P. Bencok, and A. Barthélémy, Phys. Rev. B - Condens. Matter Mater. Phys. **74**, 3 (2006).

[53] Y. Shimakawa, M. Azuma, and N. Ichikawa, Materials (Basel). **4**, 153 (2011).

[54] G. Koster, M. Huijben, and G. Rijnders, *Epitaxial Growth of Complex Metal Oxides* (Elsevier Ltd., 2015).

[55] X. Yu, T.J. Marks, and A. Facchetti, Nat. Mater. **15**, 383 (2016).

[56] R.P. Howson, Pure Appl. Chem. **66**, 1311 (1994).

[57] R. Eason, *Pulsed Laser Deposition of Thin Films: Applications-Led Growth of Functional Materials* (John Wiley & Sons, Inc., Hoboken, New Jersey, 2007).

[58] H.M. Christen and G. Eres, J. Phys. Condens. Matter **20**, 264005 (2008).

[59] W. Donner, C. Chen, M. Liu, A.J. Jacobson, Y.L. Lee, M. Gadre, and D. Morgan, Chem. Mater. **23**, 984 (2011).

[60] T.K. Kenji Ueda, Hitoshi Tabata, Science **280**, 1064 (1998).

[61] S. Chakraverty, A. Ohtomo, D. Okuyama, M. Saito, M. Okude, R. Kumai, T. Arima, Y. Tokura, S. Tsukimoto, Y. Ikuhara, and M. Kawasaki, Phys. Rev. B **84**, 64436 (2011).

[62] S. Chakraverty, K. Yoshimatsu, Y. Kozuka, H. Kumigashira, M. Oshima, T. Makino, A. Ohtomo, and M. Kawasaki, Phys. Rev. B **84**, 132411 (2011).

[63] S. Chakraverty, X.Z. Yu, M. Kawasaki, Y. Tokura, and H.Y. Hwang, Appl. Phys. Lett. **102**, 222406 (2013).

[64] A. Ohtomo, S. Chakraverty, H. Mashiko, T. Oshima, and M. Kawasaki, J. Mater. Res. **28**, 689 (2013).

[65] C. Ederer and N.A. Spaldin, Phys. Rev. Lett. **95**, 2 (2005).

[66] D.G. Schlom, L.-Q. Chen, X. Pan, A. Schmehl, and M.A. Zurbuchen, J. Am. Ceram. Soc. **91**, 2429 (2008).

[67] J. Mannhart and D.G. Schlom, Science **327**, 1607 (2010).

[68] G. Koster, B.L. Kropman, G.J.H.M. Rijnders, D.H.A. Blank, and H. Rogalla, Appl. Phys. Lett. **73**, 2920 (1998).

[69] J.G. Connell, B.J. Isaac, G.B. Ekanayake, D.R. Strachan, and S.S.A. Seo, Appl. Phys. Lett. **101**, 251607 (2012).

[70] M. Kawasaki, T. Maeda, R. Tsuchiya, and H. Koinuma, Science **266**, 1540 (1994).

[71] S. Wolf and R.N. Tauber, *Silicon Processing for the VLSI Era* (Lattice Press, Sunset Beach, CA, 1986).

[72] D.B. Chrisey and G.K. Hubler, *Pulsed Laser Deposition of Thin Films* (John Wiley & Sons, Inc., United States of America, 1994).

[73] Z.A. Munir, U. Anselmi-Tamburini, and M. Ohyanagi, J. Mater. Sci. **41**, 763 (2006).

[74] M. Wehner, in *Excimer Laser Technol.*, edited by D. Basting and G. Marowsky (Springer, 2005).

[75] P. Komissinskiy and A. Radetinac, *Thin Film Growth by Pulsed Laser Deposition (PLD) and in-Situ RHEED Monitoring (Unpublished Lab Manual)* (2015).

[76] B.D. Cullity, *Elements of X-Ray Diffraction* (Pearson Education Limited, 2001).

[77] D.K. Bowen and B.K. Tanner, *High Resolution X-Ray Diffractometry and Topography* (Taylor & Francis Ltd., United Kingdom, 1998).

[78] M. De Graef and M.E. Mchenry, *Structure of Materials*, 1st ed. (Cambridge University Press, 2007).

[79]*Rigaku SmartLab Training Textbook*, 1st ed. (Rigaku Corporation, 2009).

[80] M. Yasaka, Rigaku J. **26**, 1 (2010).

[81] M. Birkholz, P.F. Fewster, and C. Genzel, *Thin Film Analysis by X-Ray Scattering* (Wiley-VCH Verlag GmbH & Co. KGaA, Germany, 2005).

[82] Peter Eaton and Paul West, *Atomic Force Microscopy* (Oxford University Press, United Kingdom, 2010).

[83] G. Binnig and C.F. Quate, Phys. Rev. Lett. **56**, 930 (1986).

[84] Joseph Goldstein, Dale E. Newbury, Patrick Echlin, David C. Joy, Alton D. Romig Jr., Charles E. Lyman, Charles Fiori, and Eric Lifshin, *Scanning Electron Microscopy and X-Ray Microanalysis* (Plenum Press, New York, 1992).

[85] L. Reimer, *Transmission Electron Microscopy : Physics of Image Formation and Microanalysis* (Springer-Verlag Berlin Heidelberg GmbH, 1984).

[86] C. Kübel, A. Voigt, R. Schoenmakers, M. Otten, D. Su, T.-C. Lee, A. Carlsson, and J. Bradley, Microsc. Microanal. **11**, 378 (2005).

[87] J.F. Moulder, W.F. Stickle, P.E. Sobol, and K.D. Bomben, *Handbook of X-Ray Photoelectron Spectroscopy* (Physical Electronics, Inc., Minnesota, 1995).

[88] D. Briggs and M. Seah, *Practical Surface Analysis, Auger and X-Ray Photoelectron Spectroscopy* (John Wiley ans Sons, Ltd., 1996).

[89] H. Weinstock, IEEE Trans. Magn. **27**, 3231 (1991).

[90] W. Buckel and R. Kleiner, *Superconductivity: Fundamentals and Applications* (Wiley-VCH, Weinheim, 2004).

[91] J. Clarke and A.I. Braginski, *The SQUID Handbook* (Wiley-VCH, Weinheim, 2004).

[92] G. Schütz, W. Wagner, W. Wilhelm, P. Kienle, R. Zeller, R. Frahm, and G. Materlik, Phys. Rev. Lett. **58**, 737 (1987).

[93] G. van der Laan and A.I. Figueroa, Coord. Chem. Rev. **277**, 95 (2014).

[94] D.C. Koningsberger and R. Prins, *X-Ray Absorption: Principles, Applications, Techniques of EXAFS, SEXAFS, and XANES* (John Wiley and Sons,New York, 1988).

[95] B.T. Thole, P. Carra, F. Sette, and G. Van Der Laan, Phys. Rev. Lett. **68**, 1943 (1992).

[96] P. Carra, B.T. Thole, M. Altarelli, and X. Wang, Phys. Rev. Lett. **70**, 694 (1993).

[97] N.S. Rogado, J. Li, A.W. Sleight, and M.A. Subramanian, Adv. Mater. **17**, 2225 (2005).

[98] M.P. Singh, K.D. Truong, and P. Fournier, Appl. Phys. Lett. **91**, 42504 (2007).

[99] P. Baettig and N.A. Spaldin, Appl. Phys. Lett. **86**, 12505 (2005).

[100] M. Sakai, A. Masuno, D. Kan, M. Hashisaka, K. Takata, M. Azuma, M. Takano, and Y. Shimakawa, Appl. Phys. Lett. **90**, 72903 (2007).

[101] L. Bi, A.R. Taussig, H.-S. Kim, L. Wang, G.F. Dionne, D. Bono, K. Persson, G. Ceder, and C.A. Ross, Phys. Rev. B **78**, 104106 (2008).

[102] M.P. Singh, K.D. Truong, P. Fournier, P. Rauwel, E. Rauwel, L.P. Carignan, and D. Ḿnard, Appl. Phys. Lett. **92**, 90 (2008).

[103] K. Ueda, H. Tabata, and T. Kawai, Phys. Rev. B **60**, R12561 (1999).

[104] K. Yoshimatsu, K. Nogami, K. Watarai, K. Horiba, H. Kumigashira, O. Sakata, T. Oshima, and a. Ohtomo, Phys. Rev. B **91**, 2 (2015).

[105] H. Guo, J. Burgess, S. Street, A. Gupta, T.G. Calvarese, and M.A. Subramanian, Appl. Phys. Lett. **89**, (2006).

[106] M. Hashisaka, D. Kan, A. Masuno, M. Takano, Y. Shimakawa, T. Terashima, and K. Mibu, Appl. Phys. Lett. **89**, (2006).

[107] M.P. Singh, S. Charpentier, K.D. Truong, and P. Fournier, Appl. Phys. Lett. **90**, 211915 (2007).

[108] H.Z. Guo, A. Gupta, T.G. Calvarese, and M.A. Subramanian, Appl. Phys. Lett. **89**, 5 (2006).

[109] R. Nechache, C. Harnagea, L.-P. Carignan, O. Gautreau, L. Pintilie, M.P. Singh, D. Ménard, P. Fournier, M. Alexe, and A. Pignolet, J. Appl. Phys. **105**, 61621 (2009).

[110] N. Ichikawa, M. Arai, Y. Imai, K. Hagiwara, H. Sakama, M. Azuma, Y. Shimakawa, M. Takano, Y. Kotaka, M. Yonetani, H. Fujisawa, M. Shimizu, K. Ishikawa, and Y. Cho, Appl. Phys. Express **1**, 101302 (2008).

[111] H. Zhao, H. Kimura, Z. Cheng, X. Wang, K. Ozawa, and T. Nishida, Phys. Status Solidi - Rapid Res. Lett. **4**, 314 (2010).

[112] P. Padhan, P. LeClair, a Gupta, and G. Srinivasan, J. Phys. Condens. Matter **20**, 355003 (2008).

[113] R. Nechache, C. Harnagea, A. Pignolet, F. Normandin, T. Veres, L.-P. Carignan, and D. Ménard, Appl. Phys. Lett. **89**, 102902 (2006).

[114] M.R. Suchomel, C.I. Thomas, M. Allix, M.J. Rosseinsky, A.M. Fogg, and M.F. Thomas, Appl. Phys. Lett. **90**, 112909 (2007).

[115] D.H. Kim, H.N. Lee, M.D. Biegalski, and H.M. Christen, Appl. Phys. Lett. **91**, 42906 (2007).

[116] F. Bai, L. Shi, H. Zhang, Z. Zhong, and W. Wang, J. Appl. Phys. **111**, 07C702 (2012).

[117] R. Nechache, C. Nauenheim, U. Lanke, A. Pignolet, and F. Rosei, J. Phys. Condens. Matter **142202**, (2012).

[118] L. Sha, J. Miao, S.Z. Wu, X.G. Xu, Y. Jiang, and L.J. Qiao, J. Alloys Compd. **554**, 299 (2013).

[119] J.L. Zhu, H.X. Yang, S.M. Feng, L.J. Wang, Q.Q. Liu, C.Q. Jin, X.H. Wang, L.T. Li, and J. Yu, Int. J. Mod. Phys. B **27**, 1362023 (2013).

[120] G. Vinai, A. Khare, D.S. Rana, E. Di Gennaro, B. Gobaut, R. Moroni, A.Y. Petrov, U. Scotti Di Uccio, G. Rossi, F. Miletto Granozio, G. Panaccione, and P. Torelli, APL Mater. **3**, 116107 (2015).

[121] J. Wang, J.B. Neaton, H. Zheng, V. Nagarajan, S.B. Ogale, B. Liu, D. Viehland, V. Vaithyanathan, D.G. Schlom, U. V Waghmare, N. a Spaldin, K.M. Rabe, M. Wuttig, and R. Ramesh, Science **299**, 1719 (2003).

[122] H. Béa, M. Bibes, A. Barthélémy, K. Bouzehouane, E. Jacquet, A. Khodan, J.P. Contour, S. Fusil, F. Wyczisk, A. Forget, D. Lebeugle, D. Colson, and M. Viret, Appl. Phys. Lett. **87**, 4 (2005).

[123] K.Y. Yun, M. Noda, M. Okuyama, H. Saeki, H. Tabata, and K. Saito, J. Appl. Phys. **96**, 3399 (2004).

[124] L. You, N. Chua, K. Yao, L. Chen, and J. Wang, Phys. Rev. B **80**, 2 (2009).

[125] D.H. Kim, H.N. Lee, M. Varela, and H.M. Christen, Appl. Phys. Lett. **89**, 2004 (2006).

[126] W. Eerenstein, F.D. Morrison, J.F. Scott, and N.D. Mathur, Appl. Phys. Lett. **87**, 6 (2005).

[127] W. Xu, J. Sun, X. Xu, G. Yuan, Y. Zhang, J. Liu, and Z. Liu, Appl. Phys. Lett. **109**, 152903 (2016).

[128] P. Schmidt, Thermodynamische Analyse Der Existenzbereiche Fester Phasen -Prinzipien Der Syntheseplanung in Der Anorganischen Festkörperchemie, TU Dresden, 2007.

[129] R. Nechache, L.-P. Carignan, L. Gunawan, C. Harnagea, G.A. Botton, D. Ménard, and A. Pignolet, J. Mater. Res. **22**, 2102 (2007).

[130] V.S. Dharmadhikari, S.R. Sainkar, S. Badrinarayan, and A. Goswami, J. Electron Spectros. Relat. Phenomena **25**, 181 (1982).

[131] M. Takahashi, M. Noda, and M. Okuyama, J. Appl. Phys. **94**, 6729 (2003).

[132] V. Kannan, M. Arredondo, F. Johann, D. Hesse, C. Labrugere, M. Maglione, and I. Vrejoiu, Thin Solid Films **545**, 130 (2013).

[133] D. Briggs, *Handbook of X-Ray Photoelectron Spectroscopy* (1981).

[134] L. Qiao, H.Y. Xiao, S.M. Heald, M.E. Bowden, T. Varga, G.J. Exarhos, M.D. Biegalski, I.N. Ivanov, W.J. Weber, T.C. Droubay, and S.A. Chambers, J. Mater. Chem. C **1**, 4527 (2013).

[135] E. Desimoni, C. Malitesta, P.G. Zambonin, and J.C. Rivière, Surf. Interface Anal. **13**, 173 (1988).

[136] M.C. Biesinger, B.P. Payne, A.P. Grosvenor, L.W.M. Lau, A.R. Gerson, and R.S.C. Smart, Appl. Surf. Sci. **257**, 2717 (2011).

[137] T. Yamashita and P. Hayes, Appl. Surf. Sci. **254**, 2441 (2008).

[138] X. Wang, Y. Lin, X. Ding, and J. Jiang, J. Alloys Compd. **509**, 6585 (2011).

[139] K. Wandelt, Surf. Sci. Rep. **2**, 1 (1982).

[140] D. Kothari, V.R. Reddy, A. Gupta, D.M. Phase, N. Lakshmi, S.K. Deshpande, and A.M. Awasthi, J. Phys. Condens. Matter **19**, 136202 (2007).

[141] L. Reinhard, J.L. Robertson, and S.C. Moss, Phys. Rev. B **45**, 2662 (1992).

[142] E. Langenberg, J. Rebled, S. Estradé, C.J.M. Daumont, J. Ventura, L.E. Coy, M.C. Polo, M. V. García-Cuenca, C. Ferrater, B. Noheda, F. Peiró, M. Varela, and J. Fontcuberta, J. Appl. Phys. **108**, 123907 (2010).

[143] W. Kraus and G. Nolzeb, J. Appl. Crystallogr. **29**, 301 (1996).

[144] P. Wadley, A. Crespi, J. Gázquez, M.A. Roldán, P. García, V. Novak, R. Campion, T. Jungwirth, C. Rinaldi, X. Martí, V. Holy, C. Frontera, and J. Rius, J. Appl. Crystallogr. **46**, 1749 (2013).

[145] B. Ravel and M. Newville, J. Synchrotron Radiat. **12**, 537 (2005).

[146] D.I. Woodward and I.M. Reaney, Acta Crystallogr. B. **61**, 387 (2005).

[147] F. Kubel and H. Schmid, Acta Crystallogr. Sect. B Struct. Sci. **46**, 698 (1990).

[148] P. Fischer, M. Polomska, I. Sosnowska, and M. Szymanski, J. Phys. C Solid St. Phys. **13**, 1931 (1979).

[149] P.C. Rout, A. Putatunda, and V. Srinivasan, Phys. Rev. B **93**, 104415 (2016).

[150] J.B. Philipp, D. Reisinger, M. Schonecke, a. Marx, a. Erb, L. Alff, R. Gross, and J. Klein, Appl. Phys. Lett. **79**, 3654 (2001).

[151] J.B. Philipp, D. Reisinger, M. Schonecke, M. Opel, A. Marx, A. Erb, L. Alff, and R. Gross, J. Appl. Phys. **93**, 6853 (2003).

[152] A.J. Hauser, J.R. Soliz, M. Dixit, R.E.A. Williams, M.A. Susner, B. Peters, L.M. Mier, T.L. Gustafson, M.D. Sumption, H.L. Fraser, P.M. Woodward, and F.Y. Yang, Phys. Rev. B **85**, 161201(R) (2012).

[153] R. Morrow, J.R. Soliz, A.J. Hauser, J.C. Gallagher, M.A. Susner, M.D. Sumption, A.A. Aczel, J. Yan, F. Yang, and P.M. Woodward, J. Solid State Chem. **238**, 46 (2016).

[154] T.K. Mandal, C. Felser, M. Greenblatt, and J. Kübler, Phys. Rev. B **78**, 134431 (2008).

[155] T. Alamelu, U. V. Varadaraju, M. Venkatesan, A.P. Douvalis, and J.M.D. Coey, J. Appl. Phys. **91**, 8909 (2002).

[156] K.-I. Kobayashi, T. Kimura, Y. Tomioka, H. Sawada, K. Terakura, and Y. Tokura, Phys. Rev. B **59**,

11159 (1999).

[157] W. Prellier, V. Smolyaninova, A. Biswas, C. Galley, R.L. Greene, K. Ramesha, and J. Gopalakrishnan, J. Phys. Condens. Matter **12**, 965 (2000).

[158] W. Witczak-Krempa, G. Chen, Y.B. Kim, and L. Balents, Annu. Rev. Condens. Matter Phys. **5**, 57 (2014).

[159] D. Pesin and L. Balents, Nat. Phys. **6**, 376 (2010).

[160] S. Calder, V.O. Garlea, D.F. McMorrow, M.D. Lumsden, M.B. Stone, J.C. Lang, J.W. Kim, J.A. Schlueter, Y.G. Shi, K. Yamaura, Y.S. Sun, Y. Tsujimoto, and A.D. Christianson, Phys. Rev. Lett. **108**, 1 (2012).

[161] S.J. Moon, H. Jin, K.W. Kim, W.S. Choi, Y.S. Lee, J. Yu, G. Cao, A. Sumi, H. Funakubo, C. Bernhard, and T.W. Noh, Phys. Rev. Lett. **101**, 2 (2008).

[162] J. Navarro, C. Frontera, L. Balcells, B. Martínez, and J. Fontcuberta, Phys. Rev. B **64**, 92411 (2001).

[163] P. Majewski, S. Geprägs, O. Sanganas, M. Opel, R. Gross, F. Wilhelm, A. Rogalev, and L. Alff, Appl. Phys. Lett. **87**, 202503 (2005).

[164] A.W. Sleight, J. Longo, and R. Ward, Inorg. Chem. **1**, 245 (1962).

[165] R. Takahashi, I. Ohkubo, K. Yamauchi, M. Kitamura, Y. Sakurai, M. Oshima, T. Oguchi, Y. Cho, and M. Lippmaa, Phys. Rev. B **91**, 134107 (2015).

[166] G. Kresse and J. Hafner, Phys. Rev. B **47**, 558 (1993).

[167] G. Kresse, Dissertation, Technische Universität Wien, 1993.

[168] G. Kresse and J. Furthmüller, Phys. Rev. B **54**, 11169 (1996).

[169] J. Kresse, G., Furthmüller, Comput. Math. Sci. **6**, 15 (1996).

[170] D. Kresse, G., Joubert, Ibid. **59**, 1758 (1999).

[171] P.E. Blöchl, Ibid. **50**, 17953 (1994).

[172] J.P. Perdew, A. Ruzsinszky, G.I. Csonka, O.A. Vydrov, G.E. Scuseria, L.A. Constantin, X. Zhou, and K. Burke, Phys. Rev. Lett. **100**, 136406 (2008).

[173] J.P. Perdew, A. Ruzsinszky, G.I. Csonka, O.A. Vydrov, G.E. Scuseria, L.A. Constantin, X. Zhou, and K. Burke, Phys. Rev. Lett. **102**, 39902 (2009).

[174] C.J. Howard, B.J. Kennedy, and P.M. Woodward, Acta Crystallogr. Sect. B **B59**, 463 (2003).

[175] W.L. Phillips, J. Less Common Met. **5**, 97 (1963).

[176] M.T. Greiner, T.C.R. Rocha, B. Johnson, A. Klyushin, A. Knop-Gericke, and R. Schlögl, Zeitschrift Fur Phys. Chemie **228**, 521 (2014).

[177] A. Kulkarni, Structure-Property Correlations in Thin Films of La2MnReO6 Grown by Pulsed Laser Deposition, Indian Institute of Technology Kanpur, 2015.

[178] J. Goniakowski, F. Finocchi, and C. Noguera, Reports Prog. Phys. **71**, 16501 (2007).

[179] I. Hallsteinsen, J.E. Boschker, M. Nord, S. Lee, M. Rzchowski, P.E. Vullum, J.K. Grepstad, R. Holmestad, C.B. Eom, and T. Tybell, J. Appl. Phys. **113**, 0 (2013).

[180] J.M. Lucy, A.J. Hauser, H.L. Wang, J.R. Soliz, M. Dixit, R.E.A. Williams, A. Holcombe, P. Morris, H.L. Fraser, D.W. McComb, P.M. Woodward, and F.Y. Yang, Appl. Phys. Lett. **103**, 1 (2013).

[181] Y. Liu, J.M. Lucy, A. Glavic, H. Ambaye, V. Lauter, F.Y. Yang, and S.G.E. te Velthuis, Phys. Rev. B **90**,

2 (2014).

[182] A.S. Ogale, S.B. Ogale, R. Ramesh, and T. Venkatesan, Appl. Phys. Lett. **75**, 537 (1999).

[183] J. Navarro, L. Balcells, F. Sandiumenge, M. Bibes, A. Roig, and B. Mart, **8481**, (2001).

[184] Y.Y. Tarasevich and T. V. Panchenko, Phys. Solid State **49**, 1283 (2007).

[185] B.L. Henke, E.M. Gullikson, and J.C. Davis, At. Data Nucl. Data Tables **54**, 181 (1993).

[186] M.S. Moreno, J.E. Gayone, M. Abbate, A. Caneiro, D. Niebieskikwiat, R.D. Sánchez, A. De Siervo, R. Landers, and G. Zampieri, Phys. B Condens. Matter **320**, 43 (2002).

[187] D.D. Sarma, Curr. Opin. Solid State Mater. Sci. **5**, 261 (2001).

[188] X. Ou, Z. Li, F. Fan, H. Wang, and H. Wu, Sci. Rep. **4**, 7542 (2014).

[189] A. Tougerti, S. Cristol, E. Berrier, V. Briois, C. La Fontaine, F. Villain, and Y. Joly, Phys. Rev. B - Condens. Matter Mater. Phys. **85**, 1 (2012).